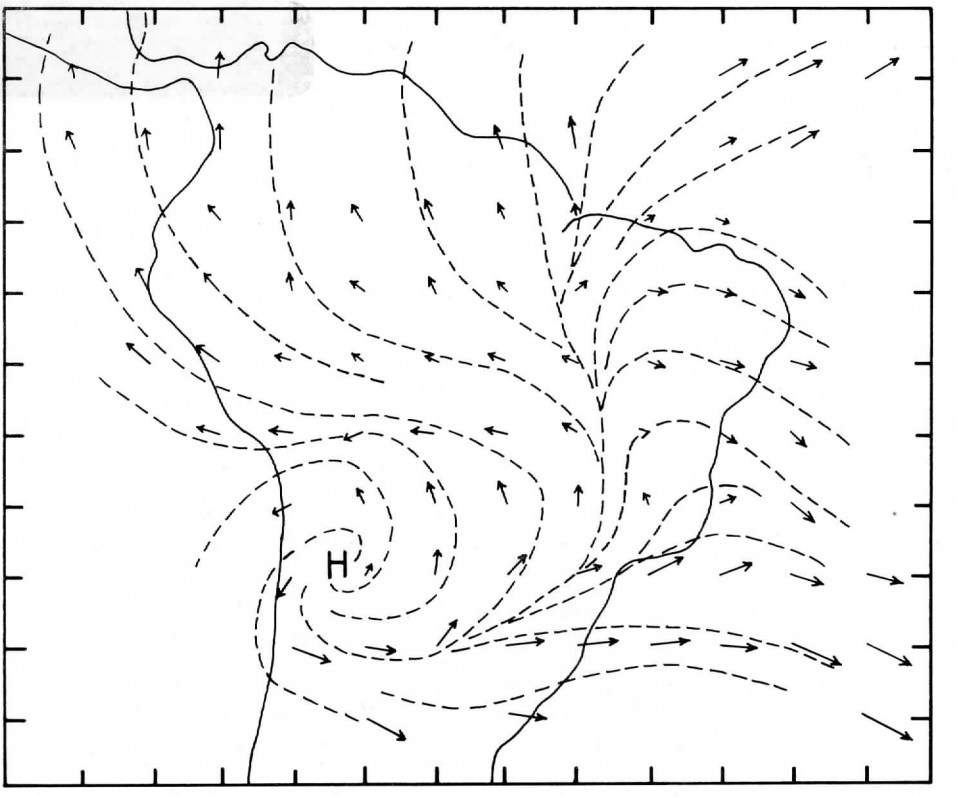


# STUDIES OF SOUNDINGS AND IMAGING MEASUREMENTS

**Final Scientific Report on NAS5-21798**
**1974-1976**

**Space Science and Engineering Center**
**The University of Wisconsin-Madison**
**Madison, Wisconsin**

**July 1977**

## COVER ILLUSTRATION

The upper level wind field (300-100 mb) over South America on 1 February 1975. This illustration from the paper by Hassan Virji is an example of the detailed quantitative information about regions of the atmosphere which is now attainable from images of the earth synchronous orbit satellites. This illustration was selected for the cover because it is typical of the work being produced by students using the Man-computer Interactive Data Access System (McIDAS). The development of this electronic system, which was sponsored by NASA and developed by SSEC, is having a profound effect upon the way in which atmospheric research is conducted.

STUDIES OF SOUNDINGS

AND IMAGING MEASUREMENTS

STUDIES OF SOUNDINGS AND IMAGING MEASUREMENTS

Final Scientific Report on NAS5-21798

1974 - 1976

The research in this document has been supported in whole or part by the National Aeronautics and Space Administration.

July 1977

Published for the Space Science and Engineering Center
by the
University of Wisconsin Press

Published 1977
The University of Wisconsin Press
Box 1379, Madison, Wisconsin 53701

The University of Wisconsin Press, Ltd.
70 Great Russell Street, London



First Printing
Printed in the United States of America
ISBN 0-299-97059-0

This work is a result of research sponsored by NASA, the National Aeronautics and Space Administration, under Contract Number NAS5-21798. The U.S. Government is authorized to produce and distribute reprints for governmental purposes notwithstanding any copyright notation that may appear hereon.

Correspondence concerning editorial matters should be addressed to:

Space Science and Engineering Center
University of Wisconsin
1225 West Dayton Street
Madison, Wisconsin 53706

Orders for copies of this report should be addressed to:

The University of Wisconsin Press

Principal Investigator: Verner E. Suomi

Contributors:
G.R. Diak
B.B. Hinton
W.W. Kuhlow
S.S. Limaye
D.W. Martin
F.R. Mosher
D.R. Phillips
D. Suchman
H. Virji
C.W. Yuen

University of Wisconsin

CONTENTS

## PREFACE

This report marks the close of a research program series which started in 1967. It has been a period of exceptional productivity and one which has seen the observations made from satellites progress from the status of novelties in which a few dreamers saw real value to the status of principal importance among all atmospheric observing techniques. I am very glad that NASA gave me the opportunity to conduct the studies and to support the education of many outstanding young scientists during this period.

The hard work of proving that it is possible to obtain accurate quantitative measures of the important atmospheric parameters from satellite observations is mostly completed. Of course, there will always be a few doubters, but they are being convinced as measurements of cloud motion winds, rainfall amounts, moisture amounts and vertical motions move from the laboratory to the operational weather service.

The means to measure have also been developed and proven, thanks to NASA's continued support. The McIDAS, and the many copies and adaptations of the McIDAS concepts, have provided the basic tools necessary to make the satellite data useful operationally. We will continue to help others make use of the McIDAS developments to the extent that we are able to do so.

What remains to be done now is to exploit the capabilities which have been developed. All of the papers in this report deal with the use of the tools which we have developed under NASA sponsorship. They are the beginning of the exploitation phase. Now we can put students into the research picture in a significant way -- and this is when the real scientific progress can start.

I am extremely proud of the role we at SSEC have been allowed to play in developing the potential of satellite meteorology. I am profoundly grateful to the scientists, students, and staff members, and to our friends in NASA who have made this study series possible.

Verner E. Suomi

# OBSERVATIONS OF SEVERE CONVECTIVE STORMS

# FROM SMS-1 SATELLITE

Chiu-Wai Yuen

## ABSTRACT

The availability of six minute interval SMS-1 visible and infrared data from 30 October 1974 allows an excellent opportunity to observe the development of squall line and tornadic storms. New cells can be observed developing explosively along the line of convergence between the mesohigh outflow and inflow to the mesolow. The four cases of tornadoes are associated with overshooting domes observed both in the visible and infrared imagery. The growth rate of the cirrus cold domes, derived from infrared digital data, can be used to indicate areas of severe convection which tend to associate with severe weather on the ground.

## 1. INTRODUCTION

Geostationary satellites have been an invaluable platform for monitoring severe convective storms. In the era of ATS geostationary satellites, many of the synoptic features associated with severe storms could be identified in the satellite imagery. Purdom (1971) gave illustrative examples of squall line development, low-level jet, and upper-level jet. The characteristics of dry air intrusion in severe storm development were clearly demonstrated by Miller (1973). In the mesoscale, triggering mechanisms such as thunderstorm induced mesohighs can be identified either as an arc-shaped line of convective clouds advancing outward from a dissipating thunderstorm area or as a large thunderstorm cluster with an oval-shaped leading edge (Purdom, 1973).

Direct observations of thunderstorms can also reveal many interesting features. Sikdar, Suomi, and Anderson (1970) have related the horizontal expansion rate of the thunderstorm anvils to the storm intensity. Overshooting turrets from the anvil top of a thunderstorm are easily identified by the shadows they cast on the anvil, especially in the terminator zone. Fujita (1973) proposed a tornado genesis

mechanism by arguing that the collapse of these turrets from a rotating thunderstorm would induce a "twisting downdraft" which enhances the local cyclonic vorticity. However, past studies of severe storms using satellite imagery were hindered by the time and space resolution of the data available; thus only the gross features of the squall line and the individual thunderstorm could be observed. With the launch of SMS-1 geostationary satellite in mid-June of 1974, visible data of 1/2 mile resolution and infrared data of 4 miles resolution are available. Moreover, sectional scans covering the whole severe storm area can be programmed so that picture frequency in the order of one every few minutes is feasible.

On 30 October 1974 severe convective storms broke out in the Texas-Oklahoma-Kansas area. The SMS-1 geostationary satellite, for the first time, took pictures every six minutes from 1830 Z to 2345 Z. The digital data were archived by the McIDAS (Man-Computer Interactive Data Access System), developed at the Space Science and Engineering Center of the University of Wisconsin. This unique data set gives an excellent opportunity to observe the severe storms in more detail.

## 2. SYNOPTIC CONDITIONS OF THE CONVECTIVE STORM ENVIRONMENT

By 1200 Z, 30 October, the environment over the western central plains became favorable for severe convective activities. The 1200 Z surface analysis (Fig. 1) shows a weak low centered over eastern Colorado, with a weak cold front extending southward to western Texas. A southerly flow of warm, moist air is drawn from the Gulf into the low. There is another low pressure system over northern Wisconsin. A trough line extends from this low into the Colorado low, separating the cool moist air in the north from the southerly warm moist air near northern Kansas.

At 850 mb (Fig. 2a), a broad region of low level jet of strength 40-50 knots is associated with the influx of warm moist air into the western central plains region. Aloft, a deep long wave trough is over Utah. At 500 mb (Fig. 2b), a well-defined 80 knot southwesterly jet is positioned just to the west of the deep trough. There has been slight cooling over the western Texas-Oklahoma-Kansas area during the past 12 hours due to the cold air advection by the upper level jet. As a result, the differential horizontal advection in the lower and upper troposphere contribute to set up a convectively unstable environment for thunderstorm formation. The lifted index is -2 at Dodge City, -1.5 at Stephenville, -3 at Oklahoma City, -4.5 at Midland, -4.5 at Amarillo, and -5 at Topeka.

However, the first organized line of thunderstorms is not formed

until 1400 Z near the Oklahoma panhandle. Another line of thunderstorms is initiated by the cold front in western Texas by 1600 Z. By 1800 Z these two systems of thunderstorms develop into a continuous line echo extending southward from Hill City to San Angelo (Fig. 3). A mesohigh-mesolow couplet is found to the west and east of the line echo in Kansas and Oklahoma. The convergence of the moist cool outflow from the mesohigh with the warm moist inflow into the mesolow provides an effective triggering mechanism for new cell development. In the course of the afternoon the mesohigh-mesolow couplet propagates eastward at about 15 knots, as shown in the hourly mesoscale analysis (Figs. 4-9).

During 2115 Z to 2200 Z, three tornadoes, five funnel clouds, heavy rain, and large hail were indicated on the 2200 Z surface analysis; another tornado was also reported at 2315 Z in south central Oklahoma (Storm Data, October 1974). These severe weather events are all associated with the mesolow near the Texas-Oklahoma border.

The system of mesohigh and mesolow in eastern Kansas dissipates by 2100 Z, though confluent flow is still present. Meanwhile, two complexes of thunderstorms form over eastern Kansas and along the trough line near the Kansas-Nebraska border. These thunderstorms were responsible for producing 2-3 inches of rain, considerable small hail, and strong damaging winds locally during the afternoon and evening for the eastern third of Kansas as well as northwestern Missouri. Funnels aloft were reported near Seneca at 2 pm and near Fredonia about 4 pm.

The synoptic environment in which the severe convective storms are imbedded is updated by the lower and upper air charts for 00 Z, 31 October. The moisture and temperature ridge at 850 mb has been pushed eastward by the cold front as the mesohigh-mesolow system propagates to the east. Dry air intrusion is very obvious along the western edge of the moisture ridge. Note the strong convergence between the southerly 40 knot low level jet at Stephenville and the westerly flow at Oklahoma City. The tornadoes reported in Texas and Oklahoma in the afternoon are all located in this convergent area with the marked intrusion of dry air (Fig. 10a). On the 500 mb chart (Fig. 10b), the 80 knot southerly jet has moved up to western Kansas as the trough progresses slowly eastward. Vertical wind shear is weak in speed and direction over most of the storm area, but it is stronger in the tornado incidence area. Soundings for 1200 Z, 30 October, and 00 Z, 31 October, at Stephenville (Fig. 11) and at Topeka (Fig. 12) illustrate the differences in vertical wind distribution over northern Texas and over eastern Kansas.

## 3. OBSERVATIONS OF THE DEVELOPMENT OF TORNADIC STORMS

The McIDAS (Smith, 1975) forms an indispensible tool in this study with its satellite imagery data. Essentially the McIDAS is an image storage, display, and processing system, consisting of data archive, data access, video display, operator console, and computer control sections. An image sector of 500 lines by 672 elements can be displayed on a color television monitor. Since the line-element resolution is 1/2 mile for visible data and 4 miles for the infrared, only the infrared image segment of this size is large enough to cover the whole storm area. Thus the 500 lines by 672 elements visible image sector is designated to cover the tornadic storms in the Oklahoma-Texas region. The designated visible and infrared data segments are extracted from the archive data tape and stored on magnetic save tape through a tape drive. To observe the development of the storms, the sequence of visible images is displayed on the television monitor. Infrared digital data, covering the same area as the visible images, are blown up to match the scale of the visible images and are converted to video gray shade display on the television screen through a separate video channel. Thus the warmest surfaces appear to be darkest, while the coldest areas appear to be brightest. The display of visible and infrared images or interlacing of the two images can be controlled through a keyboard.

Looping of these six minute interval images gives a "smooth" feeling in the development of the convective storm. The high resolution visible images reveal many cloud features which are not clearly discernible in the ATS images; for example, overshooting turrets and individual convective storms within a thunderstorm complex are observable. Convective cells can be traced back to the cumulus stage. The infrared images, due to their 4 mile resolution, do not show up the detailed cloud features as do the visible images. However, the relative height for various cloud features can be determined from the relative gray shades. In addition, an operator can request the original infrared digital data of a subset of the displayed image be shown on the operator console or the line printer. The subset area is specified with a joy-stick controlled cursor. Equivalent blackbody temperature of infrared digital data can also be displayed on the operator console by a single key-in through the keyboard. To illustrate the development of the squall line and the tornadic storms, the sequence of the visible images and the blown-up infrared images are photographed from the television screen (Fig. 13-14). Hourly surface analyses are superimposed on the corresponding visible imagery in order to correlate the surface mesoscale features with the cloud pattern. The imagery will be described in the following time sections.

1832 Z to 1902 Z

The squall line is first triggered off at about 1630 Z by the weak cold front over western Texas. By 1832 Z, it has developed into a band of cumulonimbus clusters with a characteristic tapering end. Anvil tops of individual cells can be identified at this stage; they exhibit different features in the northern and southern halves of the squall line. In the south, the bubbling characteristics of the cloud tops indicate vigorous convection is still going on. This inference is supported by the rapid expansion of the cirrus anvil. Development of new cells can also be observed at the southernmost tip of the squall line. In contrast, anvil tops in the north are rather smooth, indicating that the storms are more mature or decaying.

The back side of the squall line is relatively clear of clouds except for the jet-associated cirrus. With reference to the 500 mb charts at 1200 Z, 30 October (Fig. 2b) and 00 Z, 31 October (Fig. 10b), the axis of the jet stream is roughly located at 100°W, running parallel to the squall line. The absence of low or middle level clouds is indicative of subsidence and advection of dry air on the anticyclonic flank of the jet stream; this subsidence and advection are essential for squall line development (Miller, 1972). There is another line of convective storms on the right edge of the picture frame, lying roughly parallel to the surface moisture ridge. It is interesting to note the more westerly direction of the elongated axis of the anvil, which is parallel to the direction of the vertical shear, for these thunderstorms than that for the squall line. The difference can be explained by the stronger veering with height of the low level southerly flow near these thunderstorms. Tracking of the cloud motion using the first five frames of the image sequence also reveals a southwesterly diffluent flow pattern in the upper troposphere and southerly flow in the lower troposphere (Houghton and Wilson, 1975).

Superposition of the 1900 Z surface analysis on the 1902 Z visible image (Fig. 15) shows a large bubble high beneath the thunderstorms with smooth anvil tops in the northern part of the squall line and an elongated mesolow along the right side of the squall line. The northerly cool moist outflow from the mesohigh converges with the southerly warm moist air near the mesolow center where new convective activities (indicated by arrows) are initiated. Thunderstorms in the southern portion of the squall are still developing under the lifting influence of the cold front.

A large isolated cumulonimbus cloud (A) has been developing rapidly on the southern end of the mesolow. The anvil top casts shadows on a lower cloud deck. Several turrets overshoot from this cloud layer as indicated by an arrow in the visible image sequence at

1850 Z, 1856 Z, and 1902 Z. Equivalent blackbody temperature of this cloud layer, derived from the infrared digital data, is about 5°C. The 1200 Z, 30 October upper air sounding at Stephenville (Fig. 11), which is just to the southeast of this cloud layer, shows inversions at 19°C and 14°C levels. Sounding at 00 Z, 31 October, also indicates a shallow inversion at 3°C. Thus it can be concluded that this flat cloud deck is capped by an inversion layer which is lifted upward and weakened by convection in the afternoon. The inactiveness of the cumulus and cumulus congestus cloud lines on the right side of the mesolow also implies the existence of an inversion layer. The popping up of the individual cumulonimbus cloud A may be the result of a strong thermal breaking through the inversion.

1902 Z to 2000 Z

During the hour, the elongated mesolow remains stationary but deepens considerably (Fig. 16). Surface pressure falls of 0.05 inch of mercury per hour (about 1.3 mb per hour) are observed at Fort Sill, Wichita Falls, and Dallas. In response to the deepening, the low level isallobaric wind converges on the pressure fall centers which are located near the mesolow axis and near Dallas. In addition this convergence is further reinforced by the lifting action of the mesohigh and the cold front behind the mesolow. As a result, convective instability is released and the cumulus and cumulus congestus clouds near the mesolow axis rapidly become cumulonimbus clouds in the latter half of the hour.

Storm A, however, after its maximum development at 1920 Z, begins to degenerate. Anvil cirrus is blown away from the new cells that form at the southwest flank of Storm A. The cumulus and cumulus congestus clouds B, further to the east of the mesolow, remain inactive in the first half of the hour, but later they start to develop slowly. There is another cluster of thunderstorms developing along the axis of the surface moisture tongue in the south, while its counterpart in the north moves out of the picture frame. A small wake-low is found at the back side of the squall line. However, there seems to be no sign of its existence from the satellite images except for the smooth anvil.

2000 Z to 2102 Z

Thunderstorms C, which formed along the axis of the mesolow and at the southern end of the squall line, grow vigorously during this period. The more intense convective cells can be located by the small protruding turrets on the anvils (indicated by arrows at 2030 Z and 2036 Z, Fig. 13a). After 2036 Z, the turrets subside, leaving behind a more smooth cirrus anvil. These storms have reached a cloud top temperature of -65°C. By 2102 Z these storms C have induced a mesohigh

of their own (Fig. 17). The mesolow is displaced eastward as the bubble high pushes forward. The outflow from this mesohigh collides head-on with the inflow into the mesolow. Thus cloud lines B and other small convective cells H to the east of the mesolow develop rapidly as the line of convergence approaches. While the whole squall line cloud system moves towards the northeast, new convective clouds continuously build up along the cold front in the south.

2102 Z to 2208 Z

Three tornadoes, six funnels, heavy rain, and "hen egg" size hail were reported in the mesolow during 2120 Z and 2200 Z. For the convenience of illustration, the visible images during the hour are enlarged (Fig. 18-27) and printer outputs of the infrared digital data of the tornadic storms are also shown (Fig. 28-36). The satellite images are accurately navigated so a point can be located on an image with an error of $\pm$1.8 n. mi (3 lines) in the north-south direction and $\pm$3.3 n. mi (6 elements) in the east-west direction.

At 2120 Z, a tornado and a funnel cloud (S) are reported near Valley View, Cook Co., Texas. Storm G seems to be the tornado producer. By tracing back in the image sequence, storm G is shown to be the merger of storm E and storm F. At 2120 Z, storm G has the lowest cloud top temperature (-65°C) among the other storms developed in the mesolow; storm H has a cloud top temperature of -62°C. Moreover, the anvil of storm G casts shadows on its neighboring anvils. It is interesting to note a tiny protrusion at the top of storm E at 2108 Z. Six minutes later it gradually built up and became a dome-shaped protrusion at 2120 Z. This dome has a radiometric temperature of -59°C while the coldest temperature (-65°C) is about four miles west of this dome. The reported tornado and funnel cloud are just on the southeastern edge of the dome and about six miles south of the coldest cloud top of storm G (Fig. 30).

Storm G, at 2126 Z, 2132 Z, and 2138 Z, still maintains a cloud top temperature of -65°C, which is the highest of the storms in the mesolow. Distinct protrusions can be seen near the western end of the anvil. Meanwhile, vigorously growing new thunderstorms built up at the southwestern flank of complex H.

At 2145 Z, a tornado, four funnel clouds, and heavy rain (T) are reported at southern Gainesville, Cook Co., Texas. The location for this severe weather is indicated in the visible image and the infrared data taken at 2144 Z. It is just south of a large overshooting dome, seen in the visible image as well as in the infrared digital data. There are also a number of tiny turrets in the immediate surrounding anvil. At this time, new cells at the southwestern flank of complex H

have attained cloud top temperatures of -67°C like complex G.

At 2200 Z, another tornado (U) touches down at Dixie, Grayson Co., Texas. Again, the location for tornado occurrence is just southeast of a very pronounced protrusion above the cloud top, as indicated in the visible image and the infrared data taken at 2202 Z. This overshooting dome is not observed in the previous image but can still be identified at 2208 Z.

2208 Z to 2321 Z

The mesolow seems to weaken during this period but its location remains stationary. Meanwhile, the anvil of the storm complex C moves northward out of the picture frame. New cells continuously develop at the southwest flank of the complex H. The bubbling cloud top and the decreasing cloud top temperature suggest intense convection within the complex. There is little cirrus blowoff from this complex as compared to other thunderstorms. Small overshooting turrets can be detected but usually disappear in the following image. Several large boiling cloud tops can be identified within the complex as indicated by arrows at 2245 Z and 2251 Z. These large domes slowly merge with one another at 2303 Z (Fig. 37). Three distinct turrets overshoot from dome D at 2309 Z (Fig. 38). The boiling features of the combined dome become more outstanding. At 2315 Z, two of the turrets on the west can still be detected while the one on the east seems to collapse. A small tornado (R) was reported six miles west of Madill, Marchall Co., Oklahoma, just under the collapsed turret (Fig. 39). The large bubbling dome D can still be observed, though the other two overshooting turrets subside by 2321 Z (Fig. 40). The infrared data for these boiling cloud tops are shown in Figs. 41-44. The domes have an average cloud top temperature of -69°C while the overshooting turrets reach a cloud top temperature of -73°C at 2321 Z and 2328 Z (not shown). Thereafter, the thunderstorms within complex H lose vigor and the cloud tops subside.

## 4. GROWTH CHARACTERISTICS OF COLD DOMES

Anvil expansion rate, determined by using visible data, has been suggested by many researchers [e.g. Sikdar, Suomi, and Anderson (1970), and Purdom (1971)] as an indicator of severe storms or even tornadic storms. However, the anvil expansion can only give a two-dimensional growth rate. A high expansion rate may be due to a large number of moderate updrafts or a few strong updrafts within the thunderstorm complex. Besides, anvils of cumulonimbus clouds within a thunderstorm complex usually merge with one another and it is difficult to define a boundary for the developing cells in anvil expansion calculation even with the high resolution SMS-1 visible data.

Interlacing the visible image with the infrared image shows that intense convective cells within a storm complex have protrusions at their cloud tops, as well as having higher infrared digital counts than their surrounding anvils. The higher digital counts indicate the existence of cloud domes above the general anvil level, from which the turrets overshoot. Cloud heights observed by radar have indicated that the probability of severe storm increases with echo height and is related to tropopause penetration of echo tops (Donaldson, 1965). It is the purpose of this section to interpret the intensity of a thunderstorm complex by using the growth characteristics of the cold domes as observed in the infrared images.

Pitts, Reese, and Medlowitz (1975) have shown the average radiometric temperature is very near the environment temperature at the top of a severe storm. The temperature of the tropopause at 00 Z, 31 October, in the severe storm area is approximately -65°C. Thus the infrared digital value of 206, corresponding to a cloud top temperature of -65°C, is chosen to define the boundary of a "cold dome." As the infrared images cover the whole storm area, it is possible to study other storms besides the tornadic storms in the Oklahoma-Texas region. The infrared image is enhanced so that the cold domes defined by digital value 206 can be easily traced. The cold domes are labelled as shown in the enhanced infrared image at 2202 Z (Fig. 45). Storms with cloud temperature warmer than -65°C are neglected. The area sums at and above certain specified digital levels--within an outline drawn around the cold dome on the McIDAS television screen with the joy-stick controlled cross-hair cursor--are calculated through software programs in the McIDAS. The specified levels in this study are 206, 208, 210, 212, and 214 which correspond to an equivalent blackbody temperature of -65°C, -67°C, -69°C, -71°C, and -73°C respectively.

The areas for the different cloud labels at and below -65°C and -71°C are plotted against time (Fig. 46-47). It must be realized that the -65°C isotherm encircles a changing set of intensely developing cells. Moreover, areas colder than -65°C are the results contributed by a few smaller cold domes which develop and collapse within the -65°C contour. This causes the pauses and spikes in the area change curves.

In Fig. 42, dome labels J and K merge at 2102 Z to form dome label L which, at 2126 Z, split up into dome labels M, N, and O. In Fig. 43, dome labels G and H merge at 2202 Z to form label D. In Fig. 44, dome label P split into dome label Q and dome label V at 2321 Z while dome label Q merges with dome label Y into dome label Z.

Dome labels D, P, and Y distinguish themselves from the rest by having a more rapid rate of area expansion of the -65°C isotherm cold domes, reaching a minimum temperature of -73°C. Such a cloud top temperature implies a protrusion of 6600 feet above the anvil level according to the 00 Z, 31 October sounding at Stephenville, Texas. For these cold domes, areas at and below -67°C occupy about 40 to 60% of the area at and below -65°C. Areas at and below -69°C also occupy about 40 to 60% of the area at and below -67°C. This implies a large cold dome protruding significantly above the anvil. The rest of the storms usually have a slower overall rate of area expansion of the -63°C isotherm. Generally, protrusions from these anvils only reach a temperature of -67°C, though a few domes having a cloud top temperature of -69°C overshoot sporadically. Areas at and below -67°C occupy only 5 to 15% of the area at and below -65°C, and the increase in area enclosed by the -65°C isotherms is mostly due to the spreading out and piling up of the cloud material from the updraft on the anvil. These imply weaker updrafts within these complexes. In addition, labels D, P, and Y persist for a longer period of time as new cells continuously build up in the vicinity. The rest of the cloud complexes develop and decay within the time of the investigation.

Though the growth characteristics of the cold domes in labels D, P, and Y are similar, the associated severe weather is different. Cloud label D is associated with the tornadic storms discussed in the last section. The time of occurrences is also indicated in the area change curve. Three tornadoes are shed under the cloud label G before it merges with label H to form label D. However, during the time of occurrence of the tornadoes, the rate of expansion is slow compared to that of other cloud labels. Another tornado touches down beneath cloud label D at 2314 Z. Though the dome area is decreasing, the minimum dome temperature decreases from -70°C at 2309 Z to -72°C at 2315 Z and to -74°C at 2321 Z.

Cloud labels P, VI, W, and I are thunderstorms that developed over the warm front near the Kansas-Nebraska border, while cloud labels M, N, and O are in the southeast Kansas region. Though intense thunderstorms producing 2-3 inches rain, considerable small hail, and strong damaging winds locally were reported in the afternoon and evening for the eastern third of Kansas, heaviest rains and flash flooding occurred in the northeast sector of Kansas. Heavy thunderstorms moving out of Kansas through northwest Missouri were reported to bring 2-3 inches rain, hail, and wind damage to northwest Missouri in the evening. Since cloud labels VI, W, and I are to the north of Kansas, thunderstorms for dome labels P and Y are most likely to be responsible for the more severe weather in northeast Kansas and northwest Missouri.

The difference in severe weather associated with cloud labels D, P, and Y may be accounted for by the synoptic environment the storms

were embedded in. The 1200 Z, 30 October sounding at Stephenville is characterized by a conditionally unstable temperature lapse rate above and below a stable layer at 650 mb. Though the lifted index is only -1.5 at 1200 Z it increases at -4 by 00 Z, 31 October. Tornadoes in this type of air mass normally occur in families on squall lines associated with mesolow (Miller, 1973). This is the case for the tornadic storms in northern Texas and southern Oklahoma. However, the slight directional shear between the lower and upper jets may be one of the reasons why only three tornadoes occurred.

On the other hand, the 1200 Z, 30 October sounding at Topeka also shows a conditionally unstable lapse rate but with no stable layer. Moisture extends to the upper atmosphere. Tornadoes in this type of air mass occur singly and have a brief life. The frequency of funnels aloft is likely. Funnels did occur in eastern Kansas near Seneca at 2 pm, near Fredonia about 4 pm, and near Garnett about 7 pm. Since no exact time and place is given for these reports, they are neglected in this study. There is very little speed and directional shear between 850 mb and 500 mb wind at 1200 Z, 30 October, and 00 Z, 30 October. Though there is slight dry air intrusion into eastern Kansas and the existence of low level boundaries, that is, the warm front over Kansas-Nebraska border and the mesohigh, the unfavorable low level and middle level wind field does not permit the development of tornadic storms (Miller, 1969).

## 5. CONCLUSION

In the four cases of tornado occurrences studied here, all of the tornadoes seem to be associated with an overshooting dome. Tornadoes at 2120 Z, 2145 Z, and 2200 Z are located near an overshooting dome which is less pronounced six minutes earlier in the image sequence. From the infrared data, the tornadoes are just a few miles south of a "cold dome." Moreover, the temperature of the cold dome at the time of tornado occurrences is lower than that six minutes earlier. Tornadoes which occurred at 2315 Z are located under an overshooting turret that appears to be collapsing, but, according to the infrared data, the temperature of the immediate cloud top remains constant. However, there are two other overshooting turrets within 10 miles to the west of the collapsed turret. Due to the inclined nature of the updraft, tornado R may be related to these two overshooting turrets rather than the collapsed turret. Thus, when observed from satellite altitude, tornadoes in this case study are found to be related to an overshooting dome.

However, Umenhofer (1975) studied the overshooting dome behavior of three tornado-producing thunderstorms using photographs shot from a Lear jet and concluded that the overshooting dome gradually collapses 6-21 minutes before associated tornadic events. The conflicting

findings about the overshooting dome behavior of tornado-producing thunderstorms may be due to the different kind of platform used to observe these overshooting domes. More observations from aircraft and satellite are needed before one can make conclusions about the behavior of overshooting domes of tornado-producing storms.

In this case study, the triggering mechanism of the mesohigh and the self-propagation mechanism of the squall line are clearly demonstrated. New cells and pre-existing inactive cumulus clouds develop explosively along the line of convergence between the mesohigh outflow and warm moist inflow into the mesolow. These storms, after their maximum development, also induce a mesohigh which triggers off new convective storms. This mesohigh-mesolow system also provides a strong shear zone where tornadic storms are likely to develop (Barnes, 1973). In this case study, the tornadic storms all develop in the mesolow and the cloud temperature reaches at least -63°C before the storm produces a tornado. Moreover, the tornadic storm has the lowest cloud top temperature among the storms developed in the mesolow. Thus, in detecting tornadic storms in satellite images, surface mesoscale analysis should be overlaid on the image. Storms triggered off in the mesolow and on the mesohigh boundary must be carefully traced in order to identify the storms that develop rapidly.

The growth characteristic of the "cold dome," determined using infrared data, can be used to interpret the strength of updrafts within a thunderstorm complex. The most severe hailstorms and thunderstorms have a distinctly rapid growth rate of the protrusions. These protrusions are also very persistent in time. These findings are consistent with the observations made by overshooting the top of a hailstorm from a jet plane by Pearl, Shenk, and Skillman (1975). However, three of the four tornadoes are associated with a thunderstorm complex that does not have a fast growing dome.

In short, tornadoes are associated with overshooting cold domes. However, this finding is in conflict with Umenhofer's conclusion. The mesohigh appears to be an important triggering mechanism for new cell development. The cirrus cold domes can be used to indicate areas of severe convection which tend to be associated with severe weather on the surface.

ACKNOWLEDGEMENTS

My warmest gratitude to Professor Verner E. Suomi whose constant encouragement and enthusiasm made this work possible. I would also like to thank Professor Charles E. Anderson for his many useful suggestions and critical evaluations of this paper and Dr. Barry Hinton

for reading the manuscript. Finally I would like to thank Mr. Gary Chatters for navigating the long sequence of satellite images; Mr. Cecil Lo for helping with the drafting; and Ms. Barbara Mueller for her typing assistance.

This research was partially supported by NOAA Grant 04-3-158-61.

## REFERENCES

Barnes, Stanley L., 1973: Radar Observed Merger of Twin Hook Echoes. Preprints of Paper--Eighth Conference of Severe Local Storms, Amer. Meteor. Soc. pp. 155-160.

Donaldson, Ralph, 1965: Methods for Identifying Severe Thunderstorms by Radar: a Guide and Bibliography. Bull. Amer. Meteor. Soc., 45, 174-193.

Fujita, Theodore T., 1973: Proposed Mechanism of Tornado Formation from Rotating Thunderstorm. Preprints of Paper--Eighth Conference of Severe Local Storms, Amer. Meteor. Soc. pp. 191-196.

Houghton, David D. and Thomas A. Wilson, 1975: Mesoscale Wind Field for a Severe Storm Situation Determined from Synchronous Meteorological Satellite (SMS) Cloud Observations. Ninth Conference of Severe Local Storms, Amer. Meteor. Soc. pp. 187-192.

Miller, Joseph A., 1973: Dry Air Intrusion into a Low Level Moist Tongue as Viewed by ATS 3. Mon. Wea. Rev., Vol. 101, No. 7, p. 594-595.

Miller, Robert C., 1969: Forecasting the Degree of Intensity of Severe Thunderstorms. Preprints of Paper--Sixth Conference on Severe Local Storms, Amer. Meteor. Soc. pp. 197-201.

_____, 1972: Notes on Analysis and Severe-Weather Forecasting Procedures of the Military Weather Warning Center. Technical Report 200. U. S. Air Force.

Pearl, Edward W., William E. Shenk, and William Skillman, 1975: Cloud-Top Parameters--a Hail Indicator. Preprint of Paper--Ninth Conference on Severe Local Storms, Amer. Meteor. Soc. pp. 464-467.

Pitts, David E., Warner K. Reese, and Maury A. Mendlowitz, 1975: Equivalent Blackbody Temperature of the Top of a Severe Storm. J. Appl. Meteor., 14, 609-618.

Purdom, James F. W., 1971: Satellite Imagery and Severe Weather Warnings. Preprints of Paper--Seventh Conference on Severe Local Storms, Amer. Meteor. Soc. pp. 120-127.

_____, 1973: Picture of the Month: Mesohigh and Satellite Imagery. Mon. Wea. Rev., 101, 180-181.

Sikdar, D. N., V. E. Suomi, and C. E. Anderson, 1970: Convective Transport of Mass and Energy in Severe Storms Over the United States--an Estimate from a Geostationary Altitude. Tellus, 22, 521-532.

Smith, E. A., 1975: The McIDAS System. IEEE Transactions on Geoscience Electronics, Vol. GE-13, No. 3.

Storm Data. October 1974. Environmental Data Service, Asheville, NC.

Umenhofer, Thomas A., 1975: Overshooting Top Behavior of Three Tornado-Producing Thunderstorms. Preprints of Paper--Ninth Conference on Severe Local Storms, Amer. Meteor. Soc. pp. 96-99.

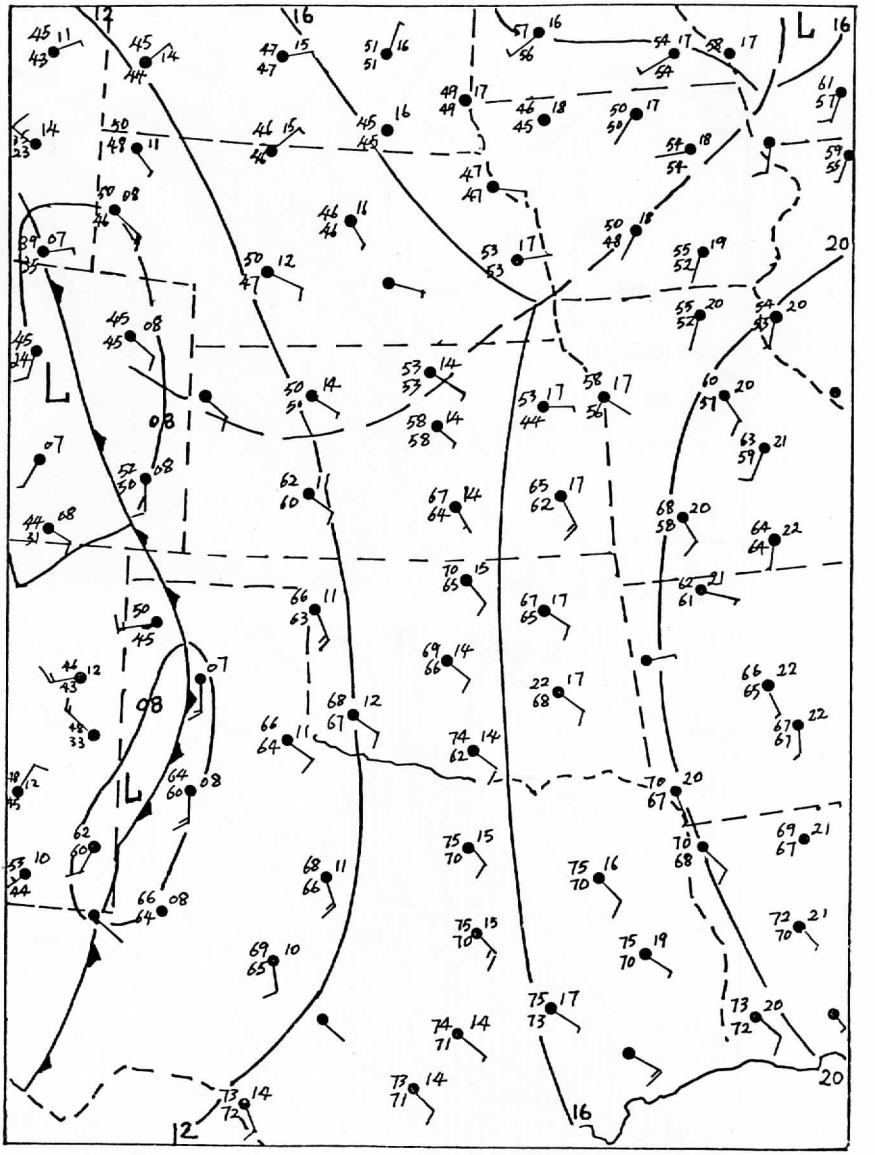

Figure 1. 1200 Z Surface Analysis, 30 October 1974

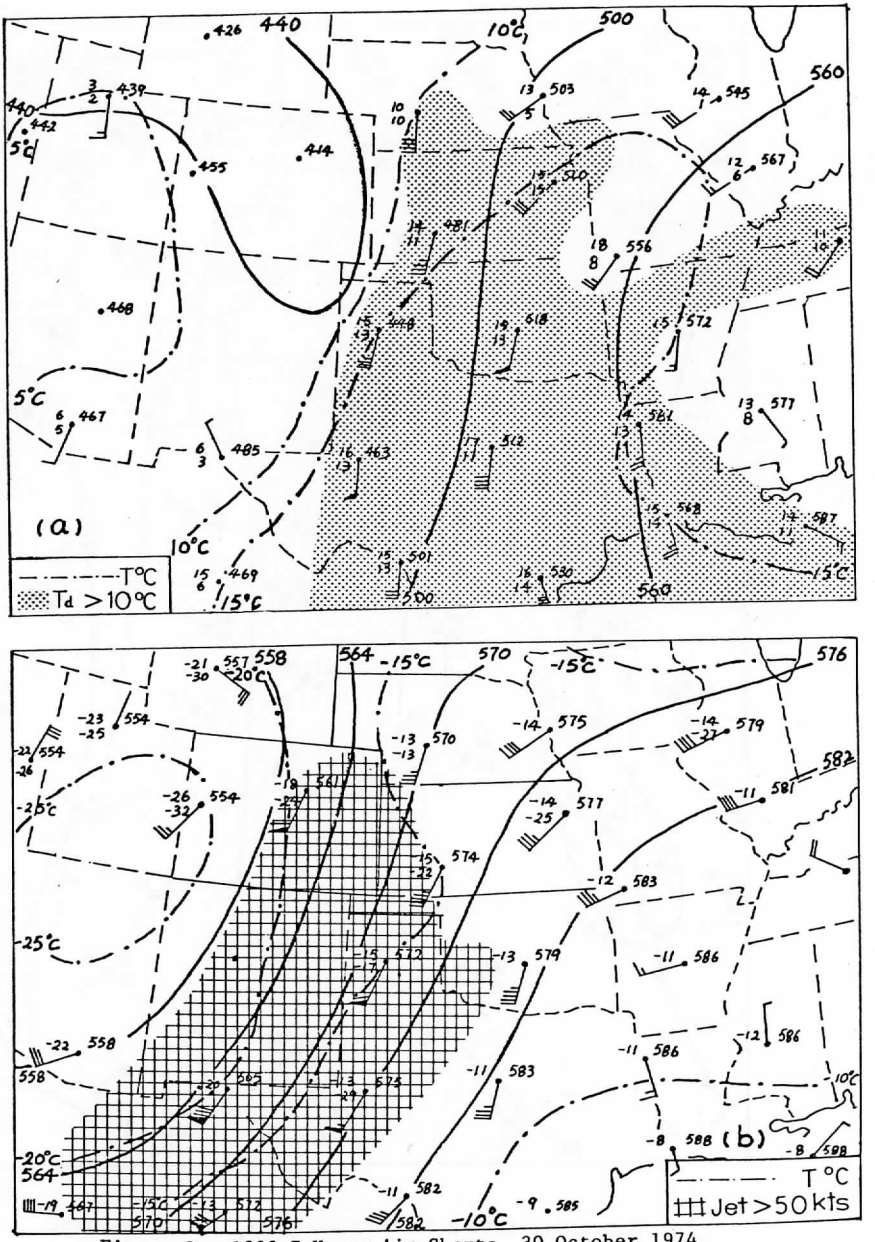


Figure 2. 1200 Z Upper Air Charts, 30 October 1974.
(a) 850 mb (b) 500 mb

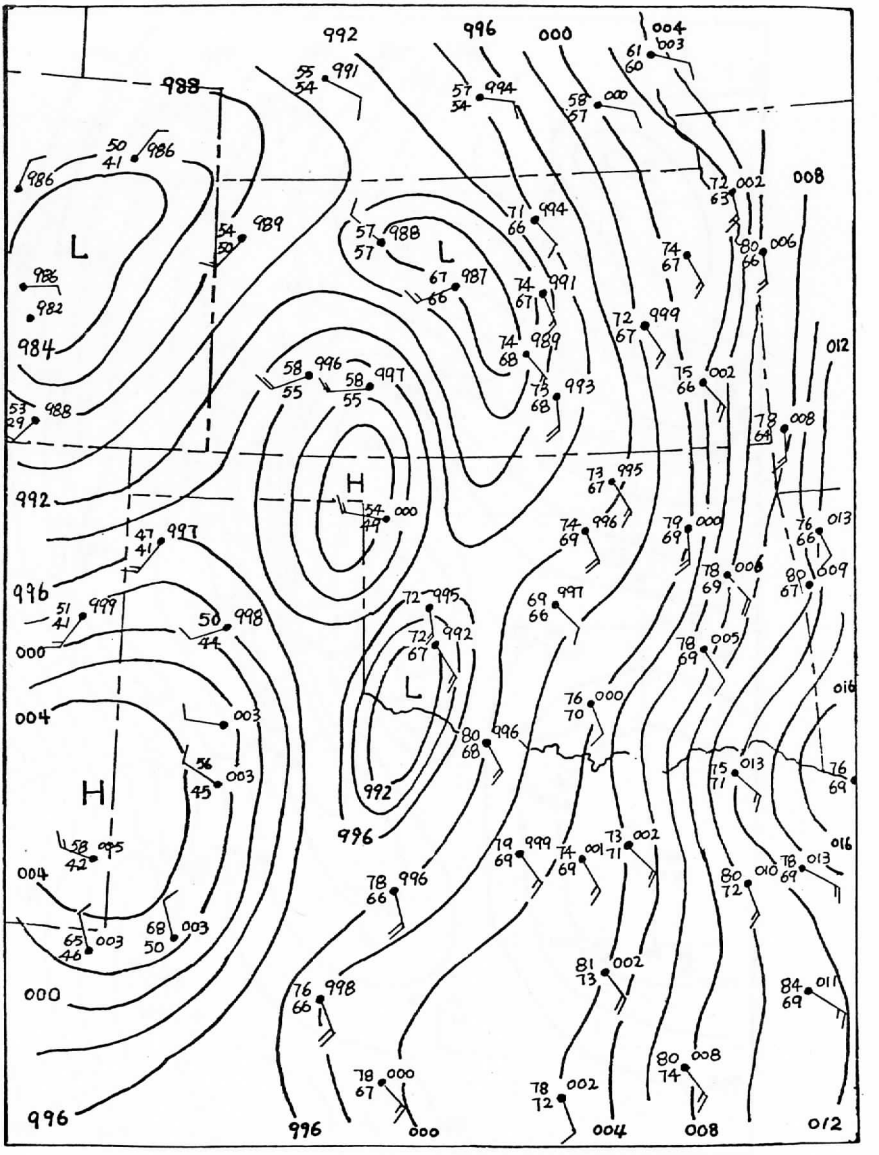


Figure 3. 1800 Z Surface Mesoscale Analysis, 30 October 1974. Surface pressure based on altimeter settings, isobars at intervals of .02 inch.

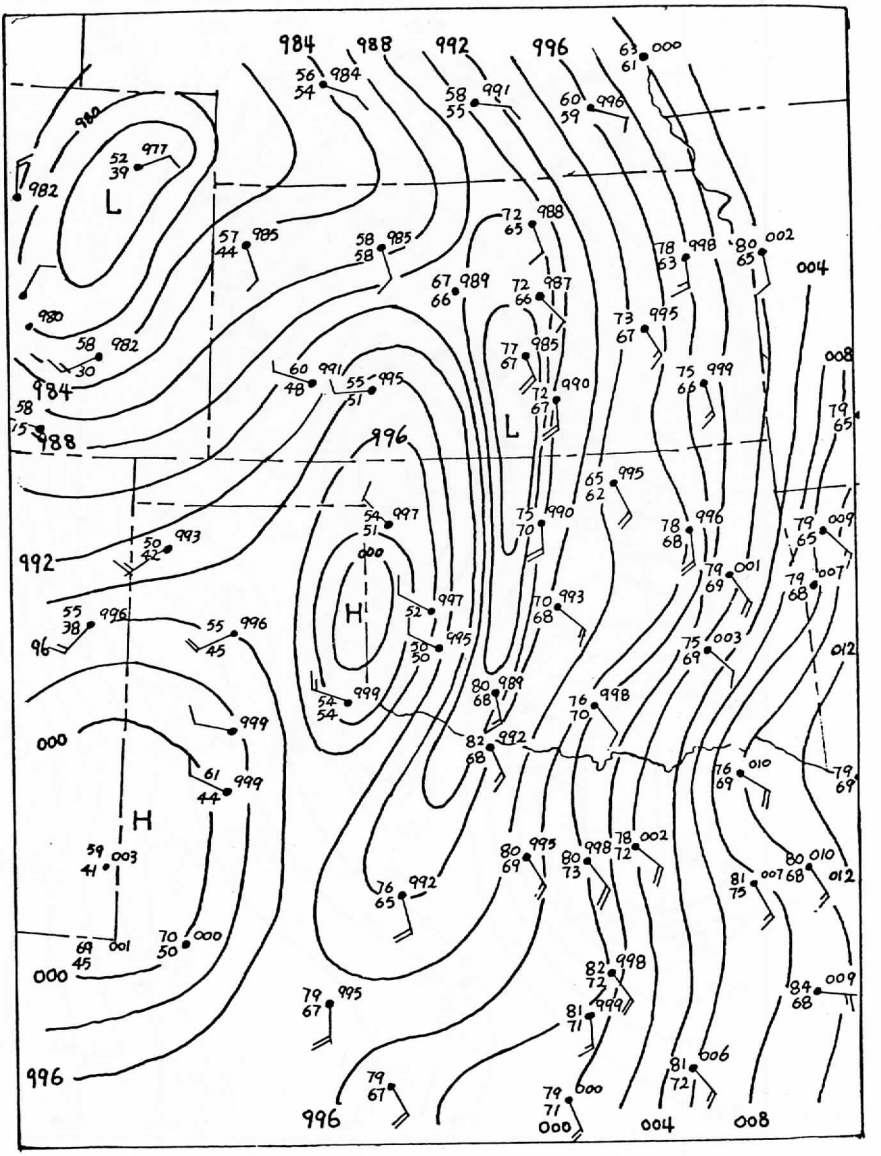


Figure 4. 1900 Z Surface Mesoscale Analysis, 30 October 1974
Surface pressure based on altimeter settings,
isobars at intervals of .02 inch.

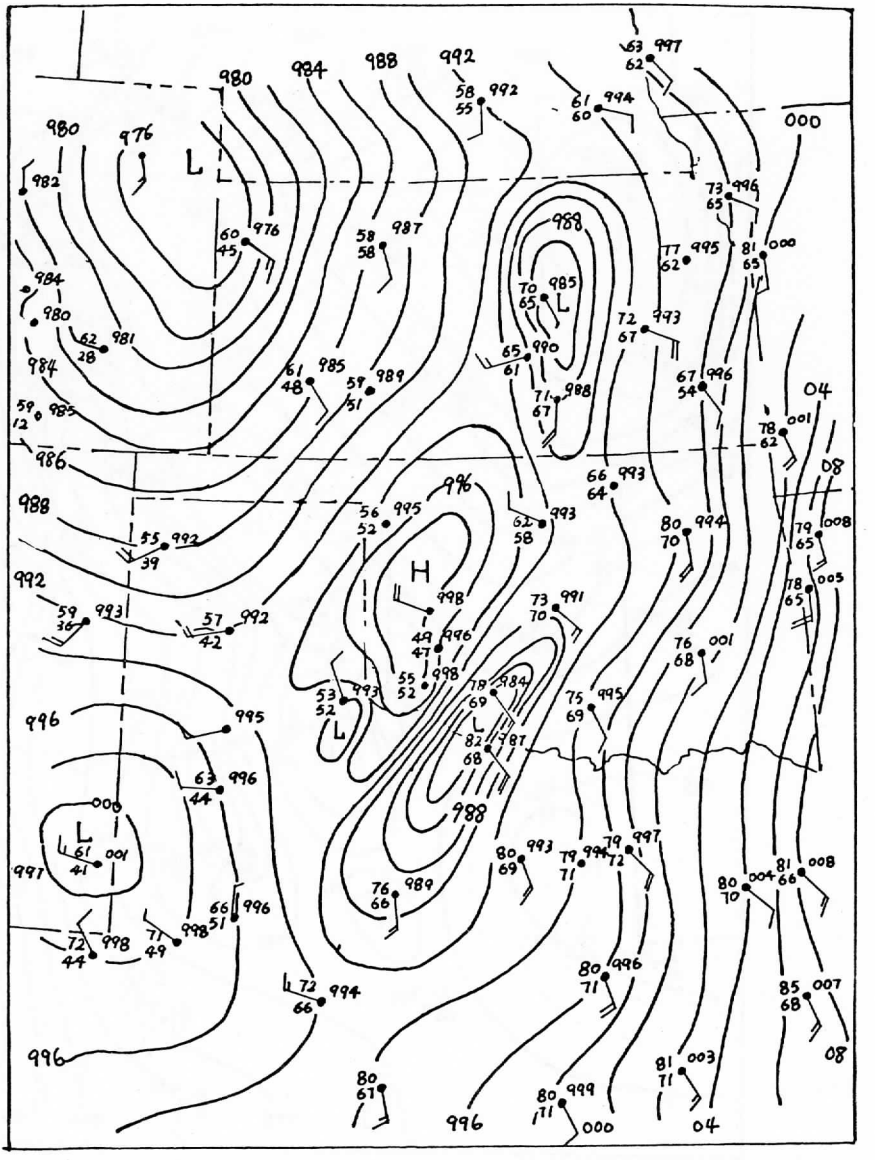


Figure 5. 2000 Z Surface Mesoscale Analysis, 30 October 1974
Surface pressure based on altimeter setting,
isobars at intervals of .02 inch.

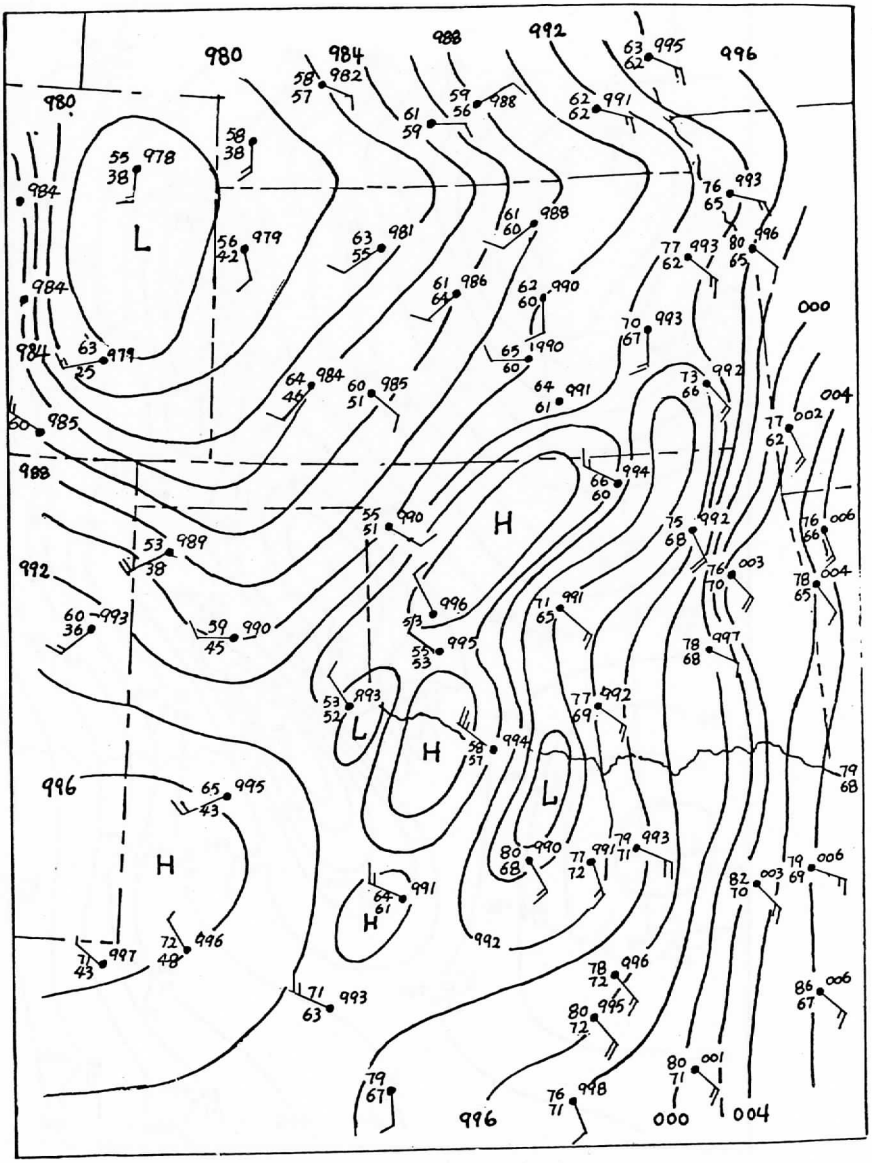


Figure 6. 2100 Z Surface Mesoscale Analysis, 30 October 1974
Surface pressure based on altimeter settings,
isobars at intervals of .02 inch.

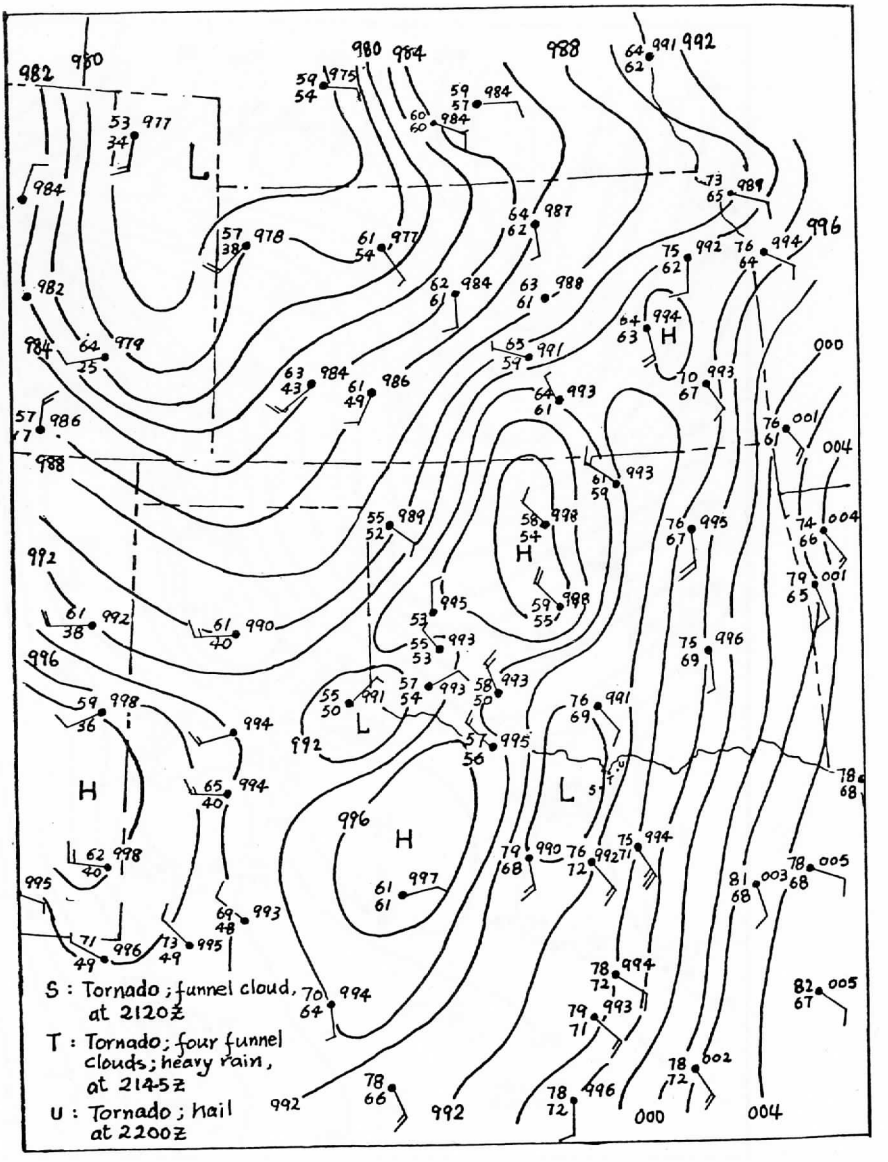


Figure 7. 2200 Z Surface Mesoscale Analysis, 30 October 1974
Surface pressure based on altimeter settings, isobars at intervals of .02 inch.

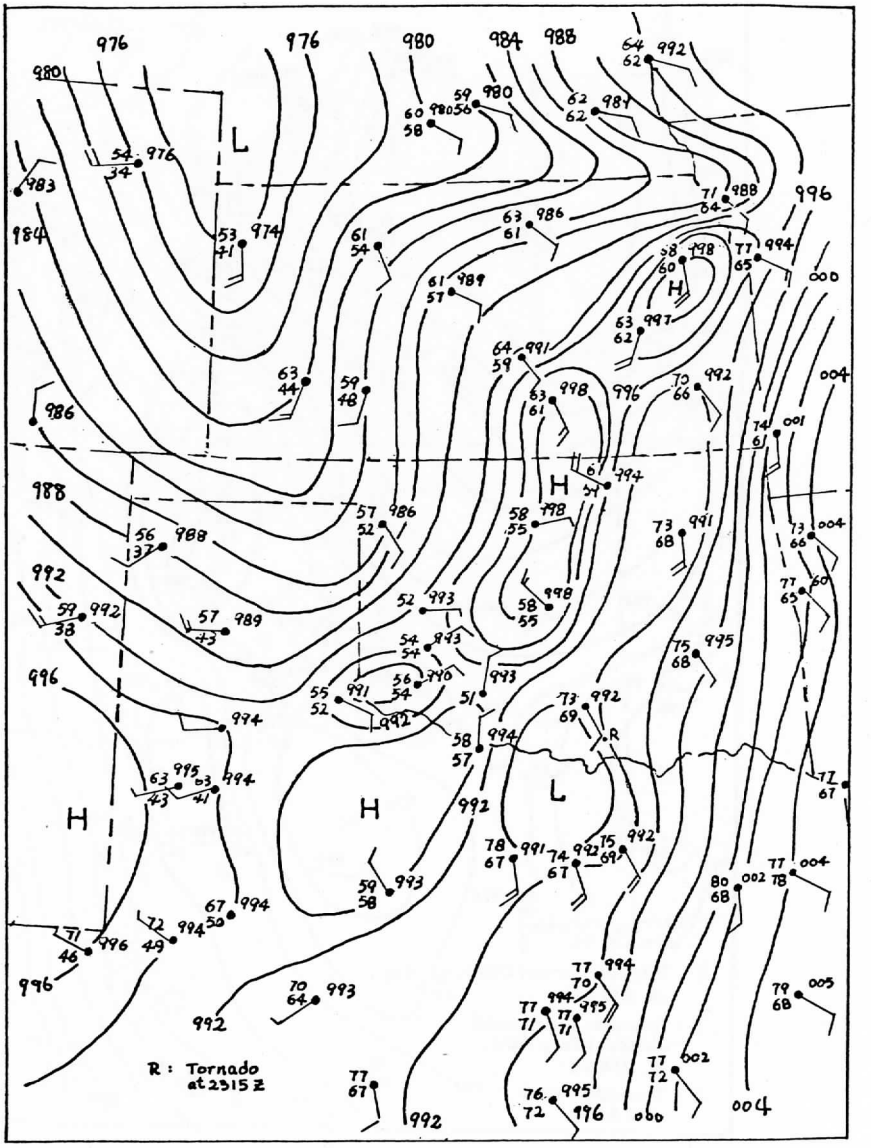


Figure 8. 2300 Z Surface Mesoscale Analysis, 30 October 1974
Surface pressure based on altimeter settings,
isobars at intervals of .02 inch.

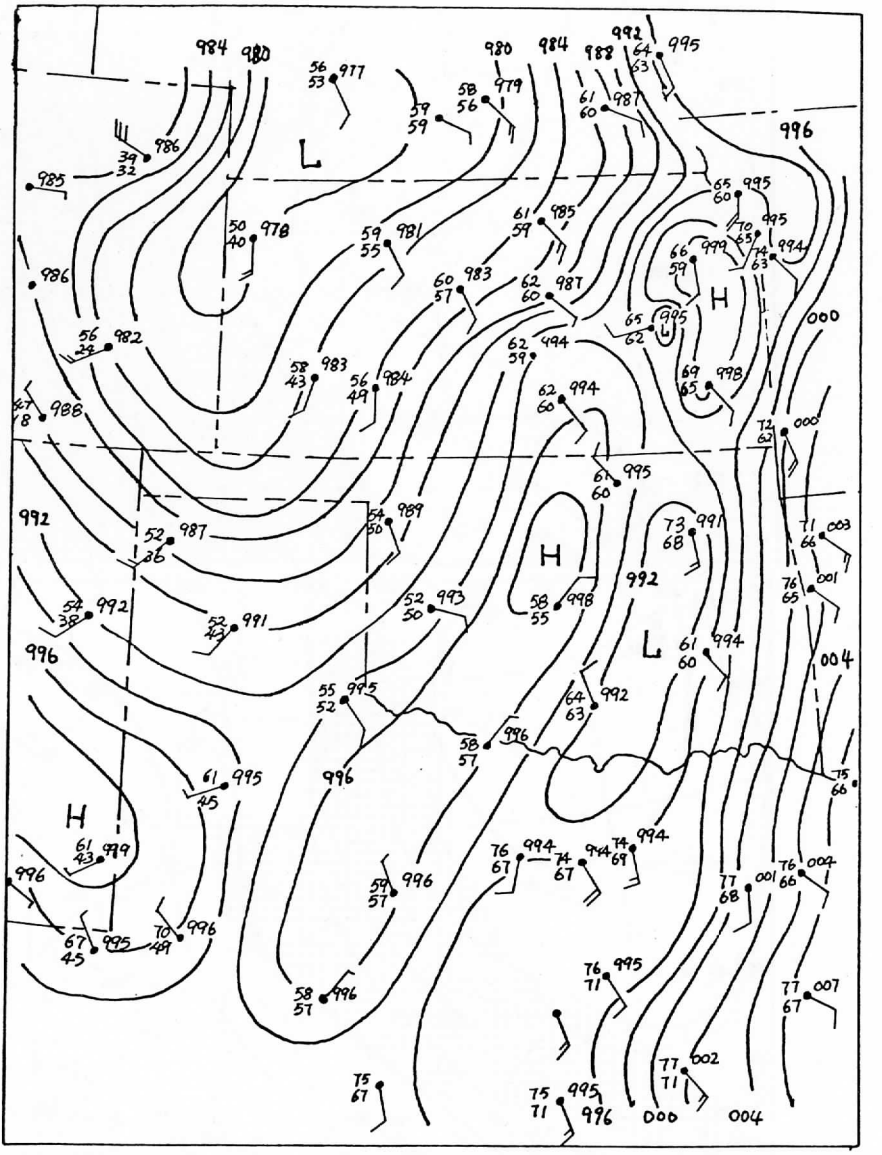


Figure 9. 0000 Z Surface Mesoscale Analysis, 30 October 1974
Surface pressure based on altimeter settings,
isobars at intervals of .02 inch.

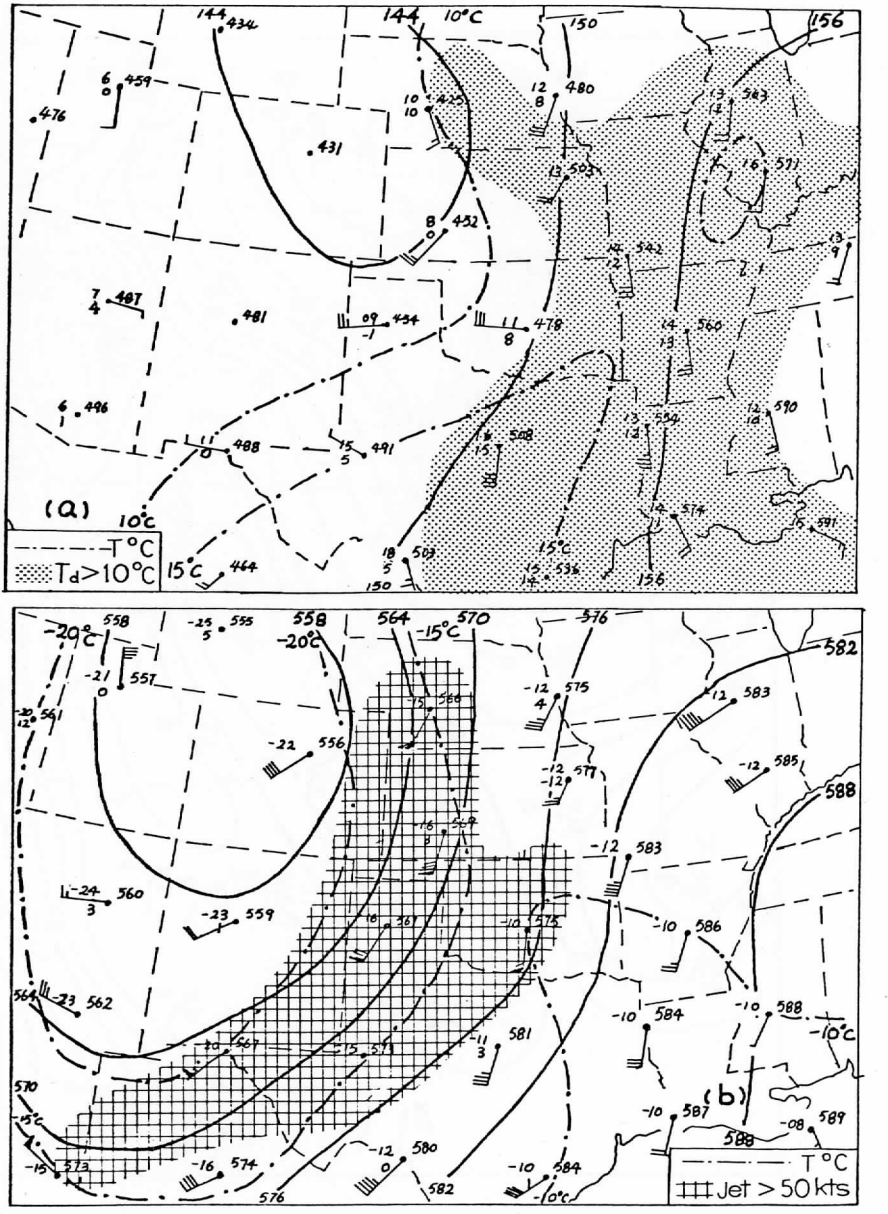


Figure 10. 0000 Z Upper Air Charts, 31 October 1974, (a) 850 mb (b) 500 mb

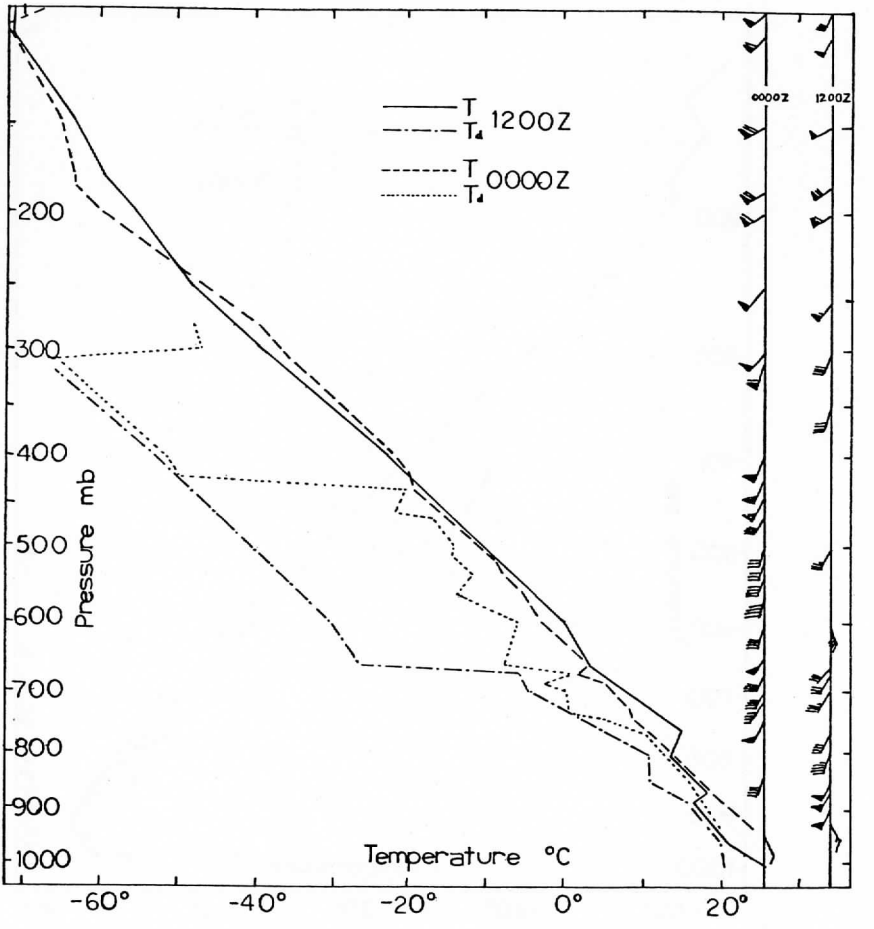


Figure 11. Upper Air Soundings at Stephenville (TX) for 1200 Z 30 October 1974 and 0000 Z, 31 October 1974

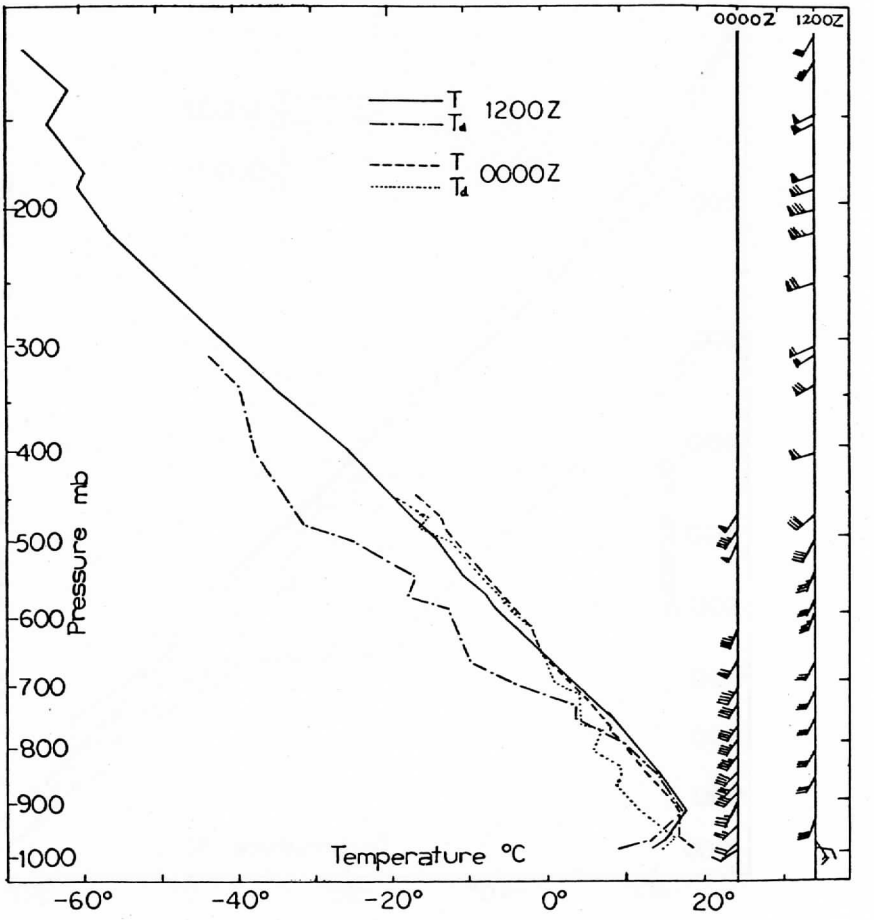


Figure 12. Upper Air Soundings at Topeka (KS) for 1200 Z, 30 October 1974 and 0000 Z, 30 October 1974

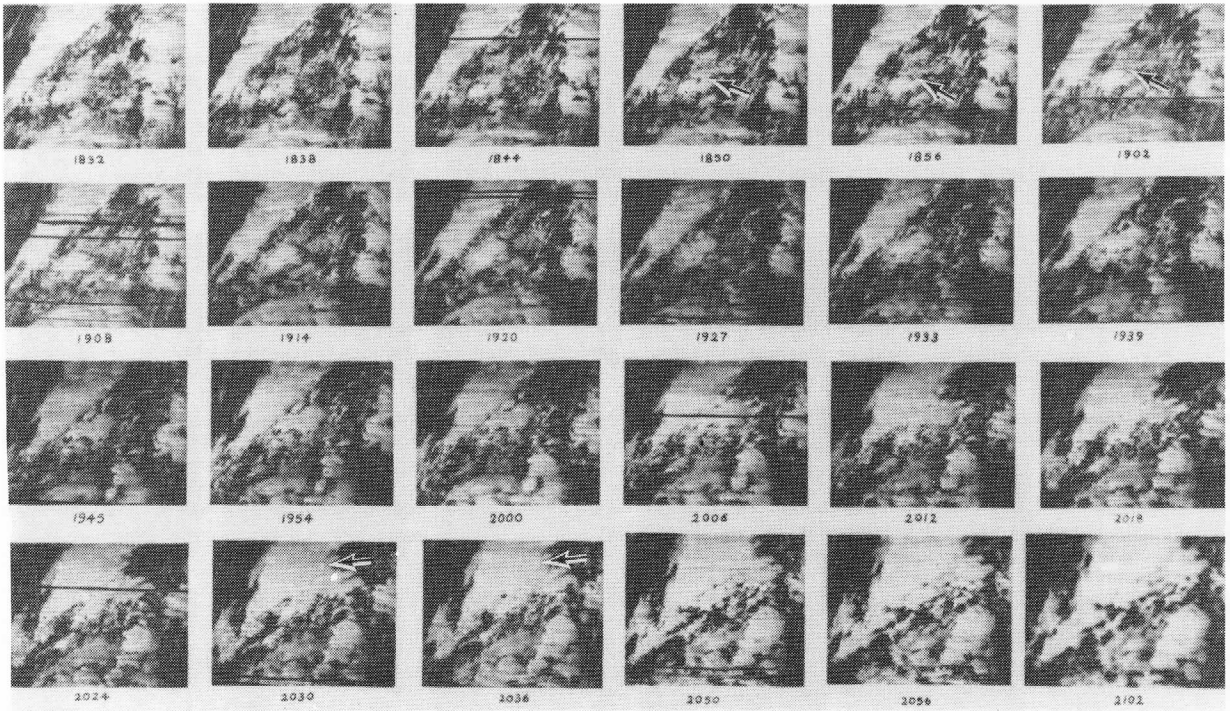


Figure 13a. Sequence of SMS Visible Images from 1832 Z to 2102 Z

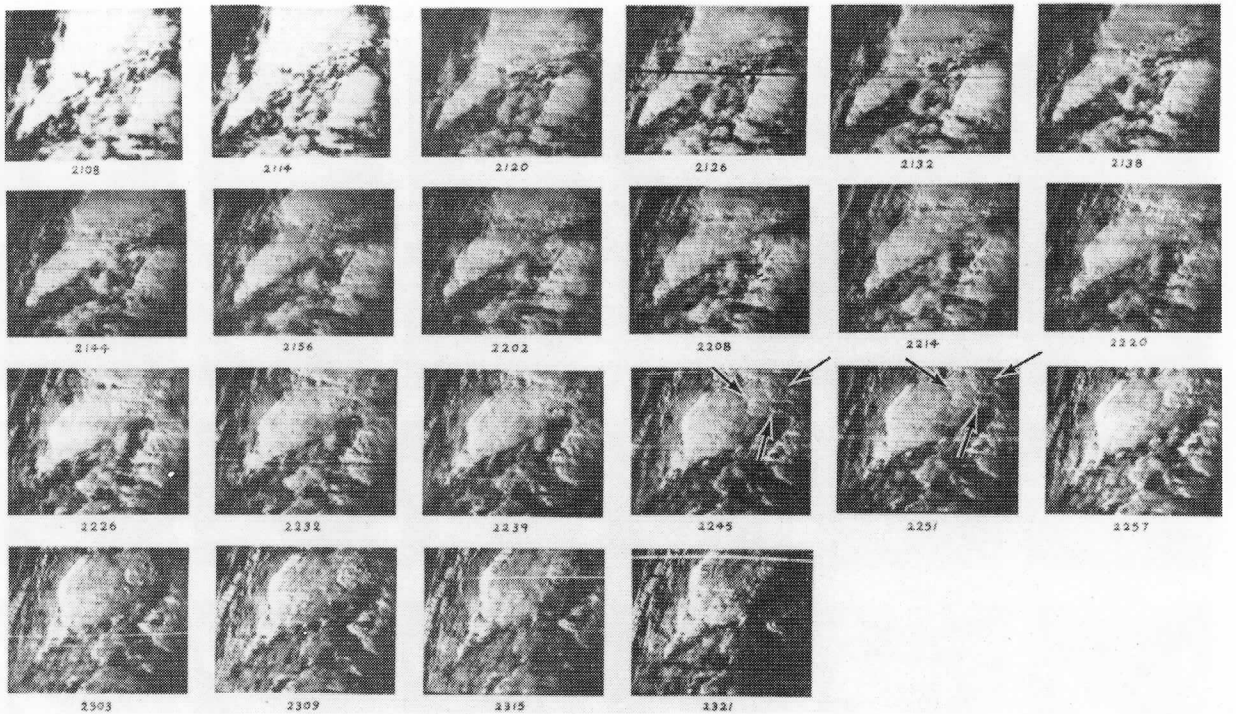


Figure 13b. Sequence of SMS Visible Images from 2108 Z to 2321 Z

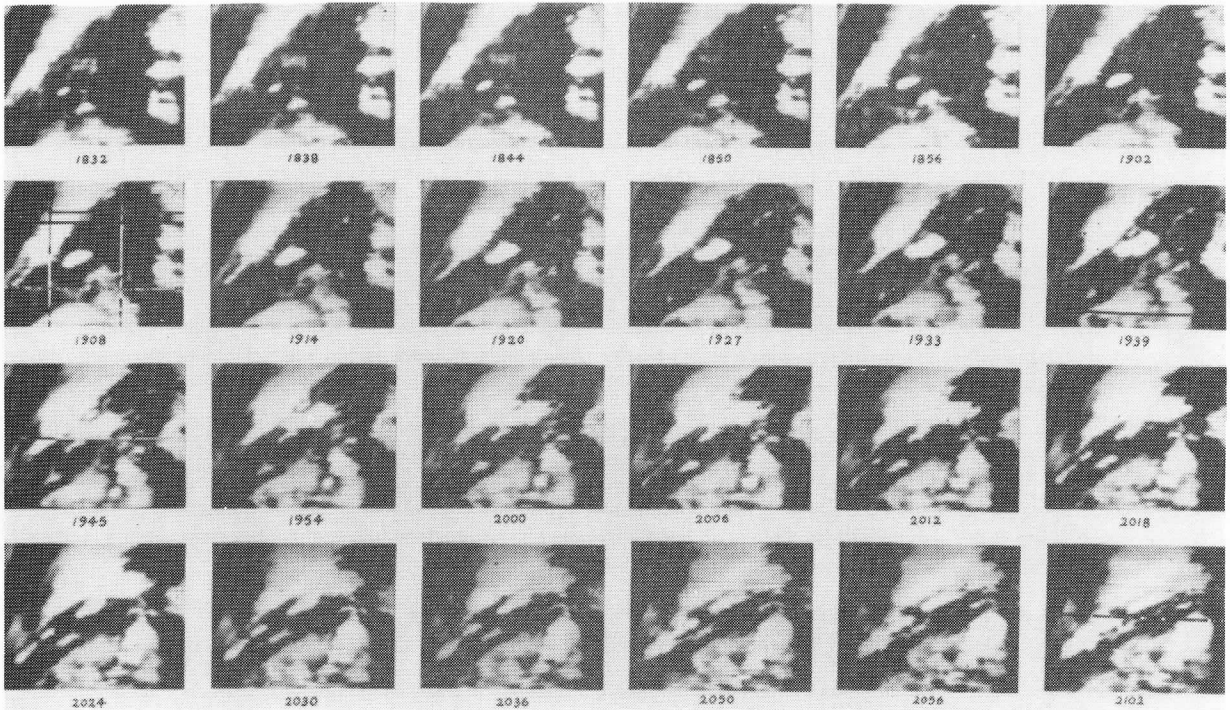


Figure 14a. Sequence of SMS Infrared Images from 1832 Z to 2102 Z

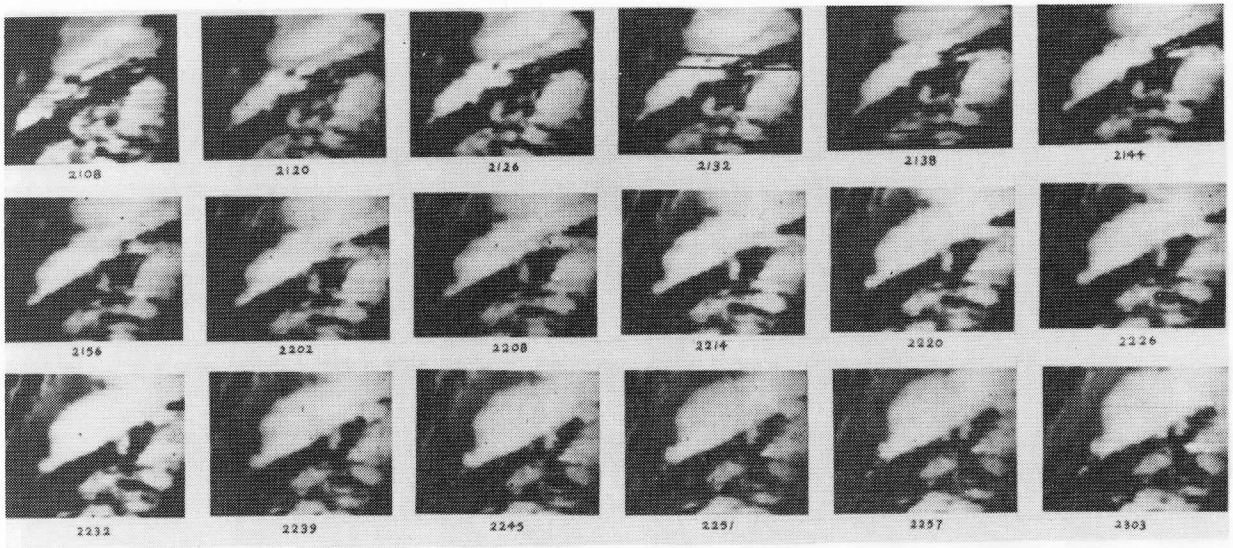


Figure 14b. Sequence of SMS Infrared Images from 2108 Z to 2303 Z

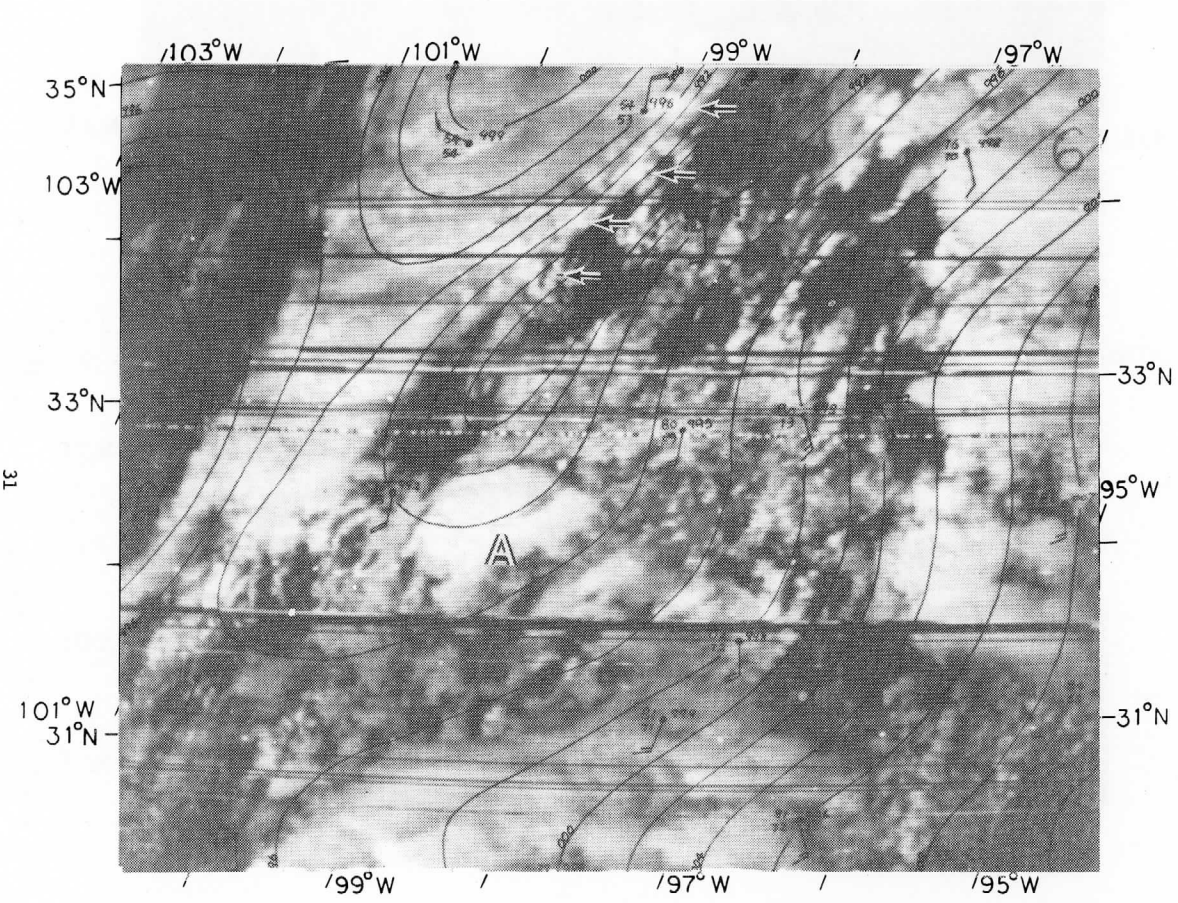


Figure 15. 1902 Z SMS Visible Image with 1900 Z Surface Mesoscale Analysis Superimposed

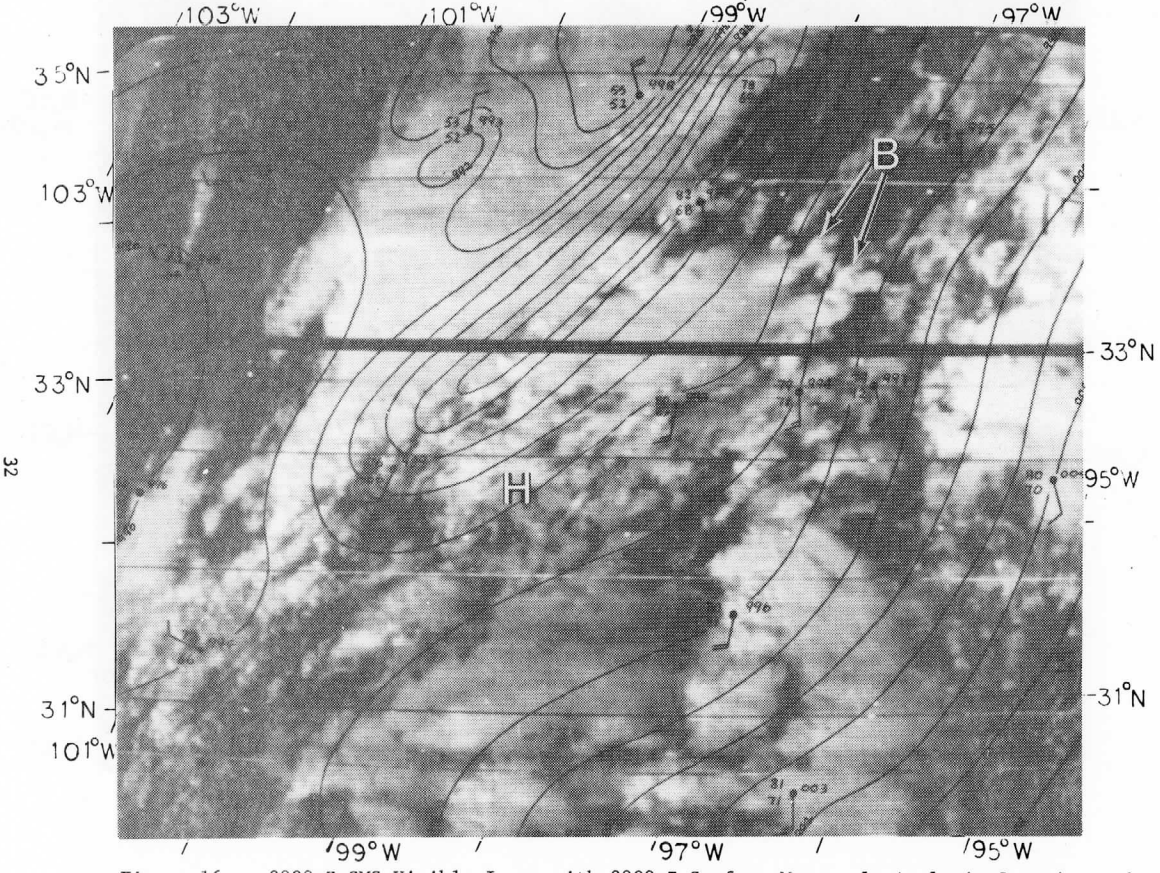


Figure 16. 2000 Z SMS Visible Image with 2000 Z Surface Mesoscale Analysis Superimposed

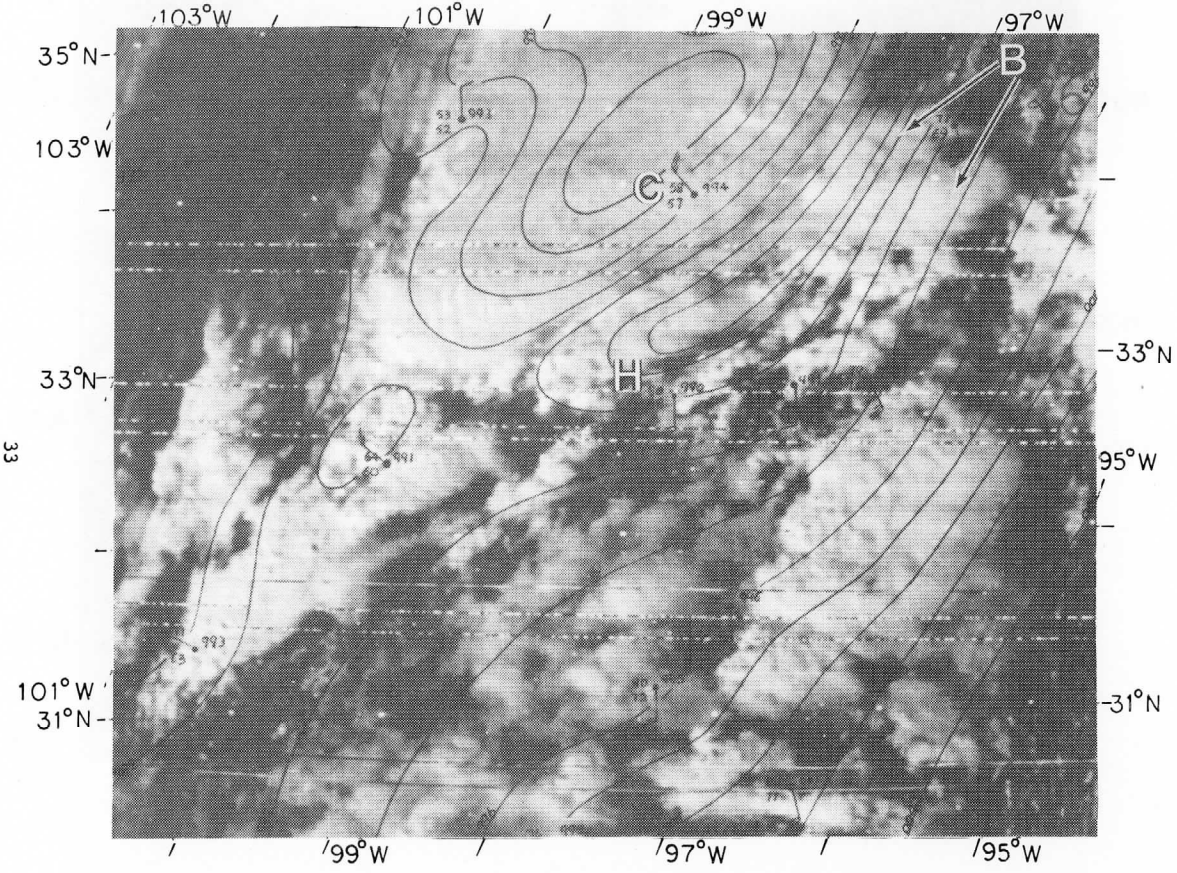


Figure 17. 2102 Z SMS Visible Image with 2100 Z Surface Mesoscale Analysis Superimposed

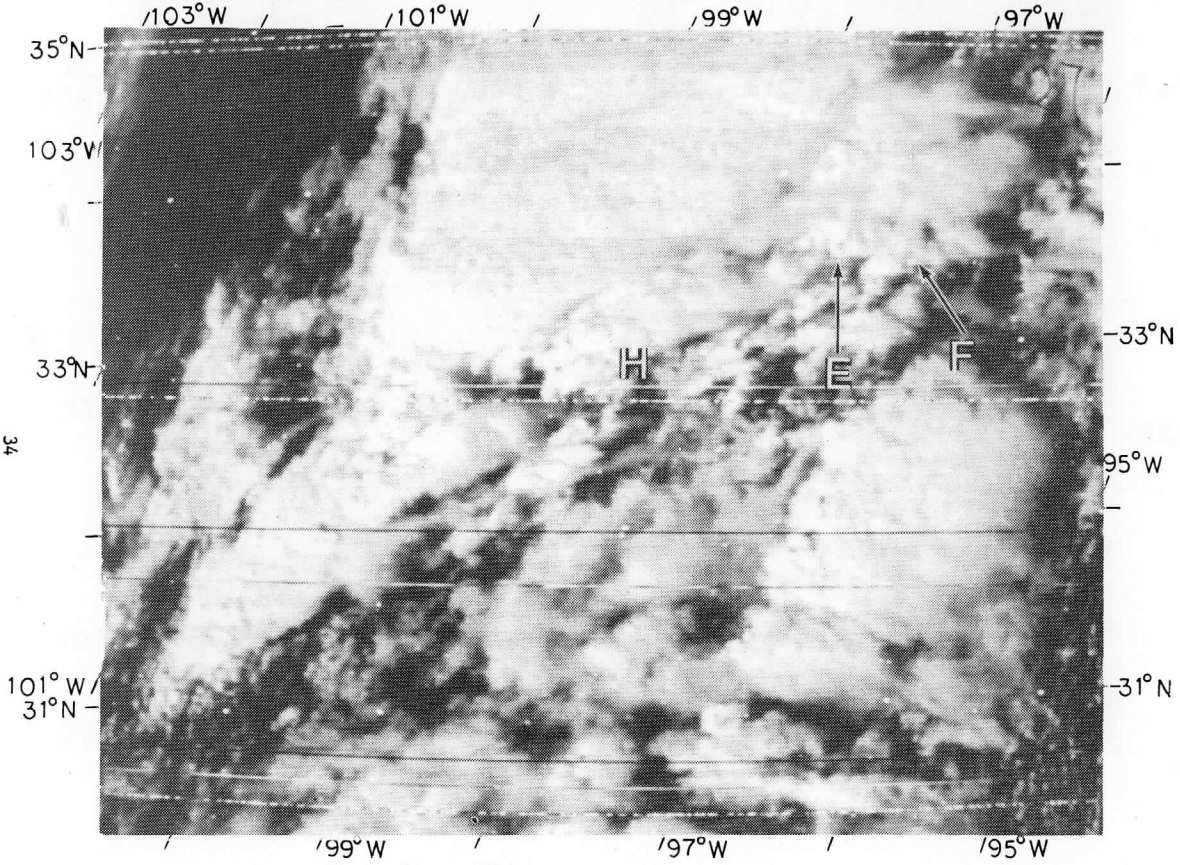


Figure 18. 2108 Z SMS Visible Image

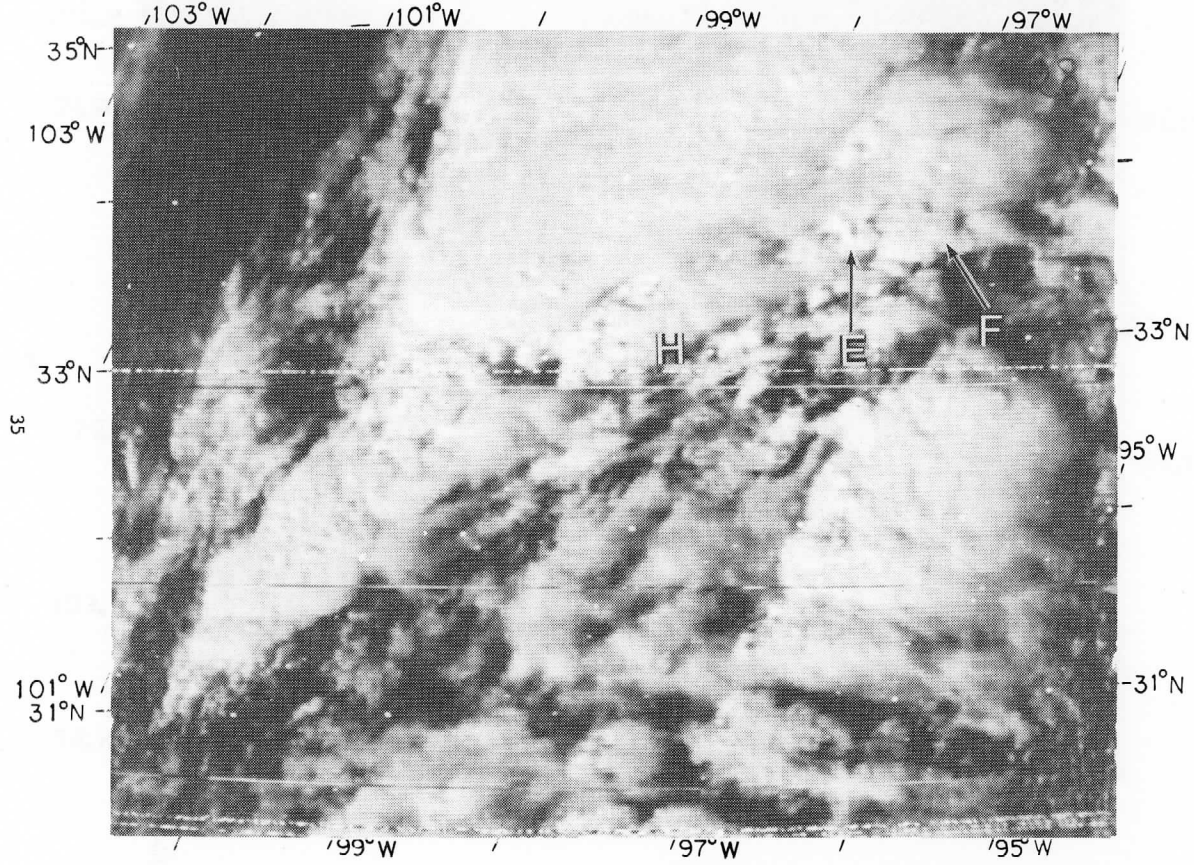


Figure 19. 2114 Z SMS Visible Image

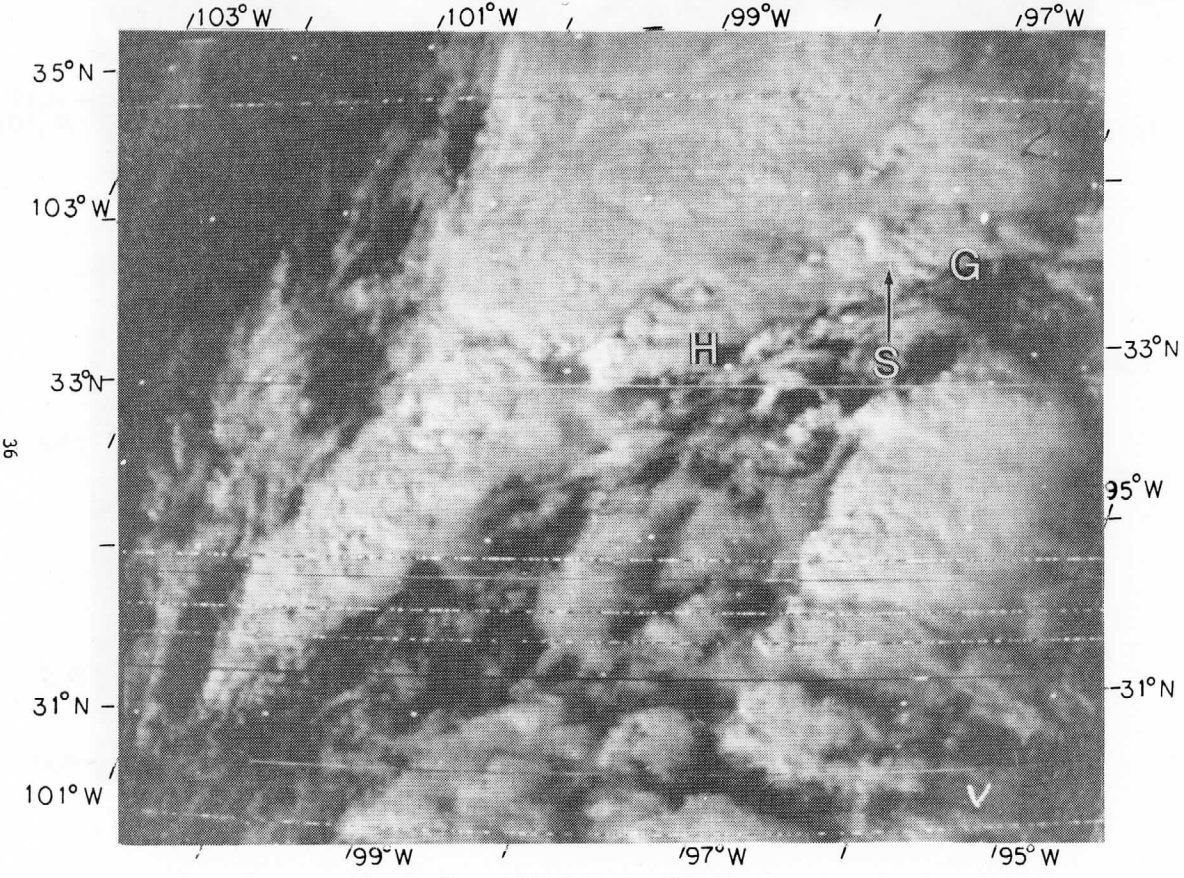


Figure 20. 2120 Z SMS Visible Image

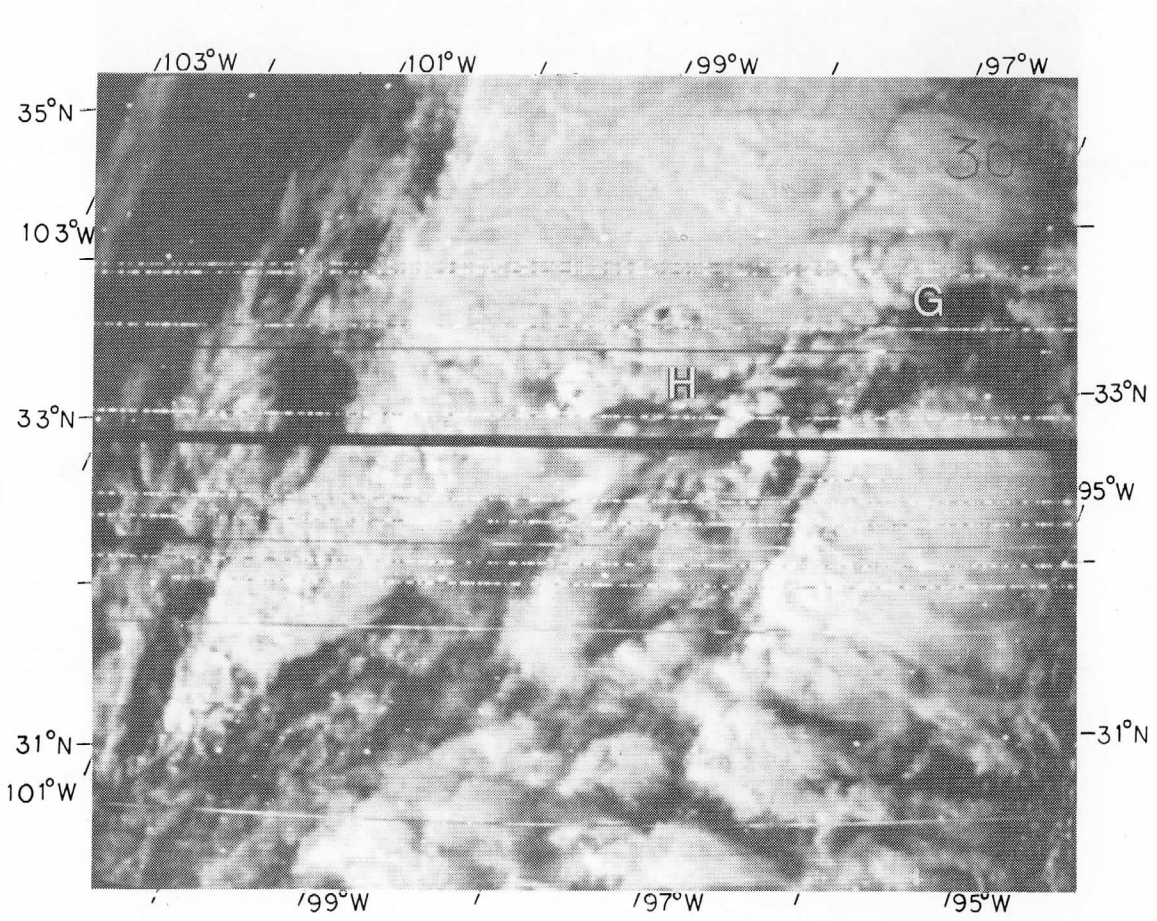


Figure 21. 2126 Z SMS Visible Image

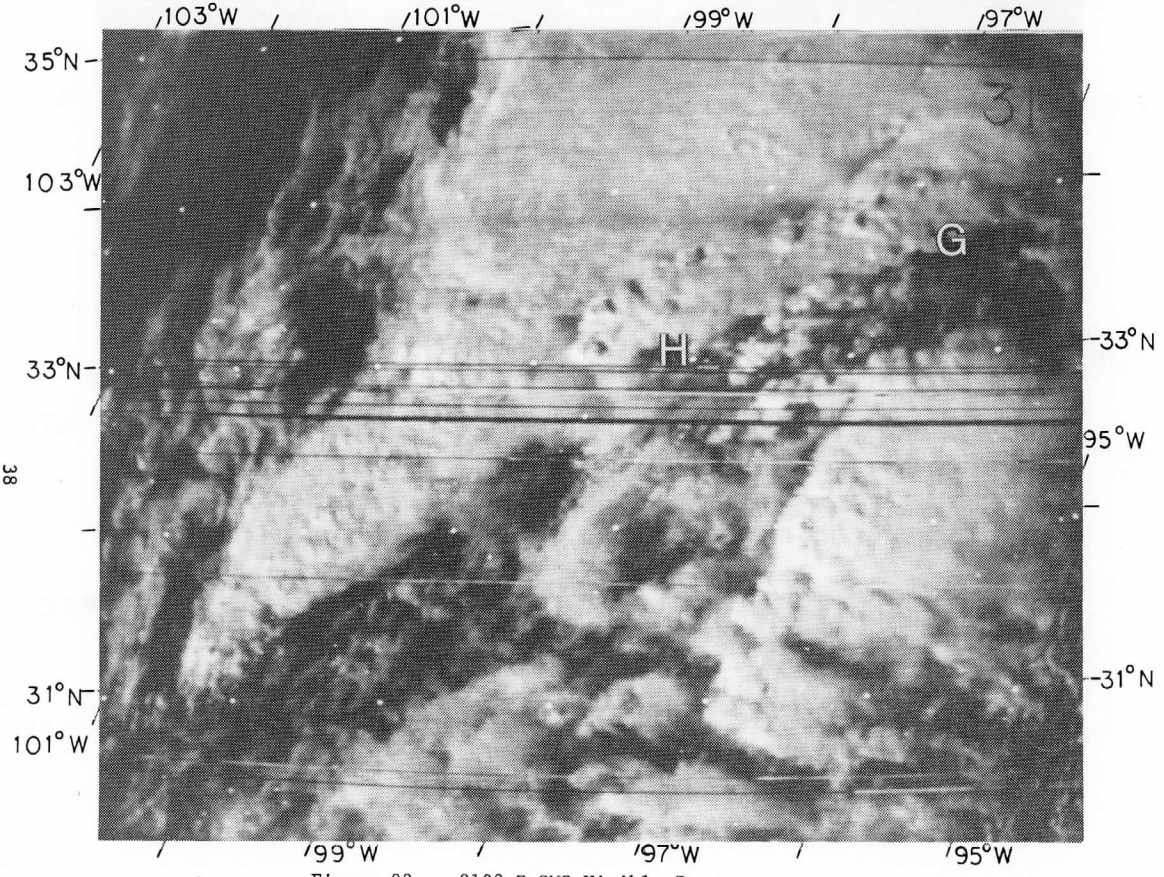


Figure 22. 2132 Z SMS Visible Image

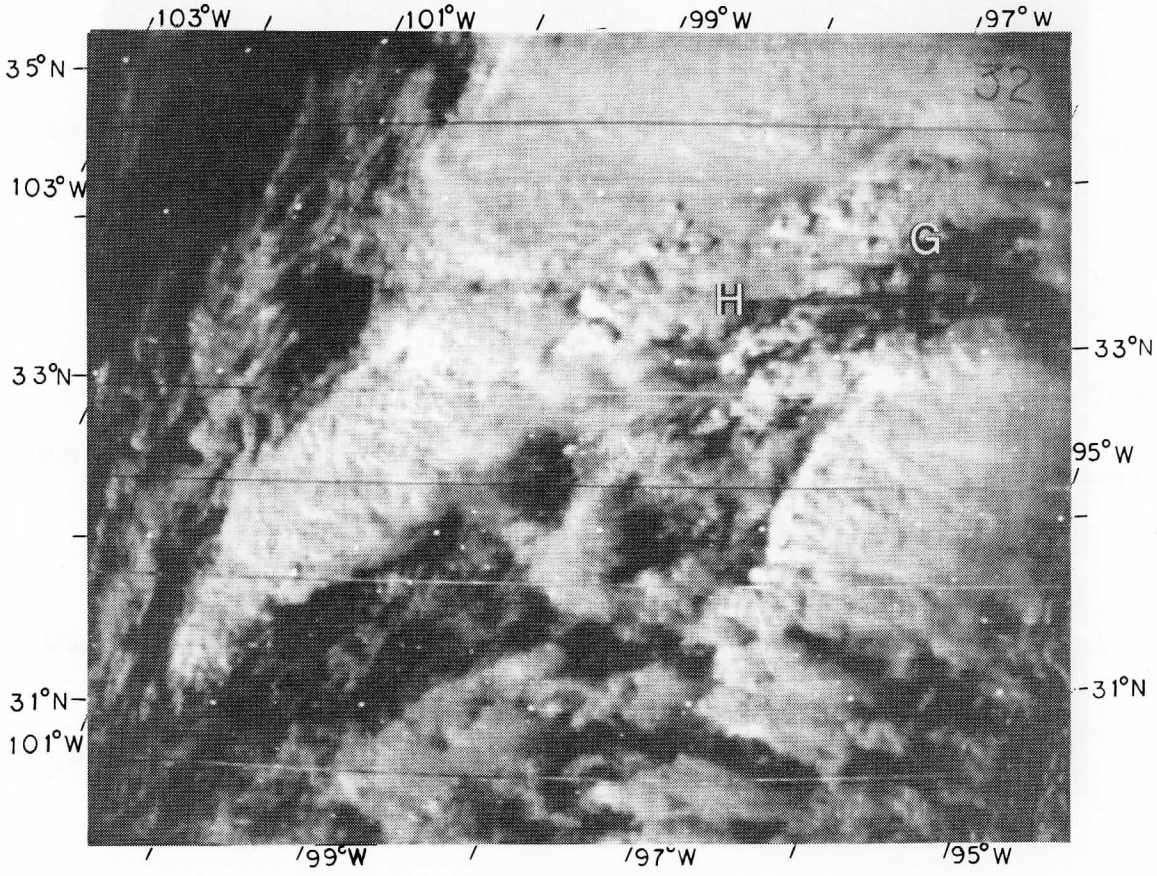


Figure 23. 2138 Z SMS Visible Image

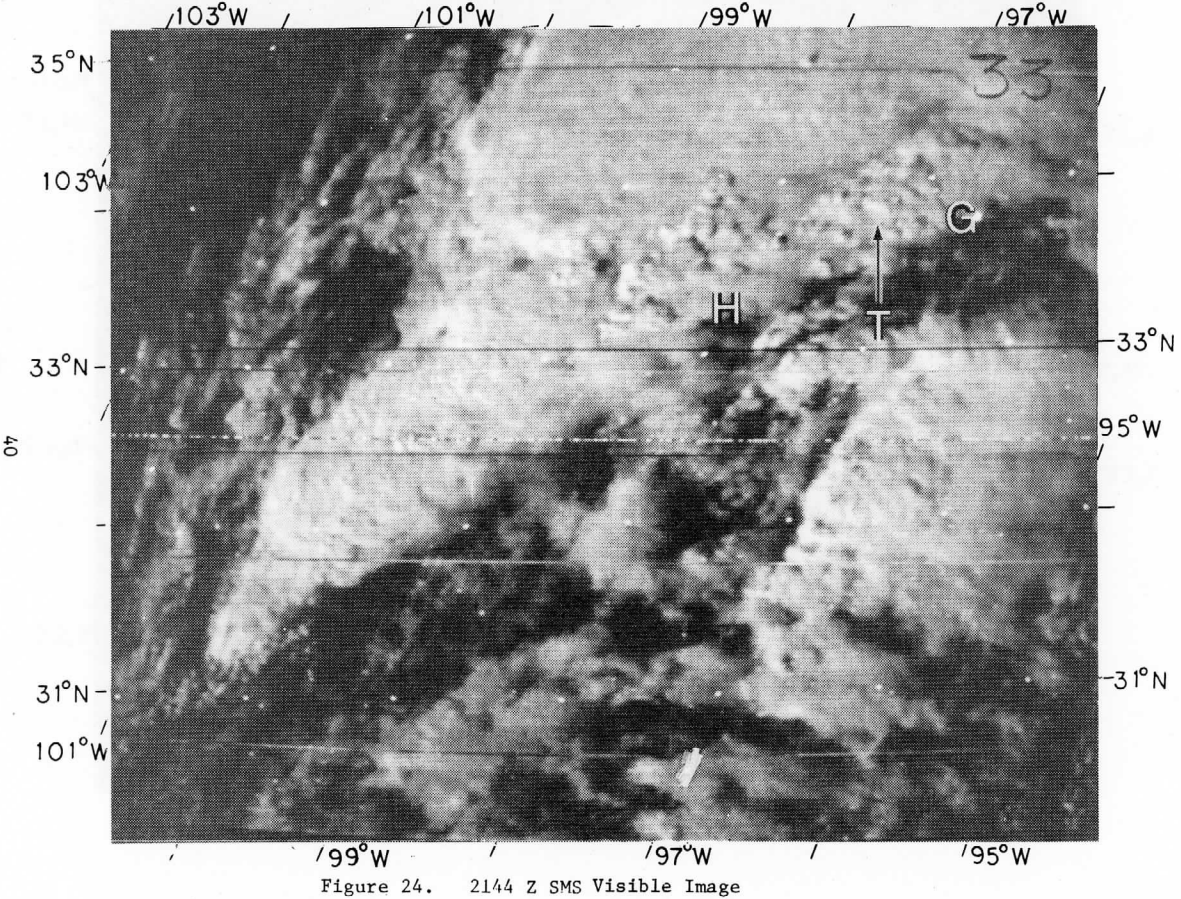


Figure 24. 2144 Z SMS Visible Image

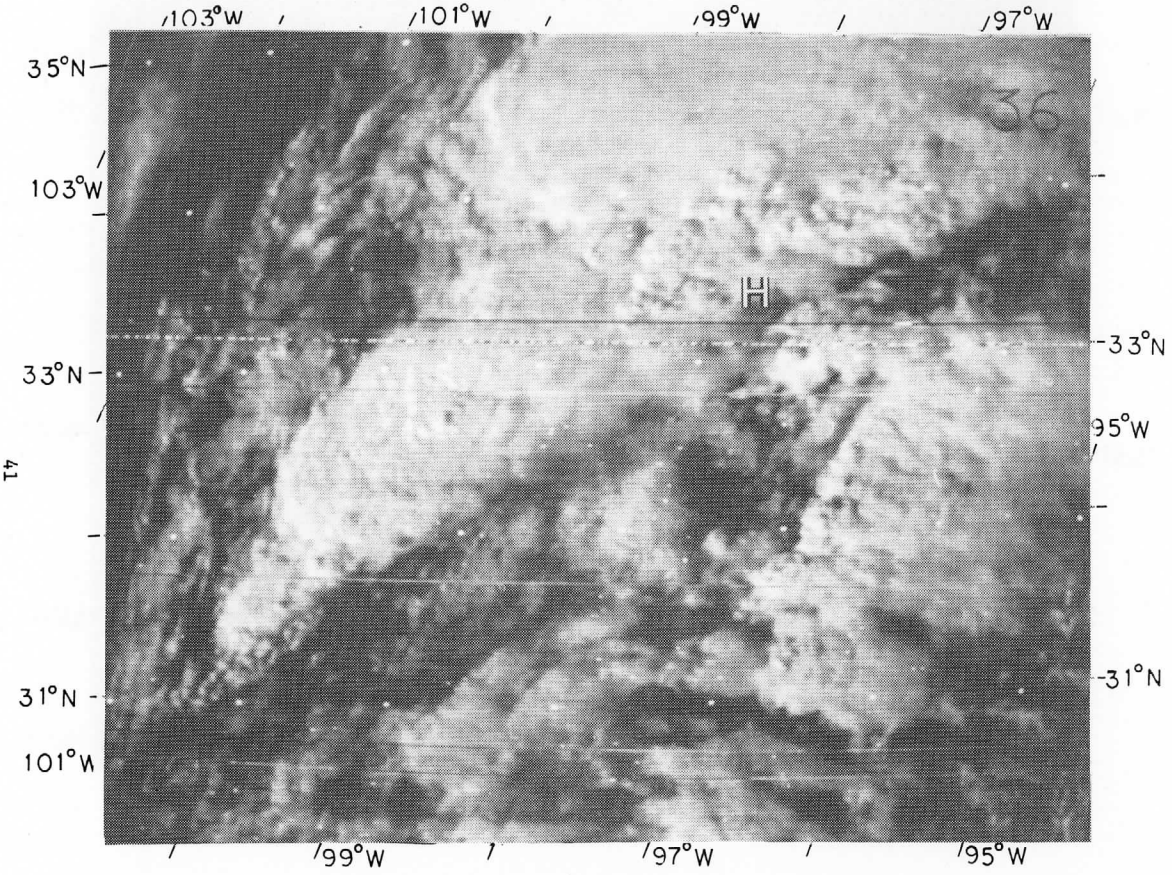


Figure 25. 2156 Z SMS Visible Image

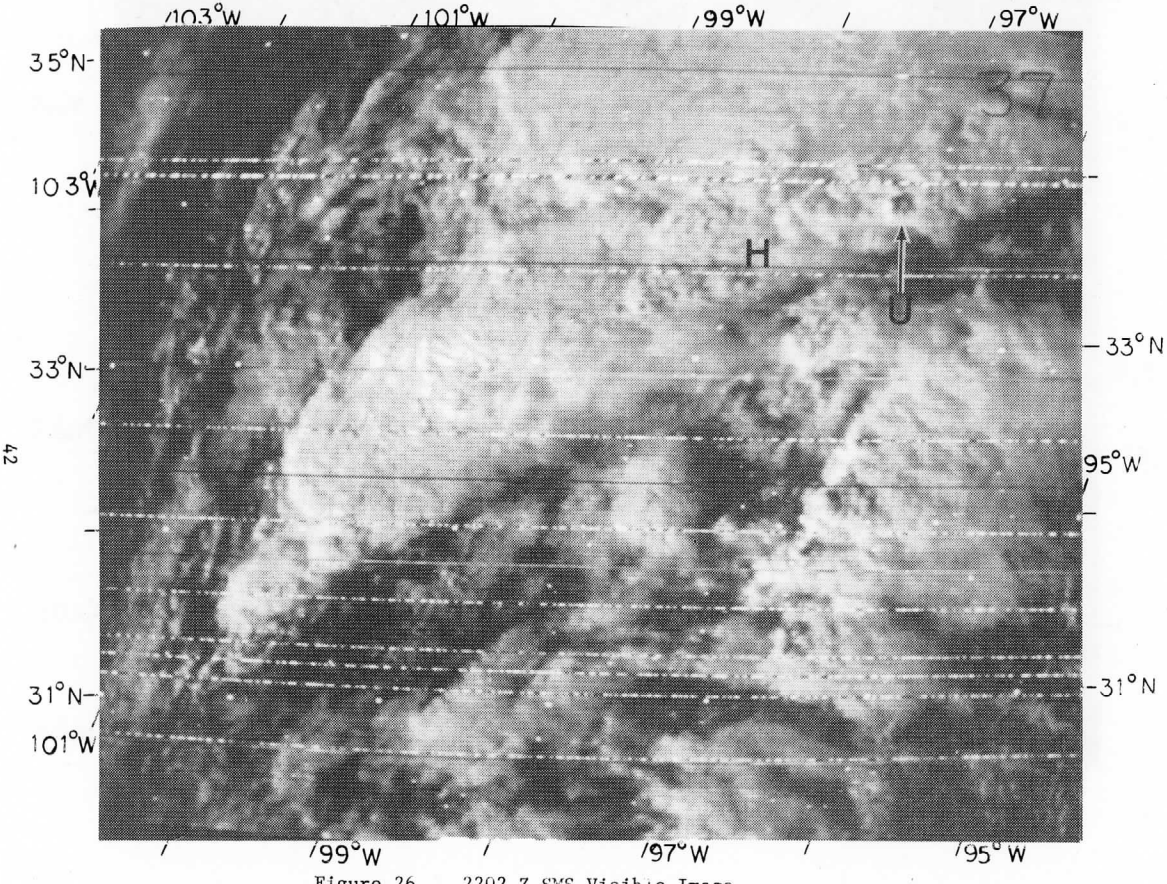


Figure 26. 2202 Z SMS Visible Image

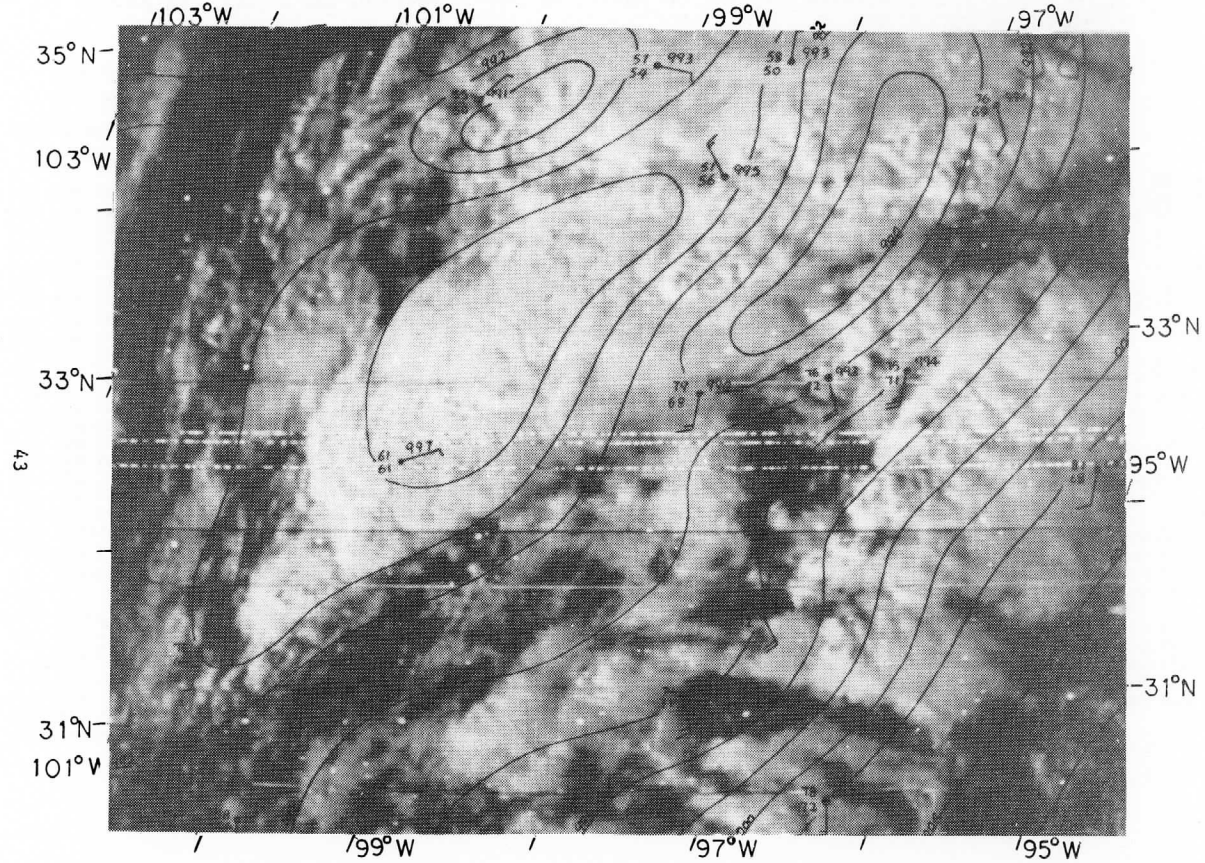


Figure 27. 2208 Z SMS Visible Image with 2200 Z Surface Mesoscale Analysis Superimposed

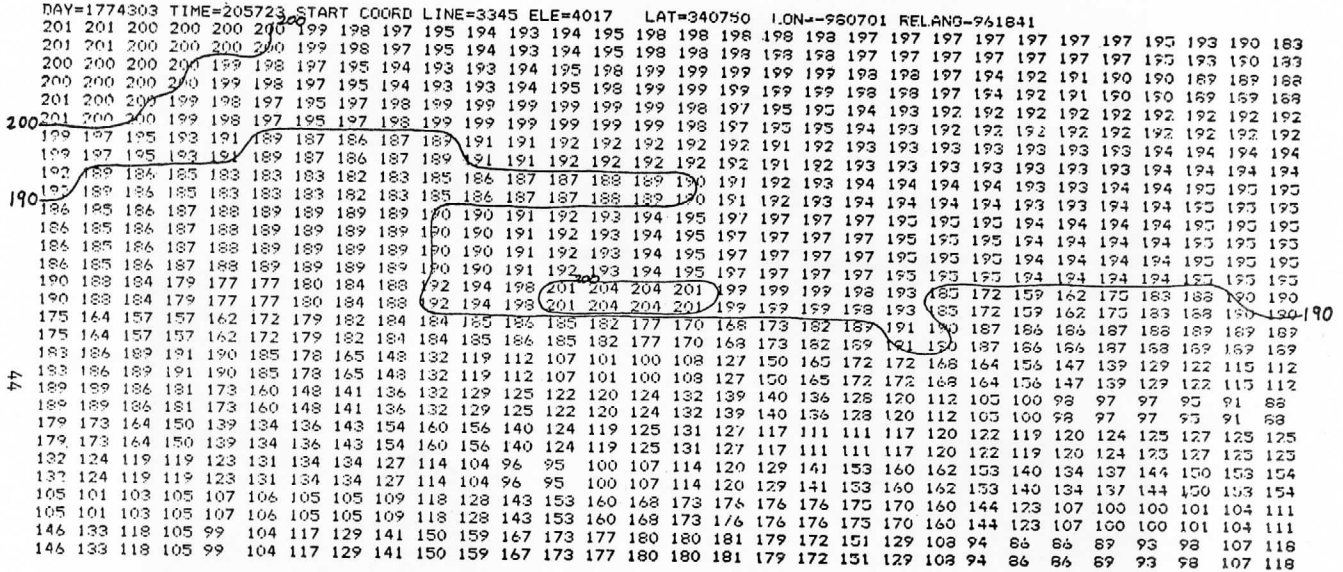


Figure 28. 2102 Z SMS Infrared Digital Data Near the Tornadic Storm G

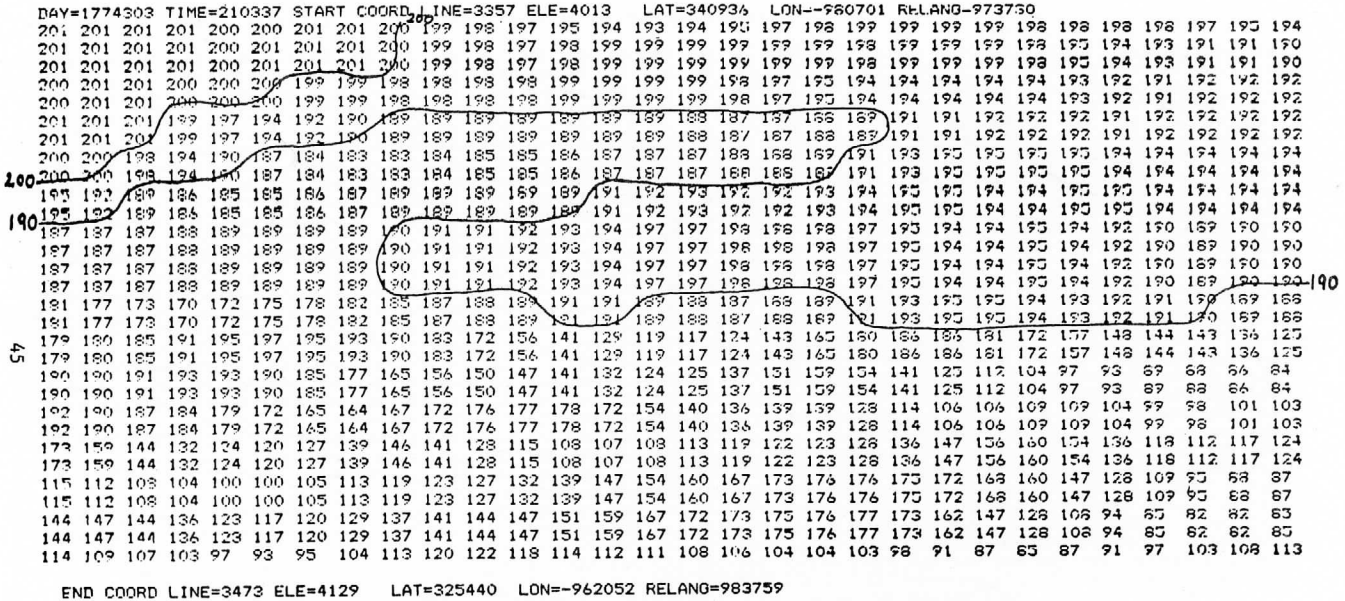


Figure 29. 2108 Z SMS Infrared Digital Data Near the Tornadic Storm G

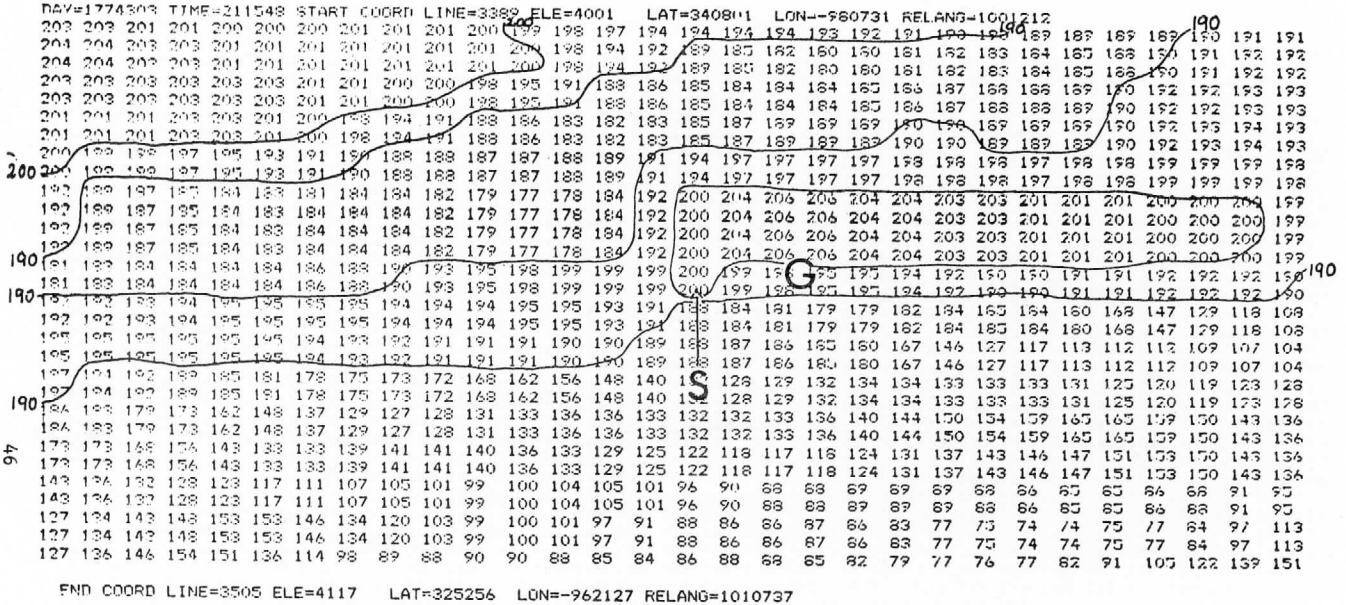


Figure 30. 2120 Z SMS Infrared Digital Data Near the Tornadic Storm G

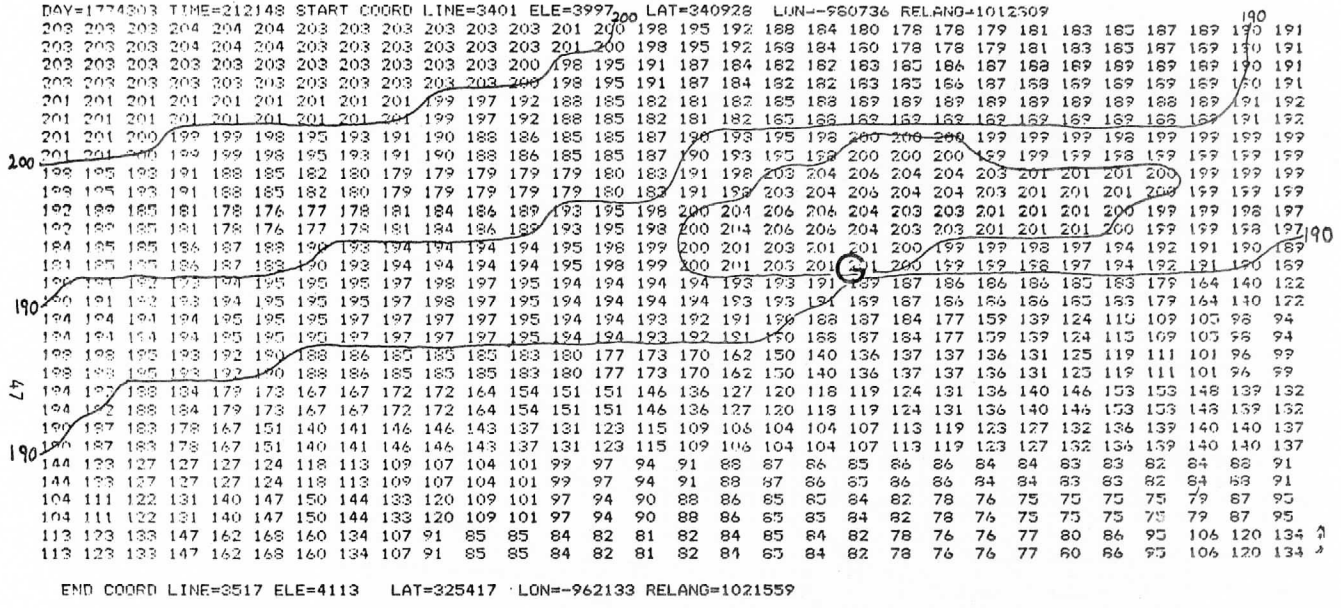


Figure 31. 2126 Z SMS Infrared Digital Data Near the Tornadic Storm G

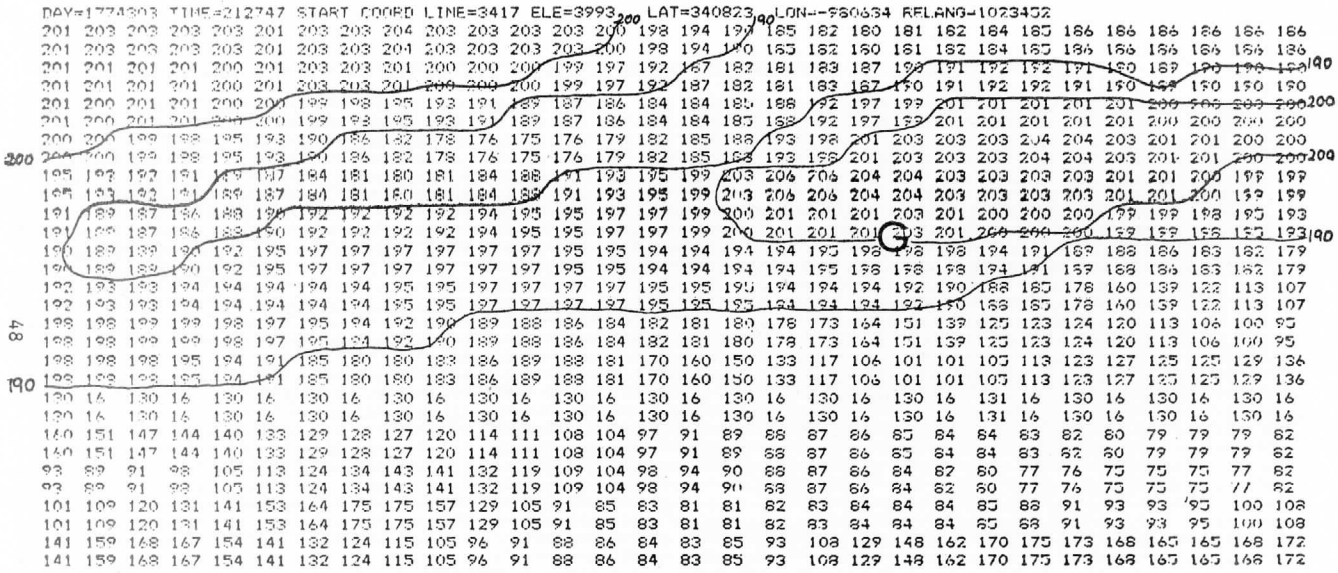


Figure 32. 2132 Z SMS Infrared Digital Data Near the Tornadic Storm G

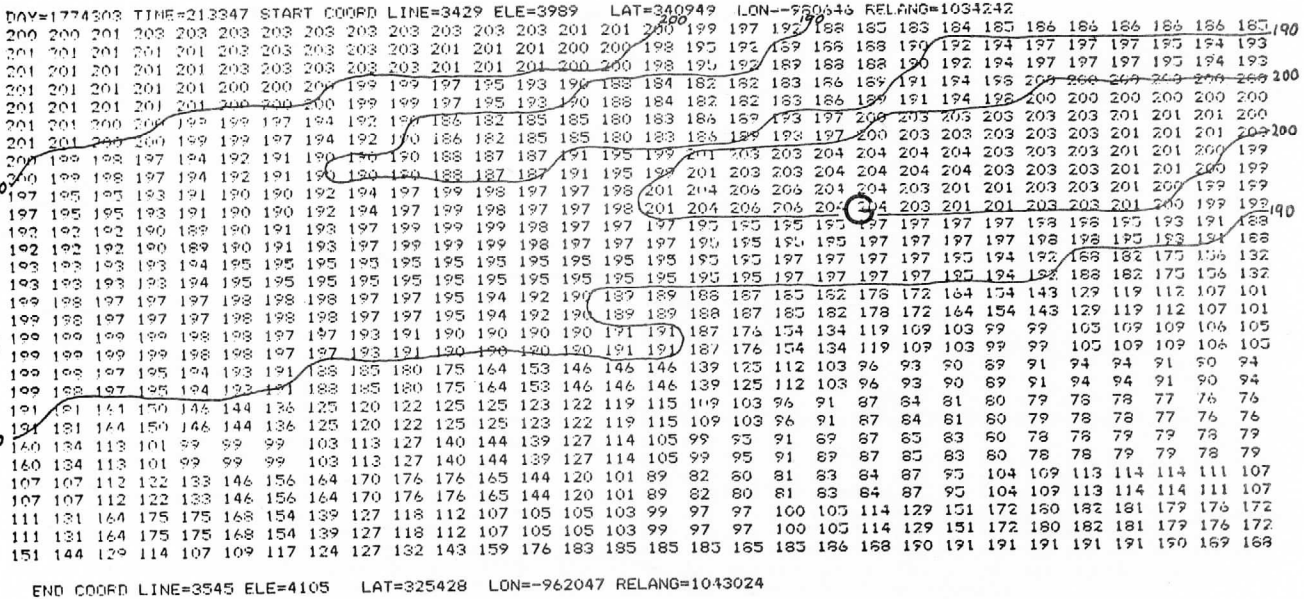


Figure 33. 2138 Z SMS Infrared Digital Data Near the Tornadic Storm G

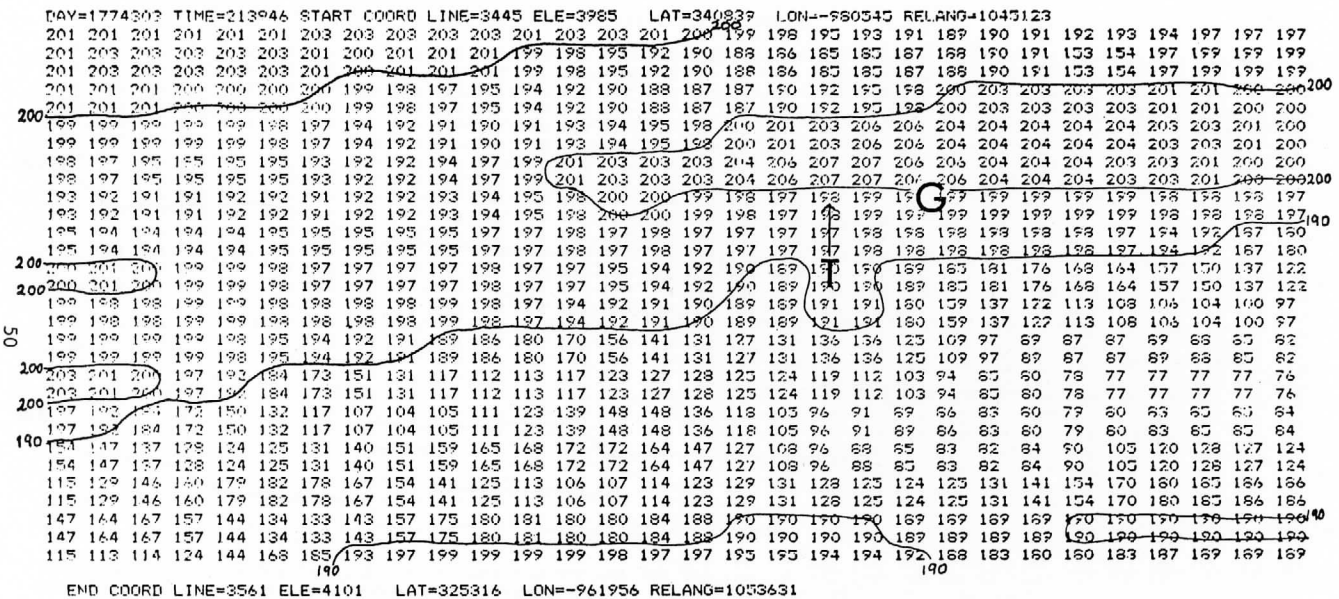


Figure 34. 2144 Z SMS Infrared Digital Data Near the Tornadic Storm G

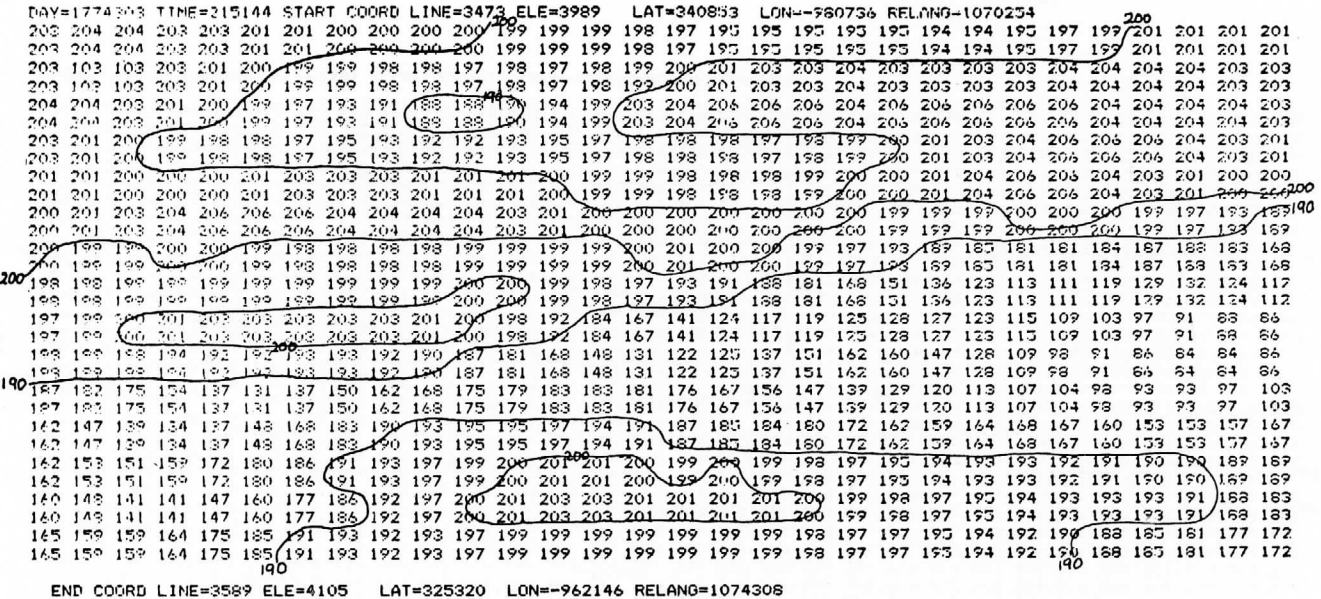


Figure 35. 2156 Z SMS Infrared Digital Data Near the Tornadic Storm G

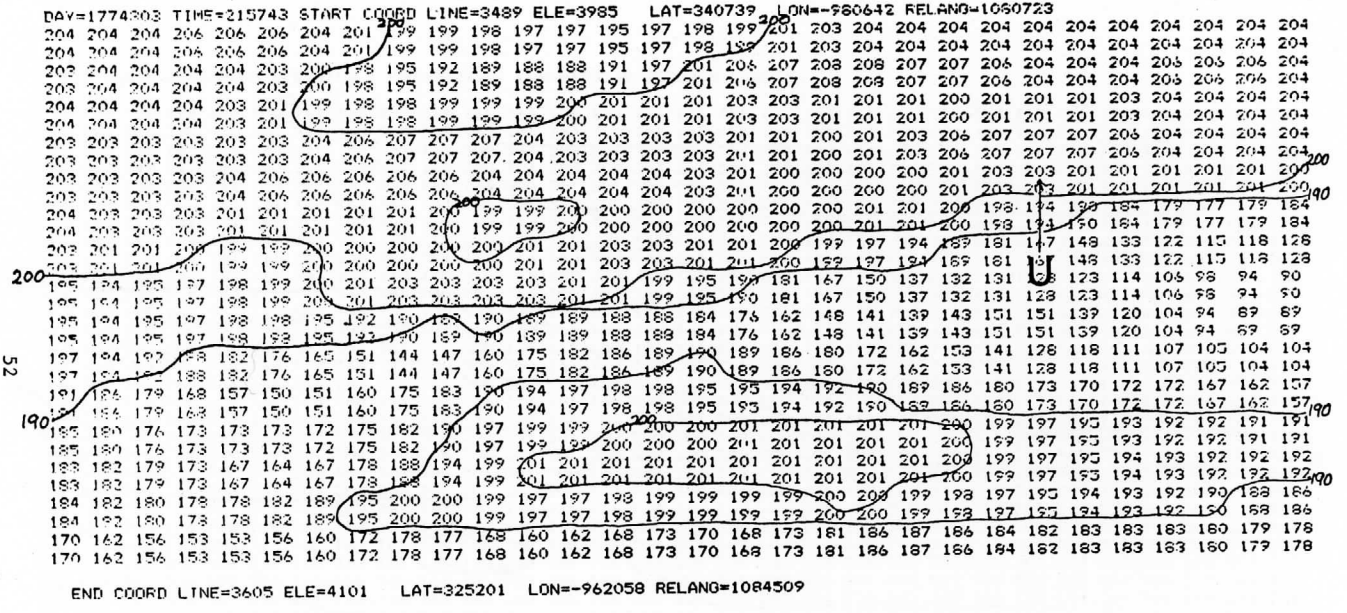


Figure 36. 2202 Z SMS Infrared Digital Data Near the Tornadic Storm G

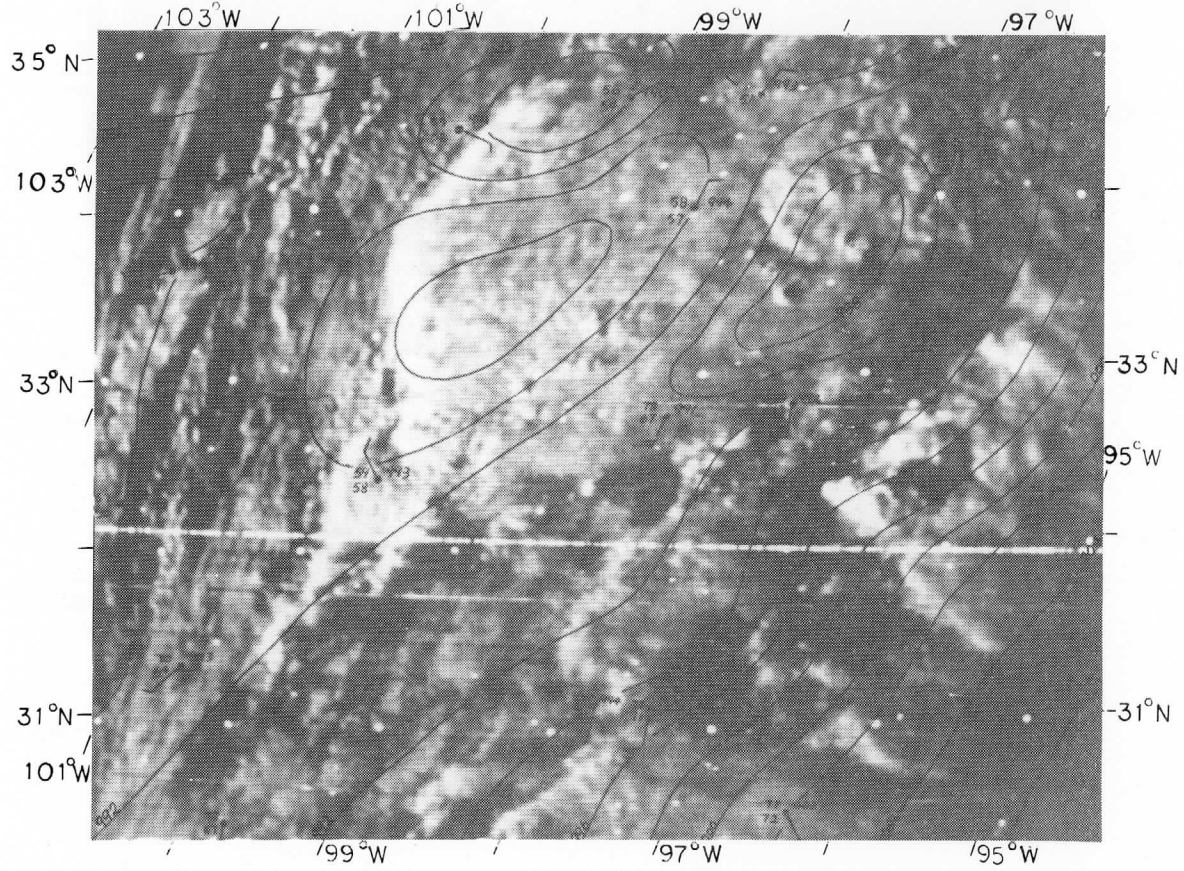


Figure 37. 2303 Z SMS Visible Image with 2300 Z Surface Mesoscale Analysis Superimposed

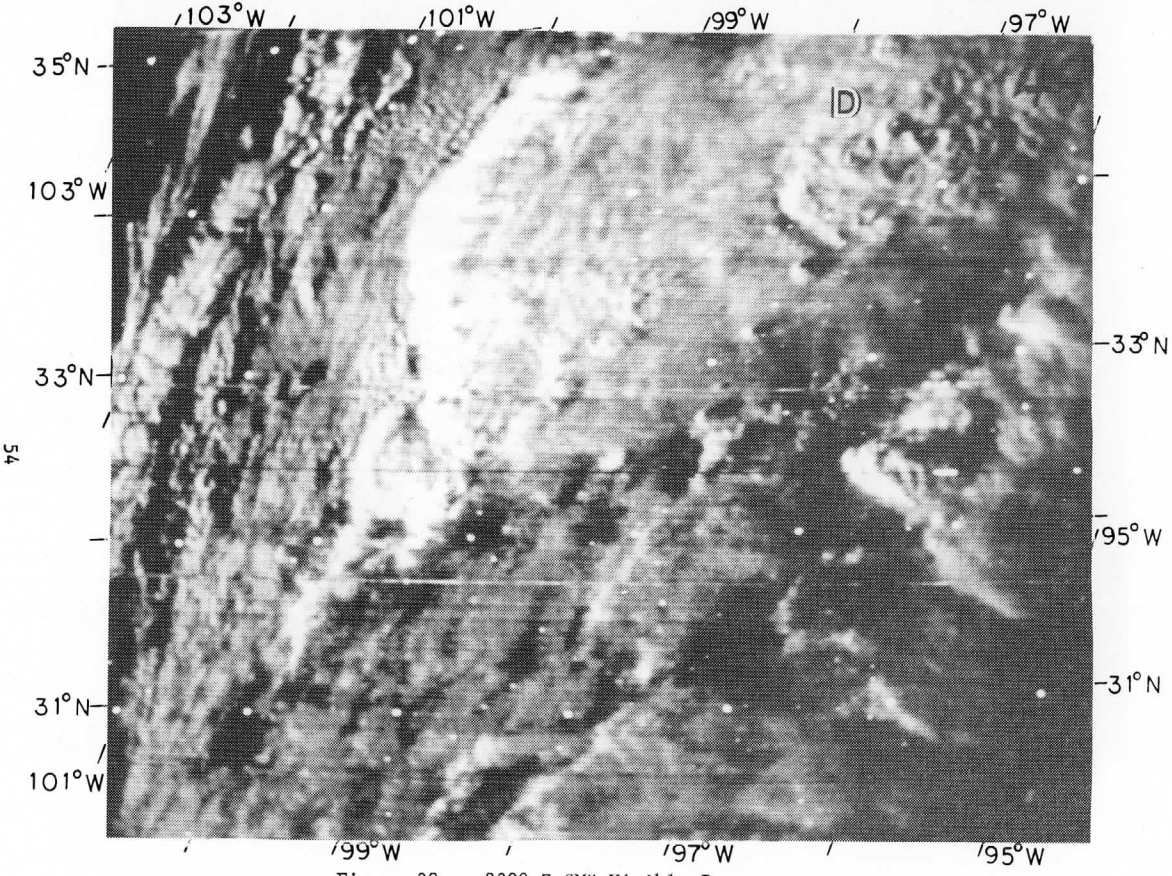


Figure 38. 2309 Z SMS Visible Image

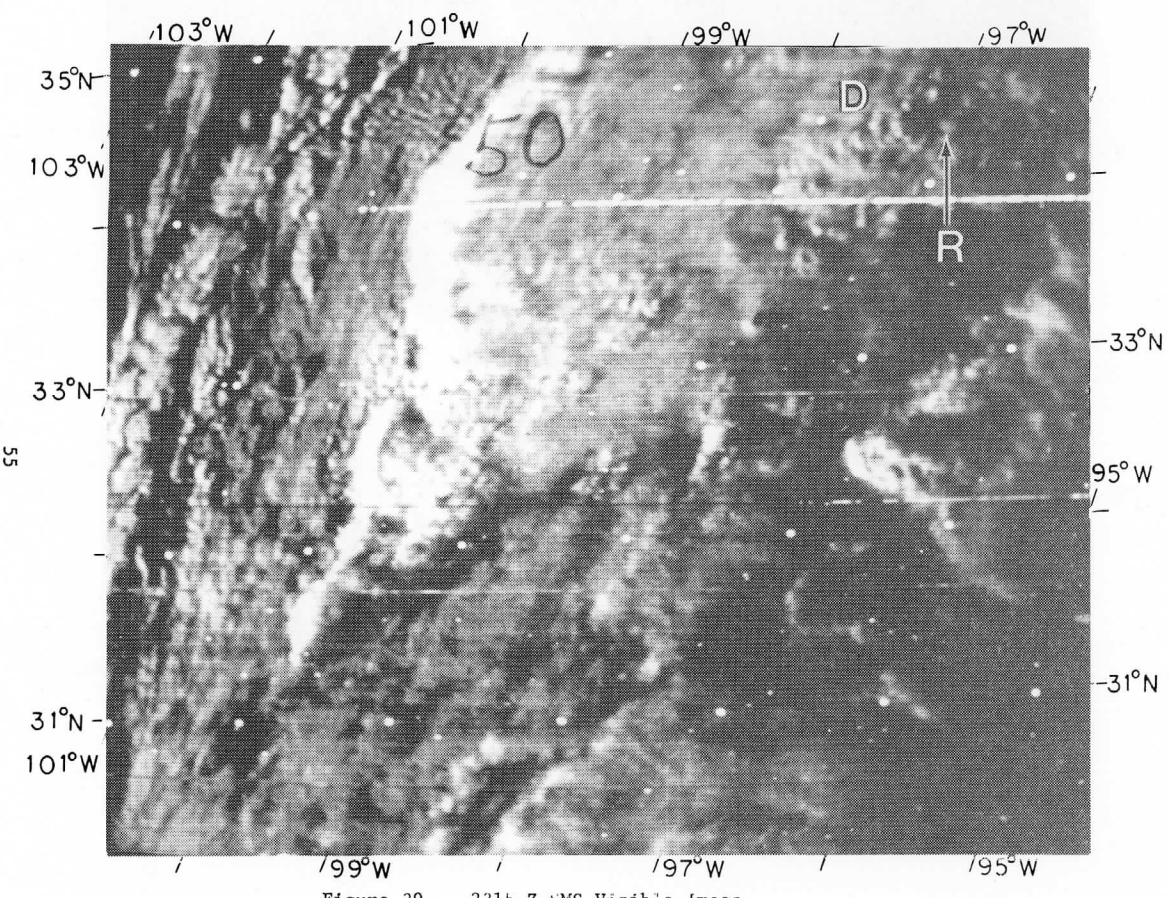


Figure 39. 2315 Z GMS Visible Image

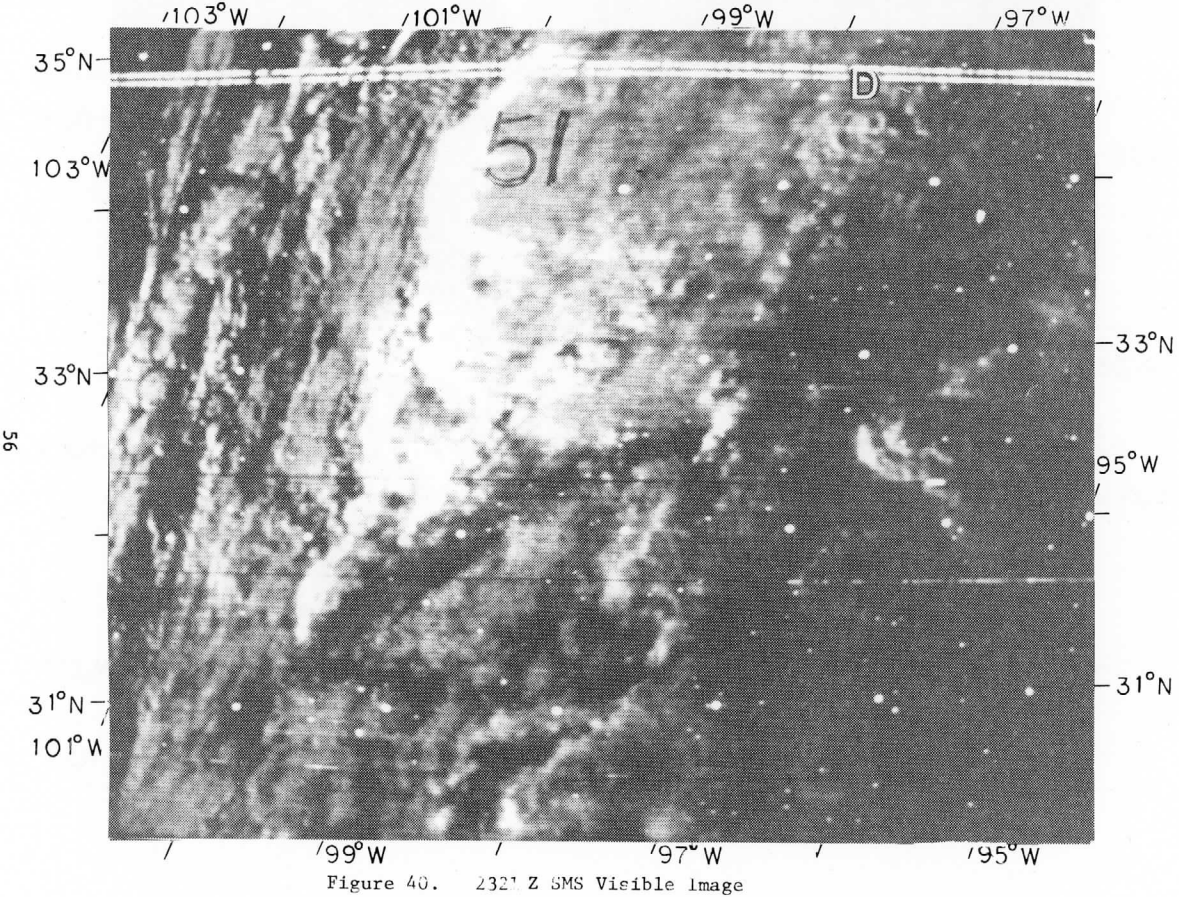


Figure 40. 2327 Z GMS Visible Image

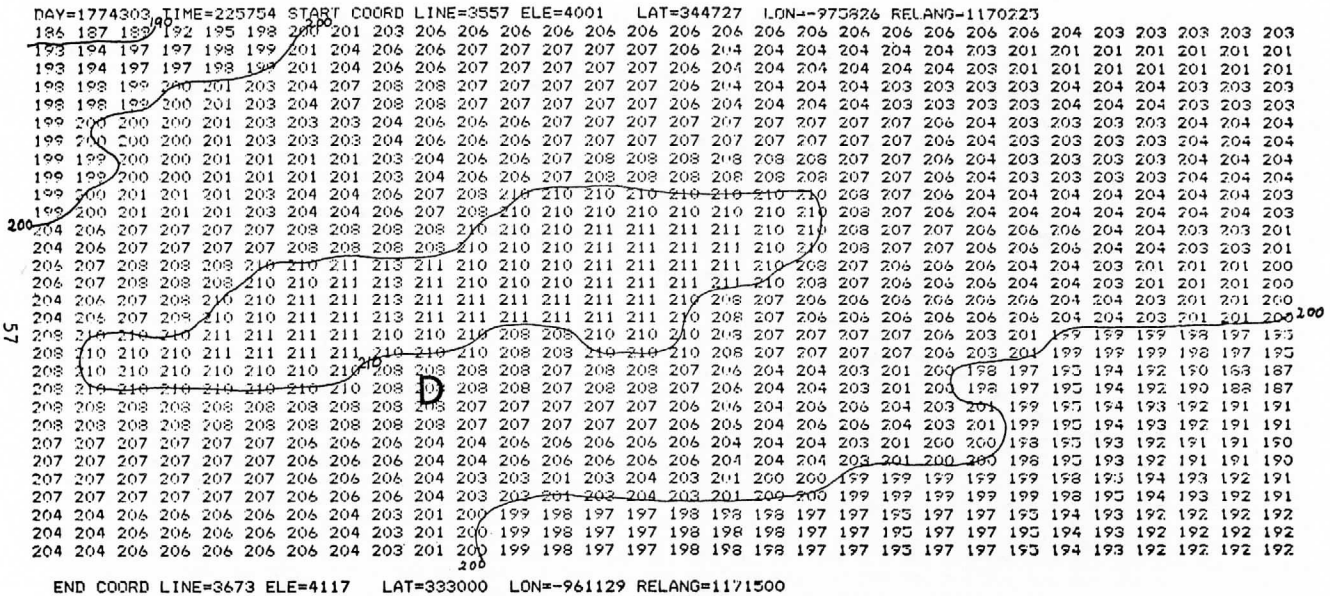


Figure 41. 2303 Z SMS Infrared Digital Data Near the Tornadic Storm D

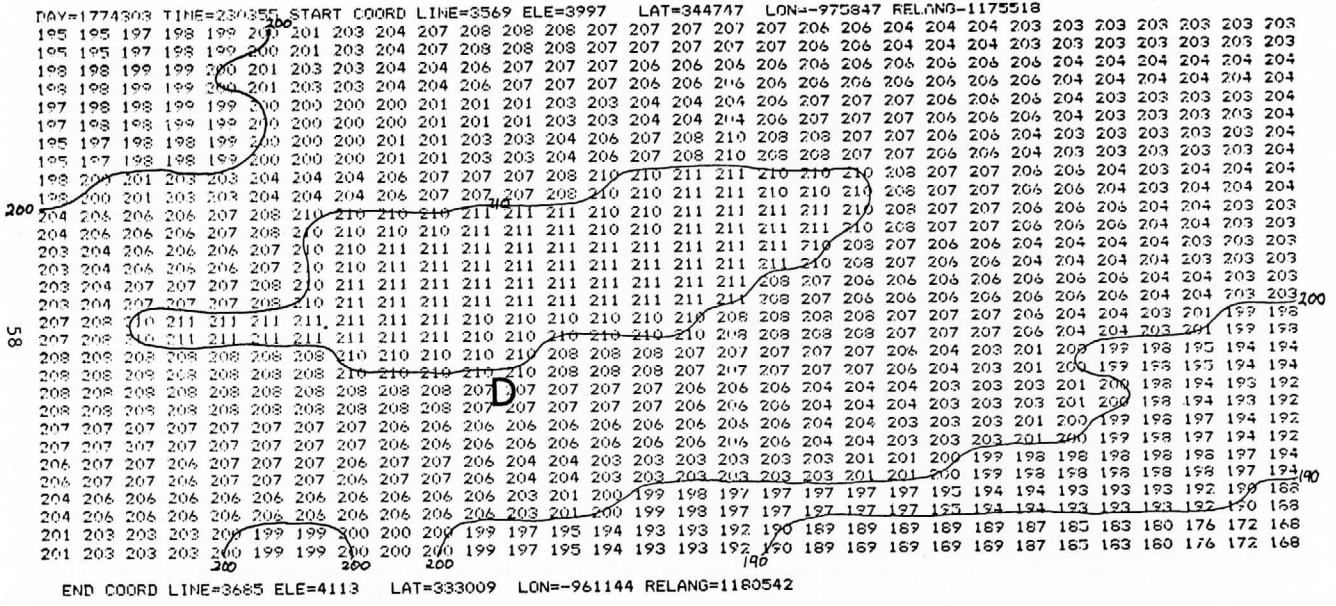


Figure 42. 2309 Z SMS Infrared Digital Data Near the Tornadic Storm D

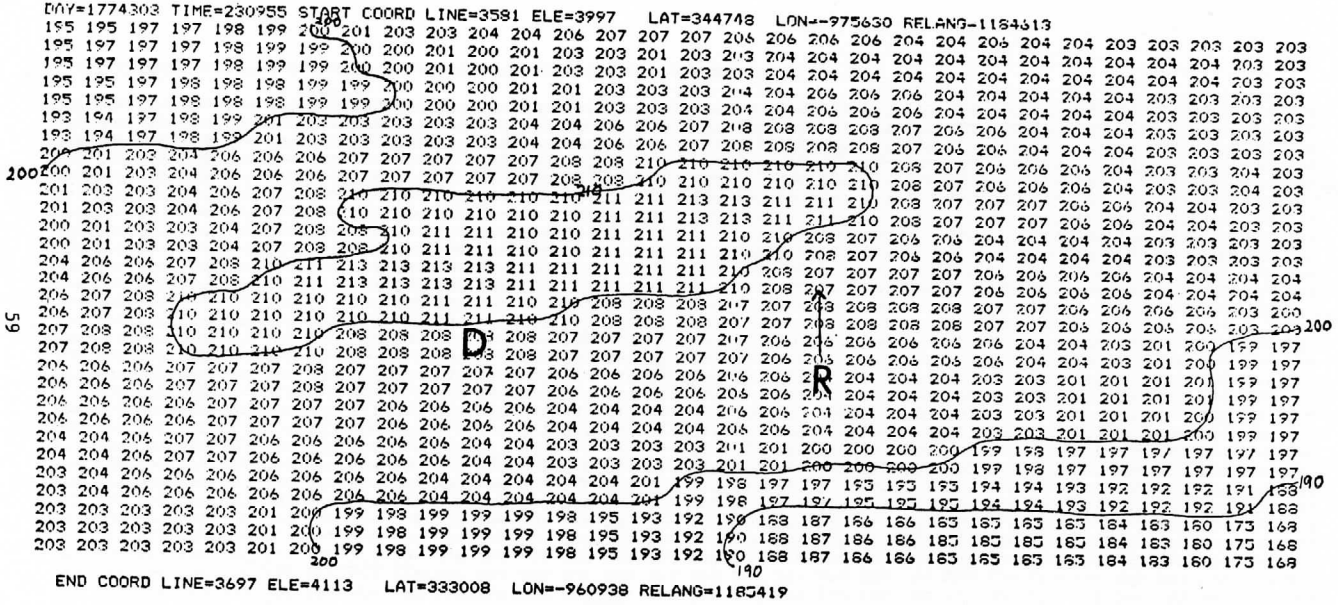


Figure 43. 2315 Z SMS Infrared Digital Data Near the Tornadic Storm D

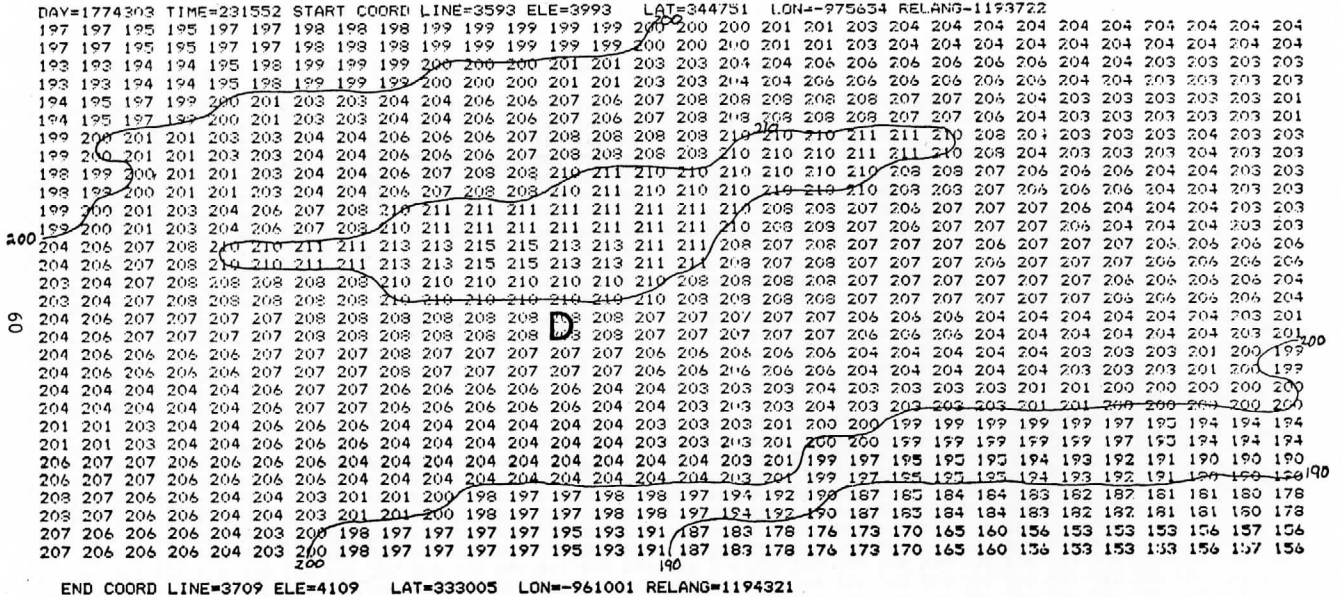


Figure 44. 2321 Z SMS Infrared Digital Data Near the Tornadic Storm D

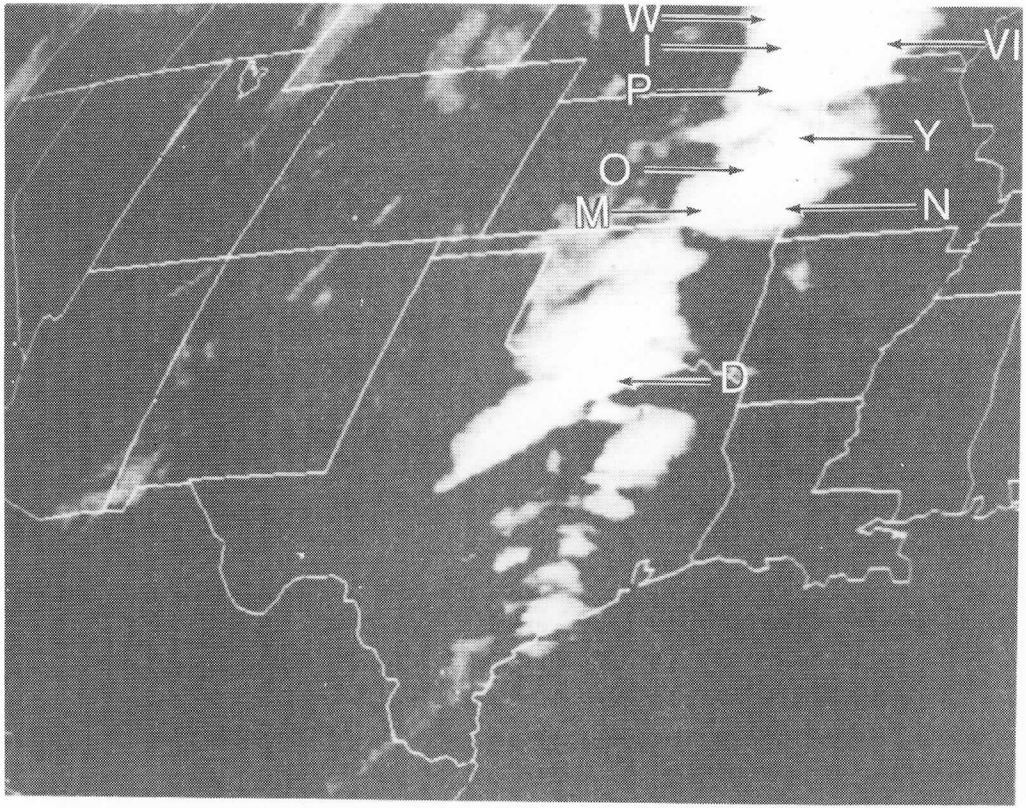


Figure 45. 2202 Z SMS Infrared Image Showing the Cold Dome Labels

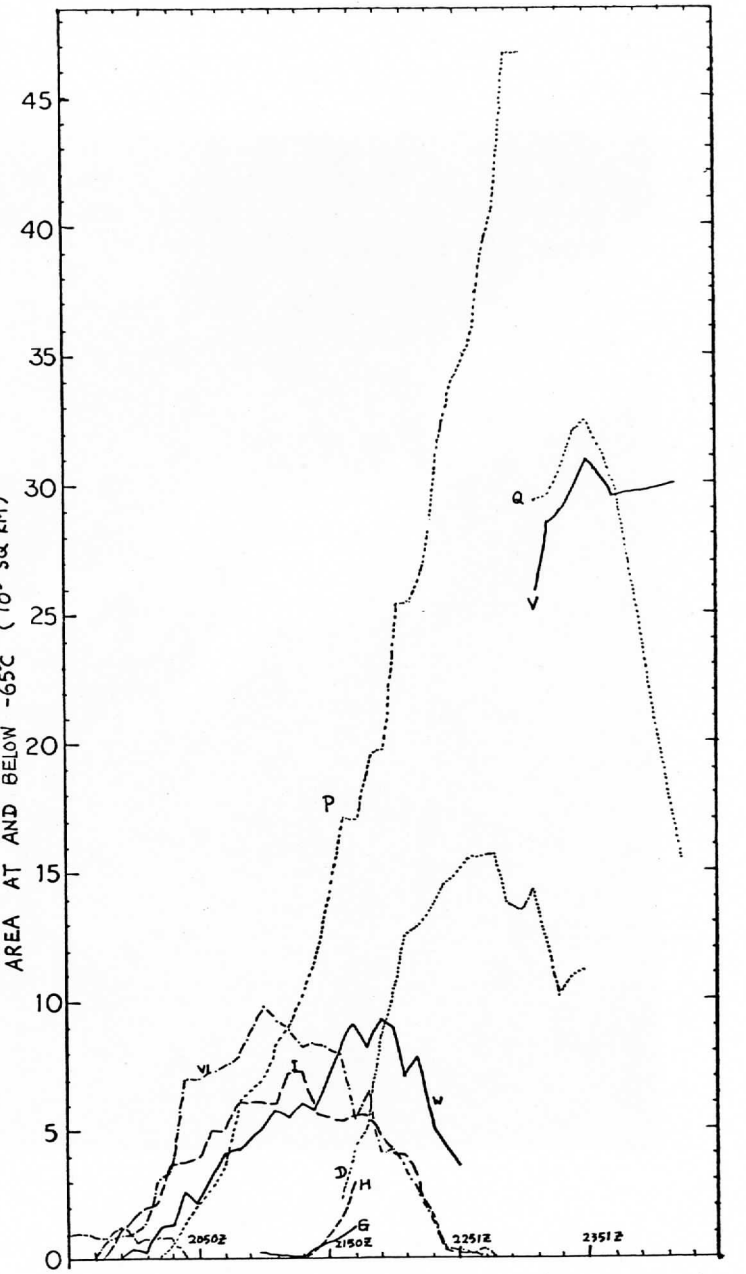


Figure 46a. Cloud Area at and Below -65°C as a Function of Time

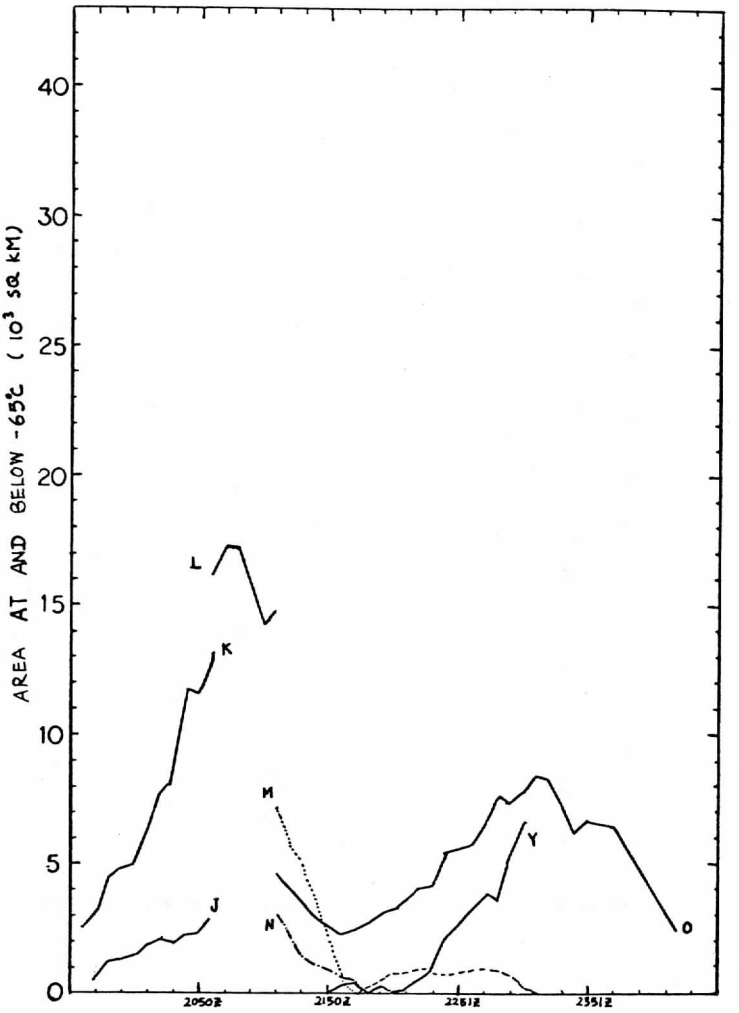


Figure 46b. Cloud Area at and Below -65°C as a Function of Time

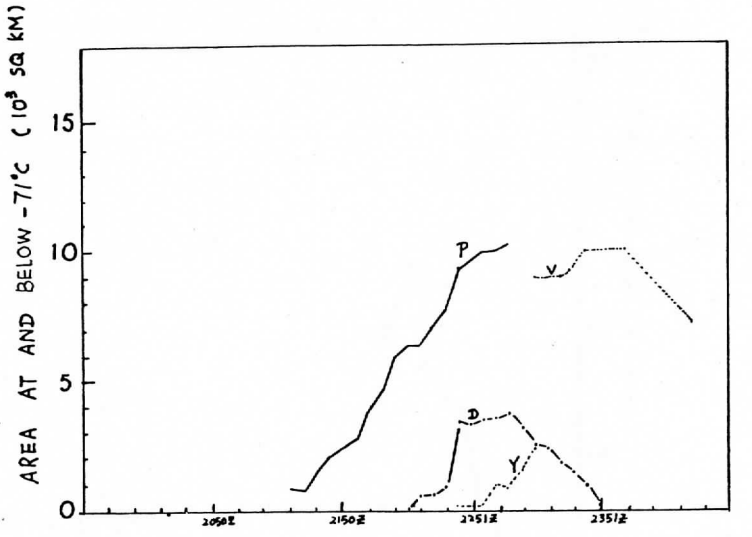


Figure 47. Cloud Area at and Below -71°C as a Function of Time

# A RADIATIVE TRANSFER SCHEME OF SOIL MOISTURE REMOTE SENSING

George R. Diak

ABSTRACT

A method of soil moisture assessment has been developed based on the solution of the Fourier heat transfer equation of a semihomogeneous solid undergoing slow release of heat. Variations of soil density, conductivity, and specific heat with moisture have previously been researched for the three main soil types. It has been found possible to approximate this variation linearly in each case.

Substituting these linear relationships in the solution of the Fourier equation, it is possible to solve for the water content of the soil as a function of the soil type, reflecting the density, specific heat and change in conductivity with change in moisture content, and also as a function of net radiation at the surface and drop in surface temperature with time.

With an empirical correction, the method has yielded good agreement with reality in experiments both with ground and satellite data.

## 1. INTRODUCTION

Variations in the temperature of the soil are a response to variations of net radiation at the surface, exchanges of sensible and latent heat with the atmosphere and heat exchanges within the soil itself.

Conditions have been sought where it is possible to minimize the air-soil exchange of sensible and latent heat (nighttime with calm winds). Under these simplifying conditions, the temperature of the soil surface becomes primarily a function of the net radiation at that surface and the amount of heat exchange and storage with the upper, thermally active layers of soil. The exchange and storage are in turn dependent on the soil's thermal characteristics; the volumetric heat capacity and the conductivity. Experiments have shown both volumetric heat capacity and thermal conductivity are sensitive functions of soil moisture.

The relationship of surface temperature to net radiation and soil heat exchanges has been used by Brunt and others to estimate the nighttime fall of temperature. E. Knighting (1950) in such a study even suggested the opposite route be taken, that is, knowing the night drop of temperature, estimate the thermal parameters of the soil.

This research examines the feasibility of such a method to estimate soil moisture content, first from ground-based data and later using satellite-based infrared temperature retrieval. The first results appear very promising.

## 2. THEORY

The heat budget equation at the soil surface can be written

$$SW\downarrow (1-A) + LW\uparrow + LW\downarrow + E_o + Q_o + S_o = 0 \qquad (1)$$

where

$SW\downarrow$ = short wave down,

$A$ = planetary albedo,

$LW\downarrow$ = long wave radiation down,

$LW\uparrow$ = long wave radiation up,

$E_o$ = air $\leftrightarrow$ sfc latent heat exchange,

$Q_o$ = air $\leftrightarrow$ sfc sensible heat exchange, and

$S_o$ = heat transfer sfc $\leftrightarrow$ thermally active soil layers.

At night with calm winds and $SW\downarrow = 0$, we make the approximations:

$$E_o \simeq 0$$

$$Q_o \simeq 0$$

and get the following simplified budget, letting $LW\uparrow + LW\downarrow = Rn$ = net radiation at surface.

$$Rn + S_o = 0 \qquad (2)$$

With certain initial and boundary conditions, the Fourier heat transfer equation can be solved. This equation of conduction of heat through the ground is:

$$\partial T/\partial t = \kappa(\partial T^2/\partial Z^2) \qquad (3)$$

$\kappa = K/\rho c$ = thermal diffusivity ($cm^2 \cdot sec^{-1}$)

$K$ = soil conductivity ($cal \cdot [cm \cdot sec \cdot °C]^{-1}$)
$\rho$ = soil density ($g \cdot cm^3$)
$c$ = soil specific heat ($cal \cdot [g \cdot °C]^{-1}$)
$t$ = time

(the quantity $\rho c$ is termed the volumetric heat capacity).

Treating the soil as a semi-infinite homogeneous solid (Ingersoll, 1948) undergoing gradual release of heat, if we assume

a) Rn = constant = Rn at t = 0, i.e., $\Delta T/T$ is small compared to 1, and

b) At t = 0, for our purpose the time at which Rn goes negative (sunset), the temperature of the soil is uniform with depth through the thermally active layer. $T(z,t) = T_o$ = constant at t = 0,

then the solution of (3) has the form

$$T - T_o = \frac{-2Rn}{(\rho cK)^{1/2}} \left(\frac{t}{\pi}\right)^{1/2} \qquad (4)$$

derived first by Brunt (1932) as a prognostic equation for the fall of temperature at night.

Under the simplifying assumptions named, the temperature of the soil surface is now a function only of net radiation at the surface, time and the heat transfer in the upper layers of soil. As (4) shows, there is an important dependence of $\Delta T$ on the density, conductivity, and specific heat of the soil, all three of which are sensitive functions of the amount of soil moisture.

## 3. THERMAL PROPERTIES OF THE SOIL AND THEIR DEPENDENCE ON SOIL MOISTURE

Thermal properties of the soil have a sharp sensitivity to the presence of liquid water. Not strictly a thermal parameter in itself, but one which influences the volumetric heat capacity $\rho c$ is the density $\rho$, which just increases linearly with the water fraction in a given amount of dry soil.

$$\rho = \rho_s + w\rho_s \tag{5}$$

where

$$\rho = \text{wetted soil density} = \frac{\text{mass soil + mass water}}{\text{bulk volume}} = \frac{m_s + m_w}{V_a} \quad (g \cdot cm^{-3})$$

$$\rho_s = \text{dry soil density} = \frac{\text{mass soil}}{\text{bulk volume}} = \frac{m_s}{V_a} \quad (g \cdot cm^{-3})$$

$$w = \text{water fraction} = \frac{\text{mass of water}}{\text{mass of soil}} = \frac{m_w}{m_s} \quad \text{(nondimensional)}$$

Specific heat, an important thermal consideration, is also a linear function of moisture content, and is just the mass-weighted average of the individual specific heats of water and the material comprising the dry-soil skeleton. Thus:

$$c = \frac{c_s + c_w w}{1 + w} \quad (cal \cdot [g \cdot °C]^{-1}) \tag{6}$$

where

$c$ = wetted soil specific heat, $(cal \cdot [g \cdot °C]^{-1})$

$w$ = water fraction, $m_w/m_s$

$c_d$ = dry soil specific heat, $(cal \cdot [g \cdot °C]^{-1})$ and

$c_w$ = specific heat of water $(cal \cdot [g \cdot °C]^{-1})$.

Thermal conductivity K is not a linear function of the amount of soil moisture. In general it increases with the addition of moisture most sharply with initial wetting of the soil, while the response flattens and even drops off at moisture contents above the normal field capacity.

The total conductivity K of moist soil (Van Wijk, 1966) can be expressed as the sum of several component conductivities. There is a component due to the heat conduction through the soil grains = $K_a$. There is also a component due to temperature gradients causing water vapor (latent heat) transport within the soil = $K_v$. Transport of sensible heat by liquid water is also possible but is usually neglected in the absence of gravity or pressure differences.

So then, $$K = K_a + K_v \, . \tag{7}$$

This introduction of conductivity components gives us the means to describe the observed K vs. w relationship. Dry soil has only the $K_a$ component of conductivity. With initial wetting, some of the interstices between soil grains are bridged by water, increasing the value of $K_a$. Also this addition of water to the soil introduces a vapor transport term $K_v$ to the total conductivity. This increase in $K_a$ and introduction of $K_v$ are responsible for the large jump in total conductivity with the first addition of moisture to dry soil.

When the soil approaches field capacity more and more of the interstices between soil grains are bridged by liquid water and water vapor movement becomes restricted by the large amount of liquid blocking. The $K_v$ component of conductivity drops and the total conductivity reflects this decrease.

Coarsely granular soils such as sand show the largest initial response of conductivity to wetting, while finely granular soils such as clay show the least. Moderately granular loam soils fall between these extremes. Sand, loam, and clay comprise the three basic soil-type categories. Though the amplitudes differ, the K vs. w curves for the three basic soil types retain the same shape (see Fig. 1).

Even though the curve of K vs. w is not linear, below the field capacity of the soil a straight line is a good approximation of reality. The conditions under which a soil will approach or exceed its field capacity are limited and setting this point as the upper limit of water content is justified in the vast majority of cases.

Using the results of Nakashabandi and Kohnke (Fig. 2) and doing a least squares fit to their data points for the three main soil types, straight lines were found for conductivity vs. water content of the form:

$$K = m_w + K_s \qquad (cal \cdot [cm^2 \cdot sec \cdot °C]^{-1}) \tag{8}$$

where

$m$ = slope

$w$ = water fraction, $m_w/m_s$

$K_s$ = conductivity of dry soil $(cal \cdot [cm^2 \cdot sec \cdot °C]^{-1})$.

The results were:

| | |
|---|---|
| fine sand | $K = .0472w + .0003$ |
| silt loam | $K = .0102w + .0005$ |
| clay | $K = .0004w + .0001$ |

with correlation coefficients of .716, .988, and .963 respectively.

So now the thermal parameters $\rho$, c, and K in Brunt's Eq. (4) have been described all linearly dependent on w. As long as the soil is below field capacity we can use these three linearly increasing functions in the denominator of (4) and get a unique value for any value of w within our predetermined range.

Substituting these three expressions

$$\rho = \rho_s + w\rho_s \ (g\cdot cm^{-3}),\ c = \frac{c_s + c_w w}{1 + w} \ (cal\cdot[g\cdot{}^\circ C]^{-1}) \text{ and } K = m_w + K_s$$

$(cal\cdot[cm\cdot sec\cdot{}^\circ C]^{-1})$ into the denominator of (4), a quadratic equation in w is the result of the form:

$$aw^2 + bw + c = 0 \qquad (9)$$

where

$$a = [\rho_s c_w m] \ (cal^2\cdot[cm^4\cdot{}^\circ C^2\cdot sec]^{-1})$$

$$b = \{\rho_s[c_w K_s + c_s m]\} \ (cal^2\cdot[cm^4\cdot{}^\circ C^2\cdot sec]^{-1}), \text{ and}$$

$$c = [K_s\rho_s c_s - (\frac{-2Rn}{T - T_o})^2 \frac{t}{\pi}] \ (cal^2\cdot[cm^4\cdot{}^\circ C^2\cdot sec]^{-1}) \ .$$

A dimensional check shows that a, b, and c have the same units and are consistent. If Rn is taken in $cal\cdot[cm^2\cdot min]^{-1}$, t is measured in hours.

Thus we now have a theory which predicts soil moisture on the basis of
1) soil type, reflecting $\Delta K/\Delta w$,
2) net radiation at the surface,
3) fall of temperature, and
4) time.

Solutions of quadratic equations are easily produced algebraically and can yield both real and complex solutions. It now remains to be shown that the real, positive solution produced by (9) is unique and provides reasonable answers.

## 4. TESTING THE THEORY

Project Great Plains, at O'Neil, Nebraska, in the summer of 1953 provided excellent data of the type needed to evaluate the soil-moisture theory developed. Detailed boundary layer measurements were

taken in seven selected observation periods. Five of these periods were suitable for use here.

The following important measurements were made:

1) soil surface temperature,
2) subsurface temperature,
3) soil moisture content,
4) soil density heat capacity and thermal conductivity,
5) net radiation at the surface,
6) wind speed,
7) heat budget terms,
8) general synoptic conditions.

Validity of Conditions

An important consideration is whether the conditions established for the theoretical validity of Eq. (4), Brunt's Equation, are met adequately by real data sources.

Recalling these conditions:

1) calm winds (sensible heat transfer ≈ 0)
Winds were considered calm if the average through the night was less than 5 kts. None of the observation periods were able to meet this standard. Stronger winds have the effect of promoting turbulent mixing and attenuating the drop in temperature that would otherwise occur. Necessary empirical corrections to account for this will be explained later.

2) latent heat transfer ≈ 0
Examination of the heat budget data from O'Neil showed the contribution of latent heat of condensation from dew deposition during the night observation periods to be inconsequential. A 5°C separation of the surface temperature and air temperature was deemed an adequate criteria to insure minimal contribution of latent heat of condensation to the heat balance.

3) $\partial T/\partial Z$ at $t = 0 = 0$ isothermal
$Rn = 0$, net radiation sunset, $t = 0$ for our periods, occurred at about 1930 local time. The soil structure at that time showed the greatest standard deviation of temperature with depth measured at twelve levels through the thermally active (diurnal wave) depth of 20 cm was 1.50°C. The average standard deviation was .98°C. Twenty cm was taken as the bottom of the diurnal wave depth. Here the greatest standard deviation of temperature with time in any observation period was 1.09°C with the average standard deviation = .92°C.

4) Rn constant during night

The maximum standard deviation of Rn through any observation period was 14.4 mcal/cm$^2$-min representing in that case the maximum of 14% change in the net radiation. The average standard deviation through all the observation periods was 8.8 mcal/cm$^2$-min. The time of maximum change was during the "transition" period of sundown, a relatively short length of time compared to the duration of the observations. Without this sundown period the variation of net radiation with time becomes much smaller and the largest standard deviation of Rn is then 8.15 mcal/cm$^2$-min, representing an 8% change in the net radiation. The average standard deviation of Rn with time under these same conditions was 6.11 mcal/cm$^2$-min.

Other Requirements of the Theory

The solution of the Fourier equation represented by Brunt's equation is for a homogeneous solid. Of course, soil is not homogeneous even through 20 cm, as O'Neil data shows. The solution we obtain for soil moisture then represents an average (nonlinear) of the conditions through this 20 cm depth.

It is important to note the theory applies to bare or vegetation-sparse soil. Experiments have shown vegetation plays an important part in modifying the thermal regime of the ground surface. Eq. 9 has no means to allow for this modification. The soil in the test case at O'Neil had sparse vegetation generally below 6 cm in height.

The soil in the O'Neil area was described as sandy loam containing sand and loam in the ratio of about 2 to 1. As such, a value of the straight line representing conductivity vs. moisture was selected 2/3 of the angular separation between loam and sand and the value for the intercept of the line similarly weighted. This produced a conductivity relationship for the O'Neil soil with the equation:

$$K = .0238K_o + .0004 \quad (\text{cal}\cdot[\text{cm}\cdot\text{sec}\cdot^\circ\text{C}]^{-1}) \tag{10}$$

From the theory we see that temperature fall is quite a sensitive function of the soil moisture content. A moderate change in soil moisture should be reflected in a large change in $\Delta T$. This is advantageous since it means that measurement errors in $\Delta T$ will produce only small errors in the moisture value calculated. For the sandy loam soil at O'Neil, for example, a difference of 1°C in a drop of 10°C in 9 hours produces only a 3% difference in the value of soil moisture obtained. It has been verified that with certain empirical corrections it is possible to evaluate soil moisture.

The O'Neil data gives the capability of working both ways through Brunt's relationship, i.e. having the soil temperature, density, and conductivity measured, as well as soil-moisture, it was possible to work through the equation as Brunt did and solve for the theoretical drop in temperature to see how it compared to the measured $\Delta T$ at the surface. As Table 1 shows, when the indicated empirical corrections were made, the values agreed in general to about 1°C. The exception is Case 5 where wind was indicated as gusting to 30 mph during the period.

More important than the closeness of the absolute values of measured and calculated moisture contents are the agreements of the variations of both of these from case to case. The method can always be "zeroed" from some known reference state, but the closeness in the trends indicates the model is showing the proper direction and sensitivity to change in soil moisture.

Empirical Corrections

Brunt in his experiments used estimated values of net radiation while O'Neil data provides measured values for increased accuracy. Additionally, Brunt's solution for night temperature fall provides a constant overestimation of the actual temperature drop for several reasons.

1) Rn is evaluated by Brunt's scheme at the beginning of the period and considered constant during the night, which is approximately but not exactly true. A drop in temperature of 10°C during the course of an observation period from 300° to 390° absolute represents a 13% change in the blackbody radiation of a surface. Since, in contrast to Brunt, one of our independent variables is net radiation, we can use an average of Rn through the period as a better representation of reality.

2) The assumption that sensible heat transfer is close to zero is never strictly true; there is always thermal interaction of the air with the ground, increasing with increasing wind speed, which has the effect of decreasing the temperature drop of the surface from the value expected from Brunt's relationship. Because we had a complete heat budget at O'Neil, empirical correction factors as a function of wind speed have been used on the data.

Temperature corrections as a function of wind speed have been researched by Dow (in Haltiner and Martin, 1957) and were found to be multipliers of 1.52 and 1.82 for Beaufort scale winds of force 2 and 3 respectively to convert actual temperature drop to a Brunt theoretical value. O'Neil results indicated multipliers of 2.22 and 2.34 for Beaufort winds of force 3 and 4.

## 5. EVALUATING SOIL MOISTURE FROM SATELLITE DATA

### Discussion

Evaluating soil moisture from satellite data has several advantages as well as several added requirements from a similar ground-based evaluation.

The advantages are a result of the position of a geosynchronous satellite and the method of temperature sensing. Additional requirements are basically a product of the remote sensing nature of the satellite platform.

### Advantage of the Method

1) Measurements of ground (skin) temperature done at the surface are extremely difficult and much experimental time has been devoted as to the type of sensor best used for this purpose and exactly how it should be positioned to indicate the true surface temperature. The satellite eliminates this particular problem by employing the radiative relationship directly and may give a more accurate reading than ground-based sensors.

2) The ability of the satellite sensor to do large area work is unsurpassed, with images taken by SMS every 30 minutes over the better portion of an entire hemisphere.

3) The method of soil-moisture evaluation outlined here gives an average value of this quantity over the depth of the diurnal pulse of heating and cooling. The other method being developed, microwave sounding, senses moisture at the surface but says nothing about the lower layers of soil. Clearly, the main use of soil moisture data is agricultural and for this purpose information about the condition of the subsoil is also valuable.

### Requirements

1) From the ground it was necessary to be quite careful in selecting the data. In the O'Neil trial most of the required selecting was done by the observers and needed little additional editing. From the satellite we must be especially careful in choosing data sets. Relatively calm winds, small temperature advection and separation of the lowest surface temperature during the night vs. the dewpoint temperature are essential. Naturally, from the satellite, clear skies to make viewing of the ground possible are an additional requirement. Clear skies must cover as wide an area around the actual data points as possible. Cold clouds have the effect of "polluting" the thermal field

of the infrared sensor and may lower the temperature retrieved from "clear" regions by several degrees. All the conditions named so far are not particularly difficult to come by, but should be observed to insure the success of the soil-moisture method.

2) From O'Neil data we have direct measurements of Rn at the soil surface. From the satellite we are not able to get at this quantity directly. There are several schemes for calculating Rn, the simplest being empirical models (Angstrom, Brunt, 1932) giving Rn as a function of the temperature of the surface and the vapor pressure in the lowest atmospheric layer. Other possible methods would be radiative transfer models or radiation charts such as the Elsasser diagram. These last two models require soundings be taken, however, increasing the dependence of the method on ground data. Also, radiosonde soundings are only taken at 12-hour intervals at select locations, whereas we can obtain a value for Rn through an empirical formula every three hours at a vastly denser network of stations. For these reasons an empirical formula for Rn will be used.

Brunt's formula for nocturnal radiation is:

$$LW\downarrow = [a + b(e)^{1/2}]\sigma T^4 \qquad (11)$$

where

a and b = empirical constants

e = vapor pressure in mb

$\sigma$ = Plank's constant

So, net radiation = $LW\uparrow - LW\downarrow$, $LW\downarrow = \varepsilon\sigma T^4$ , (12)

and

$$Rn = \varepsilon\sigma T^4 - [a + b(e)^{1/2}]\sigma T^4 \quad \text{or} \quad \sigma T^4\{\varepsilon - [a + b(e)^{1/2}]\} \qquad (13)$$

where

$\varepsilon$ = infrared emissivity.

This form has been modified slightly from Brunt's with the addition of the infrared emissivity. In Brunt's empirical formula for $LW\downarrow$ it has been absorbed statistically in the constants a and b. Recent experiments have demonstrated (Buettner and Kern, 1965; Kondrat'yev, 1965) the infrared emissivity of soil surfaces may deviate enough from unity to retain the emissivity term in the evaluation of $LW\uparrow$. Kondrat'yev lists the following values of infrared emissivity for sand

and loam.

| Sand | | Loam | |
|---|---|---|---|
| dry | .949 | dry | .954 |
| wet | .962 | wet | .968 |

As shown, the variation of emissivity with water content is on the order of only .01 over the range of moisture of the soil. This variation is small enough to be ignored in the soil-moisture evaluation method.

3) The success of the soil-moisture method depends on how accurately we can measure both the absolute temperature of the surface and the change in temperature throughout the observation period. Of these two, however, the measurement of $\Delta T$ is by far the most important. The absolute temperature only enters into the calculation in the determination of Rn, and Rn is relatively insensitive to small errors in the measured temperature. For example, an error of 2°K at a temperature of 290°K makes only a 3% difference in the value obtained for Rn. Errors in $\Delta T$, however, have far more potential to produce errors in the final value for moisture obtained. Again, judicious data selection is the key to avoiding errors of this type and the criteria already established go a long way towards this goal.

The satellite looks through the atmosphere and even in the "window" channel there is a certain amount of atmospheric attenuation of upwelling radiation from the ground, typically resulting in the surface reading about 5°C colder than it actually is. Statistical corrections are applied to the data (Reunt and Joffe, 1959; Smith and Byers, 1938), involving the magnitude of the correction depending on the window channel used and the viewing angle, indicating the length of the atmospheric path through which the signal is attenuated. Large changes in the water content of the atmospheric column during an observation period would cause the infrared instrument to register changes in temperature which in fact do not exist. These situations must be avoided with the condition that the dewpoint temperature not vary significantly during the course of the observation period.

4) Items 1, 2, and 3 of this section establish a reliance of the satellite method on a certain amount of ground-based data. It is the natural desire of the satellite meteorologist to make this dependence minimal. Summing up the required ground-data we find the necessary information is: 1. wind speed 2. vapor pressure 3. dewpoint 4. general synoptic condition. All these quantities can be obtained from the ordinary three-hour station report.

5) Resolution of the O'Neil data was virtually at a point. Infrared images from the SMS satellite provides a resolution of two-miles at the sub-satellite point. As such the values obtained for soil moisture will represent an average over a minimum of four square miles. Preliminary results from the satellite experiment are shown in Table 2.

## 6. CONCLUSION

It cannot be stressed enough that judicious data selection is the key to the success and accuracy of this method. Again, the conditions are not difficult to come by but must be observed. Large high pressure areas give generally favorable conditions for employment of the technique and are frequent in the period for which information would most likely be desired, the North American growing season. Evaluation of soil moisture on a weekly basis over large areas does not seem an unreasonable goal.

Even in these early stages, the soil moisture method has yielded good results. The possibilities of "fine tuning" the model still lie ahead and are tremendous. Additional research on correction factors for winds and data on the thermal parameters of more specific soil types can increase the accuracy. Two satellites, one measuring radiation in the window channel, the other measuring net radiation at the top of the atmosphere can provide estimates on net radiation at the surface, possibly better estimates than those based on empirical models such as Brunt's. Adding to the method corrective factors for vegetation is the next area to be researched.

Several other moisture sensing techniques (Idso et al., 1975) are currently being explored by other researchers. Short wave reflectivity and microwave emissivity of the surface have both been shown as indicators of soil water amount. Most closely related to the method developed here is that of Idso et al. (1975) who have found: 1) the diurnal range of soil temperature may be correlated with its moisture content and, 2) the soil-air temperature difference can be related to its moisture pressure potential. Diurnal temperature range of a soil depends on its type and this must be known to obtain soil moisture. Idso et al. have found however the pressure potential relationship is independent of soil type, although again the soil type must be known to make an exact moisture determination.

An advantage to the method developed here is that it takes into account, with the determination of net radiation, the seasonal variability in temperature differences to be expected with variations in this important "forcing function."

The uses of a fully developed remote sensing soil moisture system are numerous and have the potential for great economic benefit (Idso et al., 1975). The current USDA crop yield prediction model uses rainfall as one of its variables; however, soil moisture has been shown a better indicator of crop development than rainfall (Idso et al., 1975). The development of certain plant pests and diseases is related to the moisture content of the soil (Idso et al., 1975). Additionally, soil moisture knowledge has shown itself useful in management of crops and rangelands and the controlled application of herbicides and pesticides (Idso et al., 1975). Undoubtedly there are many more uses for this remote sensing technique.

## REFERENCES


Brunt, David: Notes on Radiation in the Atmosphere. Quarterly Journal of the Royal Meteorological Society, Vol. 58, 1932, pp. 389-418.

Buettner, K. and D. Kern: The Determination of Infrared Emissivities of Terrestrial Surfaces. Journal of Geophysical Research, Vol. 70, No. 6, 1965, pp. 1329-1337.

Griggs, M.: Emissivities of Natural Surfaces in the 8- to 14-Micron Spectral Region. Journal of Geophysical Research, Vol. 73, No. 24, 1968, pp. 7545-7551.

Haltiner, G. and F. Martin: Dynamical and Physical Meteorology. New York, McGraw-Hill Book Company, 1957.

Idso, Sherwood B., Ray D. Jackson, and Robert J. Reginato: Detection of Soil Moisture by Remote Surveillance. American Scientist, Sept.-Oct. 1975, pp. 549-556.

Ingersoll, L. R.: An Introduction to the Mathematical Theory of Heat Conduction with Engineering and Geological Applications. New York, McGraw-Hill Book Company, 1948.

Knighting, E.: A Note on Nocturnal Cooling. Quarterly Journal of the Royal Meteorological Society, No. 76, 1950, pp. 173-181.

Kondrat'yev, K. Ya.: Actinometry. National Aeronautics and Space Administration, Washington, D.C., November 1965.

Lettau, H. and B. Davidson: Exploring the Atmosphere's First Mile. New York, Pergammon Press, 1957. Volumes I and II.

Nakashabandi, A. and H. Kohnke: Thermal Conductivity and Diffusivity of Soils as Related to Moisture Tension and Other Physical Properties. Agricultural Meteorology, Vol. 2, 1965, pp. 271-279.

Revut, I. and A. Joffe, editors: Fundamentals of Agrophysics. National Science Foundation and United States Dept. of Agriculture, translated from Russian, 1959.

Smith, W. and H. Byers: The Thermal Conductivity of Certain of the Great Soil Groups. Soil Science Society of America, Proceedings, No. 3, 1938, pp. 13-19.

Smith, W., P. Rao, R. Koffler, and W. Curtis: The Determination of Sea-Surface Temperature from Satellite High Resolution Infrared Window Measurements. Monthly Weather Review, Vol. 98, No. 8, August 1970, pp. 10-14.

Strahler, A.: Physical Geography. New York, John Wiley and Sons, Inc., 1969.

Sutton, O.: Micrometeorology. New York, McGraw-Hill Book Company, 1953.

Van Wijk, W. R., editor: Physics of Plant Environment. Amsterdam, North-Holland Publishing Company, 1966.

Wiegman, E., R. Hadfield, and P. Davis: Infrared Emissivities and Upper Tropospheric Cloud Motions. Stanford Research Institute, Menlo, Park, California, August 1973.

TABLE 1: O'NEIL RESULTS

| Observation period | $\Delta T_{actual}$ | $\Delta T_{corrected}$ | $\Delta T_{theory}$ | $\overline{w}_{measured}$ | $\overline{w}_{calc}$ | $\Delta w$ |
|---|---|---|---|---|---|---|
| 1 | 5.89° | 12.84° | 13.28° | 10.2% | 6.6% | 3.6% |
| 3 | 6.45° | 14.06° | 13.30° | 8.0% | 4.7% | 3.3% |
| 5* | 5.99° | 13.05° | 17.21° | 4.5% | 8.5% | 4.0% |
| 6 | 7.62° | 18.50° | 17.92° | 3.0% | 3.4% | .4% |
| 7 | 8.46° | 19.79° | 18.20° | 4.5% | 2.5% | 2.0% |

*winds gusting to 30 mph during period

$\Delta T_{actual}$ is the actual fall of temperature observed during the period,

$\Delta T_{corrected}$ has been adjusted by the empirical multiplier mentioned, and

$\Delta T_{theory}$ is the figure obtained by substituting the measured values of soil parameters into Brunt's equation.

Close fit between columns 2 and 3 is therfore desirable. Last three columns show fit between calculated and measured values of moisture content.

TABLE 2: SATELLITE DATA 8 May 1975 OKLAHOMA

| Area | Digital Counts from SMS | Corresponds to ΔT corrected for Emissivity & Atmospherics | ΔT Corrected for Wind Speed |
|---|---|---|---|
| 1 | 90 → 99 | 5.5°K | 12.1°K |
| 2 | 89 → 97 | 5.0°K | 11.0°K |
| 3 | 94 → 103 | 5.5°K | 12.1°K |
| 4 | 95 → 106 | 7.0°K | 15.4°K |

$\Delta T$ = 8.5 hours

Emissivity for "sandy loam" soil averaged at .955.

Dew point temperature for period ≃ 45°F = 7.2°C

e = 10.1 mb

$Rn = \sigma T^4\{\varepsilon - [a + b(e)^{1/2}]\}$

$Rn_1 = -.157 \text{ cal}\cdot\text{cm}^{-2}\cdot\text{min}^{-1}$

$Rn_2 = -.146 \text{ cal}\cdot\text{cm}^{-2}\cdot\text{min}^{-1}$

$\overline{Rn} = -.151 \text{ cal}\cdot\text{cm}^{-2}\cdot\text{min}^{-1}$

Quadratic equation for "sandy loam" soil:

$$.0333w^2 + .0072w + [.0001 - (\frac{-2Rn}{T - T_o})^2(\frac{t}{\pi})] = 0$$

Results--Soil Moisture (weight %)

Area 1. 14%

Area 2. 16%

Area 3. 14%

Area 4. 9%

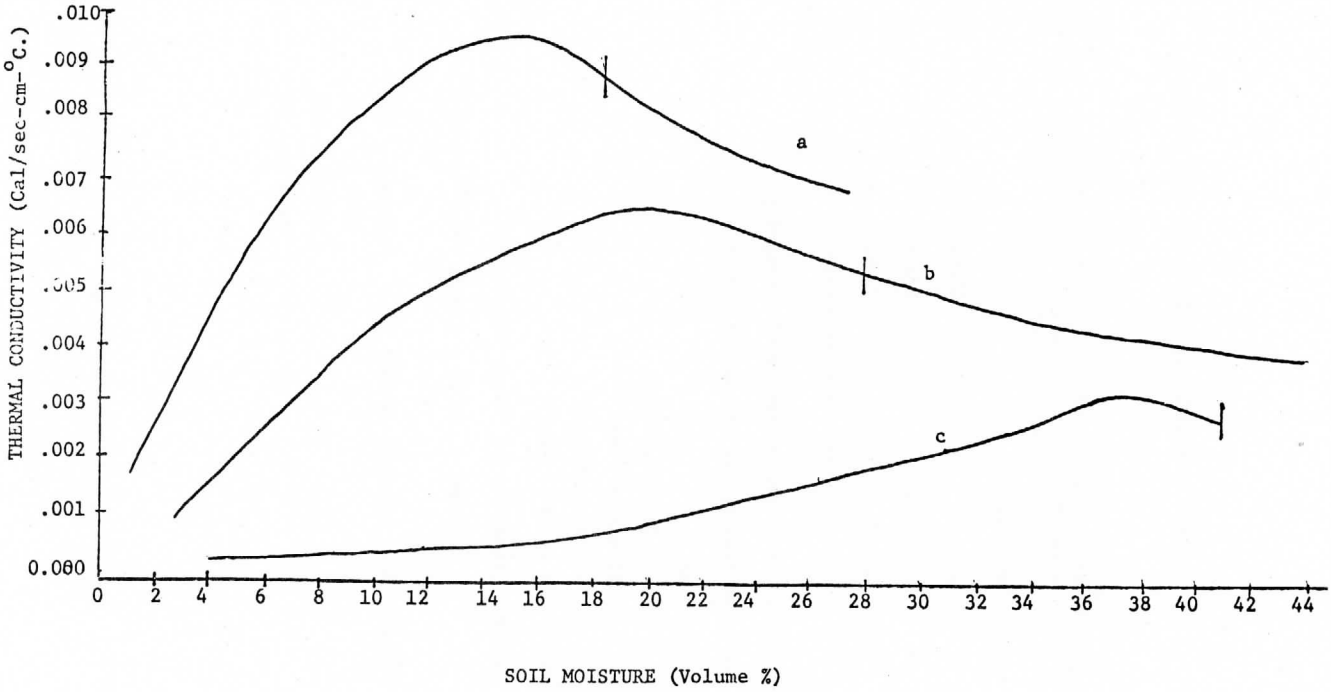


Figure 1 General form of conductivity vs. moisture for a) sod-podzolic sandy soil, b) sod-podzolic heavy loamy soil, and c) clayey soils (After A. F. Chudnovskii, in Revut and Joffe, 1959). Vertical bars indicate approximate point of field capacity.

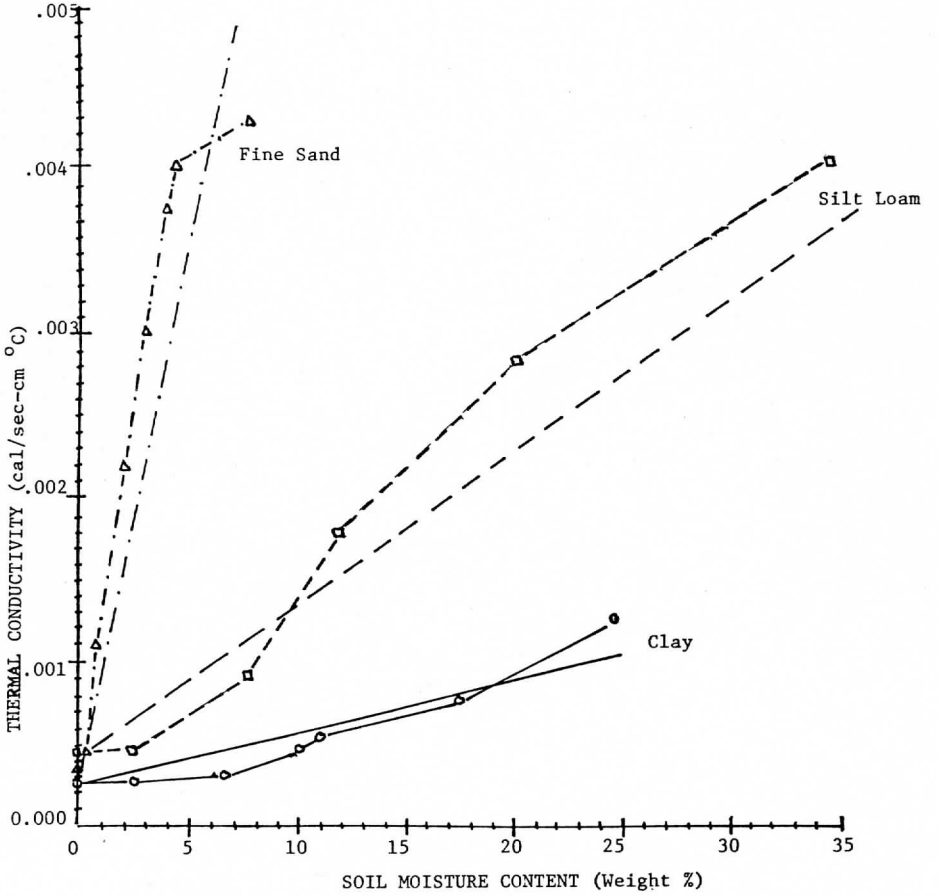


Figure 2 Results of Nakashabandi and Kohnke (1965) for conductivity vs. weight % moisture. Straight lines are those fitted to their results by least-squares.

# DETERMINATION OF SOIL MOISTURE FROM SATELLITE SENSOR DATA

George R. Diak

ABSTRACT

This study examines the possibilities of extending remote sensing of soil moisture from bare-soil areas to vegetated regimes, using a model of the heat budget of plant leaves. To verify this model, experiments using both satellite and ground-station thermal data are proposed.

## 1. INTRODUCTION

Evaluation of soil moisture using a remote sensor could have important value in crop production models, in pest and disease control and in other related agricultural areas. Idso et al. (1975) explored such applications using a statistical approach that related soil moisture to maximum and minimum diurnal temperatures. In a previous report by the author (Diak, 1975), the theory of heat transfer of a homogeneous solid was used to evaluate bare-soil moisture levels as a function of the night-time fall of ground surface temperature.

Moisture evaluation of the soil beneath vegetation, however, is much more complex than bare-soil analysis. Plants modify the thermal regime of the soil so extensively that it is extremely difficult to try to "see through" the plant cover or to remove its effects with a model. A moisture sensing scheme that relies on thermal radiation information must take into account the ways in which vegetation affects the energy balance of the soil/plant/air system.

## 2. DISCUSSION

Although there is no simple scheme for evaluating soil moisture, an experiment using plants themselves as indicators of soil moisture level does appear to be potentially useful. The rate at which plants transpire water depends on available solar energy, wind speed, air temperature and humidity, and -- as examined in this paper -- on the availability of soil moisture. In conditions favoring high transpiration rates, as much as one-third to one-half of the total radiant energy impinging on a plant leaf may be utilized in transpiration (Meyer et al., 1970).

The heat budget of a plant leaf may be written as:

$$Q_{abs} = R \pm C \pm LE \pm M \qquad (1)$$

$Q_{abs}$ = total energy absorbed by plant leaf

$R$ = thermal radiation from the leaf = $\varepsilon\sigma T_\ell^4$

where $\varepsilon$ = leaf emissivity

$\sigma$ = Stefan-Boltzmann constant

$T_\ell$ = leaf temperature

$C$ = sensible heat flux between leaf and air

$L$ = latent heat of evaporation of water at $T_\ell$

$E$ = amount of evaporated water

$M$ = = heat of metabolic plant processes (usually neglected).

Gates (1972) worked with this heat budget model and attempted to evaluate empirically the terms C and LE in equation (1). He expressed his results in the following form:

$$Q_{abs} = \varepsilon\sigma T_\ell^4 + K_1\{V/D\}^{1/2}(T_\ell - T_a) + L(T_\ell)\frac{[S\rho_\ell(T_\ell) - RHS\rho_a(T_a)]}{r_1 + K_2\{\frac{D^{.35}\ W^{.20}}{V^{.55}}\}} \qquad (2)$$

1 2 3 4

Term 3 of equation (2), $K_1\{V/D\}^{1/2}(T_\ell - T_a)$, is an expression for sensible heat transfer between leaf and air. This transfer is proportional to the temperature difference between leaf and air, and to wind speed; it is inversely proportional to the dimension of the leaf in the downwind direction, indicating that an increase in the depth of the boundary layer of still air adjacent to the leaf hinders heat transfer.

$K_1$ = proportionality constant

$V$ = wind speed

$D$ = downwind dimension of leaf

$T_\ell$ = leaf temperature

$T_a$ = air temperature.

Term 4 of equation (2), $L(T_\ell) \dfrac{[S\rho_\ell(T_\ell) - RHS\rho_a(T_a)]}{r_1 + K_2\{\dfrac{D^{.35}\, W^{.20}}{V^{.55}}\}}$, is an

empirical formula for the flux of latent heat from a leaf surface, in a form often used in plant physiology. It is analogous to Ohm's Law, expressed in this case as:

$$\text{energy flux} = \frac{\text{forcing function}}{\text{path resistance}}$$

The numerator of term 4 expresses the difference in water vapor density between the plant leaf (assumed at saturation at $T_\ell$) and the adjacent air at relative humidity RH:

$L(T_\ell)$ = latent heat of water at $T_\ell$

$S\rho_\ell(T_\ell)$ = saturation water vapor density of air at $T_\ell$

$S\rho_a(T_a)$ = saturation water vapor density of air at $T_a$

RH = relative humidity of air

The denominator of term 4 represents the sum of the resistances to water vapor transfer in the soil-plant-atmosphere system. The expression $K_2\{\dfrac{D^{.35}\, W^{.20}}{V^{.55}}\}$ is an empirical description of the resistance to water vapor transfer across the boundary layer of still air adjacent to the leaf surface. Such transfer varies with the dimensions of the leaf relative to the wind (W and D), reflecting different boundary layer depths for different leaf sizes. It also varies inversely with wind speed, indicating that as V increases, the boundary layer becomes more shallow.

$K_2$ = proportionality constant

D = downwind dimension of leaf

W = crosswind dimension of leaf

V = wind speed.

The second resistance term in the denominator of term 4 , $r_1$ , is the one with which this paper is directly concerned. It represents the resistance of the entire plant system to water transfer, and is a combination of a number of series/parallel resistances that constitute the soil-root-stem-leaf system of a plant. This resistance sum is sensitive to changes in the availability of soil water to the plant.

## 3. IMPLICATIONS OF THE PLANT HEAT-BUDGET MODEL

The Gates model -- equation (2) -- can be solved for the factor $r_1$, the resistance of the plant to water transfer:

$$r_1 = -\frac{L(T_\ell)[S\rho_\ell(T_\ell)-RHS\rho_a(T_a)]}{K_1\{V/D\}^{1/2}(T_\ell-T_a)+R-Q_{abs}} - K_2\{\frac{D^{.35}\ W^{.20}}{V^{.55}}\}$$

which can be expressed in the form:

$$\text{resistance} = \frac{\text{forcing function}}{\text{energy flux}} .$$

Thus, if we know $T_\ell$, $T_a$, V, RH, and $(Q_{abs}-R)$ -- which equals the net radiation, R -- then the resistance to water transfer, $r_1$, can be calculated and the resistance of the boundary layer specified. The basic "signal" of interest is the factor $(T_\ell-T_a)$, the difference between leaf temperature and ambient air temperature. Maximizing the variations in this signal with variations in $r_1$ is the goal of the experiments proposed below.

Periods of high solar heat loading and low wind speed are then the basic criteria for maximizing the value of $(T_\ell-T_a)$ for a given $r_1$. The same conditions also are advantageous in terms of plant physiology, as will be discussed below. Further, as can be seen from the equations, the larger the plant leaves, the deeper the adjacent boundary layer. This reduces the coupling between leaf temperature and air temperature, again maximizing $(T_\ell-T_a)$ for a given set of conditions.

Gates solved the heat-budget formula, equation (2), for $(T_\ell-T_a)$, specifying the independent variables V, W, D, RH and $r_1$, and using experimentally deduced values for the constants $K_1$ and $K_2$. His results indicate the kind of signal to be expected with variations in $r_1$. Table 1 describes his findings for typical conditions that would maximize the signal $(T_\ell-T_a)$, that is, with:

$Q_{abs} = 1.0\text{x}10^6$ erg-cm$^{-2}$sec$^{-1}$ = 1.43 cal-cm$^{-2}$min$^{-1}$

V = 50 cm-sec$^{-1}$

W = 10 cm

D = 20 cm

RH = 50%.

As shown in Table 1, leaf temperatures could be expected to range from about 3 to 18°C above air temperature at $T_a$ = 30°C, when plant resistances ($r_l$) vary between 0 and 5 cm-min$^{-1}$. (Leaf temperatures for values of relative humidity between 0 and 100% can be linearly interpolated from the temperatures that correspond to 0 and 100% RH.) The model predicts a sizeable signal when $r_l$ varies as shown in Table 1.

Study so far suggests that the effect is most pronounced during periods of high potential evaporation (high solar heat loading). (Potential transpiration is the upper limit of water which would evaporate from an agricultural crop under a given set of radiation and wind conditions, with soil moisture non-limiting.) This is another reason for making observations during periods of high heat loading.

Fig. 1 is a graph of the variation in the ratio of actual to potential transpiration versus soil moisture for different conditions. Sizeable continuous changes in evaporation with changing soil moisture are indicated during periods of high potential transpiration; further review of the literature is underway to examine these variations.

## 4. EXPERIMENTAL STUDY OF THE PLANT HEAT-BUDGET MODEL

A "quick-look" project in the late summer of 1976 by Diak examined the feasibility of the heat-budget approach to soil moisture investigation. The experiment was set up in a cornfield in Madison, Wisconsin, for an observation period of 23 data-days from mid-July to mid-August. Instruments (see Fig. 2) consisted of thermistors at the ground surface and at two air heights; a net radiometer and an anemometer at the top of the observation stand; and a remote infrared thermometer, directed at an angle toward the top leaves of corn to minimize the input of thermal data from the ground surface and lower leaves.

The summer was one of the driest in Madison history, and the soil was extremely dry until the last days of observation, when one inch of rain fell in a twenty-four-hour period. By the time this rain fell, however, the corn was stunted, wilting and abnormal.

Data from the experiment indicate a difference in calculated values for $r_l$ between the extremely dry conditions before the rain and the extremely wet conditions the day after. Further study is underway to try to recognize smaller gradations in moisture between those two extremes. If smaller gradations can be established, further investigation of the heat-budget model would be valuable.

A more extensive future experiment has been proposed, drawing on the experience gained in the first project and utilizing a new temperature data source: satellites. In the spring of 1977, satellite data will be used to refine techniques for sensing the moisture in bare soils. Then, in the summer, a ground-based project -- similar to the 1976 "quick-look" study -- will examine the processes involved in the regulated heat-budget formulation. Several observation sites are planned so that more accurate data-averaging techniques can be used. Also, shorter sampling times will be used to improve the measurement of net radiation.

Leaf temperature, unlike ground temperature, responds very quickly to changing energy levels, because leaves have a very small thermal mass. Leaf temperature is not an integrated history of prior energy conditions (as is ground temperature), but is virtually an instantaneous measurement. This means that temperature-difference measurements based on average or integrated net ratiation is not possible with vegetation. On the other hand, the small thermal mass of leaves can be an advantage. Since leaf temperature differences develop very rapidly, measurements can be made immediately, when sampling conditions are favorable. A large number of measurements can be taken and then averaged for greater accuracy.

The summer project will also utilize satellite temperature data; satellite data for a wide area can be averaged quickly and easily to provide more representative information than could be obtained from individual ground stations.

Early in the growing season when vegetation is thin, the satellite often will view ground surface area as well as plant cover. The summer project may include a shift from bare-soil moisture measurement techniques to vegetated-surface moisture measurement techniques as vegetated areas increase in size through the summer.

Both satellite and ground-based investigations will examine the size of the signal, $(T_{\ell}-T_a)$, and both studies will rely on the measurement of air temperature. Ideally, this temperature should be taken at the site under study, but this is not practical if a large area is being investigated. If the $(T_{\ell}-T_a)$ signal obtained from satellite data is large enough, the reported air temperature at the nearest meteorological station may be used instead of an on-site temperature measurement.

Satellite sensors are better able to measure temperature differences rather than absolute temperature because variability in atmospheric attenuation causes uncontrollable measurement errors. But remote sensing of soil moisture demands information about absolute temperatures. One solution to the problem may be the use of reference temperatures in interpreting satellite data. For example, water bodies maintain a virtually uniform temperature, so satellite sensor data could be calibrated with actual water-temperature measurements. Also, use could be made of the

fact that around sunrise and sunset (when net radiation is zero), plant, air and ground-surface temperatures are essentially equal.

Idso et al.(1977) have defined a "stress degree day" (SDD) based on the measurement of the ($T_\ell - T_a$) signal. Integrating this signal over a growing season, they found a strong negative correlation between total SDD's and crop yield. The experiments proposed above would use satellite-derived ($T_\ell - T_a$) data to examine this SDD concept from a new viewpoint.

## 5. CONCLUSION

It would be misleading to assume that the Gates model of a plant leaf heat budget is exact; there are too many variables, empirical factors and potential error sources that complicate the measurement of absolute temperatures and moisture levels. More useful would be the remote measurement -- using satellite sensors -- of changes in soil water content. Ground reference data on temperature and soil moisture could provide an initial data point. Then, by calibrating changes in plant-system water-vapor transfer resistances with changes in soil moisture levels, subsequent soil moisture levels could be determined.

Using remote satellite sensors, effective experimental values might be found for the constants in the heat-budget equation for a regional mixture of crops. An alternative might be to determine these constants for broadleaf vegetation. Stands of broadleaf plants then might serve as "indicators" of soil moisture content for a region. Either an energy-exchange analysis (such as the Gates model) or a strictly empirical/statistical analysis correlating ($T_\ell - T_a$) with soil moisture could be used to determine soil moisture levels for vegetated areas from satellite observations.

## REFERENCES


DeVries and Afgan, 1975: Editors, Advances in Thermal Engineering, Volume 3, Heat and Mass Transfer in the Biosphere. John Wiley and Sons, New York.

Diak, George R., 1975: A Radiative Transfer Scheme of Soil Moisture Remote Sensing. M.S. thesis. Madison: University of Wisconsin-Madison.

Gates, David M. and LaVerne E. Papun, 1972: Atlas of Energy Budget of Plant Leaves. Academic Press, New York.

Idso, Sherwood B., R.D. Jackson and R.J. Reginato, 1975: The Utility of Surface Temperature Measurements for the Remote Sensing of Surface Soil Water Status, Journal of Geophysical Research, (80), 3044 - 3049.

_____, 1975: Detection of Soil Moisture by Remote Surveillance, American Scientist, Sept.-Oct. 1975, 549 - 556.

_____, 1977: Remote Sensing of Crop Yields, Science, (19), 19 - 25.

Meyer, S., D.B. Anderson, R.H. Bohning and D.G. Fratianne, 1973: Introduction to Plant Physiology. Van Norstrand, Cincinnati.

Monteith, J.L, 1975: Vegetation and the Atmosphere, Academic Press, New York.

| $T_a$ | RH | INTERNAL PLANT RESISTANCE, $r_1$ | | | | | | |
|---|---|---|---|---|---|---|---|---|
| | | **0* | **1* | **2* | **5* | *10* | *20* | INF* |
| 0 | 0 | 20.0 | 26.0 | 29.2 | 33.9 | 36.9 | 39.2 | 42.4 |
| 0 | 100 | 22.6 | 27.7 | 30.5 | 34.7 | 37.4 | 39.4 | 42.4 |
| 10 | 0 | 22.7 | 29.3 | 32.9 | 38.2 | 41.8 | 44.5 | 48.5 |
| 10 | 100 | 27.3 | 32.2 | 35.1 | 39.5 | 42.6 | 45.0 | 48.5 |
| 20 | 0 | 25.2 | 32.3 | 36.2 | 42.1 | 46.3 | 49.5 | 54.5 |
| 20 | 100 | 32.7 | 37.2 | 40.0 | 44.5 | 47.8 | 50.4 | 54.5 |
| 30 | 0 | 27.6 | 35.1 | 39.3 | 45.9 | 50.6 | 54.3 | 60.3 |
| 30 | 100 | 38.9 | 42.8 | 45.3 | 49.6 | 52.9 | 55.7 | 60.3 |
| 40 | 0 | 29.8 | 37.7 | 42.3 | 49.4 | 54.6 | 58.8 | 66.1 |
| 40 | 100 | 46.0 | 49.0 | 51.2 | 55.1 | 58.3 | 61.1 | 66.1 |

Dimension along airflow = W = 20 cm

Dimension across airflow = D = 10 cm

Wind speed = V = 50 $cm\text{-}sec^{-1}$

Radiation absorbed = $Q_{abs} = 1.0 \times 10^6$ $erg\text{-}cm^{-2}sec^{-1}$

TABLE 1: Leaf temperature from Gates model for varying humidity, air temperature and internal resistance under high heat loading and low wind speed conditions. (From Gates, 1971)

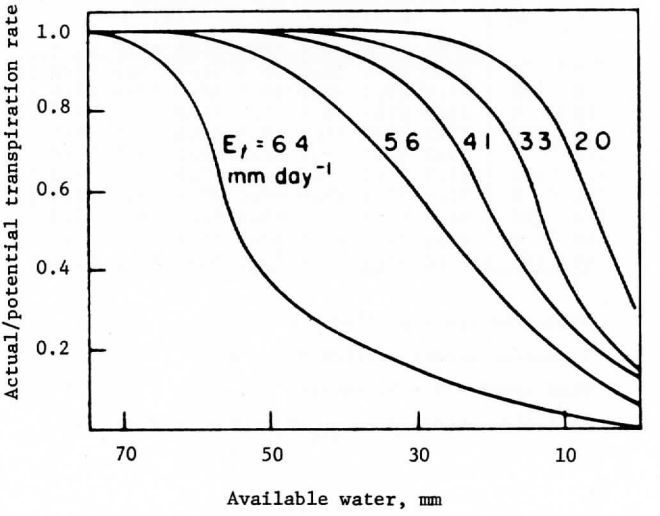


FIGURE 1: Actual/potential transpiration rate versus soil moisture content for different levels of potential transpiration rate, $E_t$ , for maize. (From Monteith, 1975)

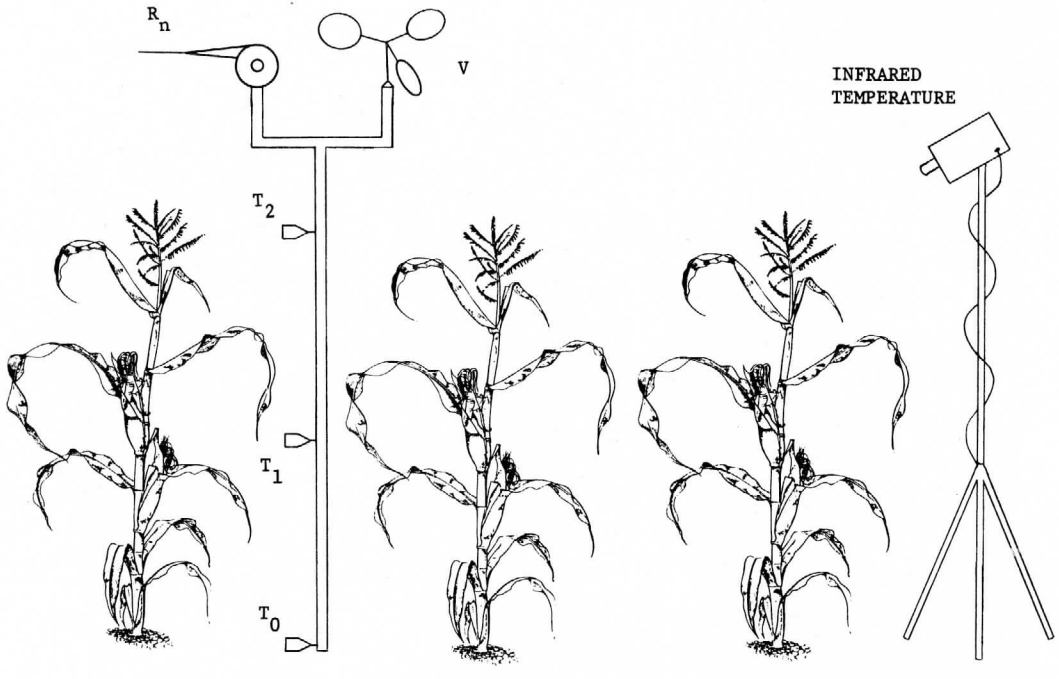


FIGURE 2: Experimental design for moisture sensing experiment.

# A STUDY OF THE UPPER TROPOSPHERIC CIRCULATION OVER SOUTH AMERICA DURING THE SOUTHERN HEMISPHERE SUMMER

Hassan Virji

## ABSTRACT

This preliminary report describes an ongoing research program to determine the mean and transient motion field over tropical and sub-tropical South America during the southern hemisphere summer, using cloud motion vectors obtained from a geostationary satellite as a primary data source. From cloud motion vectors it is evident that the large-scale circulation over South America, including the region of the Bolivian Altiplano, is similar in certain important respects to the monsoon circulation over southern Asia in the vicinity of the Tibetian plateau.

The main characteristic of the summertime circulation over South America is a strong upper tropospheric anticyclone. A band of easterly flow around 15S (weak easterly 'jet') and strong cross-equatorial flow, often extending to 15N, occur in association with this circulation. Since these regions of South America are almost devoid of conventional aerological measurements, horizontal wind fields derived from cloud motion vectors are being utilized to obtain initial estimates of the characteristics of the diurnal and time-averaged circulation.

## 1. INTRODUCTION

Several preliminary studies have reported the possible control exerted by the diurnal convection cycle upon the large-scale circulation over tropical and sub-tropical South America. Schwerdtfeger (1961), Gutman and Schwerdtfeger (1965) and Kruger (1970) have pointed out that the convectively active highlands of Altiplano (altitude 3700-4100 m, latitude 15-21S, area about $2 \times 10^5$ sq. km.) act as an elevated heat source during summer (Nov.-Mar.), so that at 200 mb, a large-scale anticyclone is maintained, due to the latent heat released in violent thunderstorms and the sensible heating of the atmosphere over the plateau. Flohn (1971) suggested possible parallels between the elevated heat sources of the Tibetian Highlands and the Altiplano, and their effects on the large-scale circulation in the vicinity. However, these studies have been based upon sparse aerological data.

The merit and use of tracer winds generated by tracking clouds in Synchronous Meteorological Satellite (SMS) images has been described previously (Sikdar and Suomi, 1969; Wilson, 1976). Suchman and Martin (1976) demonstrated that reliable information about horizontal wind fields can be acquired from cloud motion vectors. The need for such data for the South

American region is obvious, since the conventional aerological data network over this region is very sparse (Fig. 1). This study is an attempt to determine the time-averaged and transient characteristics of the kinematic field over South America, using geostationary satellite data as a primary source of information. The results should show the adequacy of satellite data as a major information source in studies of large scale circulations, especially the FGGE and MONEX projects.

## 2. DATA

Full-resolution SMS-I images (visible and infra-red) were obtained for the South American region for the period 25 Jan. to 7 Feb. 1975, at half hour intervals each day (from about 0500Z-1200Z and 1600Z-2330Z), during the Data Systems Test for the First Garp Global Experiment. From this data set, five consecutive images, each centered around 0600Z (IR) and 1800Z (visible and IR), were analyzed to obtain initial estimates of the large-scale diurnal wind fields. These data were then reduced to a resolution of 11.2 km to diminish the 'noise' generated by local, small-scale convection and to obtain cloud motions representative of the larger-scale circulation.

These images were displayed on the University of Wisconsin's Man-Computer Interactive Data Access System (McIDAS), and winds were carefully derived using the single pixel method by tracking clouds in consecutive images for the region bounded by latitudes 15N-35S and longitudes 40W-90W. When necessary, full-resolution data were also used to track some targets. Besides the usual reliability checks used in processing these winds (see Suchman et al., 1975), the vectors generated for each target were subjectively scrutinized for internal consistency, then averaged for each target to yield consistent wind fields for high (100-300 mb) and medium (400-600 mb) layers. No winds were generated at lower levels over the continental region.

A typical example of such a wind field for high level (for 1 Feb. 1975, at 0600Z) is shown in Fig. 3, corresponding to the satellite image shown in Fig. 2. Following Mosher and Sawyer (1975), a subjective comparison between these winds and the nearest available (in space and time) rawindsonde observations gives a mean absolute value difference in wind speed of about 5 $m.s^{-1}$.

At the time of this report, data for the six day period from 27 Jan. to 1 Feb. 1975 have been processed. The following section describes some of the kinematic analysis performed on the wind fields generated from satellite data.

## 3. ANALYSIS

The raw wind sets were analyzed on a 5 x 5 degree grid using a modified version of the scheme developed by Mancuso and Endlich (1973). Careful restrictions were used in extrapolating to data-free regions. The

resulting grid point values of the u and v velocity components were then used to estimate the corresponding fields of divergence and relative vorticity.

The following discussion concerns the kinematic analysis pertaining to the upper level (100-300 mb) motion field at 0600Z on 1 Feb. 1975, since it illustrates the major features of the circulation over South America.

The motion field is shown in Figs. 4-6. Fig. 4 shows the objectively analyzed wind field (grid point wind vectors and streamlines); Figs. 5 and 6 portray, respectively, the u and v components. The following features are clearly evident:

(i) A strong upper level anticyclone is centered at 25S,65W. The anticyclonic circulation dominates most of the tropical and sub-tropical regions of South America, including the convectively active and moisture-rich Amazon River Basin. Associated relative vorticity near the center of the high (Fig. 7) is about $5 \times 10^{-5}$ $s^{-1}$. This value compares well with the daily extreme relative vorticity of about $8 \times 10^{-5}$ $s^{-1}$ associated with the Tibetian High during the northern hemisphere summer (Krishnamurti, 1971).

The distribution of horizontal divergence is shown in Fig. 8. Note that the upper level large-scale flow over most of the region is divergent, indicative of the general rising motion in the atmosphere beneath. This is reasonable in view of the vigorous convection and subsequent ascending motions that occur over most of this region, particularly in late summer, when the frequency of thunderstorms is maximum. The outflow from the thunderstorms over this active continental region causes a predominantly divergent upper level flow. A comparison between the infrared satellite image (Fig. 2) and the horizontal divergence field (Fig. 8) shows that maxima of divergence occur over the regions where the cirrus outflow from large Cb clusters is most evident. Strong divergence of about $2 \times 10^{-5}$ $s^{-1}$ occurs in the vicinity of the upper anticyclone and over some regions of the Amazon River Basin. This value compares well with the average cirrus level divergence estimates of $2.5 \times 10^{-5}$ $s^{-1}$ over the ITCZ and the tropical oceanic (GATE) regions as reported by Suchman and Martin (1976). To compare the divergence estimates from the GATE region (1 x 1 degree grid) with the estimates over South America (5 x 5 degree grid), the GATE estimates were smoothed over large regions of upper level outflow and reduced to a 5 x 5 degree grid.

The clear zone around 17S,60W (Fig. 2), surrounded by Cb clusters represents a region where sinking motions in the atmosphere may be expected. In this location, a small region of convergence (Fig. 8) of maximum value of about $1 \times 10^{-5}$ has been calculated.

(ii) A broad band of easterly flow regime dominates the region equatorward of the anticyclonic center. Embeded within this flow is a zone of maximum winds between 10S-20S (Fig. 5). While maximum wind speed in this particular example is about 15 $m.s^{-1}$, speeds as high as 25 $m.s^{-1}$ have been observed at other times. These winds seem to indicate that a weak easterly jet-type flow to the equatorward side of the upper anticyclone may exist.

(iii) The distribution of the meridional wind component (Fig. 6) illustrates that in the southern summer, most of tropical South America is dominated by a cross-equator flow which extends as far as 15N. Relatively strong flow of this type (magnitude about 15 $m.s^{-1}$) at upper levels indicates the strength of the Hadley circulation over this convectively active continental region. Such strong cross-equatorial flow is not evident in the mean 200 mb circulation derived from conventional rawinsonde and commerical aircraft data (compare Figs. 4 and 9). By definition, of course, cloud motion winds tend to be biased towards divergent outflow situations, and this inherent bias should be taken into account in deriving mean circulation statistics.

## 4. CONCLUSION

The results presented above demonstrate the use of cloud motion vectors to study large-scale circulations over the tropical and sub-tropical continents. Further efforts are underway to analyze data for the periods 25-26 Jan. and 2-7 Feb. 1975 using McIDAS. Additional cloud motion data, operationally derived by the National Environmental Satellite Service, have been acquired for the summers of 1975-1977. These data are being analyzed for compatibility with McIDAS-derived cloud motions so that the two data sets can be merged if appropriate. These data will be used to derive a seasonal mean and diurnal mean picture of the circulation over the Altiplano and the surrounding regions. The time-averaged and transient characteristics of the circulations will be derived and reported later.

## ACKNOWLEDGEMENTS

I wish to express my appreciation to Prof. J. Kutzbach for many valuable discussions. Thanks are due to the McIDAS facility staff for continued assistance. This work is supported under National Science Foundation Grant NSF #ATM74-23041 A01 and NASA Contract #NAS5-21798.

## REFERENCES

Flohn, H., 1971: Tropical Circulation Patterns. Bonner Met. Abhandlungen, Met. Inst. der Univ. Bonn, Heft (15), 55 pp.

Gutman, G. and W. Schwerdtfeger, 1965: The role of latent and sensible heat for the development of a high pressure system over the Sub-tropical Andes, in summer. Met. Randschau., pp 1-7.

Krishnamurti, T. N., 1971: Observational study of the upper tropospheric motion field during the northern hemisphere summer. J. Appl. Met., 10:1066-1096.

Kruger, A. F., 1970: The zonal variation of cloudiness and convection over the tropics. Proc. Symposium on Tropical Met., Univ. of Hawaii, 1970.

Mancuso, R. L., and R. M. Endlich, 1973: User's Manual, Wind Editing and Analysis Program: Spherical Grid WEAP-1A, Stanford Research Institute.

Mosher, F. R., and B. Sawyer, 1975: Comparison of wind measurement systems: Cloud tracked winds and rawinsonde winds vs. rawinsonde winds. Preliminary assessment of the cloud tracking system developed at the University of Wisconsin, SSEC, University of Wisconsin, Madison.

Sadler, J. C., 1976: The Upper Tropospheric Circulation over the Global Tropics. Publication of the Univ. of Hawaii, Dept. of Met., UHMET-75-05.

Schwerdtfeger, W., 1961: Stromungs- und temperaturefeld der freien atmosphare uber der Anden. Met. Randschau., Heft 1, pp 1-6.

Sikdar, D. N. and V. Suomi, 1969: An objective technique for evaluating meso-scale convective heat transport in the tropics from geosynchronous satellite cloud photographs. Annual Report, Space Science and Engineering Center, Univ. of Wisconsin, Madison.

Suchman, D., et al., 1975: Preliminary assessment of cloud tracking system developed at the University of Wisconsin. (Mimeographed), Space Science and Engineering Center, Univ. of Wisconsin, Madison.

Suchman, D. and D. Martin, 1976: Wind sets from SMS images: an assessment of quality for GATE. J. Appl. Met., 15(12):1265-1278.

Wilson, T., 1976: The determination of meso-scale horizontal and vertical wind fields from SMS-I satellite observations. MS Thesis (Unpublished) Dept. of Meteorology, Univ. of Wisconsin, Madison.

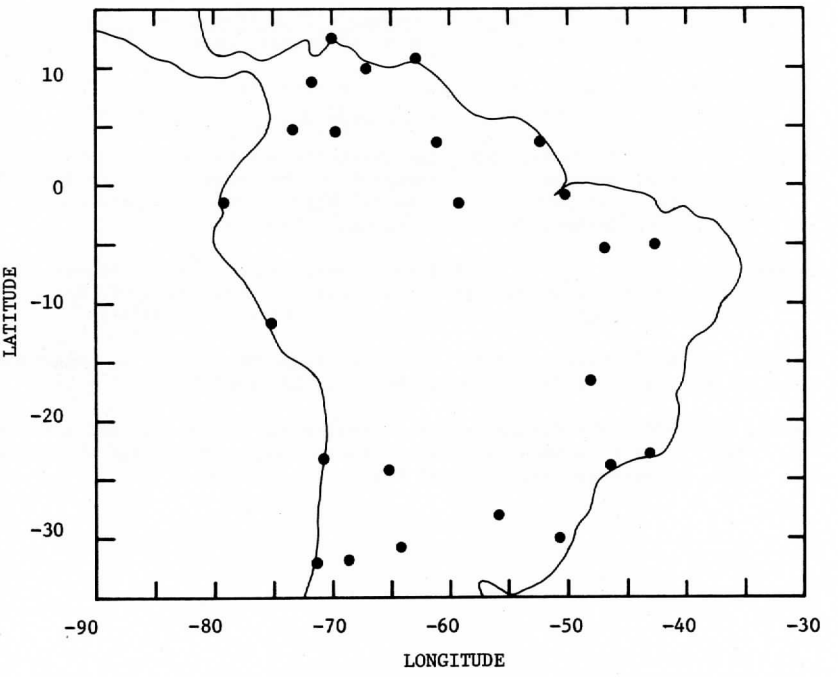


FIGURE 1: Conventional Rawindsonde Observational Network over Tropical and Subtropical South America during February, 1975. (Source - World Weather Records)

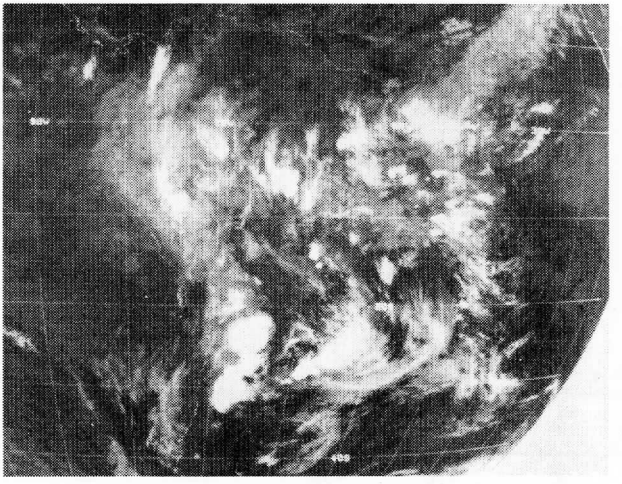

FIGURE 2: SMS-I Infrared image (4x4 nm resolution) for 0600Z on 1 February, 1975.

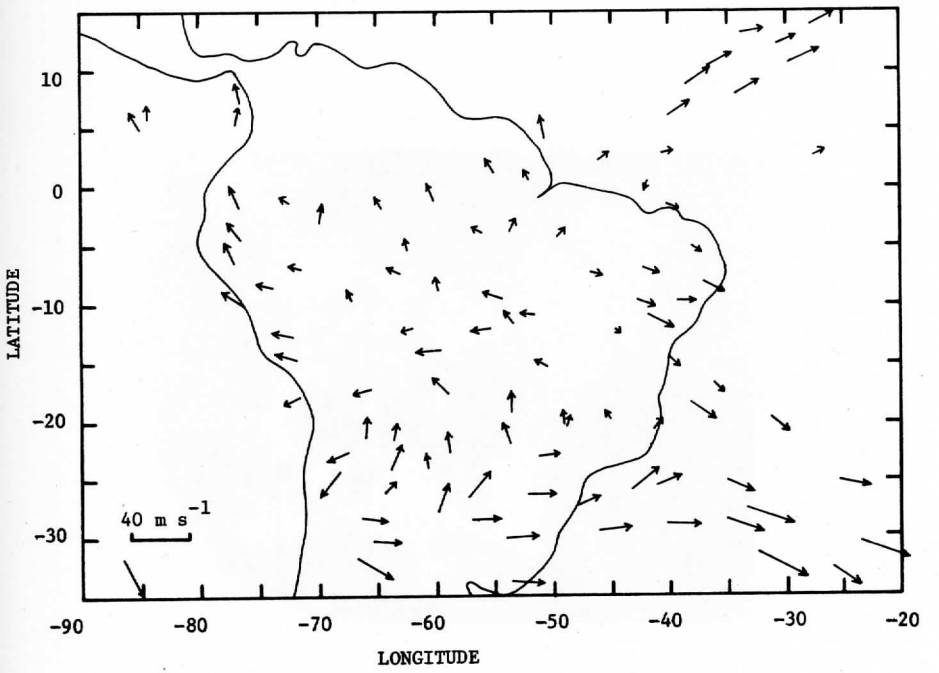


FIGURE 3: Cloud Motion Vectors at upper level (300-100mb) for 0600Z on 1 February, 1975. ($m.s^{-1}$)

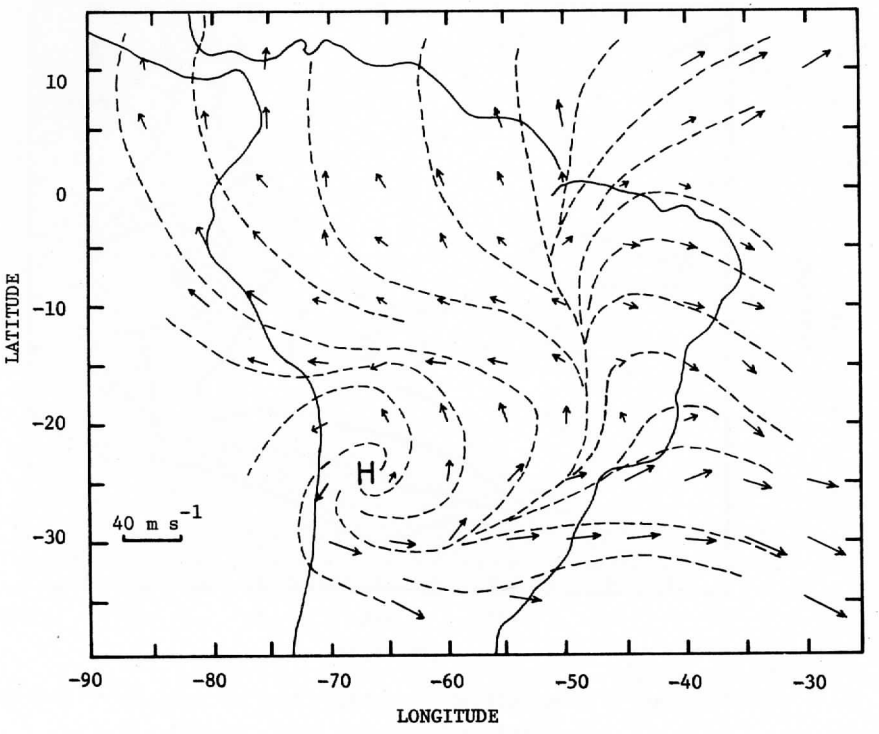


FIGURE 4: Objectively analyzed Wind Field at upper level (300-100mb) for 0600Z on 1 February, 1975. (m.s$^{-1}$)

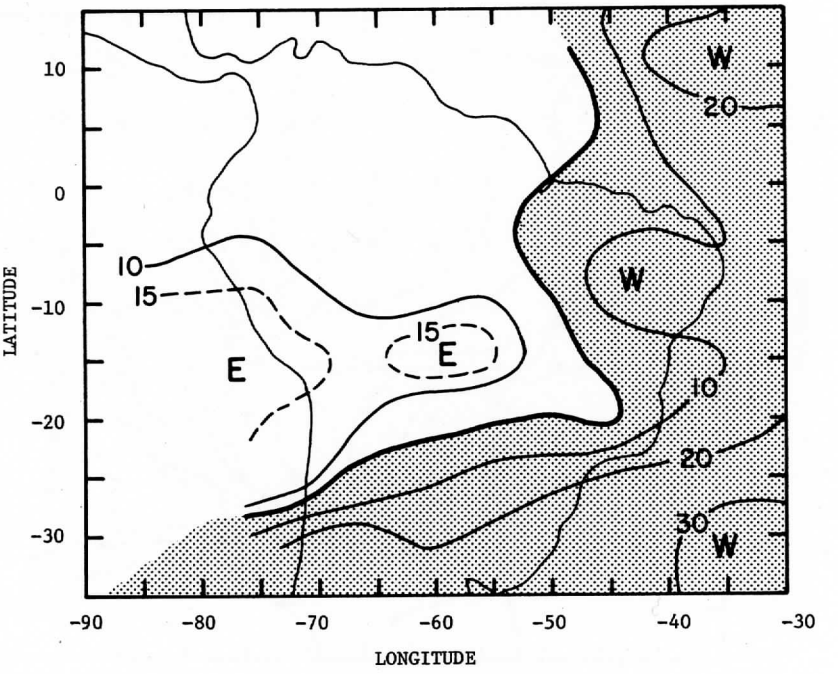


FIGURE 5: The u component of the motion field at upper level (300-100mb) for 0600Z on 1 February, 1975. ($m.s^{-1}$)

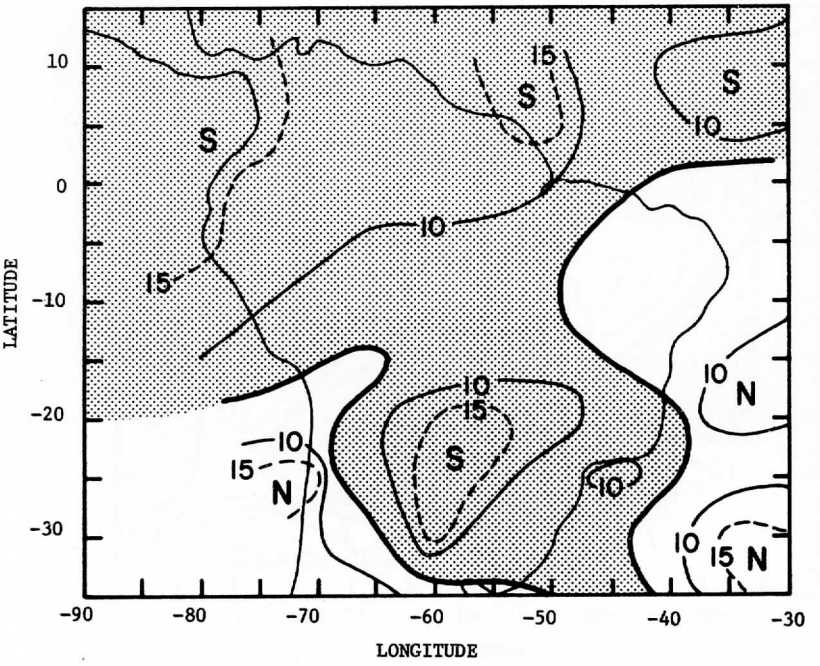


FIGURE 6: The v component of the motion field at upper level (300-100mb) for 0600Z on 1 February, 1975. ($m.s^{-1}$)

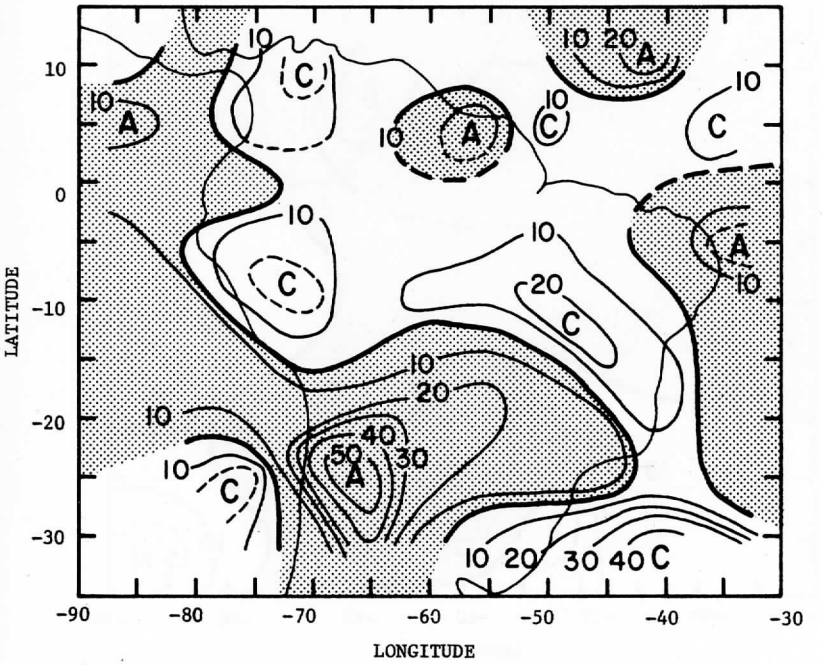


FIGURE 7: Relative Vorticity Field for the upper level (300-100mb) for 0600Z on 1 February, 1975. ($x10^{-6}$ $s^{-1}$)

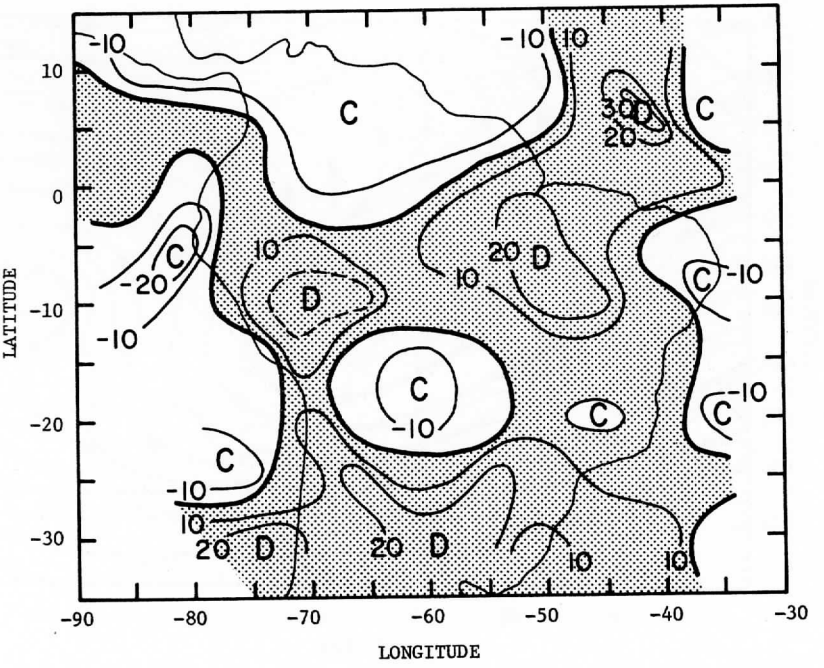


FIGURE 8: Horizontal Divergence Field for the upper level (300-100mb) for 0600Z on 1 February, 1975. ($x10^{-6}$ $s^{-1}$)

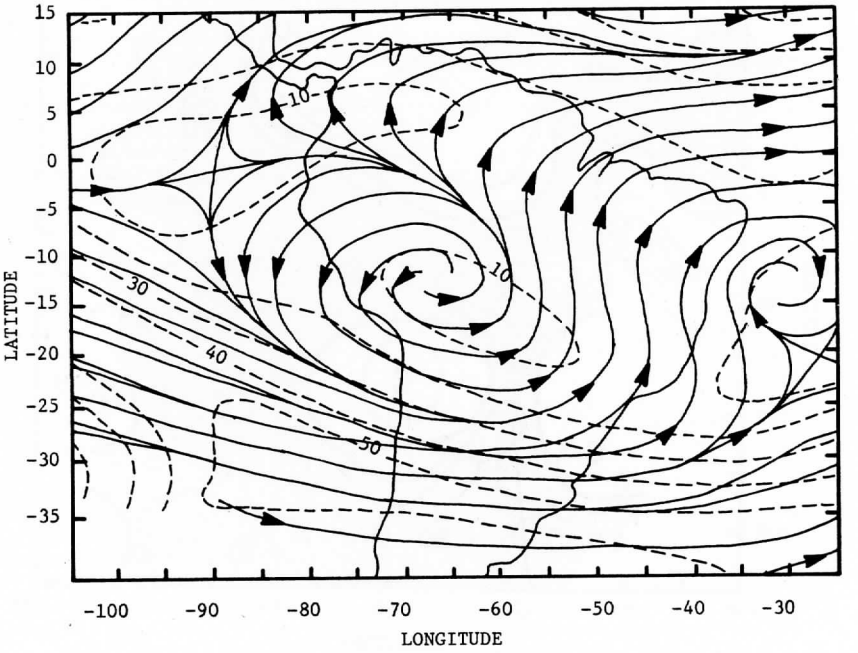


FIGURE 9: Mean Wind Field at 200 mb during February ($m.s^{-1}$).
(From Sadler, 1976)

# COMPOSITE IMAGES USING NAVIGATED SMS/GOES DATA

Frederick R. Mosher

ABSTRACT

Improvements in geostationary satellite navigation and in computerized image processing have made possible the production of high-resolution composite images from digital satellite data. One such composite--the "minimum brightness" composite--can be used to remove cloud cover from visible and infrared images, thereby improving image clarity and utility. It is also possible to produce "average cloud cover" composites for different levels of the atmosphere to aid in cloud parameterization and climate study.

## 1. INTRODUCTION

Recent advances in techniques to predict the position and attitude of geostationary meteorological satellites (Young, 1976) make it possible routinely to align satellite images to within a single picture element. This alignment capability is currently available at the University of Wisconsin on the McIDAS (Man-Computer Interactive Data Acquisition System) (Chatters and Suomi, 1975), and will be available in the near future at the National Environmental Satellite Service (NESS) for the sectorizers which transmit images to forecast offices.

The availability of precisely aligned digital images greatly extends the usefulness of geostationary satellite data, making possible the production of composite images which maintain the original high resolution of the satellite data. Two possible applications of composite-image analysis are the "removal" of clouds from satellite data by compositing "minimum brightness" images, and the generation of "average cloud cover" images for different levels of the atmosphere.

## 2. MINIMUM BRIGHTNESS COMPOSITES

Composite images of polar orbiter satellite data--computer-generated cloud mosaics of polar or mercator projections--have been produced by NESS for more than 10 years (Bristor et al., 1965). Minimum brightness composites can be produced from such images, but navigation uncertainties and computer

load requirements have kept the resolution of such images low. Five-day minimum brightness composites of both visible and infrared images have been used mainly for ice analysis. Kukla and Kukla (1974), for example, have done hand analysis of such composite images to study variations of total areas of ice and snow in the northern hemisphere.

With improvements in image navigation and computer processing, composite images based on the minimum brightness of each pixel in a series of aligned satellite images can now be produced. Clouds move but the underlying surface does not, and since clouds are usually brighter than the underlying surface, clouds can be made to disappear by using a composite of minimum brightness. Figs. 1-5 show visible images of the Gulf of Mexico and the Caribbean area for the days February 2-6, 1975 at 1800 GMT. Figs. 6-8 show the progressive composite of minimum brightness done on the McIDAS at the University of Wisconsin of these five images. Fig. 8, the five-day minimum brightness composite is almost completely cloud free except for the mountain areas of South America, and some very small cumulus over the Gulf of Mexico.

A minimum brightness visible composite can be used for surface albedo studies or for snow and ice mapping. In one such study, Ron Gird of NESS is undertaking a snow-basin mapping experiment using composite full-resolution visible GOES images on the McIDAS (private communications, 1977).

Because of the low noise characteristics of the SMS/GOES infrared sensor, the composite minimum brightness technique can also be used on infrared images to remove the effects of clouds when mapping sea surface temperature. Traditional methods of sea surface temperature mapping must sense between clouds on a single image, and so produce a grid point analysis field of reduced resolution. Frequently, small scale features such as Gulf Stream eddies are lost in this processing. While some observations of Gulf Stream eddies have been produced on clear days from infrared satellite data (Richardson et al., 1973), cold air flowing from the land to the sea during many winter days makes the Gulf Stream area cloudy, limiting the opportunity for clear observations.

In the present study, images for January 28-31, 1975 at 1800 GMT were combined to produce a minimum brightness composite image for both the visible and the IR spectrum. The IR image in Fig. 9 is for January 28, the clearest of the four observation days over the Gulf Stream region, yet the area north of the Carolina coast was obscured by heavy jet stream cirrus that persisted for the entire four day period. Figs. 10 (the visible composite) and 11 (the IR composite) show the successful removal of this heavy cloud contamination, though some cloud effects remained off the Delaware coast, off Long Island, and further out in the ocean.

Fig. 12 is a blow-up of Fig. 11 (off the Carolina coast) with some contrast enhancement applied. The image shows the cold upwelling off the coast and the warmer (darker) Gulf Stream. A warm eddy circulates east

of the Chesapeake Bay, and the main body of the Gulf Stream flows to the northeast until it disappears under the residual cloud cover. The interface between the colder waters off the Delaware coast and the Gulf Stream is evident.

The eastern boundary of the Gulf Stream is somewhat obscured by the residual cloud cover that shows up on the visible image (Fig. 10). These residual clouds could be removed by using more images in the composite. If the time scale of the surface feature is small, a composite could be made using only images covering that time scale; then conventional techniques, such as histogram analysis, could be used on the composite to produce a reduced-resolution analysis of the data.

Data processing for composite images is reasonably simple. The aligned images are stored on the digital disk, and processing is done line-by-line, with the main time constraint being disk access time. For a typical sequence of 5 images with 500 lines/image, and a typical 30 millisecond disk access time, the processing time for an image of 500 lines x 672 elements is approximately 2 minutes. The only core requirement is for the five arrays containing the input lines and one output line array.

## 3. AVERAGE CLOUD COVER COMPOSITES

In addition to minimum brightness composites, "average cloud cover" composites also can be generated from satellite images. Kornfield and Hasler (1969) produced average images of the earth's cloud cover using multiple exposure photographic processing. Averaging of more sophisticated digital images could be done quickly and easily to produce digital composites.

Multilayer composites as well as simple averaged images could be made from digital data. The first stage in creation of multilayer composites is the use of infrared temperature data to discriminate the visible pixels into three or four levels of the atmosphere where the clouds are occurring. Then, for each level an average composite could be generated. The resultant images would be average cloud cover for each level of the atmosphere, which could be used for cloud parameterization and climate studies. To detect areas of rapid cloud change, a first time-derivative could be generated by subtracting two images for the same area obtained at different times.

## 4. CONCLUSIONS

The availability of accurately aligned geostationary images makes it possible to process satellite data in the original image plane; thus, data can be processed on a line-by-line basis using minimal computer resources. Composite images can be generated easily from aligned satellite images, and

one such image--the minimum brightness composite--can be used to remove most, if not all, clouds from a visible or infrared image. The composite cloud-free visible image can be used for surface albedo studies or for snow and ice mapping, while the composite infrared image can be used for sea surface temperature analysis. A composite of atmospheric infrared data could provide average cloud cover data for different levels of the atmosphere.

## REFERENCES


Chatters, Gary C. and Verner E. Suomi, 1975: The Applications of McIDAS. IEEE Transactions on Geoscience Electronics, Vol. GE-13, No. 3, 137-146.

Bristor, C. H., W. M. Calicott, and R. E. Bradford, 1965: Operational Processing of Satellite Cloud Pictures by Computer. Monthly Weather Review, 94, 515-527.

Kornfield, Jack and A. Frederick Hasler, 1969: A Photographic Summary of the Earth's Cloud Cover for the Year 1967. Journal of Applied Meteorology, Vol. 8, No. 4, 687-700.

Kukla, G. I. and H. J. Kukla, 1974: Increased Surface Albedo in the Northern Hemisphere. Science, Vol. 183, No. 4126, 609-714.

Richardson, P. L., A. E. Strong, and J. A. Knauss, 1973: Gulf Stream Eddies; Recent Observations in the Western Sargasso Sea. Journal of Physical Oceanography, Vol. 3, No. 3, 297-301.

Young, J. T., 1976: Navigation of Geostationary Images. Proceedings of COSPAR Symposium on Meteorological Observations from Space: Their Contributions to the First GARP Global Experiment, June 8-10, 1976. Technical Editing and Preparation by J. Kelly and S. Ruttenberg, NCAR, Boulder, CO, 198-200.

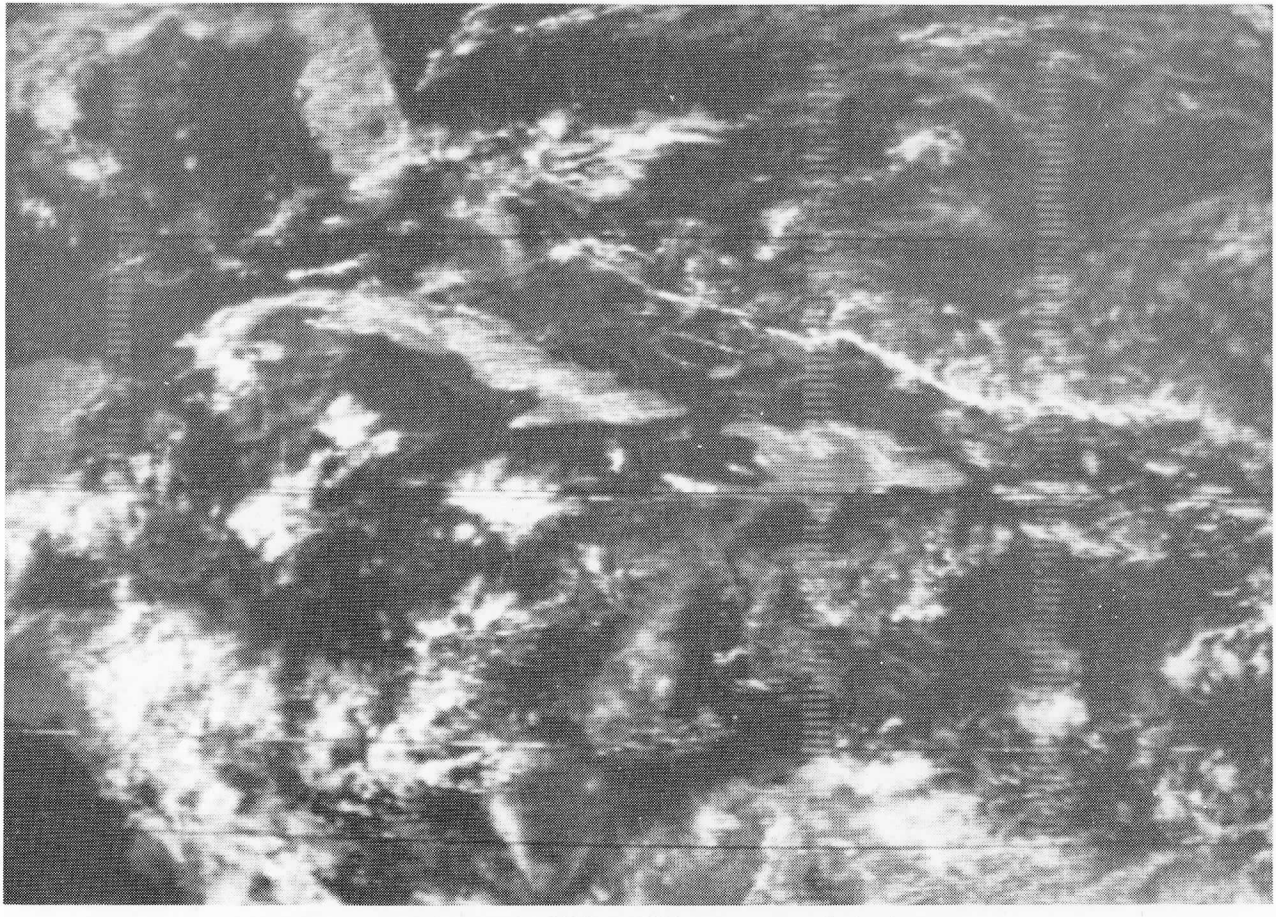

FIGURE 1: February 2, 1975 at 1800 GMT. One of the images used in the five-day minimum brightness composite.

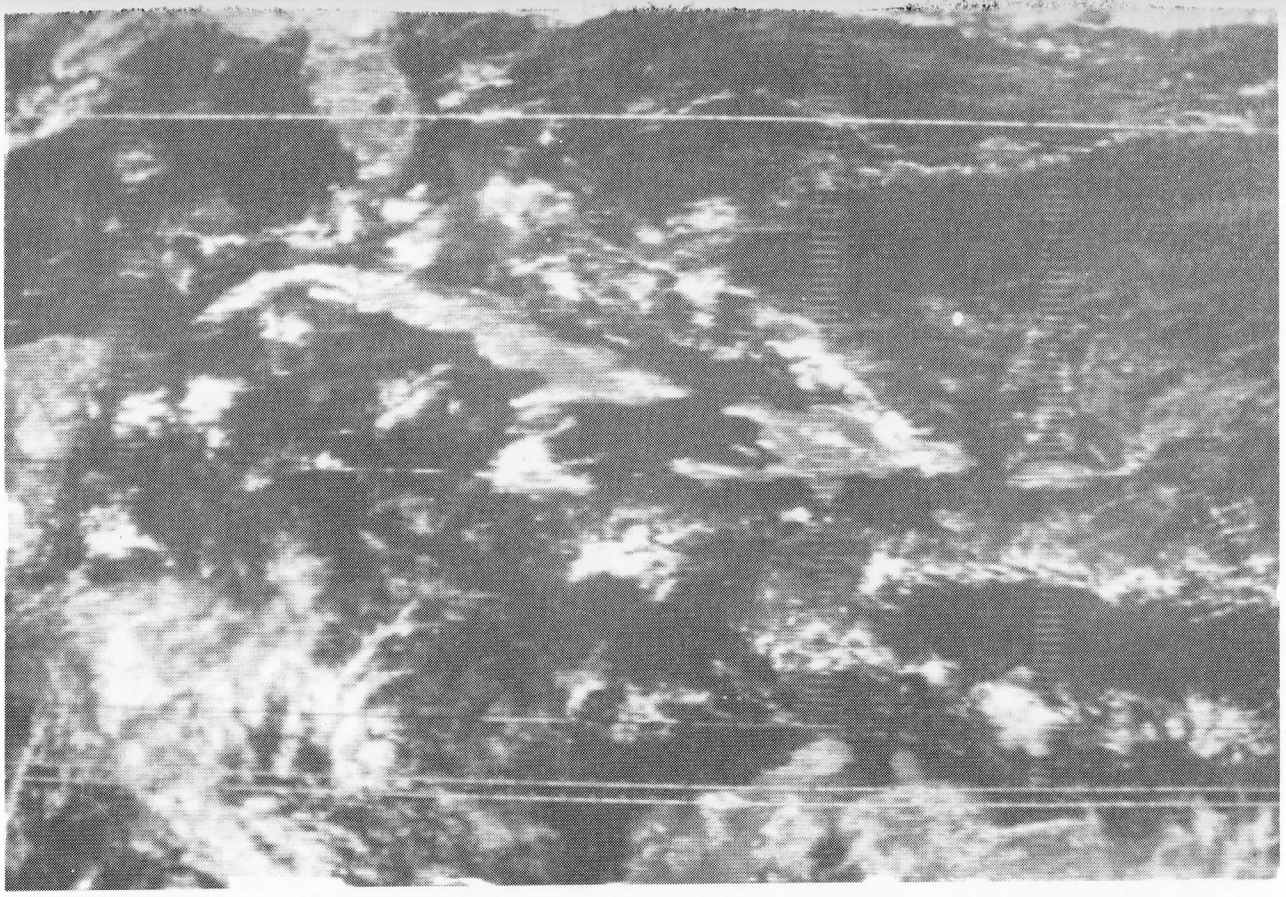

FIGURE 2: February 3, 1975 at 1800 GMT.

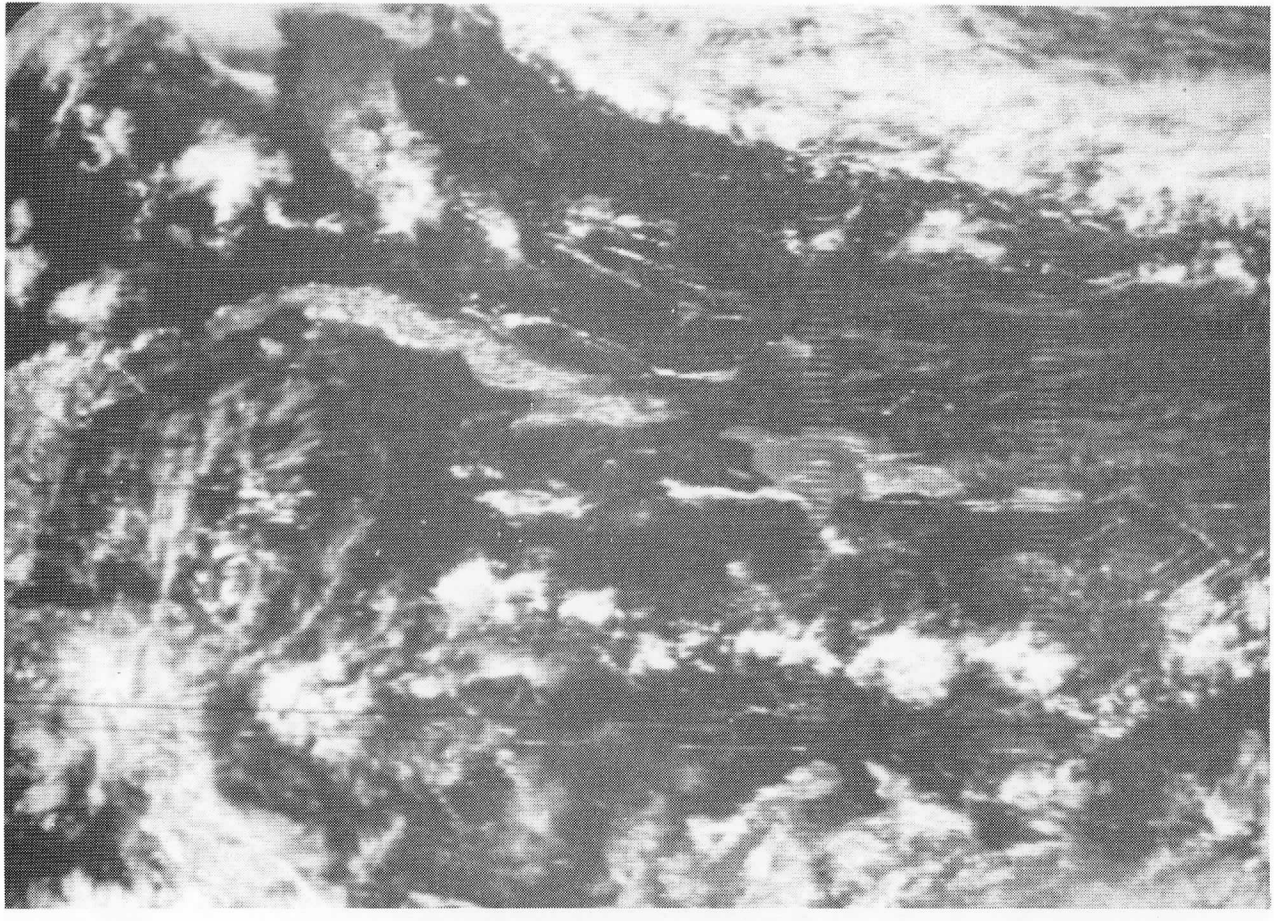

FIGURE 3: February 4, 1975 at 1800 GMT.

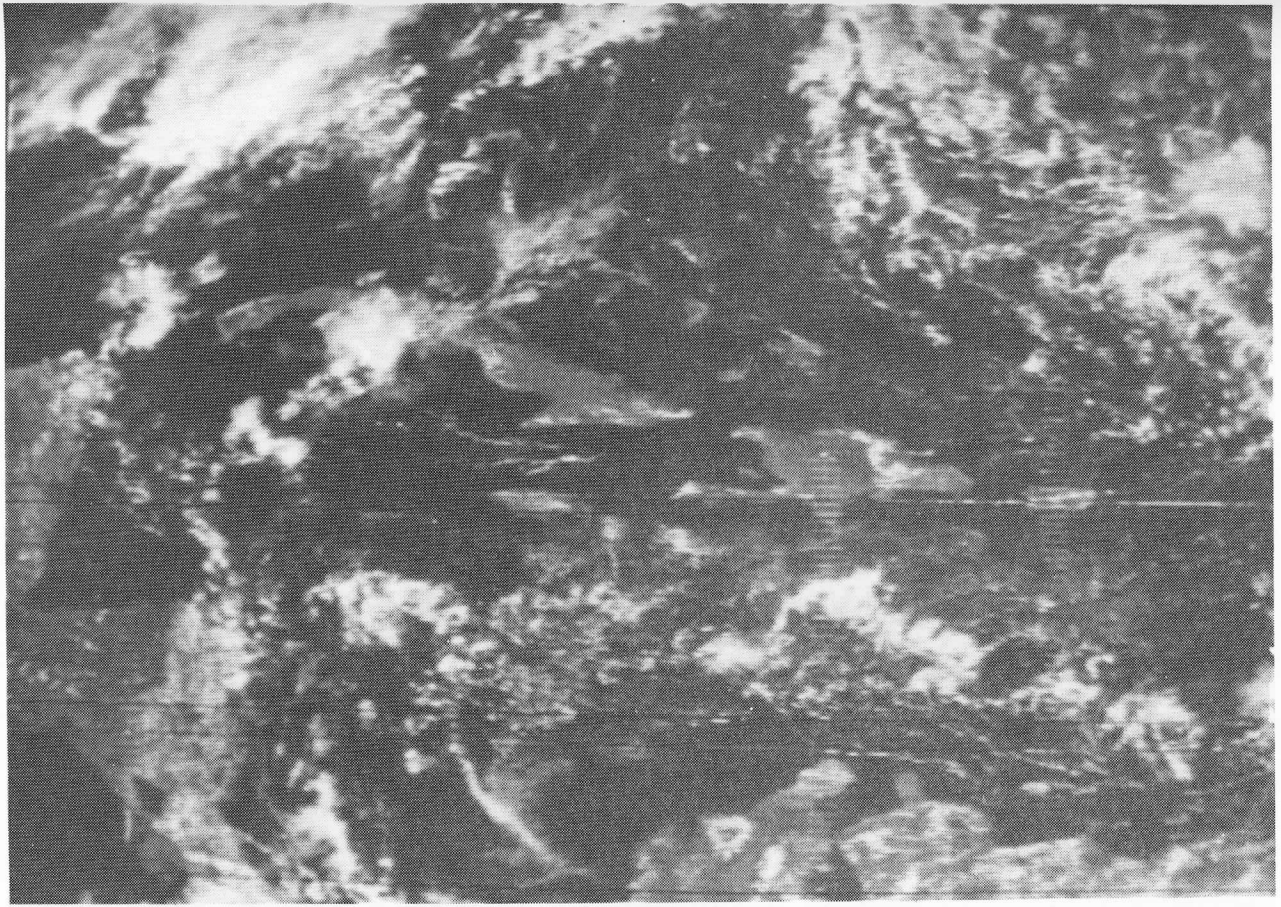

FIGURE 4: February 5, 1975 at 1800 GMT.

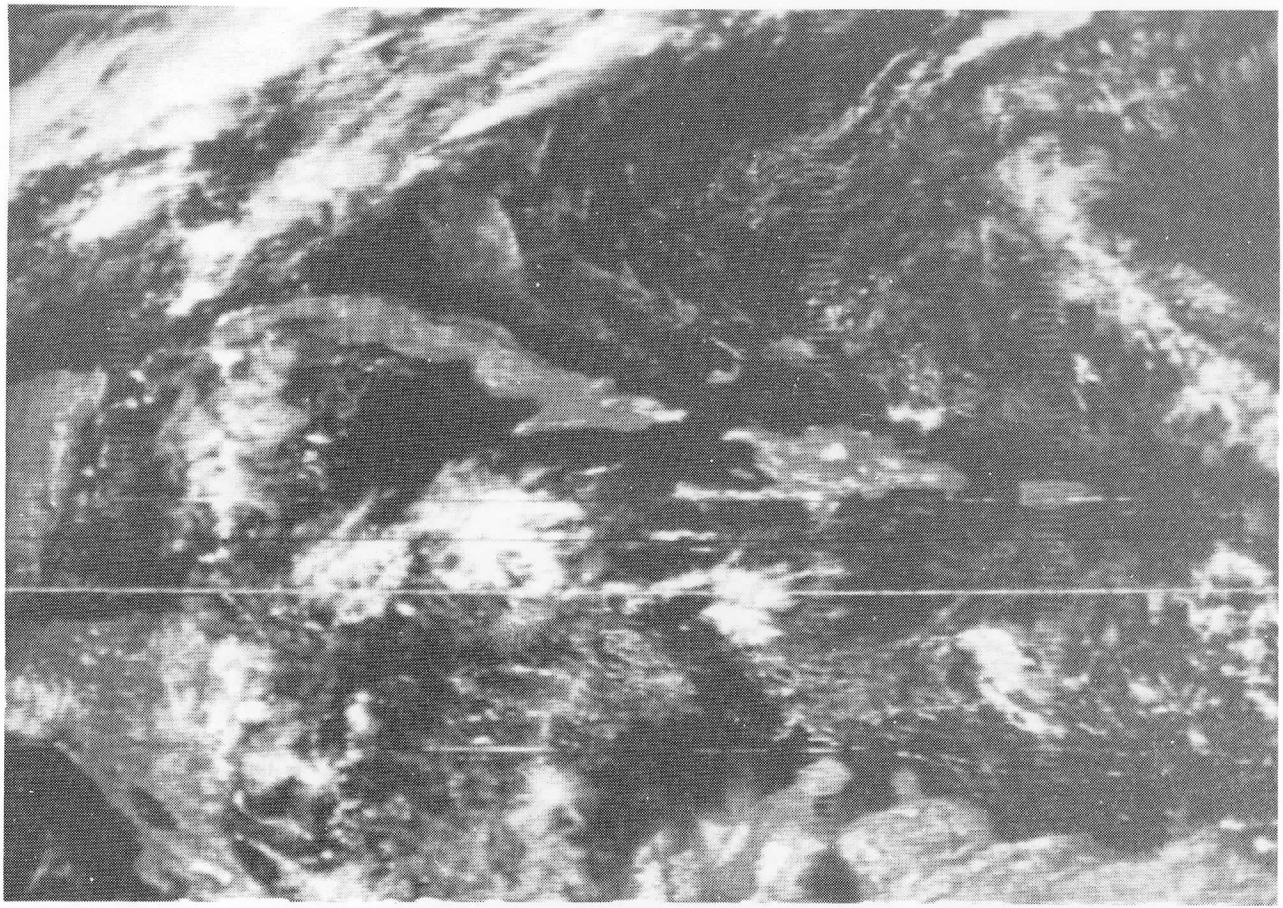

FIGURE 5: February 6, 1975 at 1800 GMT.

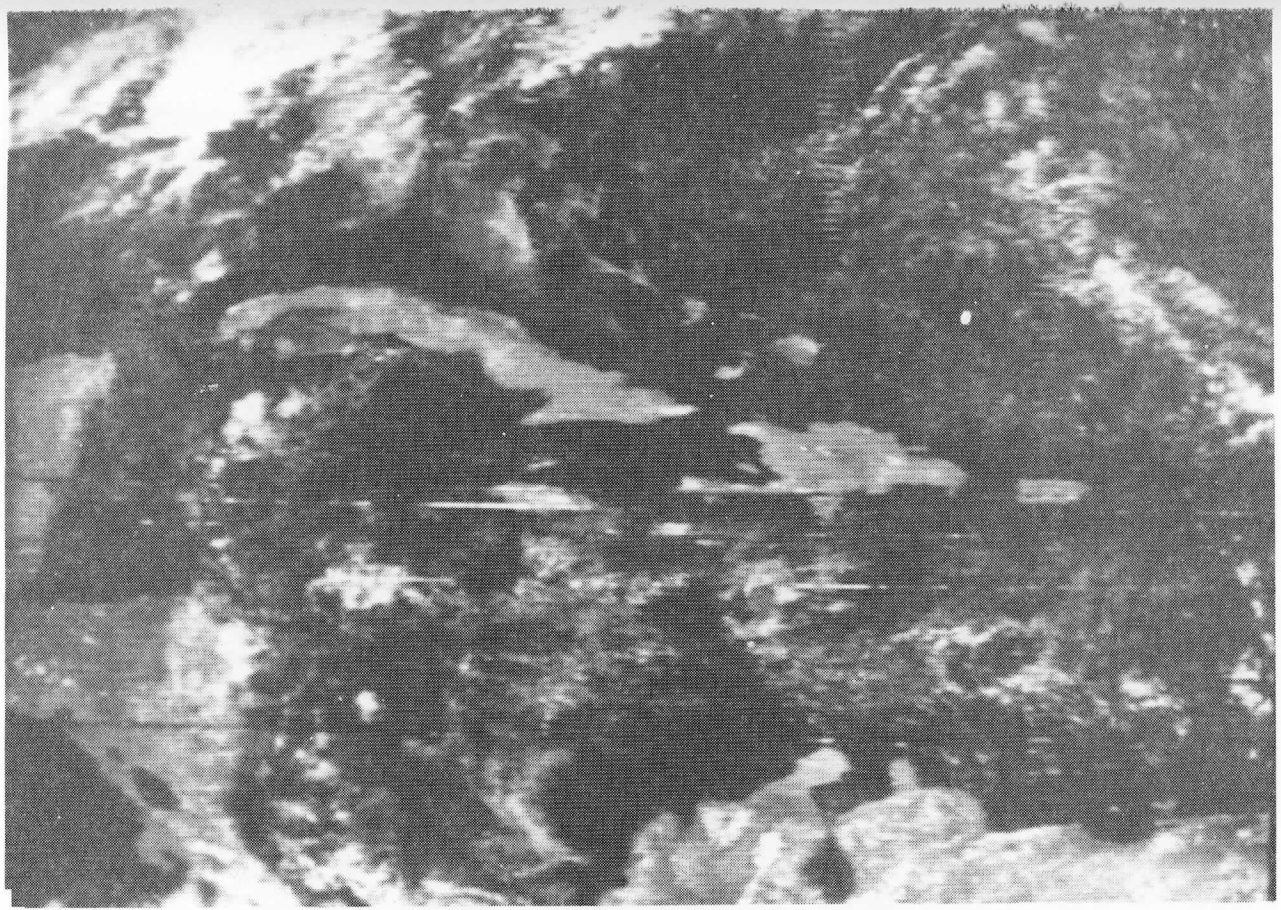

FIGURE 6: Two-day minimum brightness composite of images for February 6 and February 5 at 1800 GMT.

FIGURE 7: Four-day minimum brightness composite of images for February 3 through February 6 at 1800 GMT.

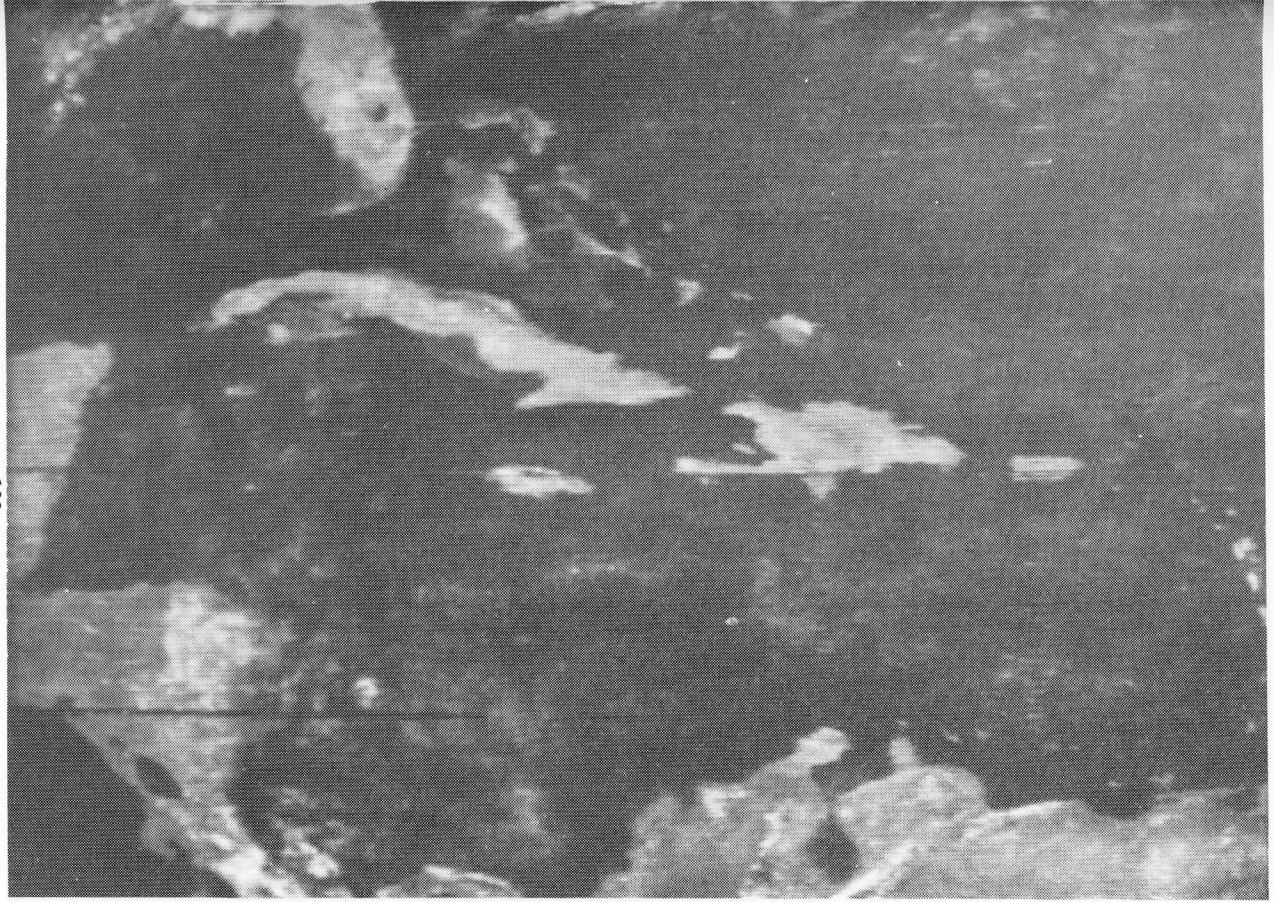

FIGURE 8: Five-day minimum brightness composite of images for February 2 through February 6 at 1800 GMT. Most of the clouds have been removed from the image.

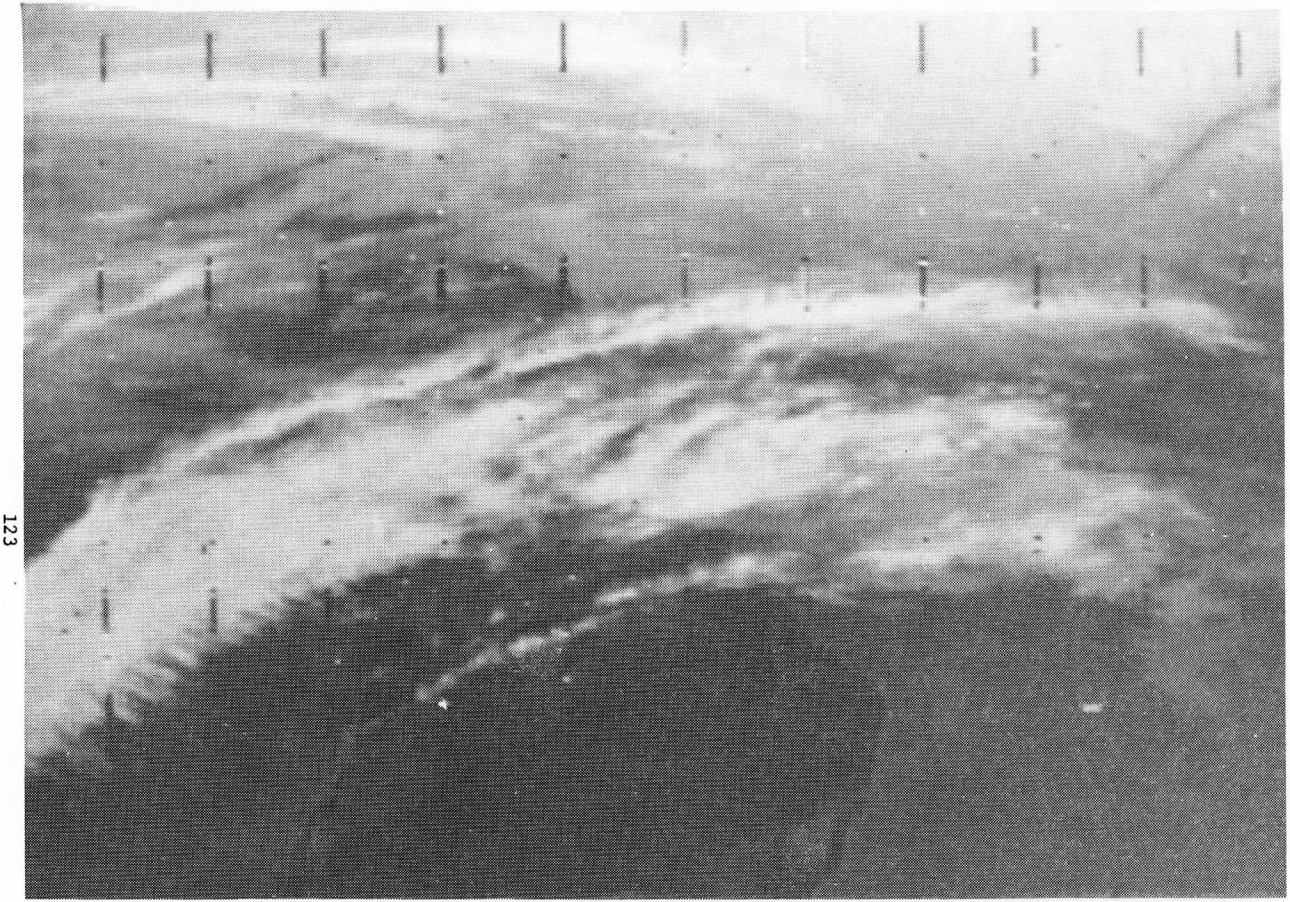

FIGURE 9: Infrared image on January 28, 1975 at 1800 GMT, of the eastern half of the United States. This was the clearest day used in the four-day composite.

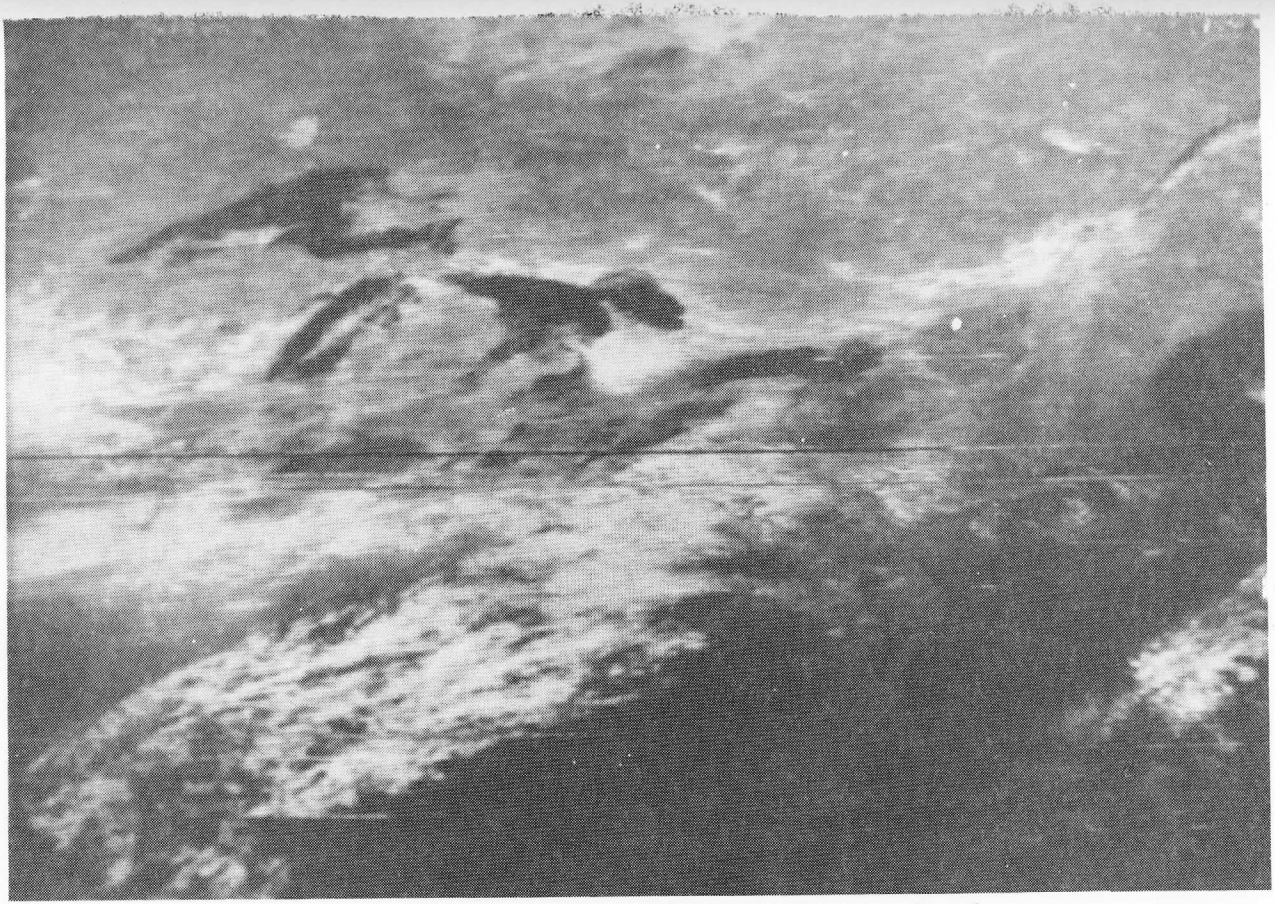

FIGURE 10: Visible minimum brightness four-day composite of images for January 28 through January 31, 1975 at 1800 GMT, for the eastern half of the United States.

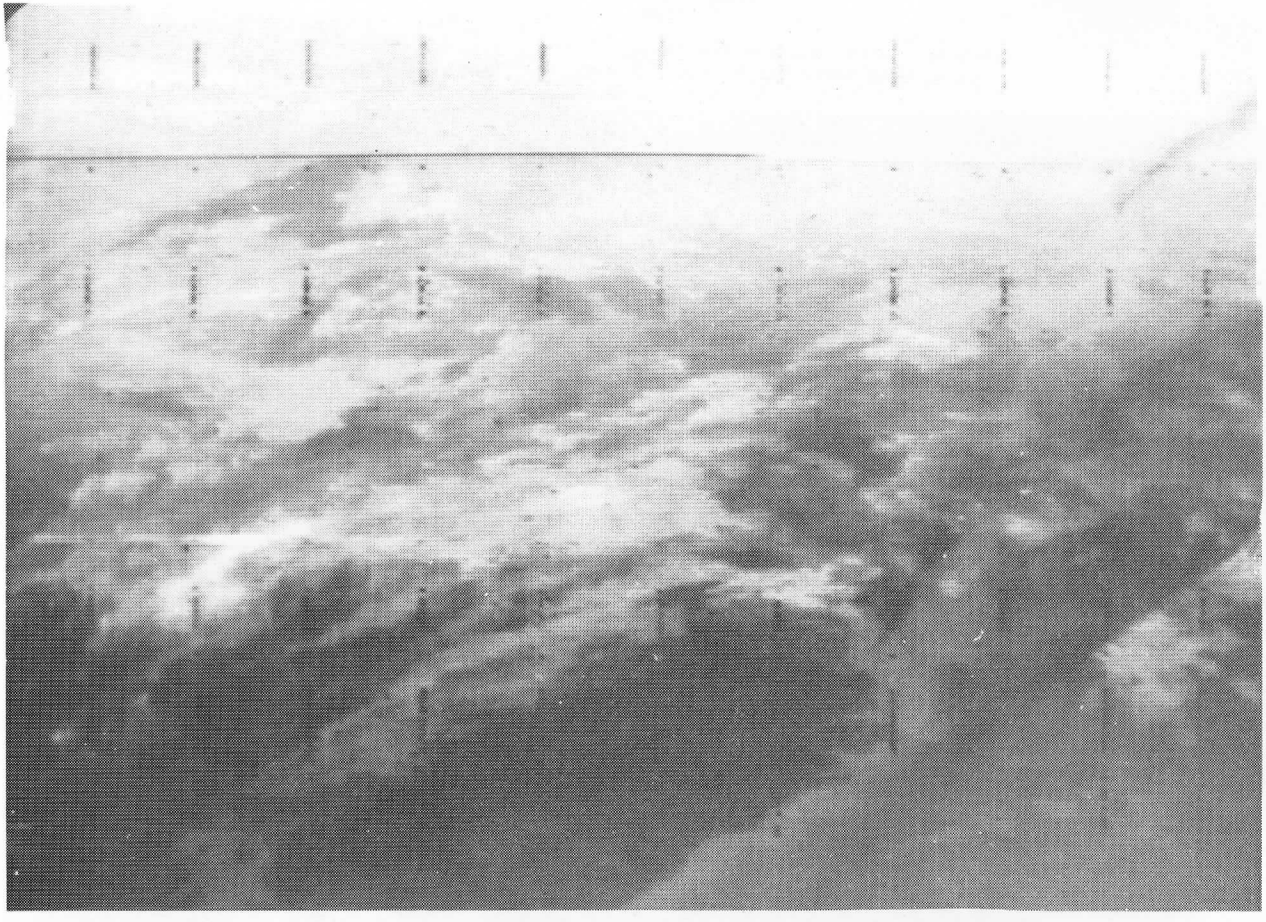

FIGURE 11: Infrared minimum brightness four-day composite of images for January 28 through January 31, 1975 at 1800 GMT for the eastern half of the United States.

FIGURE 12: Blow-up of Figure 11 showing the coast from North Carolina through New Jersey and the warmer (darker) Gulf Stream.

# NAVIGATION OF VENUS MULTIFRAME MOSAICS

William W. Kuhlow and Dennis R. Phillips

ABSTRACT

Accurate determination of Venus coordinates from Mariner 10 data image coordinates have been restricted, until recently, to single frames of resolution around 8 km, in which a sufficient portion of the bright Venus limb was in view. Image coordinate measurements from this bright edge were necessary to uniquely determine the navigation transform from image to Venus coordinates.

Navigation of high resolution image frames is more difficult because most of the frames making up a Venus mosaic do not contain bright edges at which measurements can be made; furthermore, each frame has a slightly different perspective of the planet due to spacecraft motion.

A self-consistent iterative procedure has been developed in which multi-frame mosaic navigation is possible for any connected configuration of overlapping high resolution image frames from a Venus sequence, providing that:

(1) some of the frames contain portions of the Venus limb from which edge measurements can be made, and that these measurements (from either the same or different frames) span a reasonably large arc-angle along the limb;

(2) a Venus feature common to each pair of overlapping frames can be identified and its image coordinates measured.

The procedure accounts for changes in the spacecraft's position and results in a unique navigation transform for each of the frames. Once navigated, each frame contains all the information necessary for accurate image-to-coordinates transformations and may be dealt with on an individual basis.

## 1. INTRODUCTION

Mariner 10 data images have provided views of feature movement and development within the Venus atmosphere. Such observations become more valuable when a Venus reference frame is provided. However, due to the inaccuracy with which the Mariner 10's orientation is known in the Mariner's ephemeris, secondary inferences about the spacecraft's orientation are necessary. One approach to inferring the spacecraft's orientation has been achieved by measuring the location of the Venus limb in each Mariner image and extrapolating these measurements to the center passing through these limb points. We can then assign the latitude and longitude of the spacecraft's subpoint (which is available from the ephemeris data) to correspond to the image coordinates of the circle's center. This linkage is sufficient to find the orientation of the spacecraft's vidicon camera. Until recently, such an extrapolation has been limited to only those low resolution (~8 km) Mariner images which contain a significant portion of the Venus limb.

The problem of determining the vidicon's orientation for each image in a collage of overlapping high resolution images, which we will call a Venus mosaic, has been solved. This process, which we call navigation, no longer requires that each image contain a significant portion of the Venus limb, but rather that each image be connected by paths of overlapping images to images whose union contains a significant portion of the Venus limb. This navigational improvement permits a quantitative measurement of cloud motion on high resolution Venus mosaics which simply was not possible previously. Movement in the Venus atmosphere can be studied with higher resolution images and over longer time periods than ever before.

The navigational process is based on the observation peculiar to Mariner 10 (this peculiarity is discussed later in the paper) that once a single correspondence is established between Venus coordinates and image coordinates, the orientation of the vidicon camera is determined. A bi-directional transformation is found between image coordinates and Venus coordinates that accounts for all the effects of spacecraft motion and orientation. We call this transformation the Venus navigation.

If one image is navigated, an overlapping adjacent image can be navigated by locating a common feature in the overlap. Since the Venus latitude and longitude of the feature are known from the navigation for the first image, a correspondence between image coordinates and Venus coordinates is established for the second image. Thus, the navigation of one image provides navigations for all the images linked to that image.

The navigation of a Venus mosaic is achieved by adjusting the Venus coordinates in a particular mosaic--a mosaic showing a correspondence between image coordinates and Venus coordinates--until limb measurements coincide with predicted limb location. One predicts a limb measurement to occur at a latitude and longitude which lies at a fixed angular distance from the subspacecraft point, depending on the height. Since these Venus coordinates have two degrees of freedom, two significantly separated limb measurements with corresponding linkage paths are necessary to uniquely navigate a mosaic. Using more measurements a steepest descent method can be applied to minimize the effect of measurement errors.

This approach for navigating Venus mosaics has been implemented in FORTRAN and tested on a single Mariner 10 image that was cut up to look like a Venus mosaic to the program modules. The programs produced the same navigational parameters and hence the same navigation as when the image was treated as a simple whole image, thus verifying the success of mosaic navigation.

Finally, a mosaic navigation was carried out successfully on a mosaic consisting of three distinct overlapping image frames. Two of these image frames contained sufficient portions of the Venus limb to allow measurement of single frame navigation parameters. Results from the "established" navigation procedure agreed, within the expected measurement errors, to those derived from the Venus Mosiac Navigation.

## 2. VENUS NAVIGATION FOR A SINGLE IMAGE FRAME

This section discusses the equations used in the navigation of a single image frame; these equations also form the mathematical basis for the Venus multiframe-mosaic navigation.

### A. Definitions

The following parameters† are available for each Venus image frame:

$(\theta_s, \phi_s)$ = Venus latitude and longitude, respectively, of the sub-spacecraft point

$(\theta_H, \phi_H)$ = Venus latitude and longitude of the sub-solar point

$a$ = Venus radius at visible limb as determined from UV images ($a$ = 6131 km)

$h$ = height of spacecraft (km)

$(\theta_L, \theta_E)$ = FOV angles in the scan line and element directions (degrees)

$(T_L, T_E)$ = total number of scan lines per FOV image and total number of elements per FOV scan line.

In addition to these available parameters, the following are defined (refer to FIGURES 2.1 and 2.2):

$(\theta, \phi)$ = Venus latitude and longitude of an arbitrary feature

$(\rho_L, \rho_E)$ = angle in radians subtended per image scan line $(\pi\theta_L/180T_L)$ and per element $(\pi\theta_E/180T_E)$

$(L, E)$ = line and element value of an arbitrary image point

$(L_c, E_c)$ = image center line and element ($L_c = T_L/2$; $E_c = T_E/2$)

$(\lambda, \delta)$ = angle between L and $L_c$ at picture center and between E and $E_c$ at picture center

$\vec{r}_v$ = vector pointing from Venus center to Venus feature ($\|\vec{r}_v\| = a$, where $\|\vec{r}_v\|$ is the vector norm of $\vec{r}_v$)

$\vec{b}$ = vector pointing from Venus center to spacecraft ($\|\vec{b}\| = h$)

---

†The parameters $(\theta_s, \phi_s)$, $(\theta_H, \phi_H)$ and $h$ are available from the JPL/Mariner 10 Supplementary Experimenter Data Records (SEDR).

$\vec{r}_h$ = vector from Venus center to Venus sub-solar point ($\|\vec{r}_h\| = a$)

$\vec{r}$ = vector pointing from the spacecraft to a Venus feature ($\vec{r}$ is expressed in Venus coordinates)

$\vec{r}'$ = vector pointing from the spacecraft to the image of the Venus feature associated with $\vec{r}$ ($\vec{r}'$ is expressed in image coordinates)

R = 3 x 3 orthogonal (rotation) matrix which transforms $\vec{r}$ into $\vec{r}'$. Finding the navigation transform for an image frame is equivalent to determining R.

The two basic coordinate systems (FIGURES 2.1 and 2.2) used in the navigation procedure are defined as follows:

(1) Venus-Centered Coordinate System

The $+X_V$, $+Y_V$ axes lie in the Venus equatorial plane. The longitude, $\phi$, of a Venus feature is measured from the $+X_V$ axis (in the $X_VY_V$ plane) in a counter clockwise sense about the $+Z_V$ axis which points into the northern celestial hemisphere and defines Venus north. (The planet Venus rotates in a clockwise sense about the $+Z_V$ axis.)

(2) Image Frame Coordinate System

The +X' axis points through the image center coordinates ($L_c$,$E_c$); the +Y' axis is parallel to the image scan lines and points towards decreasing element numbers (nominally west); the +Z' axis is perpindicular to the scan lines and points towards decreasing line numbers (nominally north). The origin of this system is so situated that the angles subtended at the image frame limits from the origin equals the FOV camera angles ($\theta_L$, $\theta_E$).

## B. Basic Transformation Equations

The basic transformation equations between Venus and image coordinates and their relationship to the navigation procedure now can be written in terms of the definitions and conditions given above.

The vector $\vec{r}$, which points from the spacecraft to a Venus feature and is expressed in Venus coordinates, is given as $\vec{r} = \vec{r}_v - \vec{b}$. It is convenient to express $\vec{r}$ as a unit vector $\hat{r}$; thus,

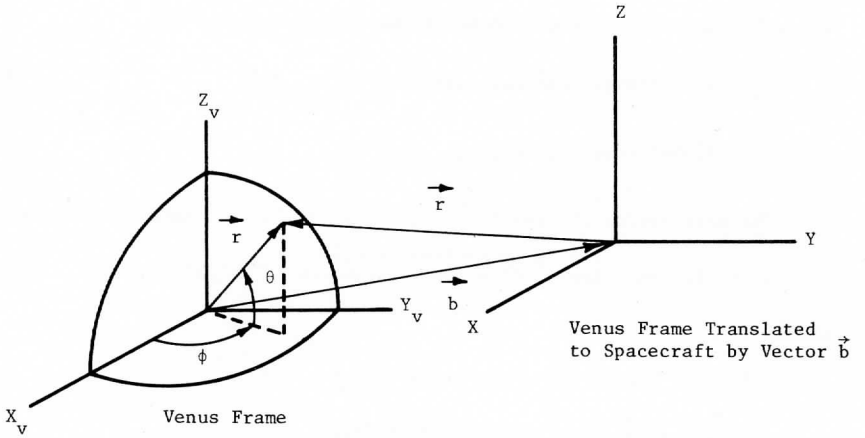


FIGURE 2.1. Venus/Spacecraft Geometry. The vector $\vec{r}$ points from the spacecraft center to a Venus feature whose components are expressed in Venus coordinates ($\vec{r} = \vec{r}_v - \vec{b}$).

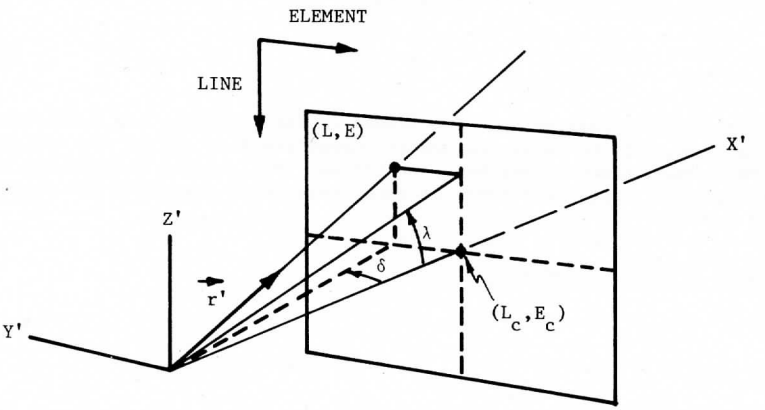


FIGURE 2.2. Image Frame Geometry. The vector $\vec{r}'$ whose components are expressed in image coordinates is associated with the vector $\vec{r}$ in FIGURE 2.1. The origins of the XYZ and X'Y'Z' coordinate systems are coincident.

$$\hat{r} = (\vec{r}_v - \vec{b})/\|\vec{r}_v - \vec{b}\| = [X,Y,Z]^T, \tag{1}$$

where "T" refers to the transpose of the column vector $\vec{r}$ and

$$\vec{r}_v = a[\cos\theta\cos\phi,\ \cos\theta\sin\phi,\ \sin\theta]^T = [X_v,Y_v,Z_v]^T, \tag{2}$$

$$\vec{b} = h[\cos\theta_s\cos\phi_s,\ \cos\theta_s\sin\phi_s,\ \sin\theta_s]^T. \tag{3}$$

The unit vector $\hat{r}'$ associated with $\hat{r}$ is defined in image coordinates as

$$\hat{r}' = [1,\ \tan\delta,\ \tan\lambda]^T/\sqrt{1 + \tan^2\delta + \tan^2\lambda} = [X',Y',Z']^T, \tag{4}$$

where

$$\left.\begin{aligned}\lambda &= (L_c - L)\rho_L = (L_c - L)(\pi/180)(\theta_L/T_L)\\ \delta &= (E_c - E)\rho_E = (E_c - E)(\pi/180)(\theta_E/T_E)\ .\end{aligned}\right\} \tag{5}$$

It should be emphasized at this point that the coordinate representations of $\hat{r}$ and $\hat{r}'$ are relative to orthogonal coordinate systems (the Venus frame translated to the spacecraft and the image frame) and therefore are related to each other by a rotation matrix R, i.e.,

$$\hat{r}' = R\,\hat{r}\ . \tag{6}$$

With the explicit determination of R (shown in the following two subsections), the frame is said to be navigated and by convention R is called the navigation transform. Thus, given R, any Venus coordinate $(\theta,\phi)$ can be transformed to its corresponding image coordinate or vice-versa using equations (1) through (6). In symbols:

Venus → Image Coordinates

$$\left.\begin{aligned}&(\theta,\phi) \to \vec{r}_v \to \hat{r}\ ,\\ &\hat{r}' = R\hat{r} \to (L,E)\ ,\end{aligned}\right\} \tag{7}$$

where

$$L = L_c - (\arctan\,(Z'/X'))/\rho_L$$

$$E = E_c - (\arctan\,(Y'/X'))/\rho_E\ ;$$

Image → Venus Coordinates

$$
\left.
\begin{aligned}
&(L,E) \rightarrow \hat{r}' \ , \\
&\hat{r} = R^{T}\hat{r}' \rightarrow \vec{r}_v \rightarrow (\theta,\phi)^{\dagger} \ ,
\end{aligned}
\right\} \qquad (8)
$$

where

$$\theta = \arcsin (Z_v/a)$$

$$\phi = \arctan (Y_v/X_v)$$

---

$^{\dagger}$In transforming from image to Venus coordinates, the magnitude of $\vec{r}$ must be determined in order to determine $\vec{r}_v$ ($\vec{r}_v = ||\vec{r}||\hat{r} + \vec{b}$; eq. (1)). This is easily accomplished by an iterative procedure with the convergence criteria that $||\vec{r}_v|| - a < 10^{-2}$ km.

C. Conditions for Determining the Navigation Transform, R

The navigation matrix R for an image frame is uniquely determined from the equations given above by implementing the conditions that:

(1) the Venus coordinates $(\theta,\phi)$ for at least one image point (L,E) in the frame are known;

(2) the scan lines of the image frame (nominally running in an east-west direction) are parallel to the plane formed by the centers of the sun, Venus, and the spacecraft.

Satisfying the first condition is the essence of image navigation and always implies the direct measurement of image coordinates from the image frame(s) under consideration. For low-resolution images navigated in the past, in which a single frame contained most or a large portion of the bright Venus limb, the measurements consisted of edge point measurements along the limb. These image points then were used to calculate (in a least-squares sense) the Venus-center image coordinates. Since this point corresponds to the sub-spacecraft point for which the Venus coordinates are given, the first condition then was satisfied.

For the higher-resolution multiframe Venus mosaics, the frames making up the mosaic may each contain only a small arc-angle of the Venus limb or, indeed, no Venus edge at all. In order to satisfy the first condition for the determination of R for multiframe mosaic navigation, not only are edge point measurements required from each of the frames containing portions of the Venus limb, but in addition, link point measurements (image coordinates for a feature common to two overlapping frames) of the overlapping

frames, which connect the multiframes into a mosaic, also are necessary. By a self-consistent interative procedure discussed in the following section, the image coordinates for the sub-spacecraft point of one of the frames in the mosaic are found to satisfy the first condition. This condition is satisfied for the rest of the frames via the iterative procedure using the link point measurements.

For the purpose of this section, however, it is assumed that the Venus coordinates for at least one image point per frame are known. Let the known vector pair be denoted by $\hat{r}_1$, $\hat{r}_1'$ where $\hat{r}_1$ is the unit vector in Venus coordinates (eq. 1) and $\hat{r}_1'$ the unit vector derived from the associated image coordinates (eq. 4). Thus, the rotation matrix must satisfy the relationship

$$\hat{r}_1' = R\,\hat{r}_1 \quad . \tag{9}$$

The second condition, that the image scan lines be parallel to the sun-Venus-spacecraft plane, is a result of the stabilization/pointing procedure employed on the Mariner 10 during the Venus image acquisition period and is assumed to be accurate within attitude error limits (± 0.25 degrees). This condition is equivalent to imposing the constraint that the normal to this plane be perpendicular to the scan lines. A unit vector normal to this plane is obtained by crossing the sub-solar vector $\vec{r}_h$ into the subspacecraft vector $\vec{b}$ and normalizing:

$$\hat{r}_2 = (\vec{r}_h \times \vec{b})/\|\vec{r}_h \times \vec{b}\| \tag{10}$$

(Note that $\hat{r}_2$ can be calculated directly from the SEDR parameters available for each image frame). That the normal of the plane be perpendicular to the scan lines, is equivalent to stating that the Y-component of $\hat{r}_2$ (expressed in image coordinates) equal zero, i.e.,

$$\begin{aligned} &\hat{r}_2' = [X_2', Y_2', Z_2']^T = R\,\hat{r}_2, \\ &Y_2' = 0 \quad . \end{aligned} \tag{11}$$

D. Determination of R

The problem of determining R now can be restated as follows: Given that R must be a 3 x 3 orthogonal matrix satisfying the equations:

$$\hat{r}'_1 = R\,\hat{r}_1,$$

$$\hat{r}'_2 = R\,\hat{r}_2,$$

where $\hat{r}_1 = [X_1, Y_1, Z_1]^T$, $\hat{r}'_1 = [X'_1, Y'_1, Z'_1]^T$, $\hat{r}_2 = [X_2, Y_2, Z_2]^T$, $Y'_2 = 0$ are known, determine R.

Use will be made of the properties of an orthogonal matrix that the scalar products and norms remain invariant under such a transformation, and that the transform of a vector product is equal to the vector product of the transform. Thus, for arbitrary vectors $\vec{r}_a$, $\vec{r}_b$, $\vec{r}$

$$(\vec{r}_a \cdot \vec{r}_b) = (\vec{r}'_a \cdot \vec{r}'_b) \tag{12a}$$

$$\|\vec{r}\| = \|\vec{r}'\| \tag{12b}$$

$$(\vec{r}_a \times \vec{r}_b)' = \vec{r}'_a \times \vec{r}'_b \tag{12c}$$

where

$$\vec{r}' = R\,\vec{r}\,.$$

The first step in the determination of R is to compute $\hat{r}'_2$; in particular, to find $X'_2$, $Z'_2$ ($Y'_2 = 0$). Applying the scalar product invariant condition expressed in eq. (12a) to $\hat{r}_1$, $\hat{r}_2$, we have:

$$\hat{r}_1 \cdot \hat{r}_2 = X_1 X_2 + Y_1 Y_2 + Z_1 Z_2 = \hat{r}'_1 \cdot \hat{r}'_2 = X'_1 X'_2 + Z'_1 Z'_2 = \alpha, \quad (Y'_2 = 0). \tag{13}$$

Similarly, as implied by eq. (12b),

$$\|\hat{r}_2\| = \|\hat{r}'_2\| = 1 = X'^2_2 + Z'^2_2\,. \tag{14}$$

Thus, eqs. (13) and (14) constitute two equations in terms of the unknowns $X'_2$, $Z'_2$, the solutions of which are:

$$Z'_2 = (\alpha Z'_1 + X'_1 \sqrt{X'^2_1 + Z'^2_1 - \alpha^2})/(X'^2_1 + Z'^2_1) \tag{15a}$$

$$X'_2 = \alpha/X'_1 \tag{15b}$$

$$Y'_2 = 0 \, . \tag{15c}$$

The choice of the positive sign in front of the radical in eq. (15a), guarantees that the +Z' axis of the image frame (FIGURE 2.2) will lie in the northern celestial hemisphere. With $\hat{r}'_2$ completely determined, computation of R can proceed.

From $\hat{r}_1$, $\hat{r}_2$ a set of mutually orthogonal unit basis vectors can be constructed in the translated Venus frame (unprimed coordinate system) as follows:

$$\left.\begin{aligned} \hat{s}_1 &= \hat{r}_1 \\ \hat{s}_2 &= (\hat{r}_2 - (\hat{r}_1 \cdot \hat{r}_2)\,\hat{r}_1)/\|\hat{r}_2 - (\hat{r}_1 \cdot \hat{r}_2)\,\hat{r}_1\| \\ \hat{s}_3 &= \hat{s}_1 \times \hat{s}_2 \, , \end{aligned}\right\} \tag{16}$$

which are used to create an orthogonal matrix

$$S = [\hat{s}_1 | \hat{s}_2 | \hat{s}_3]^T, \tag{17}$$

where the $\hat{s}_i$ are column vectors. (That S is an orthogonal matrix can be easily shown by carrying out the multiplications $S^TS$ and $SS^T$, each product of which equals the unit matrix. This result is necessary and sufficient to guarantee that S is orthogonal). Thus for an arbitrary vector $\vec{r}$,

$$S\vec{r} = [\hat{s}_1 \cdot \vec{r}, \hat{s}_2 \cdot \vec{r}, \hat{s}_3 \cdot \vec{r}]^T \, . \tag{18}$$

Expressing the $\hat{s}_i$ in the primed system (image coordinate frame) is easily achieved by operating on both sides of eqs. (16) with R ($\hat{s}'_i = R\hat{s}_i$, i = 1,3) using the conditions implied in eqs. (12) and the equations $\hat{r}'_1 = R\hat{r}_1$,

$\hat{r}'_2 = R\hat{r}_2$. The result is

$$\left.\begin{aligned} \hat{s}'_1 &= \hat{r}'_1 \\ \hat{s}'_2 &= (\hat{r}'_2 - (\hat{r}'_1\cdot\hat{r}'_2)\hat{r}'_1)/\|\hat{r}'_2 - (\hat{r}'_1\cdot\hat{r}'_2)\hat{r}'_1\| \\ \hat{s}'_3 &= \hat{s}'_1 \times \hat{s}'_2 \,. \end{aligned}\right\} \tag{19}$$

The significance of eqs. (19) is that the basis vectors $\hat{s}'_i$ can be calculated directly from $\hat{r}_1$, $\hat{r}'_2$, which can then be used to generate the orthogonal matrix

$$S' = [\hat{s}'_1|\hat{s}'_2|\hat{s}'_3]^T \,. \tag{20}$$

Now because a scalar product remains invariant under an orthogonal transformation, the components $\hat{s}_i\cdot\vec{r}$ in eq. (18) are each equal to $\hat{s}'_i\cdot\vec{r}'$ and therefore the RHS of (18) is equal to

$$[\hat{s}'_1\cdot\vec{r}',\ \hat{s}'_2\cdot\vec{r}',\ \hat{s}'_3\cdot\vec{r}'] = S'\vec{r}' \,. \tag{21}$$

Combining (18) and (21),

$$S\vec{r} = S'\vec{r}'$$

or

$$S'^T S\vec{r} = \vec{r}', \tag{22}$$

and since S and S' are each orthogonal, $S'^T S$ is orthogonal; thus from (22)

$$R = S'^T S \tag{23}$$

or expressing R in terms of its components $R_{ij}$,

$$R_{ij} = \sum_{k=1}^{3} S'^T_{ik} S_{kj} = \sum_{k=1}^{3} S'_{ki} S_{kj} \,. \tag{24}$$

Since the $S'_{ki}$, $S_{kj}$ are derived from their orthogonal basis vectors $\hat{s}_i$, $\hat{s}'_i$[†] which in turn are calculated from $\hat{r}_1$, $\hat{r}_2$, $\hat{r}_1$, $\hat{r}_2$, the matrix R is completely determined.

---

[†]The relationship is $S_{ij} = (\hat{s}_i^T)_j$.

## 3. VENUS MULTI-FRAME MOSAIC NAVIGATION

### A. Basic Procedure

The procedure outlined in the previous section forms the basis for multiframe mosaic navigation. The following requirements for this general navigation procedure are:

(1) The configuration of frames making up a partial or full mosaic must be connected, with enough overlap between the connecting frames that at least one small Venus feature common to both frames can be identified and a link point measurement made. A link point measurement consists of the image point coordinates of the feature for each of the two overlapping frames.

(2) The multiframe mosaic must contain at least one frame from which Venus limb edge point measurements are available. (An edge point measurement consists of the image point coordinates on the limb where the gradient of the brightness values reaches a user-specified threshold; for the threshold used on the UV images this method has been proven to be very consistent resulting in a radius of 6131 km). For maximum accuracy in the navigation, it is best to have two frames containing Venus limbs, separated by as large an arc-angle along the limb as is practicable.

Using the link and edge point measurements and the available parameters for each image frame (see Section 2, Subsection A), the multiframe configuration is navigated using the self-consistent procedure described below:

(i) One of the frames is arbitrarily chosen as a reference frame. For ease of implementation, one furthest from the Venus limb, or one occurring at frame branch point, is chosen. This reference frame is navigated by making a first-guess of the sub-spacecraft image coordinates, then using the navigation transform for that frame.

The first-guess coordinates are computed by expressing the edge point measurements in reference frame coordinates. The assumption is made that all frames currently under consideration have the same resolution and simply are translated one from the other. Using the link and edge point measurements, the total displacement of the edge points in pixels from the reference frame can be obtained by simple addition. The two edge points with the largest arc-angle separation then are used (with the given radius of 6131 km converted to pixels) to compute the sub-spacecraft image coordinates of the reference frame. These values usually agree with the final convergence values to within a few pixels.

(ii) With the reference frame navigated, the Venus coordinates associated with the reference frame link point coordinates can be calculated. Since the image coordinates of this point associated with the linked frame are available from the measurements, this "link-to" frame likewise can be navigated. The navigation from this frame is in turn used to predict the

Venus coordinates of the frame to which it is linked, so that the third frame can be navigated. This "leap-frog" method of frame navigation follows a path of linked frames (constraint path) until it terminates on a frame containing edge measurements.

(iii) From the navigation transform computed for this edge frame, the sub-spacecraft vector $\hat{r}'_c$ in image coordinates is computed using the SEDR-available Venus sub-spacecraft coordinates. The measured edge point image coordinates are converted to a unit vector $\hat{r}'_e$ in the image frame and used with $\hat{r}_c$ to compute $\sin\theta'$, where $\theta'$ is the approximate half-angle Venus subtends at the spacecraft (FIGURE 3.1). In addition, a direct calculation of this half angle (called $\theta$) is made from the frame-available parameters a and h, the Venus

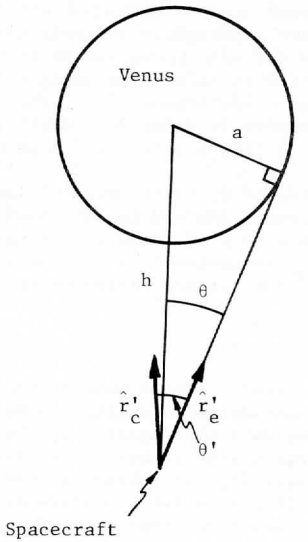


FIGURE 3.1. The angle $\theta$ is the correct half-angle Venus subtends at the spacecraft; $\theta'$ is the half-angle derived from an edge measurement ($\hat{r}'_e$) and the mosaic model-computed sub-spacecraft point ($\hat{r}'_c$) expressed in image coordinates.

radius and spacecraft height, respectively. Thus,

$$\sin\theta' = \| \hat{r}'_e \times \hat{r}'_c \| ,$$

$$\sin\theta = a/h.$$

The squared difference, $(\sin\theta - \sin\theta')^2$, for this constraint path is accumulated as part of a sum, S, which is discussed below.

(iv) Steps 2 and 3 are repeated for all uniquely defined constraint paths, producing for this first-iteration navigation a navigation transform matrix for each of the frames, and the sum, S, where

$$S = \sum_k (\sin\theta_k - \sin\theta'_k)^2 ,$$

where "k" is summed over all constraint paths.

(v) The function of S is minimized relative to the reference frame sub-spacecraft image coordinates using a method of steepest descent and variable step size until the appropriate convergence criteria are met. Although steps (i) through (iv) are repeated for each iteration in minimizing S (indeed, for each iteration the gradient of S is calculated using a difference technique which requires four additional computations of S), the CPU time required on the SSEC/McIDAS Datacraft minicomputer is relatively small (about 30 seconds for 50 iterations using 3 images, 2 link points and 3 edge points).

With the minimization of S, there results a unique navigation transform for each of the image frames involved in this self-consistent multiframe mosaic navigation. Thus, since each of these frames have been navigated, any of these individual frames may be employed in studies requiring accurate image-to-planet transformations without further reference to their parent mosaic.

B. Example and Results

FIGURE 3.2 shows a pseudo 3-frame mosaic (fabricated from a single Venus frame) used in testing the mosaic navigation computer model. TABLE 3.1 is the model output associated with the figure. Of these three frames, the one not containing a Venus edge (frame numbered one) was arbitrarily chosen as the reference frame (the frames, FM, are labeled by the encircled numbers in FIGURE 3.2). With the two link points (LP - denoted by solid triangles) and three earth edge points (EP - solid circles) labeled as shown in the figure, the three constraint paths used were

$$\text{FM-1} \xrightarrow{\text{LP-1}} \text{FM-2} \rightarrow \text{EP-1}$$

$$\text{FM-2} \rightarrow \text{EP-3}$$

$$\text{FM-1} \xrightarrow{\text{LP-2}} \text{FM-3} \rightarrow \text{EP-2} .$$

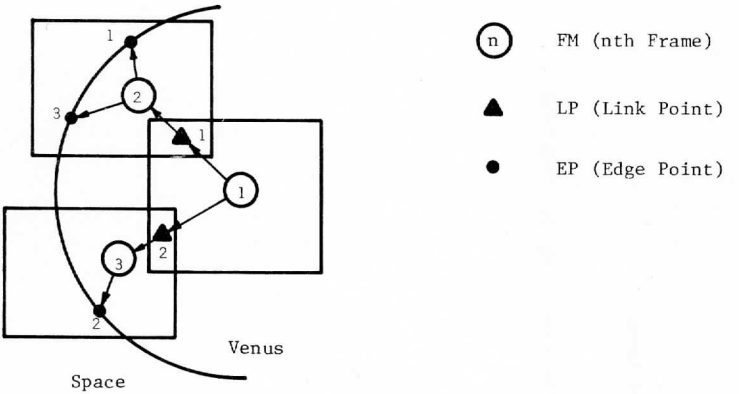


FIGURE 3.2. A three-frame mosaic configuration demonstrating link points (LP), edge points (EP) and constraint paths.

The manner in which these measurements and constraint paths are entered into the computer model is discussed in the Appendix. The first block of output data in TABLE 3.1 records these input values. In the second block, the "CALCULATED INPUT POINT" is the first estimation of the reference frame sub-spacecraft image coordinates (line, element) derived from edge points 1 and 2 in the manner discussed in Section 3-A (Step 1 of the algorithm). The "FINAL CONVERGENCE POINT" is the result of minimizing the function S relative to this sub-spacecraft point with a "CONVERGENCE ACCURACY" given by

$$(\sqrt{S_f/N})(1/\sqrt{\rho_L \rho_E}) \ ,$$

where

$S_f$ = final convergence value of S

N = total number of distinct edge points

$\rho_L$ = radians/image scan line

$\rho_E$ = radians/image element

Edge and link point number and measurements are recorded in the third and fourth blocks of data with their associated FRAME ID's (a number associated with and unique to each image frame). The "LINK POINT RESIDUALS" are differences between measured coordinates and the coordinates derived by transforming the measured image link point coordinates to Venus coordinates

```
* * * * * * * * * * * * * * * * * * * * * * * * * * * * * * * * * * * * *
*                                                                       *
*                          VENUS MOSAIC NAVIGATION                      *
*                                                                       *
* * * * * * * * * * * * * * * * * * * * * * * * * * * * * * * * * * * * *
```

| NO. OF FRAMES | NO. OF EDGE POINTS | NO. OF LINK POINTS | NO. OF CONSTRAINT PATHS |
|---|---|---|---|
| 3 | 3 | 2 | 3 |

| CALCULATED INPUT POINT | | FINAL CONVERGENCE POINT | | CONVERGENCE ACCURACY(PIXELS-RMS) | NO. OF ITERATIONS |
|---|---|---|---|---|---|
| LIN | ELE | LIN | ELE | | |
| 264.222 | 363.700 | 264.428 | 363.939 | 370 | 50 |

EDGE POINTS USED IN NAVIGATION

| NUMBER | FRAME ID | LIN | ELE |
|---|---|---|---|
| 1 | 2 | 64 | 194 |
| 2 | 3 | 314 | 106 |
| 3 | 2 | 164 | 122 |

LINK POINTS USED IN NAVIGATION AND LINK POINT RESIDUALS

| NUMBER | FRAME ID | LIN | ELE | DELTA LIN | DELTA ELE |
|---|---|---|---|---|---|
| 1 | 1 | 150 | 250 | -.007 | .003 |
| 1 | 2 | 150 | 250 | .006 | -.010 |
| 2 | 1 | 300 | 200 | .003 | -.007 |
| 2 | 3 | 300 | 200 | .002 | -.006 |

NAVIGATED SUB-SPACECRAFT IMAGE COORDINATES

| NFRAME | FRAME ID | LIN | ELE |
|---|---|---|---|
| 1 | 1 | 264.441 | 363.949 |
| 2 | 2 | 264.426 | 363.979 |
| 3 | 3 | 264.441 | 363.950 |

**TABLE 3.1. This table shows multiframe mosaic navigation results for a three-frame mosaic derived from a single image frame and is associated with FIGURE 3.2. See text for further explanation.**

and back into image coordinates. These residuals are not a gauge of absolute navigation accuracy, but serve to show that the transformations for each image frame are at least internally consistent. They also give a measure of the computational error associated with the transformations.

The final output block of data is the computed image coordinates of the sub-spacecraft point for each of the image frames. In this example, they are identical since all three frames were, in fact, derived from the same image frame. These navigation results (sub-spacecraft point image coordinates and components of the matrix R) were compared to those derived for this image frame (ID number 4901018) from the single frame navigation model currently running on SSEC's McIDAS.† (The formulation of this current single frame navigation procedure was such that it could not easily be generalized to include multi-frame navigation). The results were identical to within the round-off and truncation errors inherent in the system.

It is also noteworthy that the linkage point measurements used in the example above were changed for the reference frame (on the order of 10 pixels) effectively to compress it relative to the two other fabricated frames. The function S converged to a final value without difficulties and the final results were what one would expect (sub-spacecraft image coordinates were least affected for the frame containing the two edge measurements). Tests on the model were also made by stretching and rotating the reference frame with the same successful results.

Following this test of the basic mosaic navigation program, the procedure was tested on a true mosaic. Three frames with overlap and with subbicient bright limb in each (IDS #'s 4608397, 4610397, and 4617397) were chosen. The images had not been FICORed or GEOMed. Usually the geometric distortions in a raw vidicon image are significantly large and increase away from the center of the frame. The bulk of the mosaic frames were not likely to be GEOMed, so it was thought desirable to examine the effect of geometric on the mosaic navigation procedure. The check on the mosaic navigation was provided by the existing navigation scheme. FIGURE 3.3 shows an overlapping view of all three frames displayed. TABLE 3.2 shows the navigations obtained from the mosaic navigation scheme.

The convergence value of 3.4 pixels is, in fact, better than expected, since the geometric distortions in the three frames were completely ignored. We surmise that the least squares scheme used in the mosaic navigation to determine the best guess for image space sub-spacecraft point also tends to treat the vidicon geometric distortions as true errors in planet limb locations. Future navigation research will use the Reseau-mark measurements available in the image data to correct for these distortions.

A second but much smaller source of error affecting the mosaic navigation accuracy is the assumption that a Venus feature common to two overlapping

---

† Phillips, D. R. and S. Limaye, Annual Report, Space Science and Engineering Center, Madison, Wisconsin, 1976; NASA Contract Report No. NGR-50-002-189.

image frames, from which link point measurements are derived, has the same Venus coordinates in both images (i.e., that the movement of the feature over the time interval between the two frames is negligible).

In the case of the MVM-73 mission, successive frames were shuttered 42 seconds apart. Since the nominal speed of the UV features seen in these images is about 100 $msec^{-1}$, the features move zonally approximately 4.2 km between two successive images. Thus, as long as the resolution per pixel is only of the order of a few kilometers, the assumption that a UV feature has the same planet co-ordinates in the two frames is a good one. The motion of UV features has been determined from lower resolution frames† so the results can be used to extrapolate the true planet co-ordinates of the same UV feature if necessary. It seems very unlikely that such a need will arise in the study of MVM-73 UV images of Venus, since the 8-bit data (6-bit in IM-3 format) is simply not sufficient to show any visible detail for resolutions greater than about 2-4/km/pixel.

## 4. CONCLUSION

Using the newly available Venus Mosaic Navigation scheme discussed above, feature movement measurements now can be made from the high resolution Mariner 10 Venus image data. Accuracy is limited to the errors associated with the use of Reseau-mark measurements to correct vidicon geometric distortions. Because the high resolution Venus images can be navigated, feature movement measurements can be made over a longer time interval during the Venus encounter imaging sequence.

The Venus Mosaic Navigation requires that users exercise more care and judgement in the navigation of a data set than has been necessary in navigating individual Venus frames. When the program is incorporated into McIDAS, an operational manual may be needed to facilitate usage and minimize training time.

## ACKNOWLEDGMENT

We are pleased to thank Robert Krauss who provided the impetus for this work. We are especially grateful to Sanjay Limaye for providing the Venus mosaic meausrements and for his helpful revisions of this report.

This research was supported by the National Aeronautics Space Administration under NASA Grant No. NGR-50-002-189.

---

†Krauss, R., Annual Report, Space Science and Engineering Center, Madison, Wisconsin, 1976; NASA Contract Report No. NGR-50-002-189.

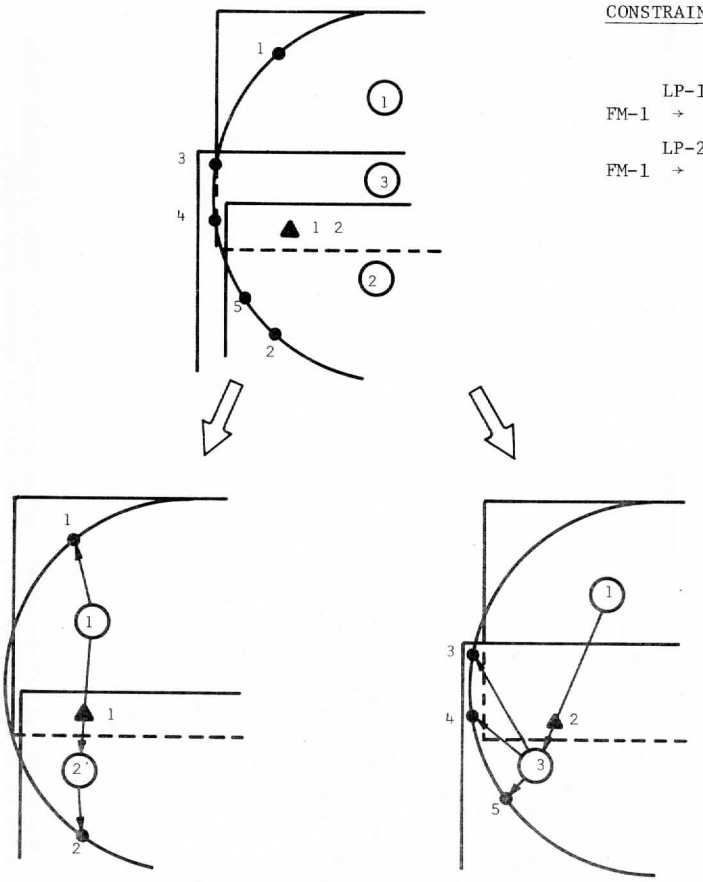


FIGURE 3.3. Three-Frame Mosaic Used in Navigation. Uppermost figure shows the configuration of the frames, edge points and link points (same link point used in FM-1). The uppermost figure is decomposed for clarity into the two lower figures where the constraint paths used in the navigation are shown.

```
* * * * * * * * * * * * * * * * * * * * * * * * * * * * * * * * * * * * *
*                                                                       *
*                          VENUS MOSAIC NAVIGATION                      *
*                                                                       *
* * * * * * * * * * * * * * * * * * * * * * * * * * * * * * * * * * * * *
```

| NO. OF FRAMES | NO. OF EDGE POINTS | NO. OF LINK POINTS | NO. OF CONSTRAINT PATHS |
|---|---|---|---|
| 3 | 5 | 2 | 5 |

| CALCULATED INPUT POINT | | FINAL CONVERGENCE POINT | | CONVERGENCE ACCURACY(PIXELS-RMS) | NO. OF ITERATIONS |
|---|---|---|---|---|---|
| LIN | ELE | LIN | ELE | | |
| 546.633 | 486.490 | 547.884 | 484.999 | 3.409 | 50 |

EDGE POINTS USED IN NAVIGATION

| NUMBER | FRAME ID | LIN | ELE |
|---|---|---|---|
| 1 | 4608397 | 137 | 156 |
| 2 | 4610397 | 348 | 110 |
| 3 | 4617397 | 10 | 64 |
| 4 | 4617397 | 202 | 60 |
| 5 | 4617397 | 442 | 164 |

LINK POINTS USED IN NAVIGATION AND LINK POINT RESIDUALS

| NUMBER | FRAME ID | LIN | ELE | DELTA LIN | DELTA ELE |
|---|---|---|---|---|---|
| 1 | 4608397 | 641 | 199 | .006 | -.014 |
| 1 | 4610397 | 57 | 181 | .012 | -.015 |
| 2 | 4608397 | 641 | 199 | .006 | -.014 |
| 2 | 4617397 | 197 | 276 | .005 | -.023 |

NAVIGATED SUB-SPACECRAFT IMAGE COORDINATES

| NAVID | FRAME ID | LIN | ELE |
|---|---|---|---|
| 1 | 4608397 | 547.880 | 485.012 |
| 2 | 4610397 | -36.041 | 466.764 |
| 3 | 4617397 | 104.054 | 561.343 |

TABLE 3.2. This table shows multiframe mosaic navigation results for three different Venus image frames and is associated with FIGURE 3.3. See text for further explanation.

## APPENDIX

### Brief FORTRAN Description of Venus Mosaic Navigation

This appendix documents the essential features of the FORTRAN program used for the Venus mosaic navigation, and describes the current procedure and format for inputting the relevant measurements (link/edge point) for a navigation.

### 1. Single Frame Navigation

Associated with each image frame is the common block VENCOM consisting of 22 words. The first 10 words consist of the basic parameters available for each image (Section 2-A); the remaining 12 words consist of the derived sub-spacecraft vector, $\vec{b}$, and the 3 x 3 navigation transform matrix, R. Listed below are these parameters in the order in which they appear in VENCOM and their FORTRAN equivalent. For details, see Section 2.

VENCOM PARAMETERS

| Algebraic Symbol | Definition | FORTRAN Equivalent |
|---|---|---|
| $(\theta_S, \phi_S)$ | sub-spacecraft latitude and longitude (decimal degrees) | (SSPLAT, SSPLON) |
| $(\theta_H, \phi_H)$ | sub-solar latitude and longitude (decimal degrees) | (SSLLAT, SSLLON) |
| a | Venus radius (km) | RADIUS |
| h | spacecraft height (km) | H |
| $(L_c, E_c)^{\dagger}$ | picture center line and element | (PCLIN, PCELE) |
| $(\rho_L, \rho_E)^{*}$ | radians per line, radians per element | (RDPLIN, RDPELE) |
| $\vec{b}$ | sub-spacecraft vector in Venus coordinates | B |
| R | navigation transform matrix | RM |

---

$^{\dagger}$These parameters are derived from the tape-available parameters of the FOV angles $(\theta_L, \theta_E)$ and the total lines and elements $(T_L, T_E)$; see Sec. 2.

$^{*}$See section 3.B.

ADDITIONAL PARAMETERS

| Algebraic Symbol | Definition | FORTRAN Equivalent |
|---|---|---|
| $(\theta,\phi)$ | latitude, longitude of a Venus feature | (XLAT, XLON) |
| (L,E) | line and element image coordinates associated with $(\theta,\phi)$ | (XLIN, XELE) |
| $\hat{r}_1$ | translated Venus vector used to determine R | R1V |
| $\hat{r}_1'$ | image of $\hat{r}_1$ - used to determine R | R1S |
| $\hat{r}_2$ | vector normal to spacecraft-sun-Venus plane - used to determine R | R2V |

Subroutine FRMNAV, given a Venus feature on planet and image coordinates (XLAT, XLON), (XLIN, XELE), computes B and RM, and stores them in VENCOM.

FRMNAV calls three basic subroutines; their name, functional description and equations associated with their function are given in the order they are called:

| Name | Function | Equations (Sec. 2) |
|---|---|---|
| VENVEC | Given XLAT, XLON,† computes R1V, R2V | (1),(2),(3),(10) |
| SATVEC | Given XLIN, XELE, computes R1S | (4),(5) |
| RMTRX | Given R1V, R1S, R2V, computes R | (13),(14),(15),(24). |

When the image frame has been navigated, transformations between arbitrary image and planet coordinates are made with the subroutine

VENTRN(XLIN,XELE,XLAT,XLON,IDIR)

†These coordinates pairs are associated with each other.

where if

IDIR = 1,

(XLAT,XLON) → (XLIN,XELE) (Eq. 7);

if

IDIR = 2,

(XLIN,XELE) → (XLAT,XLON) (Eq. 8).

2. Multi-frame Mosaic Navigation

This section describes the procedure and format for entering the link/edge point measurements and constraint paths for a multiframe mosaic navigation. See also Section 3.

As indicated in the text of Section 3 and shown in FIGURES 3.2 and 3.3, distinct integer values NAVID, ILINK, INEDG are assigned to identify the frame number (FM-NAVID), the link point number (LP-ILINK) and the edge point number (EP-INEDG) for the configuration of image frames to be mosaic-navigated. The frame to serve as the reference frame may be arbitrarily chosen and for bookkeeping convenience should be assigned the value 1. In general

NAVID = 1, 2, 3, ..., total number of frames
ILINK = 1, 2, 3, ..., total number of link points
INEDG = 1, 2, 3, ..., total number of edge points.

After the assignment of the integer indices defined above, the constraint paths are determined. As stated in the main text, one complete iteration of the multiframe mosaic navigation starts with the navigation of the reference frame (by using a calculated guess of the sub-spacecraft image coordinates), then navigates a frame linked to it using the information supplied by the link point measurement, and proceeds in such a manner from frame to frame via link point measurements and terminates on an "edge point" frame. The half-angle subtended by the Venus image is calculated, subtracted from the actual half angle, squared and accumulated in the function S. The path of frames and link points used in the computation is called a constraint path. The procedure is repeated until all the edge point measurements have been utilized in the computation of S. The integer indices of the link points (ILINK) and edge points (INEDG) are stored in the order in which they are encountered along each constraint path in the one dimensional array, ICNSTR.

ICNSTR consists of K + 1 segments where K is the number of constraint paths used in the navigation. Letting $I_J$ be the index of ICNSTR which is the first value in the Jth segment, then

ICNSTR($I_J$) = number of link points in the Jth constraint path plus 1;

if there are N link points in this Jth constraint path, then

ICNSTR($I_J$ + 1) = ILINK for the 1st LP (link point),

ICNSTR($I_J$ + 2) = ILINK for the 2nd LP

.
.
.

ICNSTR($I_J$ + N) = ILINK for Nth LP,

ICNSTR($I_J$ + N + 1) = INEDG for Jth path.

If J = K, then

ICNSTR($I_K$ + N + 2) = 0,

and ICNSTR is terminated. (If J < K, then $I_J + N + 2 = I_{J+1}$, and a new segment or constraint path is begun.) Note that except for the last segment, the value of ICNSTR for the last element in each segment always equals an edge point number INEDG. Note also, that constraint paths need not start with the reference frame (except for the first constraint path); they may start with any navigated frame (frames through which previous constraint paths have passed). In fact, for the sake of computational efficiency, it is best to choose a navigated frame from which the minimal number of link points need be traversed to arrive at the edge point terminating the constraint path.

ICNSTR directly or indirectly references all the other arrays containing the information necessary for the navigation. These arrays and their definitions are:

IDCOR (1, ILINK) = NAVID of "link-from" frame
IDCOR (2, ILINK) = NAVID of "link-to" frame
IDEDG (INEDG) = NAVID of edge point, INEDG
ARYNAV (22, NAVID) = VENCOM (22)
common block associated with frame NAVID

$$\text{ARYCOR}\left(\begin{Bmatrix}1\\2\end{Bmatrix}, \text{ILINK}\right) = \begin{Bmatrix}\text{XLIN}\\\text{XELE}\end{Bmatrix} \text{ of link point, ILINK, of the "link-from" frame}$$

$$\text{ARYCOR}\left(\begin{Bmatrix}3\\4\end{Bmatrix}, \text{ILINK}\right) = \begin{Bmatrix}\text{XLIN}\\\text{XELE}\end{Bmatrix} \text{ of link point, ILINK, of the "link-to" frame}$$

$$\text{ARYEDG}\left(\begin{Bmatrix}1\\2\end{Bmatrix}, \text{INEDG}\right) = \begin{Bmatrix}\text{XLIN}\\\text{XELE}\end{Bmatrix} \text{ of edge point, INEDG.}$$

3. An Example

Correctly filling these arrays is actually quite a simple task. The array values in FIGURE A are those used in navigating the three-frame mosaic discussed in Section 3, and are associated with FIGURE 3.3 and TABLE 3.2.

```
ICNSTR(1)=1
ICNSTR(2)=1
ICNSTR(3)=2
ICNSTR(4)=1
ICNSTR(5)=2
ICNSTR(6)=2
ICNSTR(7)=2
ICNSTR(8)=3
ICNSTR(9)=1
ICNSTR(10)=4
ICNSTR(11)=1
ICNSTR(12)=5
ICNSTR(13)=0

IDCOR(1,1)=1
IDCOR(2,1)=2
IDCOR(1,2)=1
IDCOR(2,2)=3
ARYCOR(1,1)=641
ARYCOR(2,1)=199
ARYCOR(3,1)=57
ARYCOR(4,1)=181
ARYCOR(1,2)=641
ARYCOR(2,2)=199
ARYCOR(3,2)=197
ARYCOR(4,2)=276

IDEDG(1)=1
IDEDG(2)=2
IDEDG(3)=3
IDEDG(4)=3
IDEDG(5)=3
ARYEDG(1,1)=137
ARYEDG(2,1)=156
ARYEDG(1,2)=348
ARYEDG(2,2)=110
ARYEDG(1,3)=10
ARYEDG(2,3)=64
ARYEDG(1,4)=202
ARYEDG(2,4)=60
ARYEDG(1,5)=442
ARYEDG(2,5)=164
```

FIGURE A. Input Arrays Used for Venus Mosaic Navigation Discussed in Section 3 (refer to FIGURE 3.3 and TABLE 3.2).

From the constraint paths shown in FIGURE 3.3 and the rules discussed above, the definition of ICNSTR is apparent. The definitions of IDCOR and IDEDG also follow immediately from the figure; the definitions of ARYCOR and ARYEDG follow from the figure and TABLE 3.2.

ARYNAV is not shown here since it was discussed in detail in the first portion of this appendix, and because the VENCOM common blocks, which make up ARYNAV, are defined according to the convention used for the single-image-frame navigation program currently running on the McIDAS system.

The only remaining array not discussed is IDFRAM, which is used to define the "FRAMEIN" in the TABLES,

```
IDFRAM (NAVID) = frame (or reel) ID.
For TABLE 3.1,
    IDFRAM (NAVID) = NAVID;
For TABLE 3.2,
    IDFRAM (NAVID) = reel number associated with each
                     Mariner 10/JPL/SEDR data image tape.
```

IDFRAM merely provides labels and plays no direct role in the mosaic navigation.

# ON THE POSSIBILITY OF OBTAINING THE WIND FIELDS FROM GEOSYNCHRONOUS SATELLITE MEASUREMENTS OF TEMPERATURE AND MOISTURE PROFILES

Sanjay Limaye

ABSTRACT

The study proposes a method to determine the complete wind field in the domain of available continuous geosynchronous observations of temperature and moisture profiles. The wind components are deduced from advection equations and as such are more suitable as input to numerical weather simulation or prediction models. The application of such a technique, if proved feasible, would be valuable in oceanic areas where in situ observations are unavailable and even more valuable in clear areas where cloud-motion vectors as approximations to the ambient flow are also unavailable. The method draws upon the relative accuracy of temperature and moisture measurements and since the short term stability of the sensors is generally quite high the computed wind components are likely to be relatively accurate.

## 1. INTRODUCTION

The importance of the three dimensional wind field in atmospheric studies is widely recognized. Operationally only the horizontal part of the wind is measured on a routine basis in weather-related studies near the surface by wind anemometer and in the upper air by tracking balloons. Recently the cloud-motion vectors obtained from geosynchronous spacecraft data have been used as approximations to ambient wind (Smith et al., 1971; Suomi et al., 1969; Mosher, 1975). It has been the experience that in numerical models the raw wind observations have to be objectively analyzed first in order to remove the noise due to smaller scale motions which otherwise lead to unrealistic solutions for the larger scale motions. The method proposed is insensitive to small scale processes and thus is likely to be a better first guess for ambient wind field.

The lack of sufficient observing stations in remote land and oceanic areas results in wide gaps in the constructed global wind fields. To facilitate global weather prediction models a need for a

Global Observing System has been identified in the Global Atmospheric Research Program. An integral part of such a system would be a number of geosynchronous satellites distributed uniformly along the equator. These geosynchronous satellites would be advanced versions of the satellites now used in the Synchronous Meteorological Satellite series. Future satellites would have instruments to obtain vertical temperature and moisture profiles. The required wind field information will be supplied by the motion vectors of tracer clouds. One problem that arises here is that of the reference level: at what altitude do the cloud vectors resemble the ambient wind? It has become clear that there are wide gaps even in the cloud motion vector field, simply due to the lack of any tracer clouds. This can be seen in any typical visible image from a geosynchronous satellite.

The method proposed here offers an attractive solution to this problem: it would yield information about the three dimensional wind in cloudless regions as it is based upon satellite measurements of temperature and water vapor profiles. Recent experiments carried out on Nimbus 4 and 5 satellites such as SIRS and ITPR have already demonstrated the capability of such measurements (Smith, et al., 1970, 1972, 1973). The ambiguity in the reduction of the radiance measurements due to unknown amounts of cloud-covered area in the field of view of the instrument leads to an error in the profiles obtained below the clouds but it can be reduced if the amount of cloud cover is known (Smith et al. 1973). Thus it may be expected that, since the vertical atmospheric sounding capability of satellite-borne sensors is best in cloud-free regions, the wind field computed from geosynchronous observations would be more accurate in cloud-free regions. This wind field computation would also provide a valuable double check in cloudy regions where cloud motion vectors serve as wind observations.

## 2. THE PROPOSED TECHNIQUE

Atmospheric motions are directly measurable by remote sensing techniques only spectrometrically through the Doppler shift. Indirectly, however, wind inference is possible through the transports of various quantities which accompany it. The simple assumption that certain tracer clouds (small enough so their own sustaining circulation is a negligible perturbation on the large scale field) are carried more or less at the speed of the ambient wind allows one to obtain the wind field at the cloud from a time sequence of cloud images. Moisture has similarly been used as a tracer in global wind field analysis from 6.3$\mu$ band water vapor measurements from Nimbus-3 spacecraft (Steranka et al. 1973). Mancuso et al. (1973) have also proposed moisture as a tracer in obtaining wind field information. In fact, as far back as 1937 Rossby and his collaborators have studied advance of moisture patterns on isentropic charts.

Through the advective properties of wind and observations of the restructured spatial and temporal gradients of quantities that are advected it is possible to compute the ambient wind which caused the restructuring of the gradients, as shown here.

To analytically determine the three components of the wind three independent equations involving the three components of the wind and other observables are needed. The three dimensional wind is instrumental in advecting temperature, water vapor, and the lapse rate of temperature. All three quantities can be measured from satellite-based instruments. Three equations for the time rate or change of these quantities are:

$$\frac{d\theta}{dt} = \frac{\partial\theta}{\partial t} + u\frac{\partial\theta}{\partial x} + v\frac{\partial\theta}{\partial y} + w_\eta\frac{\partial\theta}{\partial\eta} \qquad (1)$$

$$\frac{d\gamma}{dt} = \frac{\partial\gamma}{\partial t} + u\frac{\partial\gamma}{\partial x} + v\frac{\partial\gamma}{\partial y} + w_\eta\frac{\partial\gamma}{\partial\eta} \qquad (2)$$

$$\frac{dq}{dt} = \frac{\partial q}{\partial t} + u\frac{\partial q}{\partial x} + v\frac{\partial q}{\partial y} + w_\eta\frac{\partial q}{\partial\eta} \qquad (3)$$

wherein $\theta$ is the potential temperature; u and v are the two horizontal components and $w_\eta = d\eta/dt$ is the vertical component of wind; $\gamma$ is the lapse rate of potential temperature; q is the specific humidity; $\eta$ is a generalized vertical coordinate. The horizontal gradients are evaluated on a constant $\eta$ surface normal to the unit vector in the $\eta$ direction. If $\eta \equiv z$ then the coordinate system reduces to the Cartesian coordinates. In Cartesian coordinates $w_\eta$ is the vertical component of the wind, with pressure as the vertical coordinate $w_\eta \equiv \omega = dp/dt$; with potential temperature as the vertical coordinate $w_\eta \equiv d\theta/dt$, i.e. the diabatic heating rate.

The space and local time derivatives can be easily obtained from geosynchronous satellite measurements. The total time derivatives which express the change following an air parcel in motion are not directly measurable. The changes are mainly due to the effects of diffusion and mixing as well as any diabatic processes; in some cases these are calculable. In any case over the time interval that is of concern here--about one hour--the total time derivatives are likely to be small.

Assuming for the time being that the total time derivatives can be independently specified, the three equations now contain only three unknowns. However, the equations represent changes following an air parcel whereas a satellite-borne sensor has a finite spatial resolution and the time interval between successive measurements is not insignificant; therefore the effects of smaller scale motions need to be properly accounted for. Over the smallest volume of the atmo-

sphere that can be resolved by the satellite-borne sensors the instantaneous value of the volume average, s, can be expressed as the sum of a time average $\bar{s}$ over the interval $\tau$ between two successive measurements and the deviation s' from it:

$$s = \bar{s} + s' \ .$$

Introducing this definition into the advection equation and taking the time average:

$$\overline{\frac{ds}{dt}} = \overline{\frac{\partial s}{\partial t}} + \overline{us_x} + \overline{vs_y} + \overline{ws_\eta} + \overline{w's_x'} + \overline{v's_y'} + \overline{w's_\eta'} \ .$$

The left had side expresses the mean time rate of change of a quantity s in a volume V over an interval $\tau$ and moving with a mean velocity with components $\bar{u}$, $\bar{v}$, and $\bar{w}$. The first term on the right hand side expresses the change in a fixed volume; the second, third, and fourth terms express the advection of the mean current; the last three terms represent contributions by the mean eddy terms. With the help of the mixing length theory the eddy terms may be expressed as

$$F_s = \frac{\partial}{\partial x}\left(K_x \frac{\partial s}{\partial x}\right) + \frac{\partial}{\partial y}\left(K_y \frac{\partial s}{\partial y}\right) + \frac{\partial}{\partial \eta}\left(K_\eta \frac{\partial s}{\partial \eta}\right)$$

$$= K_x \frac{\partial^2 s}{\partial x^2} + K_y \frac{\partial^2 s}{\partial y^2} + K_\eta \frac{\partial^2 s}{\partial \eta^2} \qquad (4)$$

if the eddy diffusivities $K_x$, $K_y$, and $K_\eta$ corresponding to the quantity s are assumed as space constants. Thus the contribution $F_s$ due to the eddy terms can also be evaluated from the satellite measurements of the quantity s. It is thus possible to obtain the space time averaged components of the wind if provision is made for the eddy terms in the advection equations:

$$\frac{d\theta}{dt} = \frac{\partial \theta}{\partial t} + u\frac{\partial \theta}{\partial x} + v\frac{\partial \theta}{\partial y} + w\frac{\partial \theta}{\partial \eta} + F_\theta \qquad \text{etc.}$$

where the horizontal bars denoting time average have been dropped.

The choice of a particular vertical coordinate may have certain advantages over others, depending on the observations. The solutions with height, pressure, and potential temperature as vertical coordinate are given next.

Solution in Cartesian Coordinates

With $\eta \equiv z$, $w = dz/dt$ and is the vertical component of velocity

in Cartesian coordinates. The horizontal gradients are obtained in this case on a level surface.

The three equations can be written for any particular level resolvable by the satellite borne sensors in the atmosphere; thus a solution of these equations for various levels in the atmosphere would yield the complete three dimensional three component-wind-field.

The three equations can be written in a matrix form:

$$\begin{bmatrix} \frac{d\theta}{dt} - \frac{\partial\theta}{\partial t} - F_\theta \\ \frac{d\gamma}{dt} - \frac{\partial\gamma}{\partial t} - F_\gamma \\ \frac{dq}{dt} - \frac{\partial q}{\partial t} - F_q \end{bmatrix} = \begin{bmatrix} \frac{\partial\theta}{\partial x} & \frac{\partial\theta}{\partial y} & \frac{\partial\theta}{\partial z} \\ \frac{\partial\gamma}{\partial x} & \frac{\partial\gamma}{\partial y} & \frac{\partial\gamma}{\partial z} \\ \frac{\partial q}{\partial x} & \frac{\partial q}{\partial y} & \frac{\partial q}{\partial z} \end{bmatrix} * \begin{bmatrix} u \\ v \\ w \end{bmatrix} \tag{5}$$

The three components of the wind are then easily obtainable:

$$\begin{bmatrix} u \\ v \\ w \end{bmatrix} = \begin{bmatrix} \frac{\partial\theta}{\partial x} & \frac{\partial\theta}{\partial y} & \frac{\partial\theta}{\partial z} \\ \frac{\partial\gamma}{\partial x} & \frac{\partial\gamma}{\partial y} & \frac{\partial\gamma}{\partial z} \\ \frac{\partial q}{\partial x} & \frac{\partial q}{\partial y} & \frac{\partial q}{\partial z} \end{bmatrix}^{-1} * \begin{bmatrix} \frac{d\theta}{dt} - \frac{\partial\theta}{\partial t} - F_\theta \\ \frac{d\gamma}{dt} - \frac{\partial\gamma}{\partial t} - F_\gamma \\ \frac{dq}{dt} - \frac{\partial q}{\partial t} - F_q \end{bmatrix} \tag{6}$$

The inverse of the coefficient matrix exists as long as the matrix is not ill-conditioned and can be shown to be:

$$\frac{\begin{bmatrix} \frac{\partial\gamma}{\partial y}\frac{\partial q}{\partial z} - \frac{\partial\gamma}{\partial z}\frac{\partial q}{\partial y} & \frac{\partial\theta}{\partial z}\frac{\partial q}{\partial y} - \frac{\partial\theta}{\partial y}\frac{\partial q}{\partial z} & \frac{\partial\theta}{\partial y}\frac{\partial\gamma}{\partial z} - \frac{\partial\theta}{\partial z}\frac{\partial\gamma}{\partial y} \\ \frac{\partial\gamma}{\partial z}\frac{\partial q}{\partial x} - \frac{\partial\gamma}{\partial x}\frac{\partial q}{\partial z} & \frac{\partial\theta}{\partial x}\frac{\partial q}{\partial z} - \frac{\partial\theta}{\partial z}\frac{\partial q}{\partial x} & \frac{\partial\theta}{\partial z}\frac{\partial\gamma}{\partial x} - \frac{\partial\theta}{\partial x}\frac{\partial\gamma}{\partial z} \\ \frac{\partial\gamma}{\partial x}\frac{\partial q}{\partial y} - \frac{\partial\gamma}{\partial y}\frac{\partial q}{\partial x} & \frac{\partial\theta}{\partial y}\frac{\partial q}{\partial x} - \frac{\partial\theta}{\partial x}\frac{\partial q}{\partial y} & \frac{\partial\theta}{\partial x}\frac{\partial\gamma}{\partial y} - \frac{\partial\theta}{\partial y}\frac{\partial\gamma}{\partial x} \end{bmatrix}}{\frac{\partial\theta}{\partial x}\left[\frac{\partial\gamma}{\partial y}\frac{\partial q}{\partial z} - \frac{\partial\gamma}{\partial z}\frac{\partial q}{\partial y}\right] + \frac{\partial\theta}{\partial y}\left[\frac{\partial\gamma}{\partial x}\frac{\partial q}{\partial z} - \frac{\partial\gamma}{\partial z}\frac{\partial q}{\partial x}\right] + \frac{\partial\theta}{\partial z}\left[\frac{\partial\gamma}{\partial x}\frac{\partial q}{\partial y} - \frac{\partial\gamma}{\partial y}\frac{\partial q}{\partial x}\right]}$$

It is clear that the accuracy with which the three wind components can be determined is ultimately limited by errors in spatial gradients of temperature, moisture, and the lapse rate. Appendix I contains an error

analysis which indicates to what degree of accuracy the spatial and temporal gradients must be known in the worst possible case to obtain the horizontal wind components with 1 $m \cdot s^{-1}$ accuracy. The required resolutions for temperature measurements are comparable to those currently achievable from instruments such as the Vertical Temperature Profile Radiometer (VTPR) on board NIMBUS-5 (Smith et al., 1974) and should be obtainable from geosynchronous satellites.

## Solution in Isobaric Coordinates

With $\eta \equiv p$, the vertical component of the wind becomes $\omega = dp/dt$; u and v, as well as the horizontal gradients, now refer to an isobaric surface rather than a level surface. The form of the solution is identical to the Cartesian case. The lapse rate of the potential temperature can now be expressed with respect to pressure:

$$\gamma = \frac{\partial \theta}{\partial p}$$

and, as derived in Appendix 2,

$$\frac{d\gamma}{dt} = \frac{d}{dt}\left(\frac{\partial \theta}{\partial p}\right) = \frac{d\theta}{dt}\left[\frac{\partial \ln T}{\partial p} - \frac{1}{p}\right] + \frac{dp}{dt}\left[\frac{\theta(1-\kappa)^2}{p^2}\right] . \qquad (7)$$

Thus with pressure as the vertical coordinate the total change of lapse rate of potential temperature can be directly expressed through the diabatic term $d\theta/dt$, and the change in the lapse rate due to the vertical motion can be properly accounted for.

The lapse rate advection may be rewritten as:

$$\left[\frac{\partial(\ln T)}{\partial p} - \frac{1}{p}\right]\frac{d\theta}{dt} = \frac{\partial \gamma}{\partial t} + u\frac{\partial \gamma}{\partial x} + v\frac{\partial \gamma}{\partial y} + \omega\left[\frac{\partial \gamma}{\partial p} - \frac{\theta(1-\kappa)^2}{p^2}\right]. \qquad (8)$$

If the equivalent potential temperature is used instead of the potential temperature itself the effects of latent heat release are also accounted for in the above equation. However if a large amount of moisture is present, i.e. if the air is saturated or close to saturation, then the water vapor equation would have to be replaced by that for total water content. The observations of the total water content may be possible by microwave measurements (Savage, 1975).

The use of pressure as the vertical coordinate thus simplifies the form of the advection equation for the lapse rate of potential

temperature. In this case the quality of the computed wind components can be checked through the use of the isobaric continuity equation:

$$-\left(\frac{\partial u}{\partial x}+\frac{\partial v}{\partial y}\right)=\frac{\partial \omega}{\partial p}\ . \tag{9}$$

Integration of (9) between two isobaric surfaces yields an independent estimate of $\omega$ or, equivalently, the computed magnitude of the isobaric divergence can be checked against that required by the continuity equation.

Solution in Isentropic Coordinates

In isentropic coordinates the vertical component $w_\eta = d\theta/dt$, i.e. it is the diabatic term. The horizontal components u and v are now obtained on a constant potential surface. If the slope of this surface is known, it is possible to obtain the Cartesian vertical velocity. The use of pressure as one "tracer" property instead of the lapse rate of potential temperature and the use of the Montgomery Stream function [$M = C_p T + gz$] would complete the set of three required equations. The two velocity components u and v, along a constant $\theta$ surface, and the diabatic term $d\theta/dt$ are the principal unknowns:

$$\omega=\frac{dp}{dt}=\frac{\partial p}{\partial \theta}+u\frac{\partial p}{\partial x}+v\frac{\partial p}{\partial y}+\frac{d\theta}{dt}\frac{\partial p}{\partial \theta}+F_p\ , \tag{10}$$

$$\frac{dM}{dt}=\frac{\partial M}{\partial t}+u\frac{\partial M}{\partial x}+v\frac{\partial M}{\partial y}+\frac{d\theta}{dt}\frac{\partial M}{\partial \theta}+F_M\ , \tag{11}$$

and

$$\frac{dq}{dt}=\frac{\partial q}{\partial t}+u\frac{\partial q}{\partial x}+v\frac{\partial q}{\partial y}+\frac{d\theta}{dt}\frac{\partial q}{\partial \theta}+F_q\ . \tag{12}$$

The difficulty here is that $\omega$ (= dp/dt) needs to be independently specified. Use can be made here of the Poisson equation relating pressure to the potential temperature $\theta$ and temperature at that pressure:

$$\theta = T\left(\frac{p_o}{p}\right)^{\kappa} \tag{13}$$

where $\kappa = R/C_p$, the ratio of the gas constant and specific heat at constant pressure for air, so that

$$p = p_o\left(\frac{T}{\theta}\right)^{1/\kappa}$$

and upon logarithmic differentiation:

$$\frac{dp}{dt}=\frac{p}{\kappa}\left[\frac{1}{T}\frac{dT}{dt}-\frac{1}{\theta}\frac{d\theta}{dt}\right] \tag{14}$$

dT/dt can be expressed through the advection equation:

$$\frac{dT}{dt} = \frac{\partial T}{\partial t} + u\frac{\partial T}{\partial x} + v\frac{\partial T}{\partial y} + \frac{d\theta}{dt}\frac{\partial T}{\partial \theta} + F_T \quad . \tag{15}$$

On substituting in Eq. 10:

$$u\left(\frac{p}{\kappa T}\frac{\partial T}{\partial x} - \frac{\partial p}{\partial x}\right) + v\left(\frac{p}{\kappa T}\frac{\partial T}{\partial y} - \frac{\partial p}{\partial y}\right) + \frac{d\theta}{dt}\left(\frac{p}{\kappa T}\frac{\partial T}{\partial \theta} - \frac{\partial p}{\partial \theta}\right) =$$

$$\left[\frac{p}{\kappa T}\frac{\partial T}{\partial t} - \frac{\partial p}{\partial t} + F_T - F_p\right] \quad . \tag{16}$$

Herein $F_T$ and $F_p$ represent the contribution due to eddy motions, however the validity of the mixing length theory in the computation of $F_p$ is unclear. In practice the terms such as $\left(\frac{p}{\kappa T}\frac{\partial T}{\partial x} - \frac{\partial p}{\partial x}\right)$ may be very small and may make evaluation of the three unknowns u, v, and $d\theta/dt$ rather difficult. There is an alternate formulation of the solution possible, however, which will allow computation of the two wind components on a constant potential temperature surface.

An Alternate Solution in Isentropic Coordinates

The Bernoulli equation can be written as:

$$\frac{dQ}{dt} = \frac{d}{dt}[K + M] - \left(\frac{\partial M}{\partial t}\right)_\theta - D \tag{17}$$

where K = kinetic energy per unit mass
M = dry static energy or the Montgomery function = $C_p T + gz$,
D = frictional energy dissipation rate, and
Q = amount of heat added or extracted from the system; thus,

$$\frac{dQ}{dt} = C_p \frac{T}{\theta}\frac{d\theta}{dt} \quad . \tag{18}$$

The hydrostatic equation with $\theta$ as the vertical coordinate becomes $\partial M/\partial\theta = C_p(T/\theta)$, so that for frictionless flow:

$$C_p \frac{T}{\theta}\frac{d\theta}{dt} = \frac{d}{dt}(K + M) - \left(\frac{\partial M}{\partial t}\right)_\theta = \frac{dK}{dt} + u\frac{\partial M}{\partial x} + v\frac{\partial M}{\partial y} + \frac{d\theta}{dt}\frac{\partial M}{\partial \theta} \tag{19}$$

or,

$$0 = u\frac{\partial M}{\partial x} + v\frac{\partial M}{\partial y} + \frac{dK}{dt} \quad .$$

In the lower troposphere the changes in kinetic energy are smaller than those in the dry static energy per unit mass so that:

$$u\frac{\partial M}{\partial x} + v\frac{\partial M}{\partial y} \doteq 0 \quad .$$

Allowing as before for contribution due to eddy motions in view of the application to satellite measurements, the advection equation for the dry static energy becomes:

$$u \frac{\partial M}{\partial x} + v \frac{\partial M}{\partial y} + F_M = 0 \ .$$

The second advection equation available is that for the specific moisture content:

$$\frac{dq}{dt} = \frac{\partial q}{\partial t} + u \frac{\partial q}{\partial x} + v \frac{\partial q}{\partial y} + \frac{d\theta}{dt} \frac{\partial q}{\partial \theta} + F_q \ . \tag{20}$$

Thus:

$$\begin{pmatrix} \frac{d\theta}{dt} C_p \frac{T}{\theta} - \frac{\partial M}{\partial \theta} - F_M \\ \frac{dq}{dt} - \frac{\partial q}{\partial t} - \frac{d\theta}{dt} \frac{\partial q}{\partial \theta} - F_q \end{pmatrix} = \begin{pmatrix} \frac{\partial M}{\partial x} & \frac{\partial M}{\partial y} \\ \frac{\partial q}{\partial x} & \frac{\partial q}{\partial y} \end{pmatrix} \begin{pmatrix} u \\ v \end{pmatrix} \tag{21}$$

or

$$u = \left(\frac{\partial M}{\partial x} \frac{\partial q}{\partial y} - \frac{\partial M}{\partial y} \frac{\partial q}{\partial x}\right)^{-1} \left\{\frac{\partial q}{\partial y}\left[\frac{d\theta}{dt}\left(C_p \frac{T}{\theta} - \frac{\partial M}{\partial \theta}\right) - F_M\right] + \frac{\partial M}{\partial y}\left(\frac{d\theta}{dt} \frac{\partial q}{\partial \theta} - \frac{\partial q}{\partial t} - F_q\right)\right\} \tag{22}$$

and

$$v = \left(\frac{\partial M}{\partial x} \frac{\partial q}{\partial y} - \frac{\partial M}{\partial y} \frac{\partial q}{\partial x}\right)^{-1} \left\{\frac{\partial q}{\partial x}\left[\frac{d\theta}{dt}\left(\frac{\partial M}{\partial \theta} - C_p \frac{T}{\theta}\right) + F_M\right] - \frac{\partial M}{\partial x}\left(\frac{d\theta}{dt} \frac{\partial q}{\partial \theta} + F_q + \frac{\partial q}{\partial t} - \frac{dq}{d\theta}\right)\right\} \ . \tag{23}$$

Under the hydrostatic assumption $\partial M/\partial \theta = C_p(T/\theta)$, with no diabatic processes allowed $d\theta/dt = 0$. Upon restricting the solution to layers of the atmosphere removed from the air/water interface the solution simplifies to:

$$u = \left(\frac{\partial M}{\partial x} \frac{\partial q}{\partial y} - \frac{\partial M}{\partial y} \frac{\partial q}{\partial x}\right)^{-1} \left\{\frac{\partial q}{\partial y} F_M - \frac{\partial M}{\partial y}\left(\frac{\partial q}{\partial t} + F_q\right)\right\}$$

and

$$v = \left(\frac{\partial M}{\partial x} \frac{\partial q}{\partial y} - \frac{\partial M}{\partial y} \frac{\partial q}{\partial x}\right)^{-1} \left\{\frac{\partial q}{\partial x} F_M - \frac{\partial M}{\partial x}\left(F_q + \frac{\partial q}{\partial t}\right)\right\} \ .$$

Once again, u and v are the wind components on a constant potential temperature surface and the horizontal gradients are also evaluated on this surface.

## 3. DISCUSSION

In the previous section it was shown how the three wind components could be obtained from temperature, moisture and lapse rate (of potential temperature) information. It was seen that the solution is easy to obtain if the flow is assumed to be adiabatic, frictionless, hydrostatic, and conserving the water vapor content or liquid water content (if measurements of latter are directly obtainable from measurements such as in the passive microwave region of the spectrum [see Savage, 1975]). Under these assumptions the three-dimensional wind is obtained from the changes that it causes in the three-dimensional fields of lapse rate, potential temperature, and water content.

The adiabatic flow assumption can be relaxed if the total heating rate can be independently specified. The mechanisms responsible for causing heating or cooling are (1) absorption of solar radiation, (2) cooling due to loss of long wave radiation to space, and (3) release of latent heat during phase changes. The heating rate can be obtained through the vertical divergence of the net flux:

$$\frac{\partial T}{\partial t} = \rho C_p \frac{\partial F_N}{\partial p}$$

where $F_N$ = net total radiation flux.

The net solar flux depends on the solar angle, the type and amount of cloudiness, and the distribution of aerosols. The net long wave flux is determined by the vertical temperature structure, amount and type of clouds, and water vapor distribution.

From a geosynchronous satellite, infrared and visible images of earth are expected to be available along with the temperature and moisture profile information. It may then be possible to estimate the heating rate through a knowledge of the amount and type of cloud cover and temperature and moisture profiles (see Cox, 1967); this would be necessary if the adiabatic flow assumption is seen to break down.

The total time rate of change of specific moisture content presents fewer problems; its change results in growth or decay of clouds. If the application is restricted to cloud-free regions larger than the air trajectory lengths over the interval between measurements then this term is zero, except in the boundary layer where evaporation of moisture into the air is possible.

Lastly one important point needs to be made about the total time rate of change of various quantities. They are Lagrangian quantities and hence can be computed only if the air trajectories are known.

Krishnamurti (1969) and Mathur (1969) discuss schemes for calculating such quantities. In the present case, however, trajectory information is what is essentially being determined. It is clear that in cases where the Lagrangian terms cannot be neglected in obtaining the wind components (as would be immediately evidenced by diagnostic equations such as the equation of continuity) the solution would have to be obtained by iteration wherein the first guess solution would be that obtained under the adiabatic assumption.

## 4. SUMMARY

It has been shown that under the adiabatic assumption it is possible to compute the wind components which represent average values over the resolution limit of satellite observation of temperature and moisture profiles from a geosynchronous platform in cloud-free regions. The application in areas of limited cloud cover with evolving clouds is possible as long as independent estimates of the Lagrangian time rate of change of moisture content or profiles of water content are available. The solution with pressure as the vertical coordinate is more attractive than the Cartesian coordinates since the Lagrangian rate of change of lapse rate of potential temperature can be more easily specified.

With potential temperature as the vertical coordinate two alternate solutions seem possible. In one the use of pressure as a tracer quantity allows a computation of the Lagrangian heating rate which happens in this case to be the third 'wind component.' In the second case the solution obtained allows computation of the wind components along a constant potential surface only.

The general technique proposed herein is best suited for application in cloud free oceanic regions where observations are scarce and wind estimates from cloud motions are also unavailable due to a scarcity of tracer clouds. In the near future the pertinent measurements--those of profiles of temperature and moisture and possibly of total water substance--are expected to be available with high enough resolution from geosynchronous platforms. If feasible the proposed technique would help fulfill the needs of the global weather simulation and prediction models.

## REFERENCES

Cox, S. K., 1967: A Radiational Model in Which the Effects of Clouds are Simulated from Moisture and Temperature Parameters. Ph.D. Thesis, University of Wisconsin, Madison.

Krishnamurti, T. N., 1969: An Experiment in Numerical Prediction in the Equatorial Latitudes. Quart. J. Roy. Meteor. Soc., (95), 594-620.

Mancuso, R. M., R. L. Endlich, and R. E. Nagle, 1972: A Proposed Method for Determining Winds in Cloud-Free Regions by Isentropic Analysis of Temperature and Water Vapor Profiles. Journ. Appl. Meteor., (11), 1019-1021.

Mathur, M. B., 1969: A Note on Quasi-Lagrangian Advective Scheme for Primitive Equations. Report No. 69-5, Florida State University, Tallahassee.

Rossby, C. G., D. P. Keily, J. W. W. Osmun, J. Holmboe, A. F. Spilhaus, 1937: Aerological Evidence of Large-scale Mixing in the Atmosphere. Trans. of Amer. Geophys. Union, 130-136.

Savage, R., 1975: Detection of Hydrometeors by Passive Microwaves. Ph.D. Thesis, University of Wisconsin, Madison.

Smith, E. A., and D. R. Phillips, 1971: Automated Cloud Tracking Using Precisely Aligned Digital ATS Pictures. Proc. Two-Dimensional Digital Signal Processing Cont. Columbia, Mo., IEEE Computer Soc., 10-2-1 to 10-2-20.

Smith, W. L., H. M. Woolf and W. J. Jacob, 1970: A Regression Method for Obtaining Realtime Temperature and Geopotential Height Profiles from Satellite Spectrometer Measurements and its Application to Nimbus 3 SIRS Observations. Mon. Wea. Rev., (98), 532-603.

_____, and H. B. Howell, 1971: Vertical Distribution of Atmospheric Water vapor from Satellite Infrared Spectrometer Measurements. J. Appl. Meteor., (10), 1026-1034.

_____, H. M. Woolf, and H. E. Fleming, 1972: Retrieval of Atmospheric Temperature Profiles from Satellite Measurements for Dynamical Forecasting. J. Appl. Meteor., (11), 113-122.

_____, D. T. Hilleary, J. C. Fischer, H. B. Howell, and H. M. Woolf, 1974: Nimbus 5 ITPR Experiment, Applied Optics, (13), 499-505.

Steranka, J., L. J. Allison, and V. V. Solomonson, 1973: Application of Nimbus 4 THIR 6.7μ Observations to Regional and Global Moisture and Wind Field Analyses. J. Appl. Meteor., (12), 386-395.

Suomi, V. E. and R. J. Parent, 1968: A Color View of Planet Earth. Bull. Amer. Meteor. Soc., (49), 74-75.

## APPENDIX 1

The solution for the wind components has been shown to be:

$$\begin{bmatrix} u \\ v \\ w \end{bmatrix} = \frac{1}{A} \begin{bmatrix} \frac{\partial\gamma}{\partial y}\frac{\partial q}{\partial z} - \frac{\partial\gamma}{\partial z}\frac{\partial q}{\partial y} & \frac{\partial\theta}{\partial z}\frac{\partial q}{\partial y} - \frac{\partial\theta}{\partial y}\frac{\partial q}{\partial z} & \frac{\partial\theta}{\partial y}\frac{\partial\gamma}{\partial z} - \frac{\partial\theta}{\partial z}\frac{\partial\gamma}{\partial y} \\ \frac{\partial\gamma}{\partial z}\frac{\partial q}{\partial x} - \frac{\partial\gamma}{\partial x}\frac{\partial q}{\partial z} & \frac{\partial\theta}{\partial x}\frac{\partial q}{\partial z} - \frac{\partial\theta}{\partial z}\frac{\partial q}{\partial x} & \frac{\partial\theta}{\partial z}\frac{\partial\gamma}{\partial x} - \frac{\partial\theta}{\partial x}\frac{\partial\gamma}{\partial z} \\ \frac{\partial\gamma}{\partial x}\frac{\partial q}{\partial y} - \frac{\partial\gamma}{\partial y}\frac{\partial q}{\partial x} & \frac{\partial\theta}{\partial y}\frac{\partial q}{\partial x} - \frac{\partial\theta}{\partial x}\frac{\partial q}{\partial y} & \frac{\partial\theta}{\partial x}\frac{\partial\gamma}{\partial y} - \frac{\partial\theta}{\partial y}\frac{\partial\gamma}{\partial x} \end{bmatrix}$$

where

$$A = \frac{\partial\theta}{\partial x}\left[\frac{\partial\gamma}{\partial y}\frac{\partial q}{\partial z} - \frac{\partial\gamma}{\partial z}\frac{\partial q}{\partial y}\right] + \frac{\partial\theta}{\partial y}\left[\frac{\partial\gamma}{\partial x}\frac{\partial q}{\partial z} - \frac{\partial\gamma}{\partial z}\frac{\partial q}{\partial x}\right] + \frac{\partial\theta}{\partial z}\left[\frac{\partial\gamma}{\partial x}\frac{\partial q}{\partial y} - \frac{\partial\gamma}{\partial y}\frac{\partial q}{\partial x}\right] .$$

The error possible in the wind components can be expressed as:

$$\Delta[\ ] = \frac{1}{A}\Delta[\qquad] + [\qquad]\Delta\left(\frac{1}{A}\right)$$

or, specifically for the u-component of the wind by:

$$\Delta U = \frac{1}{A}\left\{\left(\frac{d\theta}{dt} - \frac{\partial\theta}{\partial t}\right) * \Delta\left[\frac{\partial\gamma}{\partial y}\frac{\partial q}{\partial z} - \frac{\partial\gamma}{\partial z}\frac{\partial q}{\partial y}\right] + \left[\frac{\partial\gamma}{\partial y}\frac{\partial q}{\partial z} - \frac{\partial\gamma}{\partial z}\frac{\partial q}{\partial y}\right] * \Delta\left[\frac{d\theta}{dt} - \frac{\partial\theta}{\partial t}\right]\right\} +$$

$$\frac{1}{A}\left\{\left(\frac{d\gamma}{dt} - \frac{\partial\gamma}{\partial t}\right) * \Delta\left[\frac{\partial\theta}{\partial z}\frac{\partial q}{\partial y} - \frac{\partial\theta}{\partial y}\frac{\partial q}{\partial z}\right] + \left[\frac{\partial\theta}{\partial z}\frac{\partial q}{\partial y} - \frac{\partial\theta}{\partial y}\frac{\partial q}{\partial z}\right] * \Delta\left[\frac{d\gamma}{dt} - \frac{\partial\gamma}{\partial t}\right]\right\} +$$

$$\frac{1}{A}\left\{\left(\frac{dq}{dt} - \frac{\partial q}{\partial t}\right) * \Delta\left[\frac{\partial\theta}{\partial y}\frac{\partial\gamma}{\partial z} - \frac{\partial\theta}{\partial z}\frac{\partial\gamma}{\partial y}\right] + \left[\frac{\partial\theta}{\partial y}\frac{\partial\gamma}{\partial z} - \frac{\partial\theta}{\partial z}\frac{\partial\gamma}{\partial y}\right] * \Delta\left[\frac{dq}{dt} - \frac{\partial q}{\partial t}\right]\right\} +$$

$$\left\{\left(\frac{d\theta}{dt} - \frac{\partial\theta}{\partial t}\right) * \left[\frac{\partial\gamma}{\partial y}\frac{\partial q}{\partial z} - \frac{\partial\gamma}{\partial z}\frac{\partial q}{\partial y}\right] + \left(\frac{d\gamma}{dt} - \frac{\partial\gamma}{\partial t}\right) * \left(\frac{\partial\theta}{\partial z}\frac{\partial q}{\partial y} - \frac{\partial\theta}{\partial y}\frac{\partial q}{\partial z}\right)\right.$$

$$\left. + \left(\frac{dq}{dt} - \frac{\partial q}{\partial t}\right) * \left(\frac{\partial\theta}{\partial y}\frac{\partial\gamma}{\partial z} - \frac{\partial\theta}{\partial z}\frac{\partial\gamma}{\partial y}\right)\right\} * \frac{\Delta A}{(-A^2)} .$$

wherein,

$$\Delta A = \Delta \left[ \frac{\partial \theta}{\partial x} \left( \frac{\partial \gamma}{\partial y} \frac{\partial q}{\partial z} - \frac{\partial \gamma}{\partial z} \frac{\partial q}{\partial y} \right) + \frac{\partial \theta}{\partial y} \left( \frac{\partial \gamma}{\partial x} \frac{\partial q}{\partial z} - \frac{\partial \gamma}{\partial z} \frac{\partial q}{\partial x} \right) + \frac{\partial \theta}{\partial z} \left( \frac{\partial \gamma}{\partial x} \frac{\partial q}{\partial y} - \frac{\partial \gamma}{\partial y} \frac{\partial q}{\partial x} \right) \right]$$

The order of magnitude of maximum error possible in the wind components can be estimated using representative values of the space and time derivatives of $\theta$, $\gamma$ and q.

In view of the fact that the proposed technique is likely to be more useful over tropical oceans,the representative values of the various terms have been taken from observations made during the Barbados Oceanic and Meteorological Experiment (BOMEX), conducted in 1969 in the Carribean. The horizontal gradients of temperature, moisture, etc. are easily obtained as the four ships involved in the experiment were stationed at the corners of a square about 500 km on a side during the first three phases of the experiment. The observations were normally taken every three hours and every 90 min on some days (BOMEX Data Set, 1974). Estimates of the uncertaintities in the satellite determinations of these quantities is a little difficult since no such observations from geosynchronous platforms are available as yet. Hence the results of some of the experiments on spacecraft in the Nimbus and NOAA series are used as guidelines. It is clear, however, that especially in cloud-free areas the relative accuracy of the satellite measurements and derived quantities is likely to be much higher than the accuracy of the absolute measurement. It is only the relative accuracy which is of any consequence here.

The u-component is then seen to be:

$$u = \left\{ \left( \frac{d\theta}{dt} - \frac{\partial \theta}{\partial t} \right)^{10^{-5}} * \left[ \frac{\partial \gamma}{\partial y}^{10^{-}} \frac{\partial q}{\partial z}^{10^{-8}} - \frac{\partial \gamma}{\partial z}^{10^{-10}} \frac{\partial q}{\partial y}^{10^{-11}} \right] + \left( \frac{d\gamma}{dt} - \frac{\partial \gamma}{\partial t} \right)^{0} * \left[ \frac{\partial \theta}{\partial z}^{10^{-8}} \frac{\partial q}{\partial y}^{10^{-9}} - \frac{\partial \theta}{\partial y}^{10^{-10}} \frac{\partial q}{\partial z}^{10^{-4}} \right] + \left( \frac{dq}{dt} - \frac{\partial q}{\partial t} \right)^{10^{-13}} * \left[ \frac{\partial \theta}{\partial y}^{10^{-9}} \frac{\partial \gamma}{\partial z}^{10^{-10}} - \frac{\partial \theta}{\partial z}^{10^{-4}} \frac{\partial \gamma}{\partial y}^{10^{-13}} \right] \right\} * \frac{1}{A}$$

$$= \frac{10^{-26} + 10^{-27} - 10^{-25}}{A} = 10^{-25}/A \text{ cm} \cdot \text{s}^{-1}$$

TABLE: REPRESENTATIVE VALUES FOR GRADIENTS AND TIME DERIVATIVES OF $\theta$, $\gamma$, AND $dq/dt$ (as obtained from observations during BOMEX)

| | | | | Error |
|---|---|---|---|---|
| TEMPERATURE | $\frac{\partial\theta}{\partial z}$ | $\sim 1°C\cdot(100\ m)^{-1}$ | $= 10^{-4}\ °C\cdot cm^{-1}$ | $\pm 10^{-5}\ °C\cdot cm^{-1}$ |
| | $\frac{\partial\theta}{\partial x} = \frac{\partial\theta}{\partial y}$ | $\sim 1°C\cdot(100\ km)^{-1}$ | $= 10^{-7}\ °C\cdot cm^{-1}$ | $\pm 10^{-9}\ °C\cdot cm^{-1}$ |
| | $\frac{d\theta}{dt} - \frac{\partial\theta}{\partial t}$ | $\sim 1°C\cdot(24\ hrs)^{-1}$ | $\simeq 10^{-5}\ °C\cdot s^{-1}$ | $\pm 10^{-5} °C\cdot s^{-1}$ |
| LAPSE RATE | $\frac{\partial\gamma}{\partial z}$ | $\sim \frac{0.1°C\cdot(100\ m)^{-1}}{1000\ m}$ | $= 10^{-10}\ °C\cdot cm^{-2}$ | $\pm 10^{-11}\ °C\cdot cm^{-2}$ |
| | $\frac{\partial\gamma}{\partial x} = \frac{\partial\gamma}{\partial y}$ | $\sim \frac{0.1°C\cdot(100\ m)^{-1}}{1000\ km}$ | $= 10^{-13}\ °C\cdot cm^{-2}$ | $\pm 10^{-14}\ °C\cdot cm^{-1}$ |
| | $\frac{d\gamma}{dt} - \frac{\partial\gamma}{\partial y}$ | $\approx 0$ | $\frac{0.1°C\cdot(100\ m)^{-1}}{3\ hrs}$ | $10^{-9}\ °C\cdot cm^{-1}\cdot s^{-1}$ |
| MOISTURE | $\frac{\partial q}{\partial x} = \frac{\partial q}{\partial y}$ | $\sim \frac{1\ gm\cdot kg^{-1}}{1000\ km}$ | $\simeq 10^{-11}\ cm^{-1}$ | $10^{-11}\ cm^{-1}$ |
| | $\frac{\partial q}{\partial z}$ | $\sim \frac{1\ gm\cdot kg^{-1}}{1000\ m}$ | $\simeq 10^{-8}\ cm^{-1}$ | $10^{-9}\ cm^{-1}$ |
| | $\frac{dq}{dt} - \frac{\partial q}{\partial t}$ | $\sim \frac{1\ gm\cdot kg^{-1}}{24\ hrs}$ | $\sim 10^{-8}\ s^{-1}$ | $10^{-9}\ s^{-1}$ |

$$A = \underbrace{10^{-7}(10^{-13}\ 10^{-8}\ 10^{-10}\ 10^{-11})}_{\frac{\partial\theta}{\partial x}\left(\frac{\partial\gamma}{\partial y}\ \frac{\partial q}{\partial z} - \frac{\partial\gamma}{\partial z}\ \frac{\partial q}{\partial y}\right)} + \underbrace{10^{-7}(10^{-13}\ 10^{-8}\ 10^{-10}\ 10^{-11})}_{\frac{\partial\theta}{\partial y}\left(\frac{\partial\gamma}{\partial z}\ \frac{\partial q}{\partial x} - \frac{\partial q}{\partial z}\ \frac{\partial\gamma}{\partial x}\right)} +$$

$$\underbrace{10^{-4}(10^{-13}\ 10^{-11}\ 10^{-13}\ 10^{-11})}_{\frac{\partial\theta}{\partial z}\left(\frac{\partial\gamma}{\partial x}\ \frac{\partial q}{\partial y} - \frac{\partial\gamma}{\partial y}\ \frac{\partial q}{\partial x}\right)}$$

$$\doteq 10^{-4}\cdot 10^{-13}\cdot 10^{-11} = 10^{-28}$$

$$\rightarrow u = 10^{-25}/10^{-28} = 10^{3}\ \text{cm}\cdot\text{s}^{-1}$$

$$= 10\ \text{m}\cdot\text{s}^{-1}$$

It is seen that the leading term in the numerator is $\left(\frac{dq}{dt} - \frac{\partial q}{\partial t}\right) * - \left[\frac{\partial\theta}{\partial z}\ \frac{\partial\gamma}{\partial y}\right]$ and in the denominator the leading term is $\frac{\partial\theta}{\partial z}\left(\frac{\partial\gamma}{\partial x}\ \frac{\partial q}{\partial y} - \frac{\partial\gamma}{\partial y}\ \frac{\partial q}{\partial x}\right)$.

The maximum error in the u component of the wind would be through these terms and is evaluated next:

$$\Delta u|_{max.} = \frac{1}{A}\left\{\left(\frac{dq}{dt} - \frac{\partial q}{\partial t}\right) * \overset{10^{+28}}{\Delta}\left[\frac{\partial\theta}{\partial y}\ \frac{\partial\gamma}{\partial z}\right] + \overset{10^{-18}+10^{-20}}{\Delta}\left[\frac{\partial\theta}{\partial z}\ \frac{\partial\gamma}{\partial y}\right]\right\} +$$

$$\overset{10^{-17}+10^{-18}}{\frac{1}{A}\left(\frac{\partial\theta}{\partial y}\ \frac{\partial\gamma}{\partial z} - \frac{\partial\theta}{\partial z}\ \frac{\partial\gamma}{\partial y}\right)} * \overset{10^{-9}}{\Delta}\left(\frac{dq}{dt} - \frac{\partial q}{\partial t}\right) +$$

$$\overset{10^{+28}}{\frac{1}{A}\left(\frac{dq}{dt} - \frac{\partial q}{\partial t}\right)} * \overset{10^{-17}}{\left(\frac{\partial\theta}{\partial y}\ \frac{\partial\gamma}{\partial z} - \frac{\partial\theta}{\partial z}\ \frac{\partial\gamma}{\partial y}\right)} * \overset{10^{-29}\cdot 10^{+28}}{\frac{\Delta A}{(-A)}}$$

where: $\Delta A = \overset{10^{-4}}{\left(\frac{\partial\theta}{\partial z}\right)} * \left\{\overset{10^{-25}+10^{-25}}{\Delta\left(\frac{\partial\gamma}{\partial x}\ \frac{\partial q}{\partial y}\right)} + \overset{10^{-25}+10^{-25}}{\Delta\left(\frac{\partial\gamma}{\partial y}\ \frac{\partial q}{\partial x}\right)}\right\} +$

$$\overset{10^{-5}}{\left(10^{-13}\ 10^{-11} - 10^{-13}\ 10^{-11}\right)}\left(\frac{\partial\gamma}{\partial x}\ \frac{\partial q}{\partial y} - \frac{\partial\gamma}{\partial y}\ \frac{\partial q}{\partial x}\right) * \Delta\left(\frac{\partial\theta}{\partial z}\right)$$

i.e. $\Delta A = 10^{-4} * 4 * 10^{-25} + 10^{-24} * 10^{-5}$

$= 5 \cdot 10^{-29}$

$\rightarrow \Delta u_{/max.} \doteq 10^{+28} * [10^{-9} \cdot 10^{-17} + 10^{-9} \cdot 10^{-17} - 10^{-25} \cdot 10^{-1}]$

$\sim 10^{+28} \cdot 10^{-26}$ cm·s$^{-1}$

i.e., 1 m·s$^{-1}$.

## APPENDIX 2

Derivation of an expression for the total time derivative of the stability parameter $(\partial\theta/\partial p)$ from Poisson's equation $\theta = T(p/p_o)^{\kappa}$:

$$\frac{d}{dt}\left(\frac{\partial\theta}{\partial p}\right) = \frac{d}{dt}\left[\frac{\theta}{T}\frac{\partial T}{\partial p} - \frac{\kappa\theta}{p}\right]$$

$$= \frac{d}{dt}\left[\frac{\theta}{T}\left(\frac{\alpha}{R} + \frac{p}{R}\frac{\partial\alpha}{\partial p}\right) - \frac{\kappa\theta}{p}\right]$$

$$= \frac{d}{dt}\left[\frac{\theta}{p}(1-\kappa) + \frac{\theta}{\alpha}\frac{\partial\alpha}{\partial p}\right]$$

using the equation of state, $\alpha p = RT$. Upon carrying out the differentiation:

$$\frac{d}{dt}\left(\frac{\partial\theta}{\partial p}\right) = \frac{(1-\kappa)}{p}\frac{d\theta}{dt} - \frac{(1-\kappa)\theta}{p^2}\frac{dp}{dt} + \frac{1}{\alpha}\frac{\partial\alpha}{\partial p}\frac{d\theta}{dt} - \frac{\theta}{\alpha^2}\frac{\partial\theta}{\partial p}\frac{d\alpha}{dt} + \frac{\theta}{\alpha}\frac{d}{dt}\frac{\partial\alpha}{\partial p}$$

$$= \left[\left(\frac{1-\kappa}{p}\right) + \frac{1}{\alpha}\frac{\partial\alpha}{\partial p}\right]\frac{d\theta}{dt} - \theta\left(\frac{1-\kappa}{p^2}\right)\frac{dp}{dt} + \frac{\theta}{\alpha}\frac{d}{dt}\left(\frac{\partial\alpha}{\partial p}\right)$$

$$= \left(\frac{1-\kappa}{p}\right)\frac{d\theta}{dt} + \frac{1}{\alpha}\frac{\partial\alpha}{\partial p}\frac{d\theta}{dt} - \theta\left(\frac{1-\kappa}{p^2}\right)\frac{dp}{dt} + \frac{\theta}{\alpha}\frac{d}{dt}\frac{\partial\alpha}{\partial p}$$

$$= \frac{d\theta}{dt}\left(\frac{1}{T}\frac{\partial T}{\partial p} - \frac{\kappa}{p}\right) - \frac{\theta(1-\kappa)}{p^2}\frac{dp}{dt} + \frac{\theta}{\alpha}\frac{d}{dt}\frac{\partial\alpha}{\partial p} \quad .$$

From equation of state and Poisson's equation:

$$\alpha = \frac{R\theta p^{\kappa-1}}{p_o^{\kappa}}$$

and thus

$$\frac{\partial \alpha}{\partial p} = \frac{R\theta(\kappa - 1)p^{\kappa-2}}{p_o^{\kappa}}$$

Hence,

$$\frac{\theta}{\alpha}\frac{d}{dt}\frac{\partial \alpha}{\partial p} = \frac{\theta p_o^{\kappa}}{R\theta p^{\kappa-1}}\left[\frac{d}{dt}\frac{R\theta(\kappa - 1)p^{\kappa-2}}{p_o^{\kappa}}\right]$$

$$= \frac{(\kappa - 1)}{p}\frac{d\theta}{dt} + \frac{\theta(\kappa - 1)(\kappa - 2)}{p^{\kappa-1}}p^{\kappa-3}\frac{dp}{dt}$$

$$= \frac{(\kappa - 1)}{p}\frac{d\theta}{dt} + \frac{\theta(\kappa - 1)(\kappa - 2)}{p^2}\frac{dp}{dt}$$

so that

$$\frac{d}{dt}\frac{\partial \theta}{\partial p} = \frac{d\theta}{dt}\left[\frac{\partial \ln T}{\partial p} - \frac{1}{p}\right] - \frac{dp}{dt}\left[\frac{\theta(1 - \kappa)}{p^2} + \frac{(1 - \kappa)(\kappa - 2)}{p^2}\right]$$

$$= \frac{d\theta}{dt}\left[\frac{\partial \ln T}{\partial p} - \frac{1}{p}\right] - \frac{dp}{dt}\left[\frac{\theta(1 - \kappa)[1 + \kappa - 2]}{p^2}\right]$$

$$= \frac{d\theta}{dt}\left[\frac{\partial \ln T}{\partial p} - \frac{1}{p}\right] + \frac{\theta(1 - \kappa)^2}{p^2}\frac{dp}{dt} \quad .$$

Thus the Lagrangian time rate of change of the lapse rate of potential temperature with pressure as the vertical coordinate can be obtained through the diabatic term, $d\theta/dt$, and the vertical motion term, $dp/dt$.

# FEASIBILITY OF USING WATER VAPOR AS A TRACER TO OBTAIN WINDS FROM SATELLITE OBSERVATIONS

Frederick R. Mosher

ABSTRACT

Cloud-tracking techniques can derive useful data on upper level winds from geostationary satellite images, but cannot measure winds in regions where no clouds exist. This study suggests a water-vapor tracking technique to obtain wind measurements in clear regions, using infrared sensor data from geostationary or polar-orbit satellites. A comparison of the cloud-tracking and water-vapor tracking techniques showed that the water-vapor tracking method can locate jet core winds that do not show up in cloud-tracking analyses. Water-vapor tracking can complement cloud-tracking in the study of global wind patterns.

## 1. INTRODUCTION

One major advance in global meteorological observations has been the development of techniques for tracking cloud displacements using geostationary satellite images to obtain wind measurements in remote regions. The state of the art of cloud tracking has progressed rapidly in the past few years.

Figs. 1, 2, and 3 show typical measurements plotted at three levels, obtained four times per day during a two month operational capability demonstration at the Data Systems Test (DST). The wind measurements shown on the plots were for 11 January 1976 at 4:15 Z and were made from infrared images of the SMS-2 satellite centered over the equator at 135°W longitude.

Superimposing Figs. 1, 2, and 3, it can be seen that there is generally a wind measurement at some level in the atmosphere at nearly every location. But at any one level there can be big gaps in the coverage. When there are high clouds, it is generally not possible to obtain measurements of the lower clouds beneath. Likewise, when low clouds can be tracked, the upper levels are clear, resulting in big gaps in the upper level flow measurements. This is particularly true in the subtropics where the upper level flow is generally sinking.

In order to fill these upper level gaps, a conservative tracer is needed in the clear regions. The purpose of this study is to investigate the possibility of using water vapor as a tracer to obtain wind measurements.

## 2. BACKGROUND

Use of moisture as a tracer was first attempted by Rossby (1937), who plotted specific humidity on isentropic charts. He observed that tongues of maximum or minimum moisture content advanced less rapidly than expected from the observed wind distribution, indicating intense mixing between the tongues and their environment.

With the advent of meteorological satellites with water vapor sensors, interest in the use of water vapor as a meteorological tracer tool was revived. Some of the TIROS satellites had a radiometric sensor centered in the water vapor absorption region near 6.3 μm, with a 5° field of view. The data was used to map relative humidity in the upper atmosphere (Raschke and Bandeen, 1967).

A greatly improved water vapor sensor, the Temperature Humidity Infrared Radiometer (THIR) has been flown on Nimbus 4, 5, and 6 spacecraft. This 6.7 μm water vapor sensor has a field of view of 1° (22.5 km ground resolution at the satellite subpoint). The 11.5 μm infrared window channel associated with the water vapor sensor has a resolution of 8.2 km at the subpoint.

The weighting function for a standard atmosphere of the THIR 6.7 μm channel is shown in Fig. 4. The portions of the atmosphere that contribute most strongly to the water vapor 6.7 μm emissions lie between 250 mb and 500 mb, but this weighting function can move up or down or be distorted as temperature and moisture change with altitude in the middle and upper troposphere. Therefore, the assignment of an exact level to the water vapor measurements is difficult. A thin, very moist layer of water vapor can appear similar to a thicker, but slightly dryer layer of water vapor. On the THIR 6.7 μm images, dry areas appear dark; areas which appear gray or white are moist. Upper level clouds, which are fairly opaque to radiation at 6.7 μm, appear white in the images.

## 3. WIND MEASUREMENTS FROM INFRARED WATER-VAPOR DATA

The Nimbus THIR data has been used by Steranka et al. (1973) to analyze global moisture and wind fields. Qualitative comparisons of the 6.7 μm moisture images and the 400 mb conventionally measured wind fields indicated that the moisture patterns generally were aligned with the wind field. Thus, streamlines could be produced from a qualitative analysis of the 6.7 μm images.

The images used by Steranka et al. (1973) were composites of photofacsimile film strips. Figs. 5 and 6 show examples of these composites for Nimbus 6 data for two passes 12 hours apart. A qualitative comparison shows changes in the structure of the patterns for a given location. (Locations on the film strips are given by grid dots for every

10° of latitude and longitude. Bench marks are indicated by X's.) However, comparison of the images 12 hours apart is complicated by the fact that the Nimbus is in a sun-synchronous polar orbit with an inclination of 81°. This means that one image is tilted in respect to the other, and that a direct overlay of the two images is not possible.

Cloud tracking techniques require that the images be aligned, so to explore the possibility of using water vapor as a tracer, the 6.7 μm images had to be remapped. Digital data for the passes labeled 979 in Fig. 5 and 986 in Fig. 6 was obtained; these two passes overlap at the equator at about 120°W. (Images of 6.7 μm data over the U.S. are not available because the satellite is reading out rather than recording data as it passes over the United States.) The data format, described in the Nimbus 6 User's Guide (1975), consists of scan lines of data with bench mark navigation points. The data is scanned at the resolution of the 11.5 μm channel so the coarser field of view of the 6.7 μm channel is oversampled. The data were remapped into a common projection, with each of the remapped pixels representing one-tenth of a degree of latitude or longitude. The temperature of each pixel was converted to the same digital scale used in the SMS data.

The remapping process produced an image which had "holes" in it, as can be seen in Fig. 7. On the original scanned image, the earth locations of the points at the edges of the image are far apart, yet on the remapped image, the edge points are the same distance apart as the points in the center. The resulting holes were filled by averaging the data on either side of the discontinuity; Figs. 8 and 9 show the remapped data with the holes filled.

The data show clouds (the white relatively sharp features) and water vapor, but the contrast is so poor that it is difficult to distinguish specific features in the water vapor. To improve the contrast, an equal-population auto-enhancement was applied. This enhancement first makes a histogram of the data in the image, then assigns gray scales according to the relative population of the histogram; this means that digital levels with a lot of data will exhibit a large variation in gray levels. This type of enhancement causes subtle features to become more pronounced, as can be seen in Figs. 10 and 11. (Figs. 12 and 13 show the bottom portion of the data used; there is some overlap between the tops and bottom images of Figs. 10, 12, and 11, 13.)

The water vapor features were rather "fuzzy" and the subjective judgement of a researcher was required to identify and track them. Strong enhancement was needed to make visible the fine structure in the water vapor. (The fine structure was more evident on an electronic display with 64 gray levels than it is on the photographic reproductions of Figs. 10-13.)

Since the features of interest were fuzzy and difficult to precisely track, an interval of 12 hours was used between the start and stop times

of the observation sequence. This allowed the feature being tracked to travel a long distance, making errors in feature identification placement less critical.

This long tracking interval is valid because water vapor is a conservative tracer substance except for precipitation and vertical motion. But there is no precipitation in the clear areas, and the synoptic vertical motion is generally small--in the order of 1-5 cm $s^{-1}$, which would cause vertical displacements of .4 to 2 km in the 12 hr period. Since the weighting function is quite broad, with the major portion having a width of 6 km, this vertical motion would not interfere with the tracking.

When the enhanced images were displayed on the McIDAS and put into a loop, motion of the water vapor was apparent, but the features of the water vapor were too fuzzy for correlation tracking; the subjective single point tracking method was used instead. The operator selected a distinguishing feature in the water vapor, and caused the cursor to move with that feature. When the operator was satisfied that the cursor was moving with the feature, the beginning and end points were recorded along with the apparent blackbody temperature of the feature. Clouds were ignored as much as possible, and only water vapor was tracked.

Fig. 14 shows the resultant wind measurements derived from water-vapor tracking. The tropical storm at approximately 15°N, 115°W had strongly divergent outflow with pronounced cross equatorial flow. In the southern hemisphere, a strong subtropical jet exhibited a wind maximum of 90 knots.

## 4. COMPARISON OF WATER-VAPOR AND CLOUD TRACKING

The water-vapor wind measurements were compared to cloud-tracked wind measurements for the same area. (Cloud winds were tracked every six hours during the January-March 1976 Data Systems Test (DST) at the University of Wisconsin's McIDAS facility.) Several factors were noted, however, in making this comparison. The cloud-tracked measurements are over a 1 1/2-hour period, while the water-vapor measurements are over a 12-hour period. Also, the cloud measurements represent a layer of the atmosphere equal to the depth of the cloud, while the water vapor measurements represent the thickness of the water vapor layer. If the moisture layer is thick, the water vapor measurement represents a layer from approximately 250 mb to 500 mb.

Figs. 15, 16, and 17 show the DST cloud measurements for 8, 14, and 20 Z with all levels between 500 and 200 mb plotted together. The center time of the water vapor measurements is approximately 14 Z.

Comparisons between the water vapor measurements and the cloud measurements shows generally good qualitative agreement. The water vapor measurements fall between the cloud measurements of the 14 Z cloud data

set, showing that the water vapor tracking was successful in avoiding clouds. Therefore, the water vapor measurements do represent wind speeds in the clear, no-data areas where cloud-tracking cannot be used.

The one region that shows considerable disagreement between cloud wind measurements and water vapor wind measurements is the subtropical jet in the southern hemisphere. The water vapor measurements show a jet maximum of 90 knots at 16°S, 109°W. The 8 Z cloud measurement (Fig. 15) shows a subtropical jet with wind speeds of 20-40 knots.

The 8 Z measurements are in an arc which does not have any measurements in the area of the water vapor maximum. The water vapor measurement of 35 knots at 15°S, 104°W is the closest measurement to this cloud arc and shows good agreement with the cloud measurements. At 14 Z there were no southern hemisphere measurements at this level. At 20 Z (Fig. 17) the cloud measurements are somewhat sparse. The region where the subtropical jet is beginning still has winds of 20-40 knots, but further downstream around 15°S, 78°W, speeds have increased to 50-60 knots.

At 2 Z of the following day (Fig. 18) the placement of cloud measurements is approximately the same as six hours previously at 20 Z, but the jet maximum has increased to 100 knots at 23°S, 78°W. It appears, then, that the water vapor measurement of 90 knots in the clear region of the subtropics was a correct measurement and that this jet core propagated downstream to be detected by the cloud measurements 12 hours after the water vapor measurement.

## 5. CONCLUSIONS

The feasibility of using water vapor images in the 6.7 μm absorption band as tracers for wind determination has been demonstrated. Water vapor tracking measurements are consistent with cloud tracked wind measurements when both are in the same general vicinity. In clear regions where no upper level cloud winds are available, it appears that water-vapor tracking can yield meteorologically significant measurements; analysis of the location and intensity of jet cores in the clear areas appear quite feasible as well. In this study, water vapor tracking was used to locate a strong jet core that did not show up in the downstream cloud tracked winds until 12 hours later.

The time between images in this study was 12 hours, due to polar-orbit pass coverage constraints, but this time interval was useable. The fuzzy nature of the water vapor images and the difficulty in precisely locating a feature require a long observation interval. Intervals less than 12 hours could be used, though it is estimated that periods no shorter than three hours would be required for accurate tracking of water vapor.

Water vapor images will be available from geostationary satellites with the European METEOSAT, and from the GOES-D which will have the VISSR Atmospheric Sounder (VAS) aboard. More extensive tracking programs can be planned using these geostationary images. The major problem foreseen with the geostationary measurements will be the height assignment of the measured water vapor winds because of the broad weighting function.

In addition to demonstrating the feasibility of using water vapor as a tracer for wind measurements, this study has also demonstrated the feasibility of making upper level wind measurements from water-vapor images of a polar orbiting satellite. Polar orbiter data is clumsier to use than geostationary data because of the remapping involved, but such data still can be valuable. Global wind measurements could be made from a single polar orbiter with a water vapor channel. During the upcoming First GARP Global Experiment (FGGE), five geostationary satellites will measure cloud tracked winds, but most of these satellites will not have backups available. If there is a failure over a critical area, the gap could be filled with water vapor wind data from a polar orbiter.

## REFERENCES


The Nimbus 6 User's Guide, Goddard Space Flight Center, Greenbelt, MD, February 1975.

Raschke, E. and W. R. Bandeen, 1967: "A Quasi-Global Analysis of Tropospheric Water Vapor Content from TIROS 4 Radiation Data," Journal of Applied Meteorology, 6, pp. 468-481.

Rossby, C. G. and Collaborators, 1937: "Isentropic Analysis," Bulletin American Meteorological Society, pp. 201-209.

Steranka, Joseph, Lewis J. Allison, and Vincent V. Salomonson, 1973: "Application of Nimbus 4 THIR 6.7 μm Observations to Regional and Global Moisture and Wind Field Analysis," Journal of Applied Meteorology, 12, pp. 386-395.

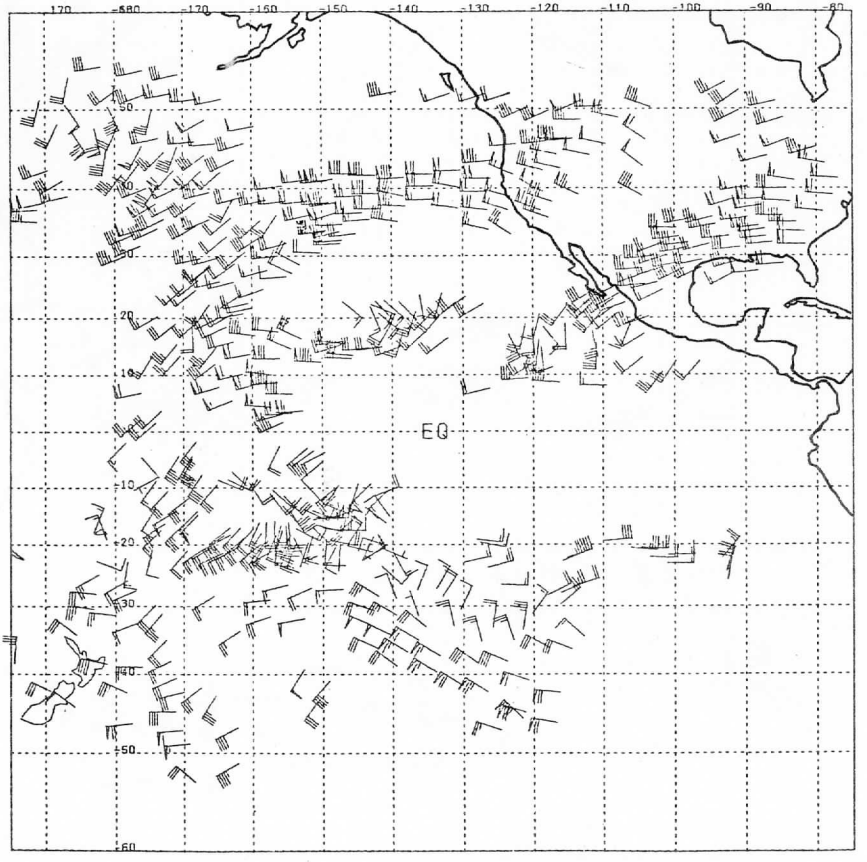


FIGURE 1: High-level cloud-tracked winds for January 11, 1976 at 04:15 GMT, produced from infrared images.

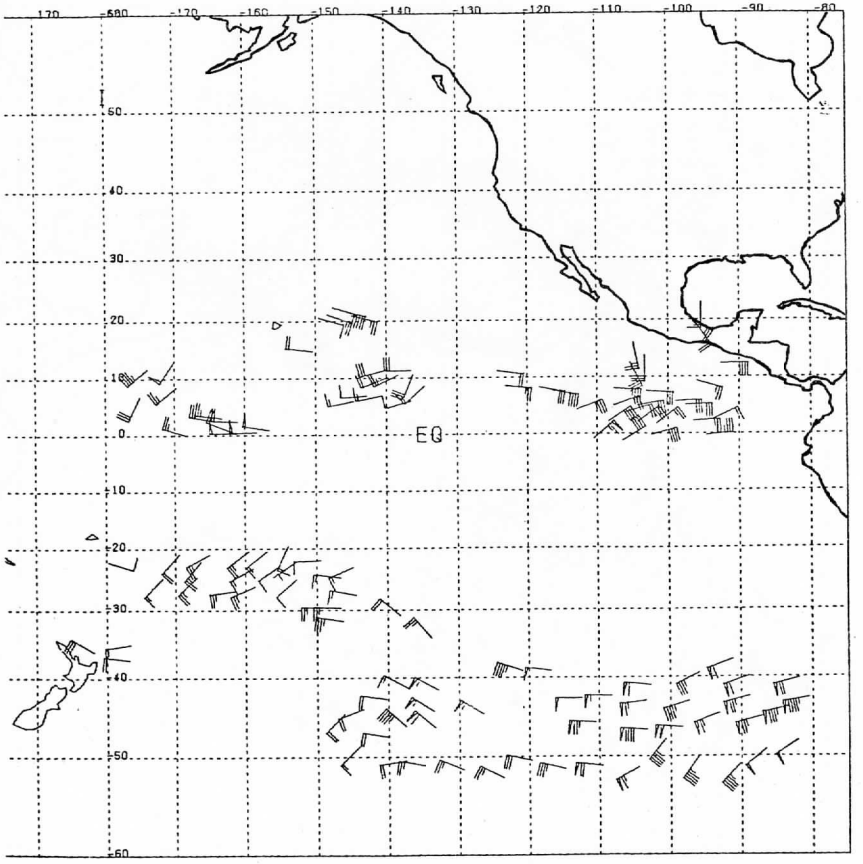


FIGURE 2: Mid-level cloud-tracked winds for January 11, 1976 at 04:15 GMT, produced from infrared images.

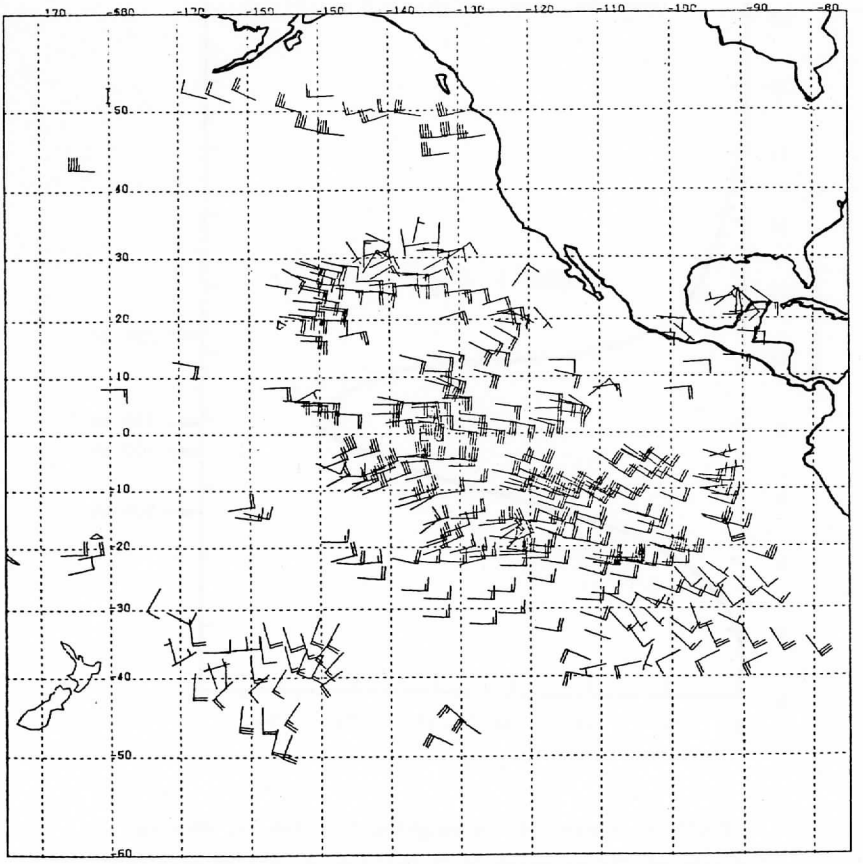


FIGURE 3: Low-level cloud-tracked winds for January 11, 1976 at 04:15 GMT produced from infrared images.

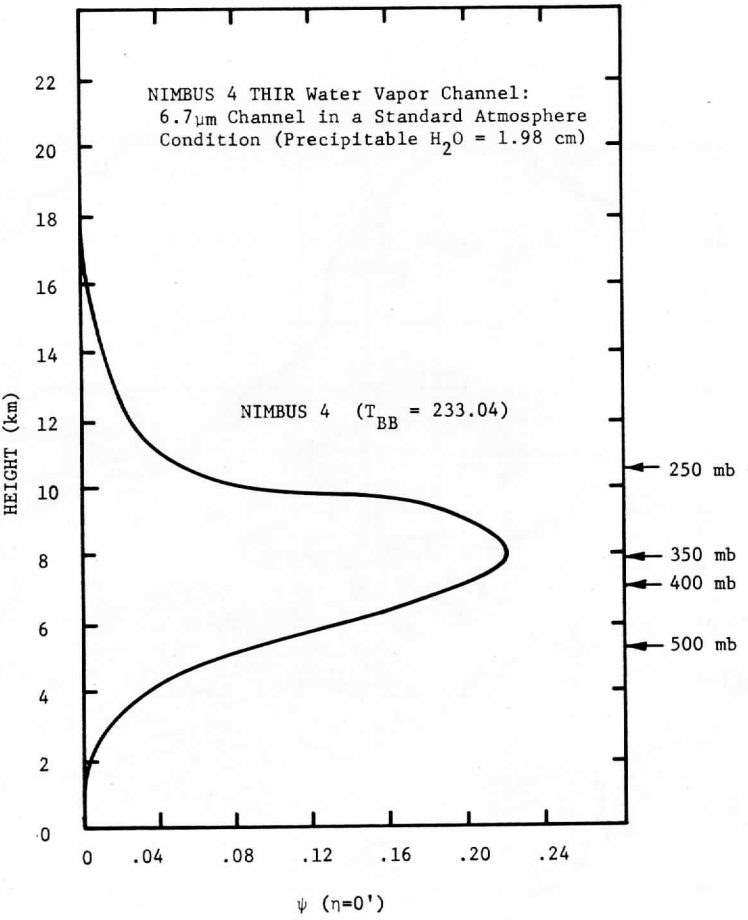


FIGURE 4: A plot of the weighing function, $\psi$, showing the atmospheric emission contributions at various altitudes to the radiance observed in the NIMBUS 4 THIR 6.7μm channel. (From Steranka et al., 1973)

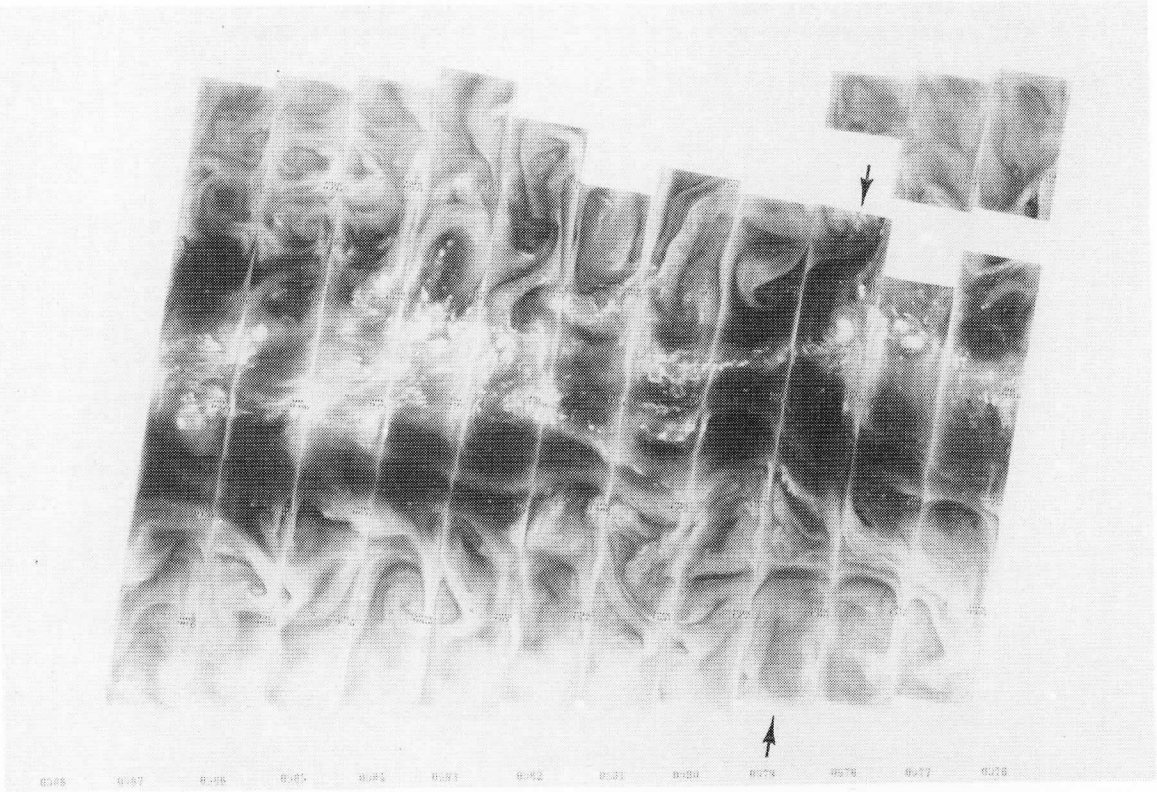

FIGURE 5: Composite of NIMBUS 6 THIR 6.7$\mu$m channel photofacsimile film strips for the night-time pass on August 24, 1975. Data from orbit 979 was used in this study.

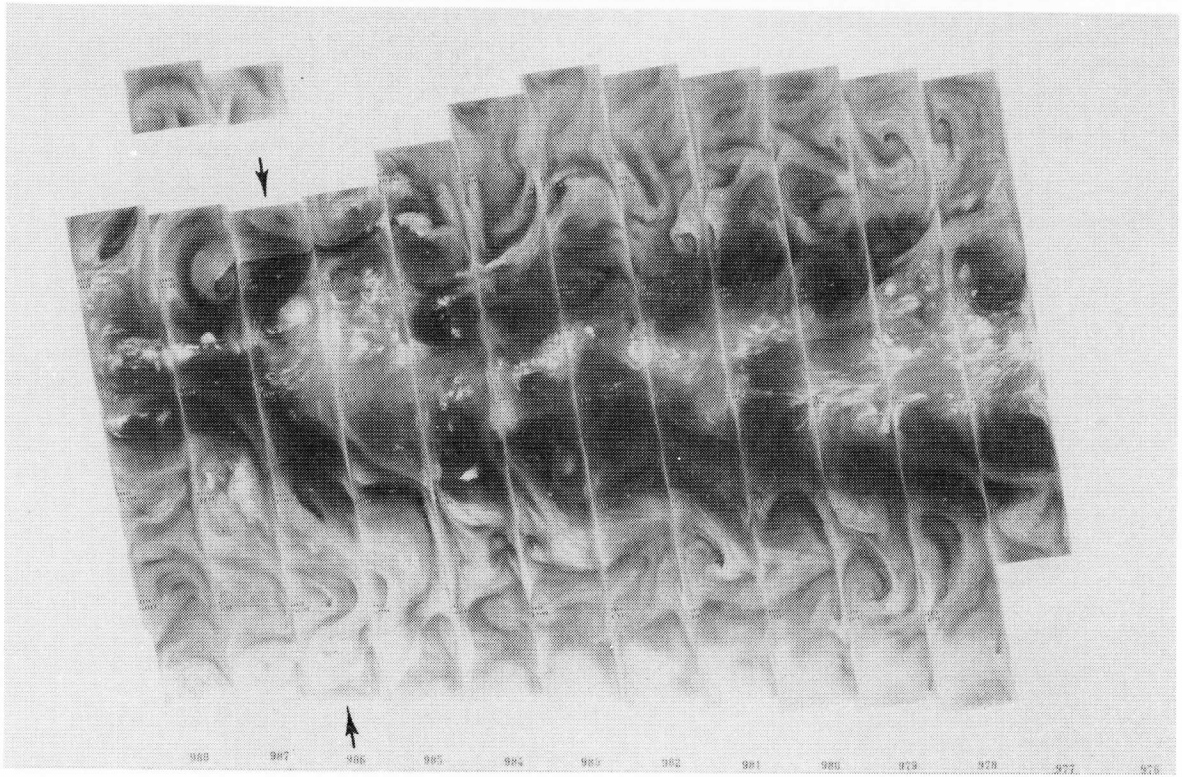

FIGURE 6: Composite of NIMBUS 6 THIR 6.7$\mu$ m channel photofacsimile film strips for the day-time pass on August 24, 1975. Data from orbit 986 was used in this study.

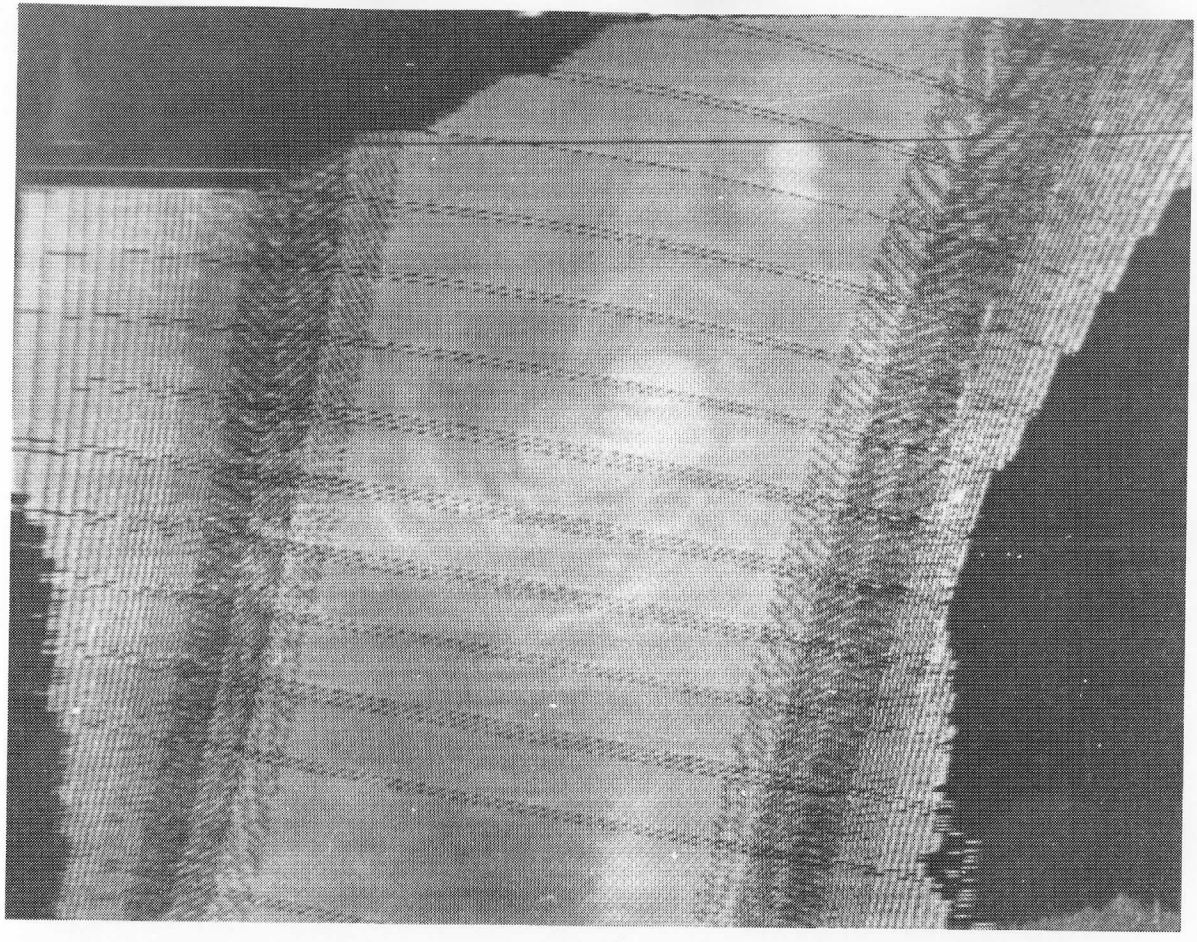

FIGURE 7: Image from orbit 979 re-mapped into cylindrical equi-distant projection.

FIGURE 8: Re-mapped image from orbit 979 with holes removed by averaging the data on either side of the hole.

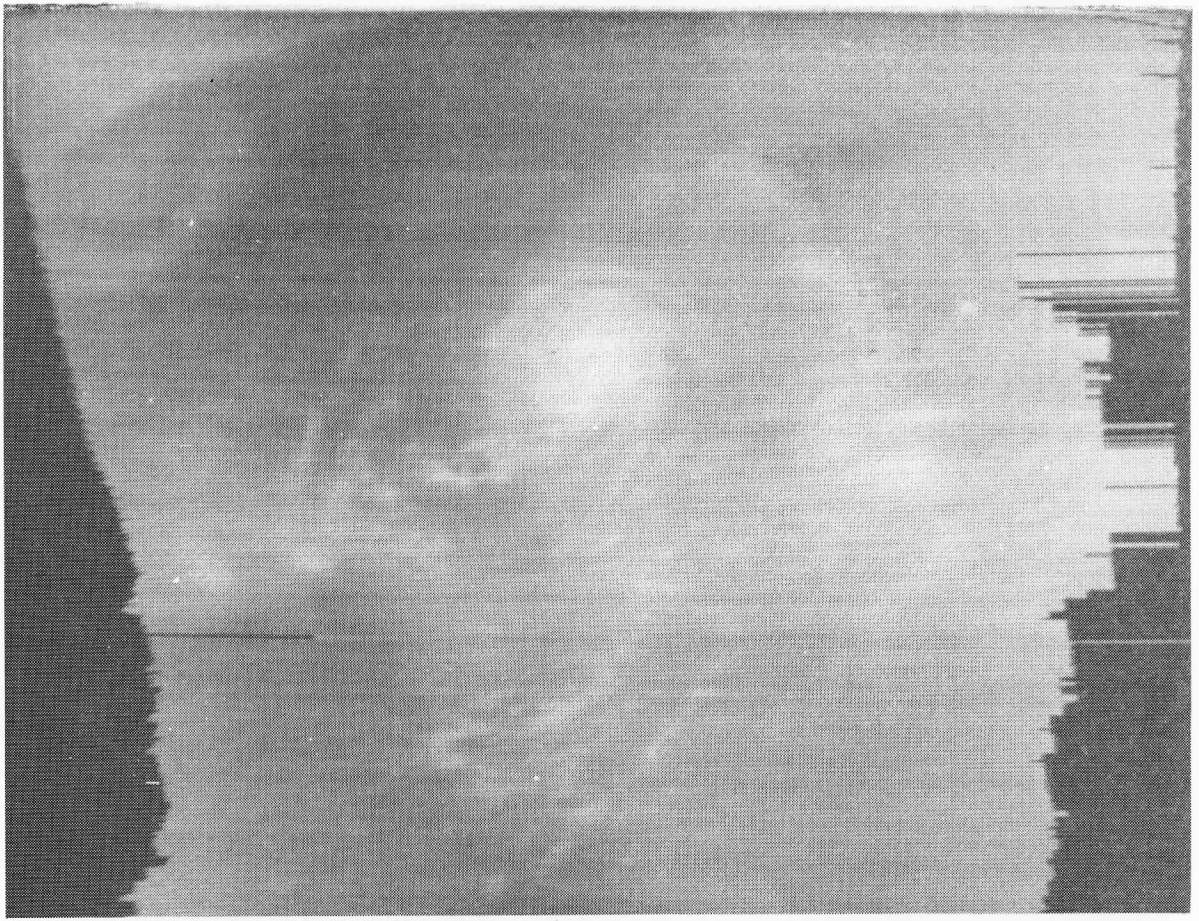

FIGURE 9: Re-mapped image from orbit 986 with holes removed by averaging the data on either side of the hole.

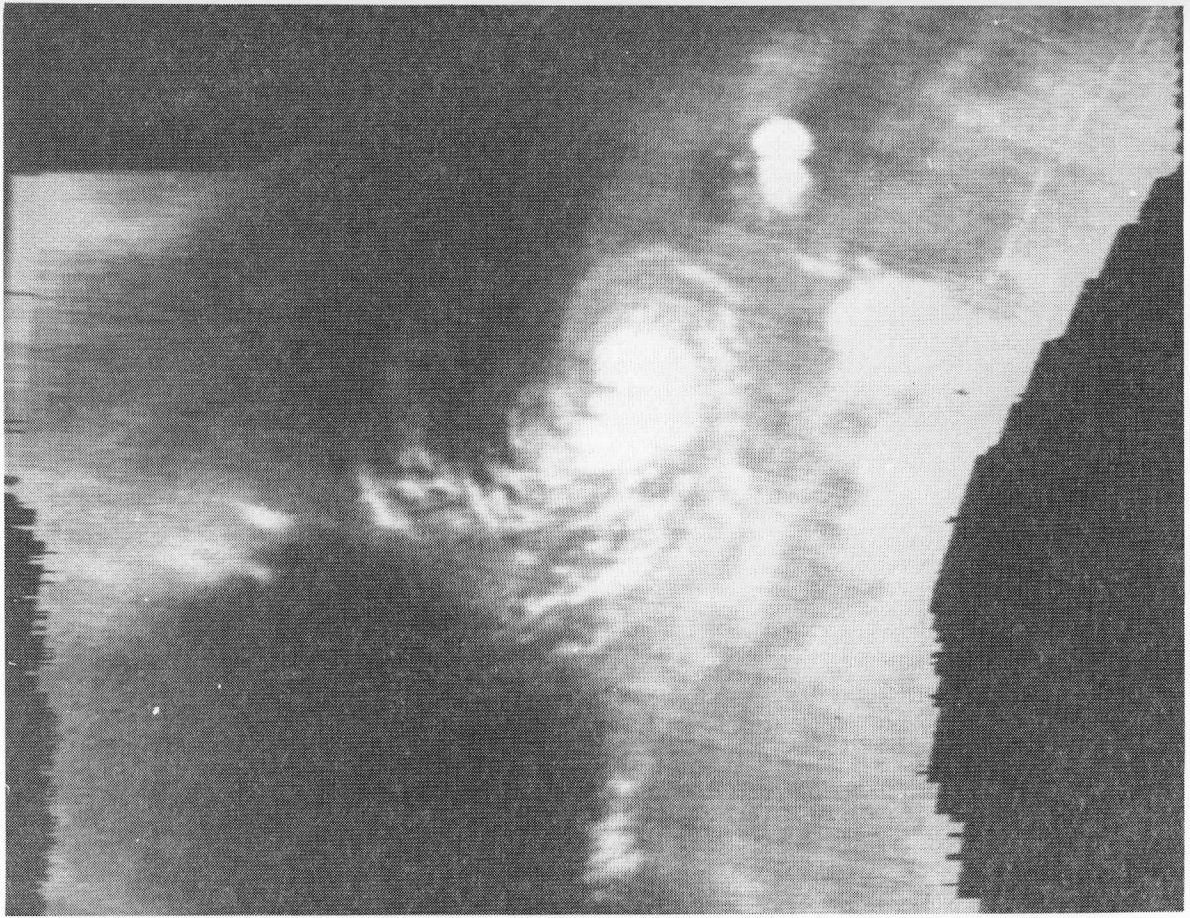

FIGURE 10: Same image as in Figure 8, but with equal population auto-enhancement applied.

FIGURE 11: Same image as in Figure 9, but with an equal population auto-enhancement applied.

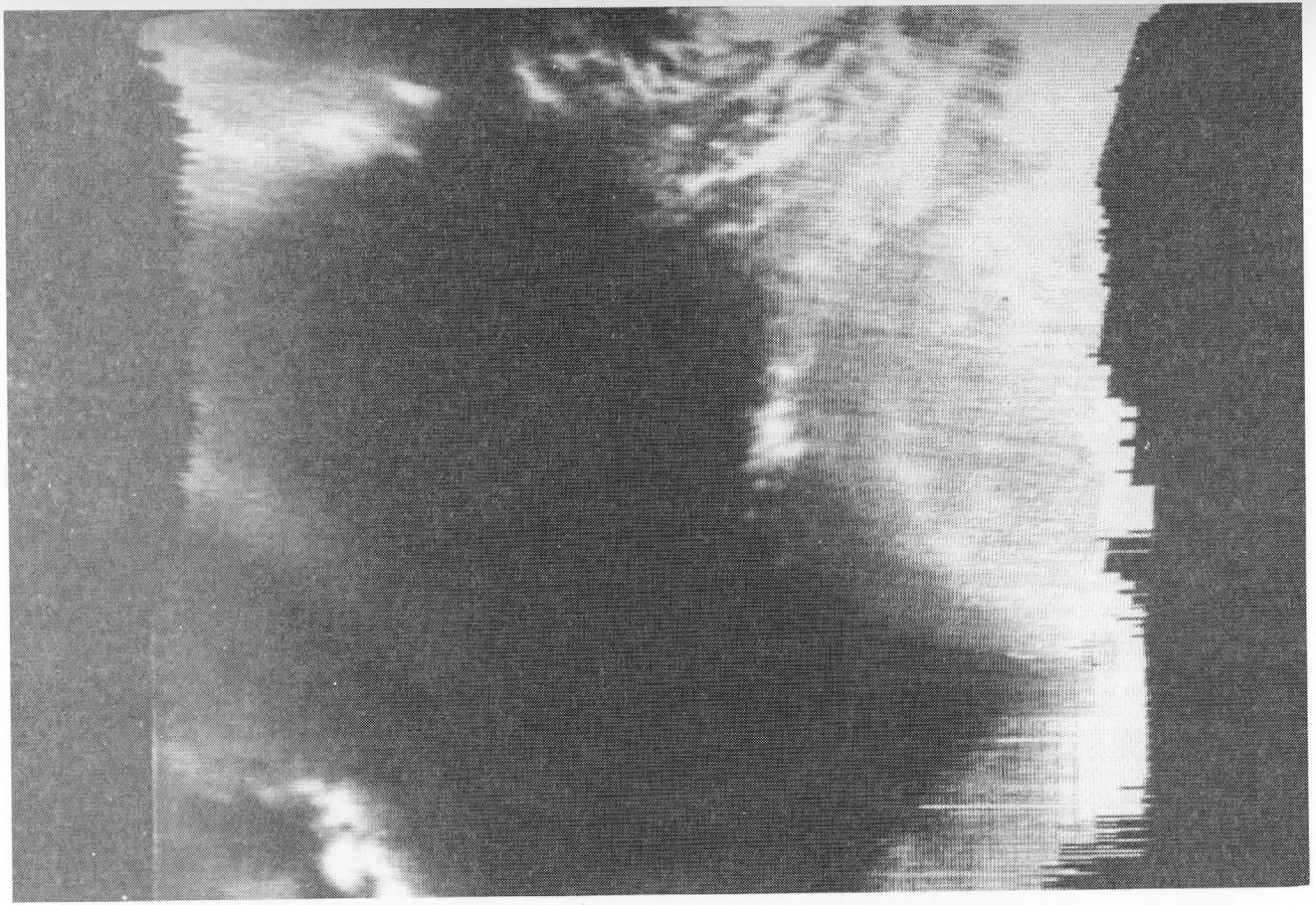

FIGURE 12: Extension of the bottom portion of Figure 10 for orbit 979.

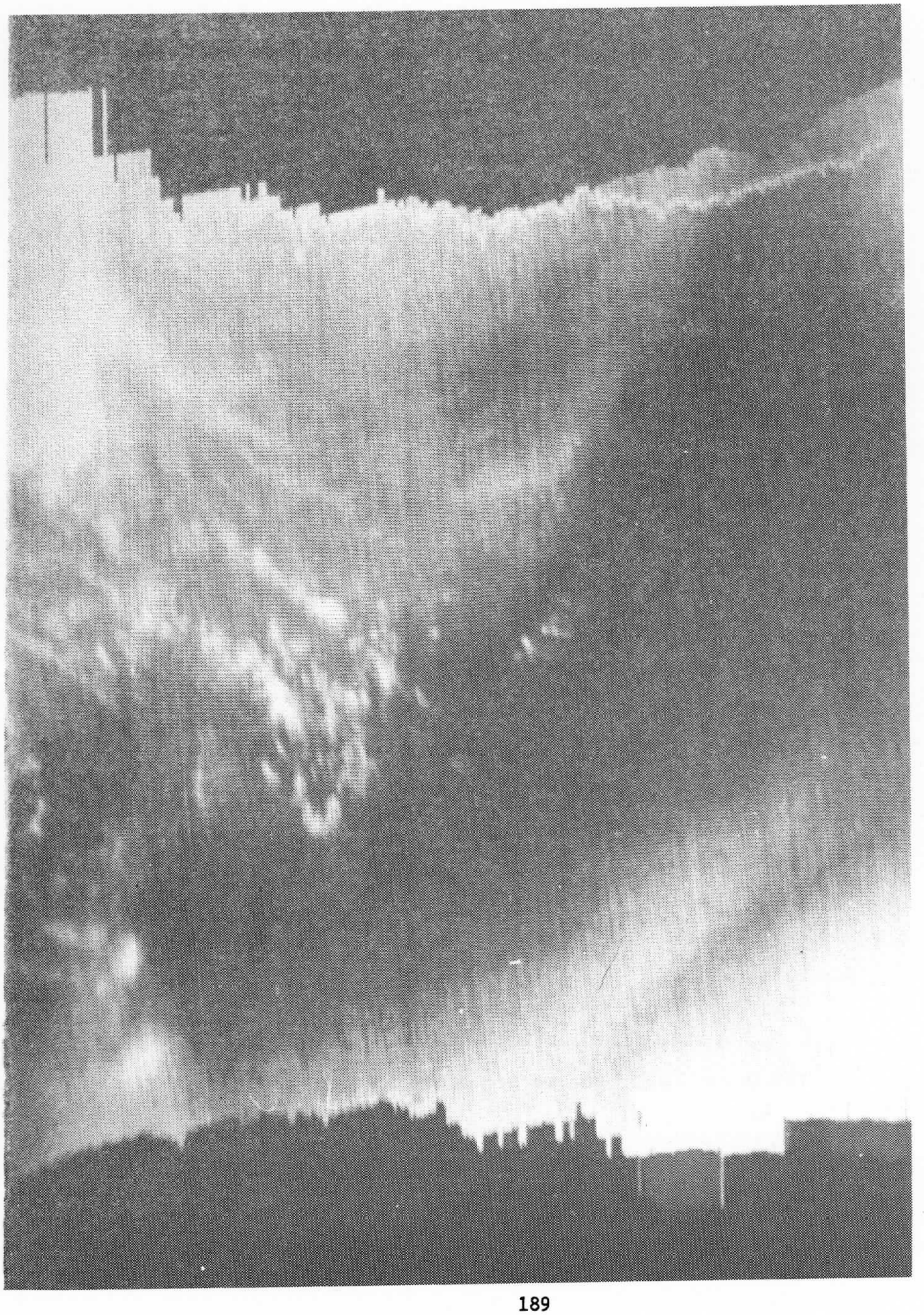

FIGURE 13: Extension of the bottom portion of Figure 11 for orbit 986.

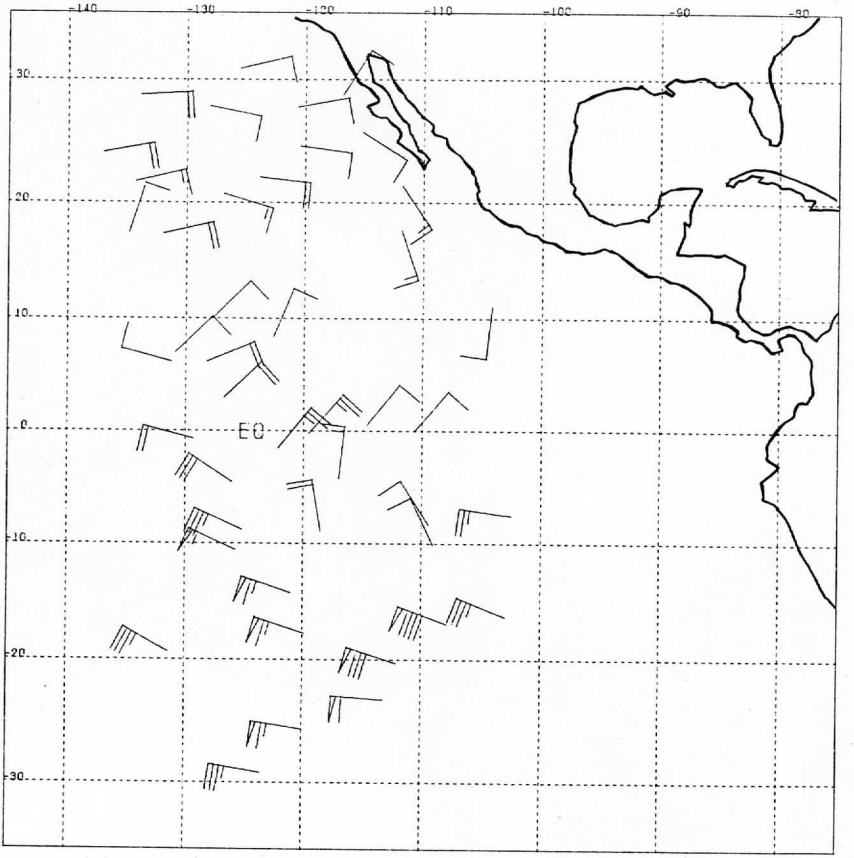


FIGURE 14: Winds measured by tracking water vapor in clear regions.

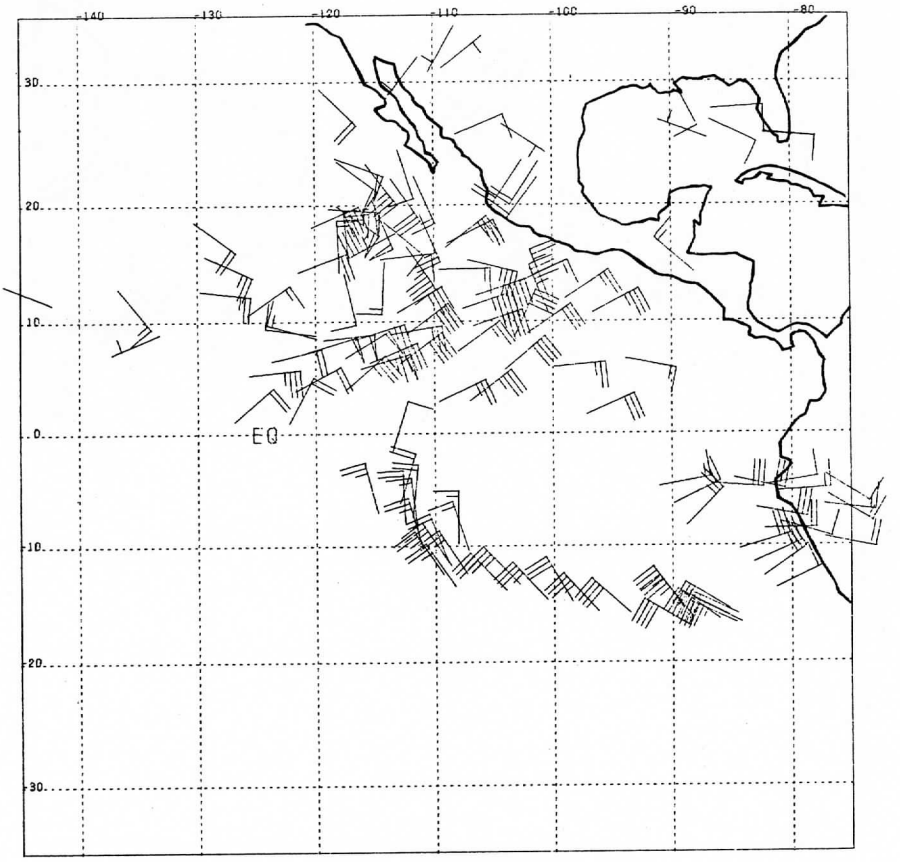


FIGURE 15: Cloud-tracked winds between 200 and 500 mb, measured during the DST at 08:00 GMT on August 24, 1975.

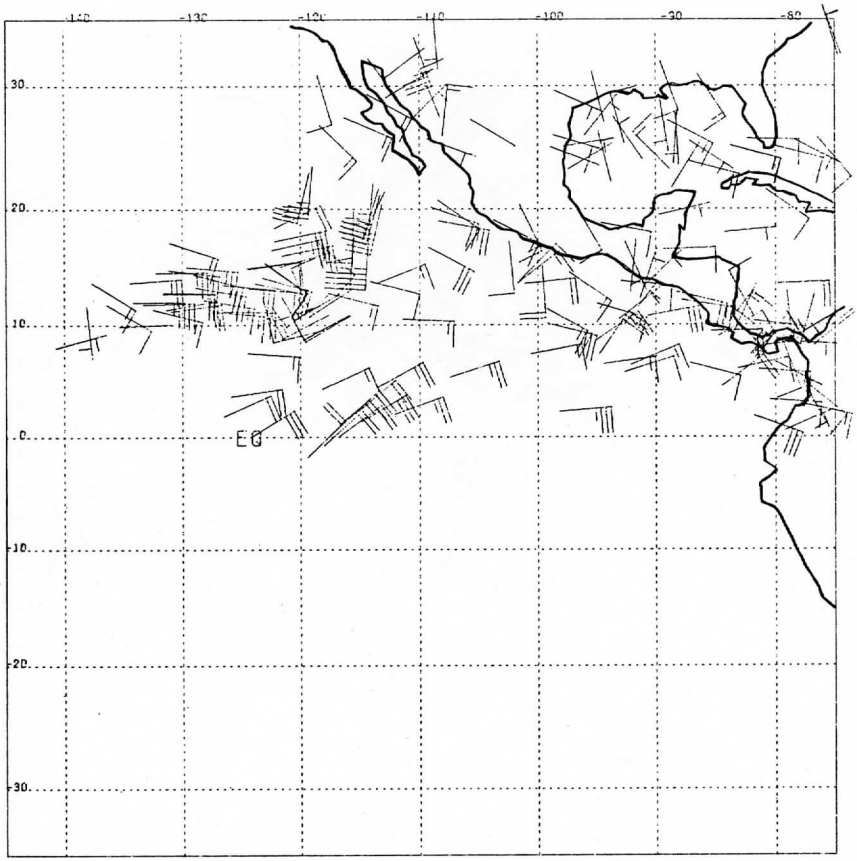


FIGURE 16: Cloud-tracked winds between 200 and 500 mb, measured during the DST at 14:00 GMT on August 24, 1975.

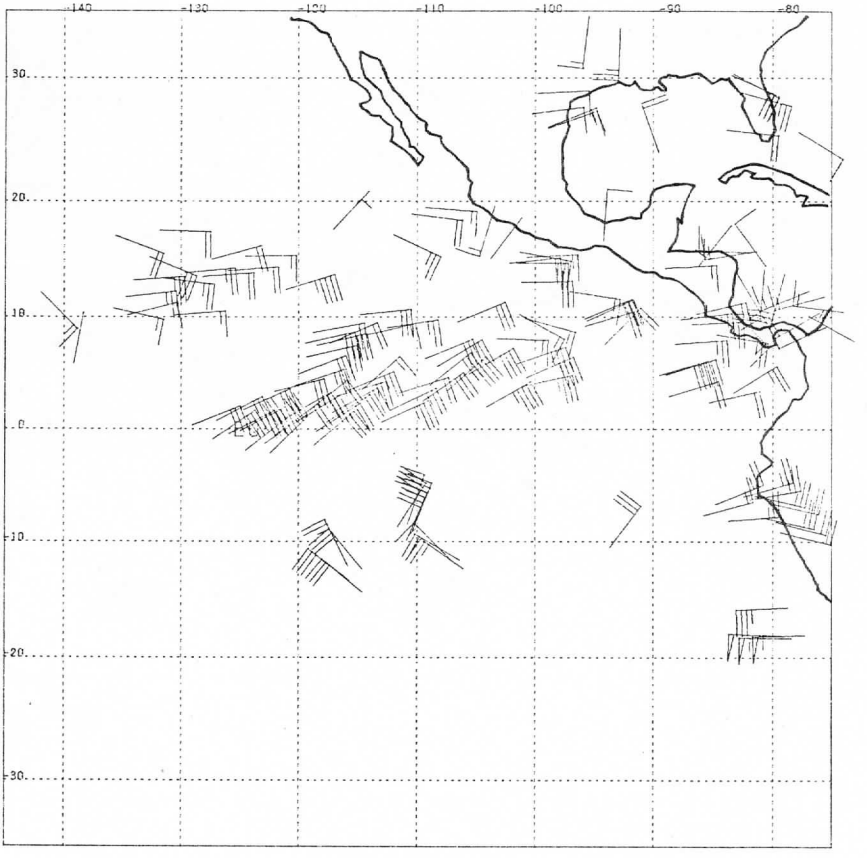


FIGURE 17: Cloud-tracked winds between 200 and 500 mb, measured during the DST at 20:00 GMT on August 24, 1975.

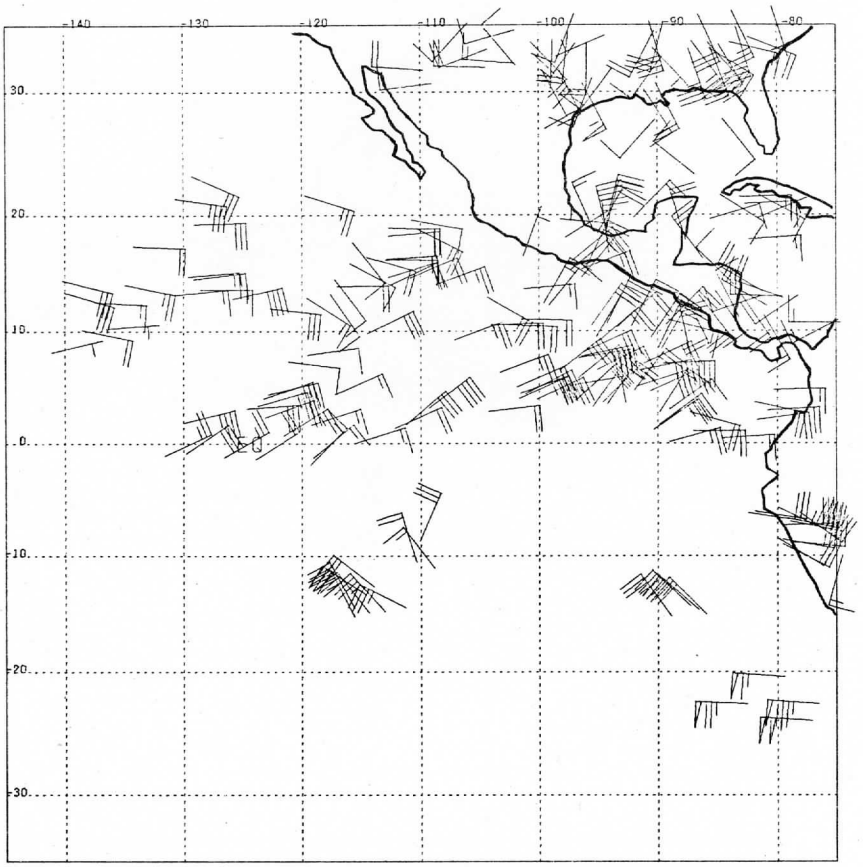


FIGURE 18: Cloud-tracked winds between 200 and 500 mb, measured during the DST at 02:00 GMT on August 25, 1975.

# WIND SETS FROM SMS IMAGES:

# AN ASSESSMENT OF QUALITY FOR GATE

David Suchman and David W. Martin

## ABSTRACT

In this study we explore the accuracy, representativeness and reproducibility of tracer winds in the area of the 1974 GARP Atlantic Tropical Experiment (GATE). These winds were generated by tracking clouds in Synchronous Meteorological Satellite (SMS) images displayed on the University of Wisconsin's Man-computer Interactive Data Access System (McIDAS). Two questions are addressed: 1) How accurately can the cloud displacements be measured? and 2) To what extent do the cloud displacements represent the wind field?

Accuracy is evaluated in terms of data characteristics, McIDAS precision and consistency. We find that for full-resolution visible data neither navigation nor resolution errors significantly affect the tracking of clouds. An examination of consistency, defined as similarity of wind sets independently produced by several scientists tracking clouds from the same set of images, yields an rms reproducibility of 2 $m\text{-}s^{-1}$ for cirrus level and 1.3 $m\text{-}s^{-1}$ for cumulus level winds. This is smaller than the "random" error generally attributed to cloud winds. In addition, the vorticity and divergence fields are qualitatively reproducible.

The discussion of representativeness centers about cloud height determination, and relating cloud motion to winds. Representativeness is examined through 1) the internal consistency of consecutive sets; 2) the consistency of the cloud wind field, including divergence and vorticity with such features as clusters, vortices, and clear areas; and 3) the difference between proximate satellite and ship winds. These differences were all under 3 $m\text{-}s^{-1}$, which is close to the noise level of ship winds and better than radiosonde-radiosonde comparison. We conclude that the representativeness of cloud tracers to cumulus and cirrus level flow is good to within the accuracy of currently available ground truth data.

## 1. INTRODUCTION

A primary data requirement for extended weather forecasting is accurate wind measurements on a global scale. For the oceans, which until recently were scarcely monitored at all, this can only be achieved through special platforms such as buoys, carrier balloons and satellites.

Satellites offer several possibilities for inferring air motions; however, only one - cloudtracking - is used routinely. To get a cloud wind, successive positions of tracer clouds are measured in a sequence of satellite images. These positions are transformed into earth-based coordinates of latitude and longitude. Velocity is calculated from changes in earth position.

Several systems now exist to measure cloud positions and generate tracer winds. At least one of these systems incorporates the hardware and software components needed to provide global winds on an operational basis. Yet there remain two major questions concerning the use of cloud displacement vectors as winds: 1) How accurately can the cloud displacements be measured? and 2) To what extend do the cloud displacements represent the wind field? These questions are the basis for this paper.

The answers to the question of accuracy appear in two forms. We begin with a brief description of the cloud tracking system developed at the University of Wisconsin, along with the problems inherent in tracking clouds, and their possible solutions. In addition, operator errors in obtaining the cloud displacements are examined in a series of reproducibility tests of wind sets.

The answers to the question of representativeness are less complete and less direct. Huber and Whitney (1971) found the "level of best fit" between satellite cloud tracer motions and nearby radar winds at 200 mb for cirrus level tracers and 850 mb for cumulus tracers. Differences at these levels of best fit were rather large: for speed, an average 9 kt low, 17 kt high; for direction, an average of less than $\pm 40^{\circ}$. In a study using ATS data, Fujita et al. (1975) concluded that the nature of low cloud motion should be better understood before cloud tracer motion can give an accurate representation of the low level wind field. Bengtsson and Morel (1974) in a GARP report concluded that the level of best fit for trade cumulus is closer to 950 mb; in addition, while expressing reasonable confidence in the accuracy of low level winds, the GARP Working Group on Numerical Experimentation (Bengtsson and Morel, 1974) questioned the utility of high level cloud winds mainly because of limitations in coverage.

In order to assess representativeness, direct comparisons of satellite winds with ground truth winds might seem most efficient in establishing satellite wind quality. However, it is rarely possible to achieve an adequate match in time, location and altitude. This is true even of the GARP Atlantic Tropical Experiment (GATE), whose data are used

as ground truth in the present study. Data availability limits comparisons to satellite winds with ship winds at the surface and at 250 mb. In addition, cloud winds typically are averaged over a one-half to one hour period and are representative of motion within a 1-2 km layer; rawinsondes represent motion over a 1-2 minute period within a 300-500 m layer. Given these limitations, the simplest comparison is visual - an overplot of ground-based winds on the satellite wind field. Another possibility is quantitative comparisons of U and V components using objective analysis of satellite fields. Both comparisons appear in this paper.

Rawins are our ground truth, yet their accuracy also is open to question. Mosher and Sawyer (1975) compared against rawins the cloud tracer winds obtained during the 25 January-7 February, 1975, Data Systems Test for the First GARP Global Experiment (FGGE). Using about 1000 vectors obtained under operational conditions each day for 1800 GMT, they found that the mean of the absolute value difference between cloud and radar winds was about 5 $m\text{-}s^{-1}$. The difference between adjacent radar winds (extrapolated downstream) was essentially the same - 5 $m\text{-}s^{-1}$. In a similar study using infrared data from 30-31 October 1974,Bauer (1976) compared cloud motions with soundings made coincidental in time and space. He also found rawinsonde/rawinsonde and cloud/rawinsonde differences to be the same - about 4.5 $m\text{-}s^{-1}$. Bengtsson (1975) reports the random error of conventional upper-air synoptic soundings as $\pm 1$ $m\text{-}s^{-1}$ with total error ranging up to 10 $m\text{-}s^{-1}$ in cases of strong winds.

Beyond direct comparisons of independently measured winds, the quality of satellite winds can be assessed through a careful comparison of the dynamics of a field with major features represented in the clouds. Examples include the association of persisting centers of low level convergence with active cloud clusters, divergence with cloud-free regions, and positive vorticity with cloud bands and vortices. Finally, we can capitalize on the inertia of the atmosphere to assess quality through the persistence of larger scale features within independently produced consecutive wind fields. Changes which do occur should be closely coupled to changes in the patterns and positions of clouds. Hence, the accuracy of cloud tracers as depictors of the wind field will be examined through direct comparisons, and through internal and physical consistency checks.

## 2. CLOUD TRACKING SYSTEM DESCRIPTION

Wind sets are generated on the University of Wisconsin's Man-computer Interactive Data Access System (McIDAS). This is an image storage, display and processing system consisting of data archive, access, video display, operator console and computer control sections. [For complete details of the McIDAS System, see Suomi(1975), Smith (1975) and Chatters and Suomi (1975).] The essential difference between this and earlier systems is that measurements on McIDAS are referred to the original digital data. This is accomplished through electronic rather than photographic display of images. The key advantage of this scheme for wind determination follows from the use of the display only to choose a small

image matrix out of the shole, thus preserving the excellent geometric fidelity of the spin scan camera (Chatters and Suomi, 1975).

Control of hardware and execution of the scientist's commands are achieved through a body of special software. With this system and associated software, it is possible by simple key-ins to enhance an image, magnify it, combine adjacent images into loops of any length, vary loop speed by up to a factor of 30, navigate pictures, locate and track clouds in TV, image or earth coordinates, and display the results as a vector plot superimposed on the original image. Two independent heads on the analog disk allow double looping of infrared and visible images, with instant single-key transfer from one to the other, or interlacing of the two images. Cloud tracking may be done by either of two primary methods: cursor tracking of the cloud to the nearest TV line and element (pixel tracking) and image match tracking of the cloud to better than TV line-element resolution (correlation tracking).

Because of the small size of the tracer clouds and the general complexity of cloud patterns in the GATE area, most clouds have been tracked by the single pixel (picture element) method. The location of the cloud is determined by the position of a cursor, which is moved around the screen by a position joy stick. Pixel tracking has been facilitated by the addition of a function called the velocity cursor, which enables the operator to compare and precisely match cursor motion to cloud motion.

Cloud top height is determined from both visible and infrared data using the method of Mosher (Suomi, 1975). Cloud emissivity is calculated from visible data. This emissivity is applied as a correction to the infrared blackbody temperature to obtain the cloud top temperature. Standard atmosphere soundings, corrected for latitude, yield a conversion of cloud top temperature to height. If visible data are absent, cloud height is computed using the uncorrected blackbody temperature. The cloud height function can either be requested independently of the wind calculation or it can be invoked as an automatic function as part of the cloud tracking subroutine. In the present case the trade cumulus and cirrus clouds sought as tracers ordinarily were sufficiently distinct to be easily recognized. A level for each type was assigned by the operator, and wind sets were generated one level at a time. The cloud height function helped in setting these levels, but its primary use was in checking the heights of clouds not immediately recognizable as trade cumulus (low) or cirrus (high).

## 3. EVALUATION OF CLOUD DISPLACEMENT MEASUREMENTS

Three principal sources of error in tracking clouds - navigation, image resolution and the operator - were described by Hubert and Whitney (1971) and Bengtsson and Morel (1974). The significance of these errors is discussed below.

Navigation errors

A sequence of geosynchronous satellite pictures typically shows motion of the earth within the image frame. The primary causes of this motion are deviation from the ideal orbit and misalignment of the spin axes of the satellite and the earth. Because it often is large compared to true cloud motion, earth motion must also be measured. Navigation is the means by which the apparent motion of the earth is removed from the cloud motion computation. Through navigation, any pixel in the image coordinate system can be converted into earth coordinates of latitude and longitude. Residual navigation errors causing false motions will appear as systematic errors. Studies (see Smith, 1975) have shown that on McIDAS, absolute navigation errors can be held to one picture element. Relative navigation errors, measured by picture-to-picture registration, are usually a small fraction of pixel size.

Resolution errors

The time and spatial resolution of the image impose the ultimate limits on the accuracy of the cloud tracked winds. If 30 minute images have a pixel size of 2 n miles, the uncertainty in the position of an unchanging pixel sized cloud is (2 n miles)x(30 minutes)$^{-1}$ = 4 n miles-hr$^{-1}$ or 2 meters-sec$^{-1}$. Increasing the size of the cloud decreases the uncertainty of its position; however, larger clouds are less likely to be strictly passive tracers of the horizontal flow. On the other hand, the smaller clouds most likely to be passive tracers usually undergo the fastest changes and the most rapid evolution. Selection of cloud tracers therefore involves compromises between size and lifetime and the match of cloud motion to ambient flow. Experience has shown that for tracking clouds in the tropics under typical conditions of cloud spacing, lifetime and movement, a 30-minute picture interval is well matched to 2 km (1 n mile) data; a 15 minute interval to 1 km data. Therefore, relatively few vectors are lost if the nominal 30 minute SMS visible data of GATE are displayed at a resolution reduced from the original by a factor of 2 or 3.

Operator errors

Prior to comparisons with ground truth, the consistency of our wind sets was examined. Consistency is a measure of the similarity of wind sets independently produced by several meteorologists tracking clouds from the same set of images. It is an assessment of the human element in cloud tracking. The sequence chosen for this reproducibility test was centered on 0900 GMT, 5 September 1974, when a rapidly developing cloud cluster was in the field of interest.

Cumulus (about 950 mb) and cirrus (about 250 mb) clouds were tracked by the single pixel method from visible and infrared pictures at 0830-0900 and 0900-0930 GMT. Wind sets for 0830-0900 and 0900-0930 GMT were averaged. Initially, six operators produced their own wind sets independently. These operators all had some experience in tracking winds.

The raw wind sets then underwent objective analysis [using a modified form of the WIND*SRI computer program (Mancuso and Endlich, 1973) with tight restrictions on extrapolations to data-free regions] to obtain grid point values of the U and V velocity components, and the fields of divergence and vorticity. These grid-point values then were intercompared for U and V, divergence and vorticity for each wind set. A total of 10 randomly chosen intercomparison sets were made in overlapping valid data regions (approximately 75 grid points per case for velocity and 40 grid points per case for divergence and vorticity).

The results of this initial reproducibility test for the four most dense wind sets are shown in Table 1. No one operator appeared to be significantly better than any other.

Two possible sources of error were noticed upon inspection of the qualitative features of the difference maps: 1) a few "bad" winds in a sparse data region often accounted for a large percentage of the mean difference between operators; and 2) some of the differences were caused by the nature of the objective analysis scheme.

To explore the reasons for wind discrepancies, the four most dense wind sets were individually displayed on McIDAS as vectors superimposed on the images used for tracking. A group of meteorologists challenged questionable vectors. If the operator who generated the wind set could not justify these winds through reference to specific clouds at the appropriate levels, they were flagged. Deleting the flagged vectors yielded four reedited wind sets. (This reediting process has been applied to all subsequent GATE area wind sets.) Over the same period the objective analysis scheme was adjusted to give a better representation of the wind fields: smoothing was applied in regions of large shear to avoid anomolous values in the vorticity and divergence field; restrictions were added on data sparse regions to minimize the influence of one of two bad winds; more winds were used in the calculation of each grid point value.

Intercomparisons were repeated for the four reedited sets using the revised objective analysis scheme. These results are shown in Table 2. For the grid point comparisons common to both Tables 1 and 2, the increase in velocity reproducibility averaged 28%, vorticity 32% and divergence 33%. Hence, by improvements in the editing and objective analysis scheme, reproducibility was aided significantly.

An rms reproducibility of 2 $m\text{-}s^{-1}$ for the cirrus level and 1.3 $m\text{-}s^{-1}$ for the cumulus level was obtained. Considering the variability inherent in the differences in cloud selection, the complexity of the case, and the inaccuracies of single-pixel tracking, this compares favorably with the $\pm 2$ $m\text{-}s^{-1}$ and $\pm 3$ $m\text{-}s^{-1}$ random error Bengtsson (1975) said was "characteristic" of low and high cloud derived winds. The better agreement found for the cumulus level clouds can be attributed to lower mean speeds, more tracers and a more distinctive appearance of cumulus compared to cirrus.

The reproducibility of the vorticity and divergence fields are such that credence is established in their qualitative features, and to a reasonable degree, their quantitative aspects. This is particularly encouraging, inasmuch as both divergence and vorticity have proven to be hightly difficult to measure with any degree of certainty by conventional methods.

Hence, the question of cloud tracking accuracy has a partial answer. On a technical level tracking accuracy is consistent with the resolution limitations of the SMS data. On a human level there remains a relatively large margin of error arising from misinterpretation. This error can be much reduced through careful peer review and editing of the raw wind sets. The accuracy of wind sets so edited is such that their divergence and vorticity are basically the same.

## 4. EVALUATION OF WIND ACCURACY

An evaluation of the representativeness of tracer winds to the true wind field is presented for three days - 5, 10 and 18 September - typifying disturbed, suppressed and moderately active conditions.

Completed wind sets are presented as maps of vectors. These vector plots include available ship winds when time and level differences are close enough to allow meaningful comparison. Except for a small group in the 1330 GMT 18 September set, all winds were generated by the single pixel method, using a velocity cursor. Tracking employed visible images; however, infrared images were available for height determination. In all cases at least five registered frames were available for viewing; tracking was done on the middle three frames at intervals of 15-30 minutes. Characteristics of individual sets are summarized in Table 3. Visible and infrared picture pairs, one for each day, show the general distribution and organization of clouds.

The quality of the tracer winds is tested in three ways: 1) by comparison of satellite winds with GATE ship or aircraft winds having a reasonable time proximity; 2) internal consistency of consecutive sets; and 3) comparison of satellite winds, derived vorticity and divergence fields with features such as clusters, vortices and squall lines.

September 5 (day 248) was one of the most convectively active days of GATE. A large, well organized cluster (see Fig. 1) dominated the center of the ship array much of the day. Two distinct centers of activity were associated with this cluster: one to the east that reached maturity early in the day; and one to the west that developed in the morning and began decaying by early afternoon. At low levels, the strong flow into the clusters in early morning (mainly from the northeast and southwest) gradually diminished as the day progressed, with the strongest inflow being in the western parts late in the afternoon. The high level flow, initially from southeast to northwest over the northern region and northeast to southwest over the southern region, became dominated by the strong outflow from the two convective centers as the day progressed.

Figs. 2 and 3 show the McIDAS derived cumulus and cirrus level cloud tracers centered on 0900, 1230 and 1500 GMT. At the time that these and the other wind sets presented in this paper were produced, satellite images were the sole source of information on winds and flow patterns in the areas of interest. Shipsonde winds taken from GATE synoptic-scale surface and 250 mb maps at 1200 GMT compose the ground truth which is the basis for these comparisons. These sonde winds and derived streamlines (Dean, 1976, personal communication) are plotted on Figs. 2b and 3b.

The correspondences for low and high level winds in regions of both satellite and sonde observations are excellent (Figs. 2b, 3b). Rather surprisingly, cloud winds are a far better match to surface than to 850 mb winds. The tendency for ship winds to exceed satellite winds in the southwestern part of the area at upper levels (Fig. 3b) may be the result of lower, layered cirrus associated with a small developing convective cell near 6°N, 27°W.

When the 1200 GMT sonde observations (given to the nearest 5 kt) were compared with the closest objectively analyzed grid point wind derived from the 1230 GMT wind set, the average absolute difference in speed was 1.9 $m\text{-}s^{-1}$ for the cumulus level and 2.9 $m\text{-}s^{-1}$ for the cirrus level. The absolute differences in direction for both cases averaged about 20°. This is certainly well within the limits of accuracy for the sonde observations, and other conventional systems as described by Bengtsson (1975). They are also less than half the deviations found by Hubert and Whitney. Differences were randomly distributed for the low level; at the cirrus level tracer winds were consistently slower, probably because of cirrus evaporation along the downstream edge.

Fig. 4 shows an example of the objectively analyzed grid point winds (as derived from the 1230 GMT cloud tracer field). At the cumulus level (Fig. 4a), two centers of convergence can be identified, corresponding to the two centers of convection: one at about 9°N, 20° 30'W, and the other at 9°N, 25° 30'W. At the cirrus level (Fig. 4b), strong divergence is found with both the mature eastern cluster and the developing western cluster.

The corresponding low and high level divergence fields (derived from the grid point winds) appear in Figs. 5a and 5b. The strong low level convergence into the developing western cluster, and the pronounced upper level divergence associated with both clusters are very clearly shown; both the qualitative and quantitative features are very reasonable. Hence, for this very active system, the cloud tracer winds depict the "true" wind field very accurately by exhibiting internal consistency of consecutive sets, good correspondence of wind and divergence fields with major cloud features, plus good agreement between cloud and sonde winds.

September 10 (day 253) was at the opposite end of the weather spectrum. There was little organized convection and few clouds (Fig. 6). Cumulus level tracers show an elongated anticyclonic gyre at 5° and 6°N (Fig. 7a). Winds in the clear area north of the gyre axis were light westerly, with a weak maximum in west-northwest flow. These features appear also in the surface ship winds. The largest discrepancies occur in the weak wind area close to the center of the gyre.

Flow at the cirrus level (Fig. 7b) was generally westward with difluence in the southeast over and around a mature cloud cluster between 5° and 7°N. Ship winds very closely match satellite winds in speed; however, through the center section between 7° and 8°N, ship wind directions are more northerly, by as much as 30° close to the cluster at 7°N.

September 18 (day 261) was neither as suppressed as 10 September nor as active as 5 September. Clouds at the trade cumulus level were abundant. In the central and northwestern parts of the analysis area these cumuli swelled to congesti and cumulonimbi, forming two small, rather disorganized clusters (Fig. 8). The maps of low cloud tracers show that these clusters developed in an anticyclonic south to southwesterly current (Fig. 9). Within this current there was a slight direction convergence, and a fairly marked speed convergence, both in the vicinity of the central cluster (at 9°21'N, 21°00'W).

Ship winds and satellite winds agree to within 10°, except at the Vanguard location (10°N, 23°20'W), where the direction difference is about 50°. Speeds also are very close.

Cirrus clouds were not as uniformly distributed; nevertheless, the large-scale pattern is well defined (Fig. 10). Flow at the cirrus level turned anticyclonically from east to southeast. There was a slight downstream decrease in speed, with a difluent pattern west and southwest of center, and over the central cluster at 1500 GMT.

Although no ship winds lie close to the satellite winds, the patterns formed by each set are mutually consistent. Principal features of the satellite field - including anticyclonic flow, difluence and downstream deceleration - appear in the ship winds as well.

Comparisons of the 1200 GMT soundings with the nearest objectively analyzed grid point winds for 1330 GMT show close agreement: differences in speed were 1.0 $m\text{-}s^{-1}$ for low level and 2.7 $m\text{-}s^{-1}$ for high level winds, while the directional differences were 25° and 16°, respectively. None of the deviations were systematic. These correspondences were somewhat better than those of 5 September partly due to the higher resolution of the data, and partly due to the relative simplicity of the flow patterns.

## 5. CONCLUSIONS

Using a variety of tests and comparisons for meso-synoptic-scale wind sets covering flow patterns from the simple to the complex, we have examined McIDAS-derived cloud tracer winds. Our evaluation is based on the accuracy of the measurement of cloud displacements and the representativeness of cloud winds to the "true" wind field. Findings on both these points are positive.

In every case examined, not only were the dominant features identified by conventional measurements contained in the fields of satellite winds, the satellite wind fields were more dense and in general contained more detail than the sonde winds. Differences between proximate satellite and ship winds were all under 3 $m\text{-}s^{-1}$, which is close to the noise levels in the ship winds and error levels inherent in making comparisons of such disparate measurements. The wind fields for 5 September are entirely consistent with the major cloud features, and the qualitative features of the divergence and vorticity fields are realistic.

Though the development of techniques for obtaining cloud tracer winds is far from complete, we conclude that if tropical cumulus and cirrus clouds are tracked with sufficient care by experienced operators, the wind fields obtained by present methods are at least on a par, in terms of point accuracies, with winds derived by conventional means. Because the weakest link now is assigning the right height to each cloud that is tracked, the principal limitation of these winds in meeting needs for global winds is likely to be vertical coverage rather than tracking accuracy. This problem is made more acute by large biases in the vertical distribution of tropical clouds. For the immediate needs of GATE, trade cumulus and cirrus cloud winds can contribute significantly to closing the observational gaps that developed in the large (A) scale sounding network over the Atlantic. More important, perhaps, is the contribution they can make to defining the dynamic structure and environment of the cloud ensembles that are the focus of GATE.

ACKNOWLEDGEMENTS

Thanks are extended to Brian Auvine, Gary Chatters, John Stout and Don Wylie, who contributed as cloud trackers. Gary Chatters served as navigator and as advisor on all aspects of McIDAS operation. Anthony Schreiner and Walter Knaack assisted in data reduction and analysis, Dana Wooldridge in drafting figures. Barbara Mueller typed the manuscript, which was reviewed by Verner Suomi.

Recognition is also due those who gave us McIDAS and keep it going: the lamplighters--Verner Suomi and Thomas Haig; the builders--Terry Schwalenberg, John Benson, Eric Smith, J. T. Young, Mahendra Shah, Fred Mosher, Dennis Phillips, and Ralph Dedecker; the keepers--Eric Suomi, Gary Chatters, and Michael Becker.

This work was supported under NASA Contracts NAS5-21798 and NAS5-23296, Verner Suomi, Principal Investigator.

## REFERENCES


Bauer, K.E., 1976: A Comparison of Cloud Motion Winds with Coinciding Radiosonde Winds. Mon. Wea. Rev., 104, 922-931.

Bengtsson, L., 1975: Four-Dimensional Assimilation of Meteorological Observations. GARP Publications Series No. 15, World Meteorological Organization.

_____ and P. Morel, 1974: The Performance of Space Observing Systems for the First GARP Global Experiment. The GARP Working Group on Numerical Experimentation, World Meteorological Organization.

Chatters, G. C. and V. E. Suomi, 1975: The Applications of McIDAS. IEEE Transactions on Geoscience Electronics, GE-13, 137-146.

Fujita, T. T., E. W. Pearl, and W. E. Shenk, 1975: Satellite-Tracked Cumulus Velocities. J. Appl. Meteor., 14, 407-413.

Hubert, L. F. and L. F. Whitney, Jr., 1971: Wind Estimation from Geostationary-Satellite Pictures. Mon. Wea. Rev., 99, 665-672.

Mancuso, R. L. and R. M. Endlich, 1973: User's Manual, Wind Editing and Analysis Program: Spherical Grid. (WEAP-1A), Stanford Research Institute.

Mosher, F. R. and B. Sawyer, 1975: Comparison of Wind Measurement Systems: Cloud Tracked Winds vs. Rawinsonde and Rawinsonde Winds vs. Rawinsonde Winds. In Preliminary Assessment of the Cloud Tracking System Developed at the University of Wisconsin, SSEC, Univ. of Wisconsin.

Smith, E. A., 1975: The McIDAS System. IEEE Transactions on Geoscience Electonics, GE-13, 123-136.

Suomi, V. E., Principal Investigator, 1975: Man-Computer Interactive Data Access System (McIDAS), Final Report Contract NAS5-23296, Univ. of Wisconsin, Madison.

TABLE 1

ORIGINAL WIND REPRODUCIBILITY

(Four Nonedited Wind Sets)

| Low Level Winds | RMS Difference Between Operators | Mean Absolute Value |
|---|---|---|
| $\overline{u}$ | $1.07\ m \cdot s^{-1}$ | $3.08\ m \cdot s^{-1}$ |
| $\overline{v}$ | $1.34\ m \cdot s^{-1}$ | $5.06\ m \cdot s^{-1}$ |
| Total Velocity | $1.71\ m \cdot s^{-1}$ | $5.93\ m \cdot s^{-1}$ |
| | | Maximum Value |
| Vorticity | $18.92 \times 10^{-6}\ s^{-1}$ | $40 \times 10^{-6}\ s^{-1}$ |
| Divergence | $17.02 \times 10^{-6}\ s^{-1}$ | $78 \times 10^{-6}\ s^{-1}$ |

| High Level Winds | RMS Difference Between Operators | Mean Absolute Value |
|---|---|---|
| $\overline{u}$ | $2.46\ m \cdot s^{-1}$ | $8.29\ m \cdot s^{-1}$ |
| $\overline{v}$ | $1.62\ m \cdot s^{-1}$ | $2.59\ m \cdot s^{-1}$ |
| Total Velocity | $2.95\ m \cdot s^{-1}$ | $8.69\ m \cdot s^{-1}$ |
| | | Maximum Value |
| Vorticity | $11.84 \times 10^{-6}\ s^{-1}$ | $50 \times 10^{-6}\ s^{-1}$ |
| Divergence | $24.46 \times 10^{-6}\ s^{-1}$ | $86 \times 10^{-6}\ s^{-1}$ |

TABLE 2

REPRODUCIBILITY OF FOUR EDITED WIND SETS

| Low Level Winds | RMS Difference Between Operators | Mean Absolute Value |
|---|---|---|
| $\bar{u}$ | 0.76 $m \cdot s^{-1}$ | 3.20 $m \cdot s^{-1}$ |
| $\bar{v}$ | 1.04 $m \cdot s^{-1}$ | 5.25 $m \cdot s^{-1}$ |
| Total Velocity | 1.29 $m \cdot s^{-1}$ | 6.15 $m \cdot s^{-1}$ |
| | | Maximum Value |
| Vorticity | $9.93 \times 10^{-6}$ $s^{-1}$ | $34 \times 10^{-6}$ $s^{-1}$ |
| Divergence | $11.62 \times 10^{-6}$ $s^{-1}$ | $86 \times 10^{-6}$ $s^{-1}$ |

| High Level Winds | RMS Difference Between Operators | Mean Absolute Value |
|---|---|---|
| $\bar{u}$ | 1.71 $m \cdot s^{-1}$ | 8.56 $m \cdot s^{-1}$ |
| $\bar{v}$ | 1.10 $m \cdot s^{-1}$ | 2.32 $m \cdot s^{-1}$ |
| Total Velocity | 2.03 $m \cdot s^{-1}$ | 8.87 $m \cdot s^{-1}$ |
| | | Maximum Value |
| Vorticity | $9.93 \times 10^{-6}$ $s^{-1}$ | $40 \times 10^{-6}$ $s^{-1}$ |
| Divergence | $16.09 \times 10^{-6}$ $s^{-1}$ | $77 \times 10^{-6}$ $s^{-1}$ |

TABLE 3

CHARACTERISTICS OF GATE WIND SETS

| Day | Sequence | Image Interval (min) | Visible Image Resolution (km) | Load Center (lat) | (long) |
|---|---|---|---|---|---|
| 5 Sept. | 0830, 0900, 0930 GMT | 30 | 2 | 0830 N | 2330 W |
| | 1200, 1230, 1300 GMT | 30 | 2 | 0830 N | 2330 W |
| | 1430, 1500, 1530 GMT | 30 | 2 | 0830 N | 2330 W |
| 10 Sept. | 1215, 1230, 1245 GMT | 15 | 1 | 1214 N | 2314 W |
| | 1215, 1230, 1245 GMT | 15 | 1 | 0830 N | 2330 W |
| | 1215, 1230, 1245 GMT | 15 | 1 | 0450 N | 2335 W |
| | 1445, 1500, 1515 GMT | 15 | 2 | 0830 N | 2330 W |
| 18 Sept. | 1315, 1330, 1345 GMT | 15 | 1 | 0925 N | 2130 W |
| | 1445, 1500, 1515 GMT | 15 | 1 | 0925 N | 2130 W |

FIGURE LEGENDS

Figure 1a SMS-1 visible image for 1230 GMT 5 September 1974 photographed from McIDAS display. Cursor is centered on the B array, at 8°30'N,23°30'W. Grid interval is 2°. Image resolution reduced by a factor of 4.

Figure 1b Same as in Fig. 1a, except full-resolution infrared channel.

Figure 2a Cumulus level cloud tracer motions, 0900 GMT 5 September 1974. One degree of the grid corresponds to a wind speed of 25 $m \cdot s^{-1}$.

Figure 2b Cumulus level cloud tracer motions, 1230 GMT 5 September 1974, with superimposed 1200 GMT surface ship winds and streamlines analysis [Dean, 1976].

Figure 2c Same as in Fig. 2a, except at 1500 GMT.

Figure 3a Cirrus level cloud tracer motions, 0900 GMT 5 September 1974.

Figure 3b Cirrus level cloud tracer motions, 1230 GMT 5 September 1974, with superimposed 1200 GMT 250 mb ship winds and streamlines analysis [Dean, 1976].

Figure 3c Same as in Fig. 3a, except at 1500 GMT.

Figure 4a Objectively analyzed cumulus level grid point winds, 1230 GMT 5 September 1974.

Figure 4b Objectively analyzed cirrus level grid point winds, 1230 GMT 5 September 1974.

Figure 5a Cumulus level divergence ($10^{-6}$ $s^{-1}$), 1230 GMT 5 September 1974.

Figure 5b Cirrus level divergence ($10^{-6}$ $s^{-1}$), 1230 GMT 5 September 1974.

Figure 6a SMS-1 visible image for 1230 GMT 10 September 1974. Cursor is centered in the B array, at 8°30'N,23°30'W. Grid interval is 1°. Full image resolution.

Figure 6b Same as in Fig. 6a, except infrared channel enlarged eight times to scale of visible image.

Figure 7a Cumulus level cloud tracer motions, 1230 GMT 10 September 1974; surface ship winds (heavy arrows), 1200 GMT.

Figure 7b Cirrus level cloud tracer motions, 1230 GMT 10 September 1974; surface ship winds (heavy arrows), 1200 GMT.

Figure 8a SMS-1 visible image for 1330 GMT 18 September 1974. Cursor located at 9°25'N,21°30'W. Grid interval is 1°. Full image resolution.

Figure 8b Same as in Fig. 8a, except infrared channel enlarged eight times to scale of visible channel.

Figure 9a Cumulus level cloud tracer motions (light arrows) for 1330 GMT 18 September 1974, plus surface ship winds (heavy arrows with circles).

Figure 9b Cumulus level cloud tracer motions for 1500 GMT 18 September 1974.

Figure 10a Cirrus level cloud tracer motions (light arrows) for 1330 GMT 18 September 1974.

Figure 10b Cirrus level cloud tracer motions for 1500 GMT 18 September 1974.

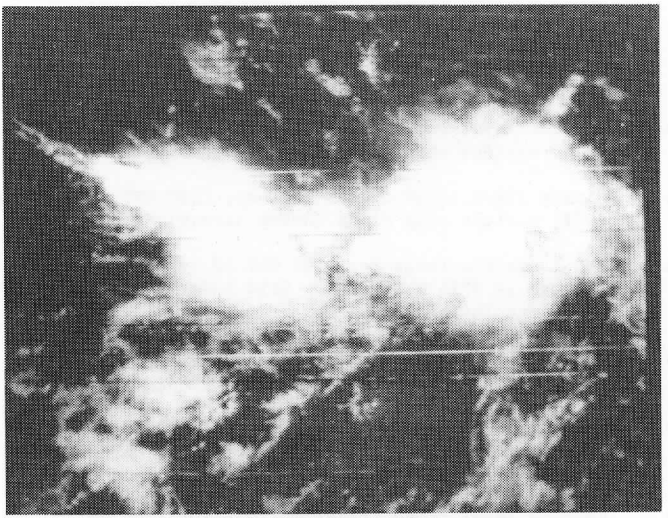

Figure 1a

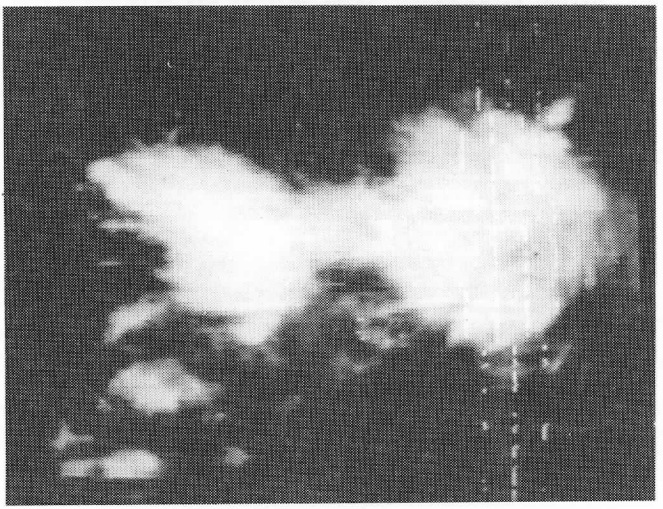

Figure 1b

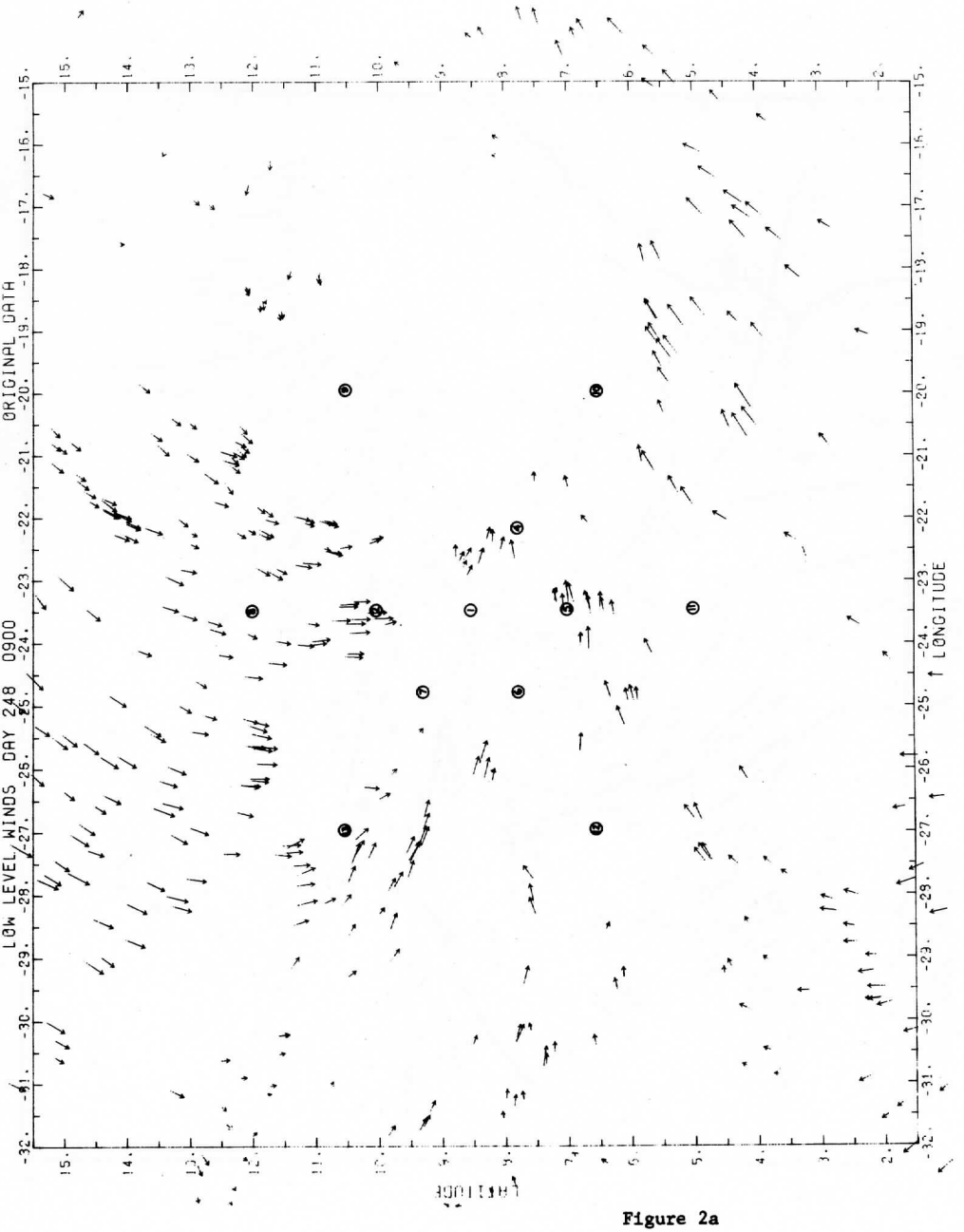
LOW LEVEL WINDS DAY 248 0900
ORIGINAL DATA
LONGITUDE
LATITUDE

Figure 2a

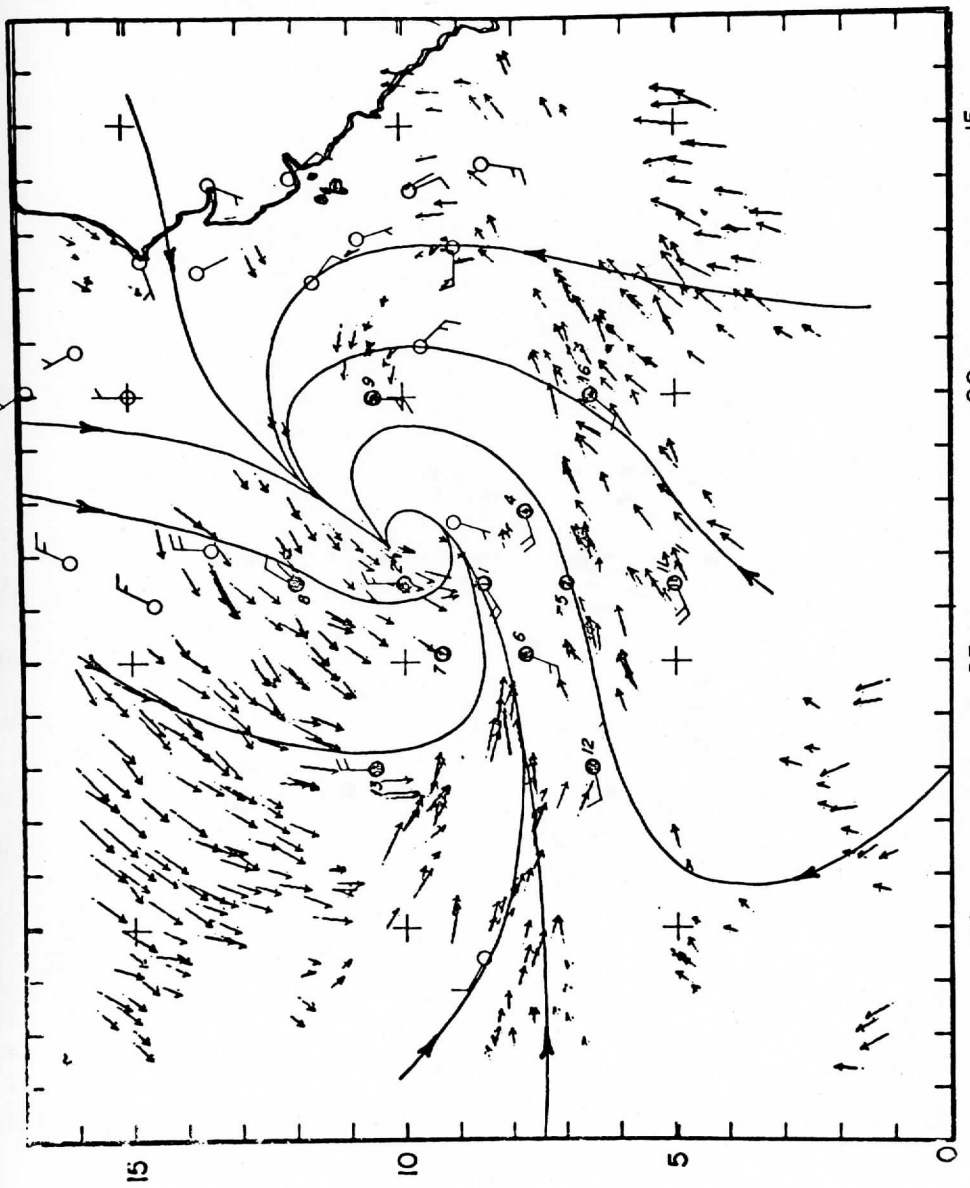


Figure 2b

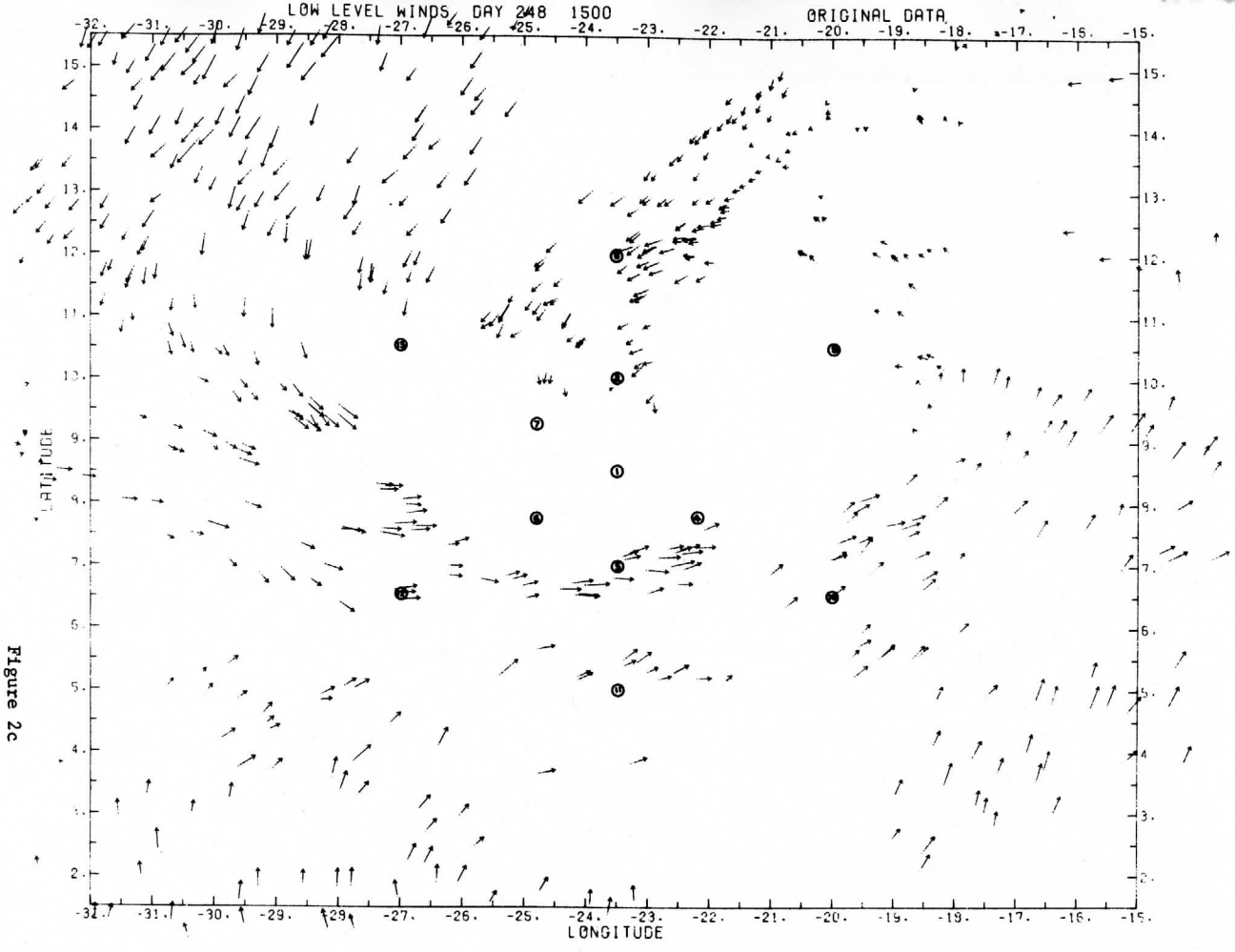
LOW LEVEL WINDS, DAY 248 1500
ORIGINAL DATA
LATITUDE
LONGITUDE

Figure 2c

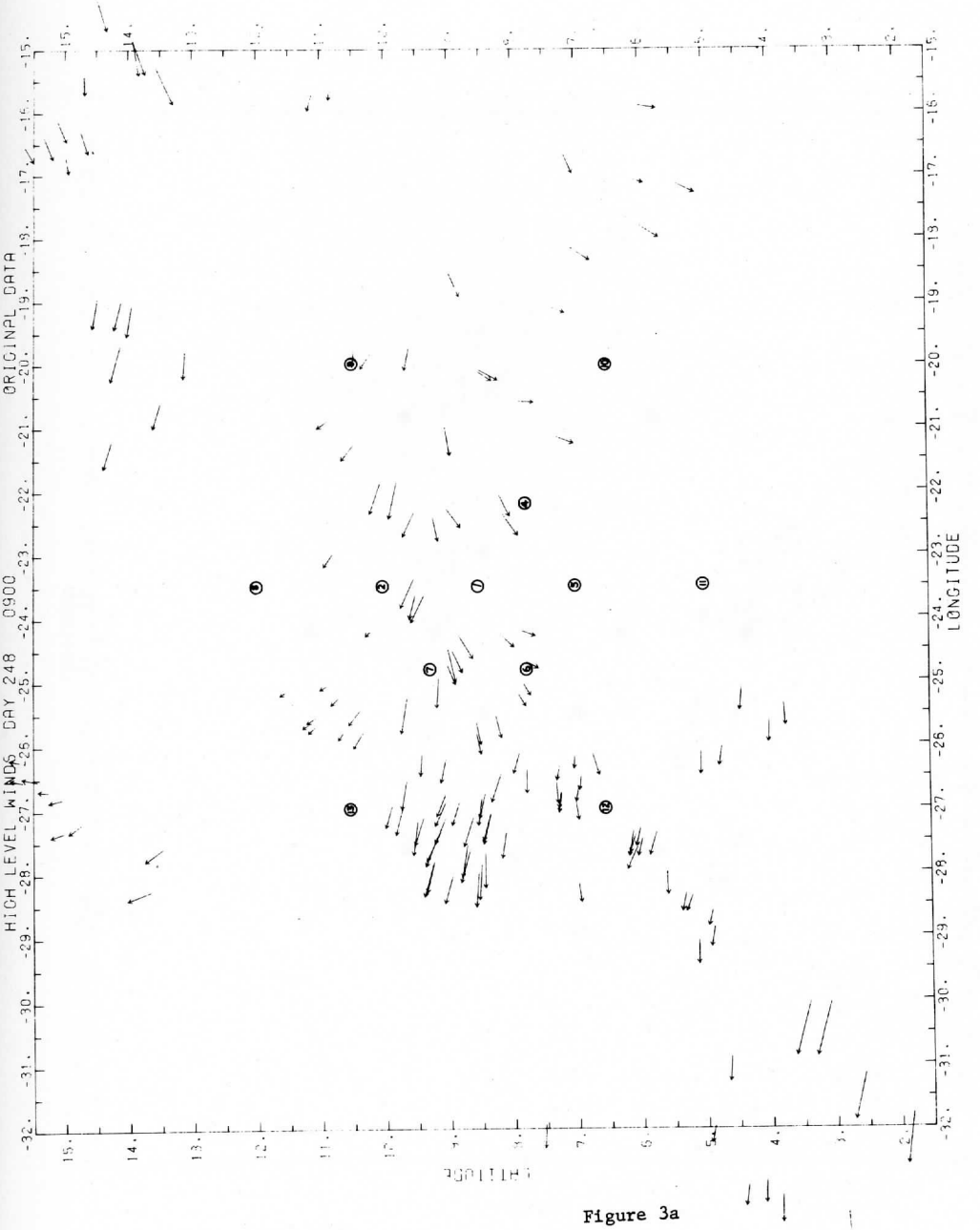
HIGH LEVEL WINDS DAY 248 0900 ORIGINAL DATA
LONGITUDE
LATITUDE

Figure 3a

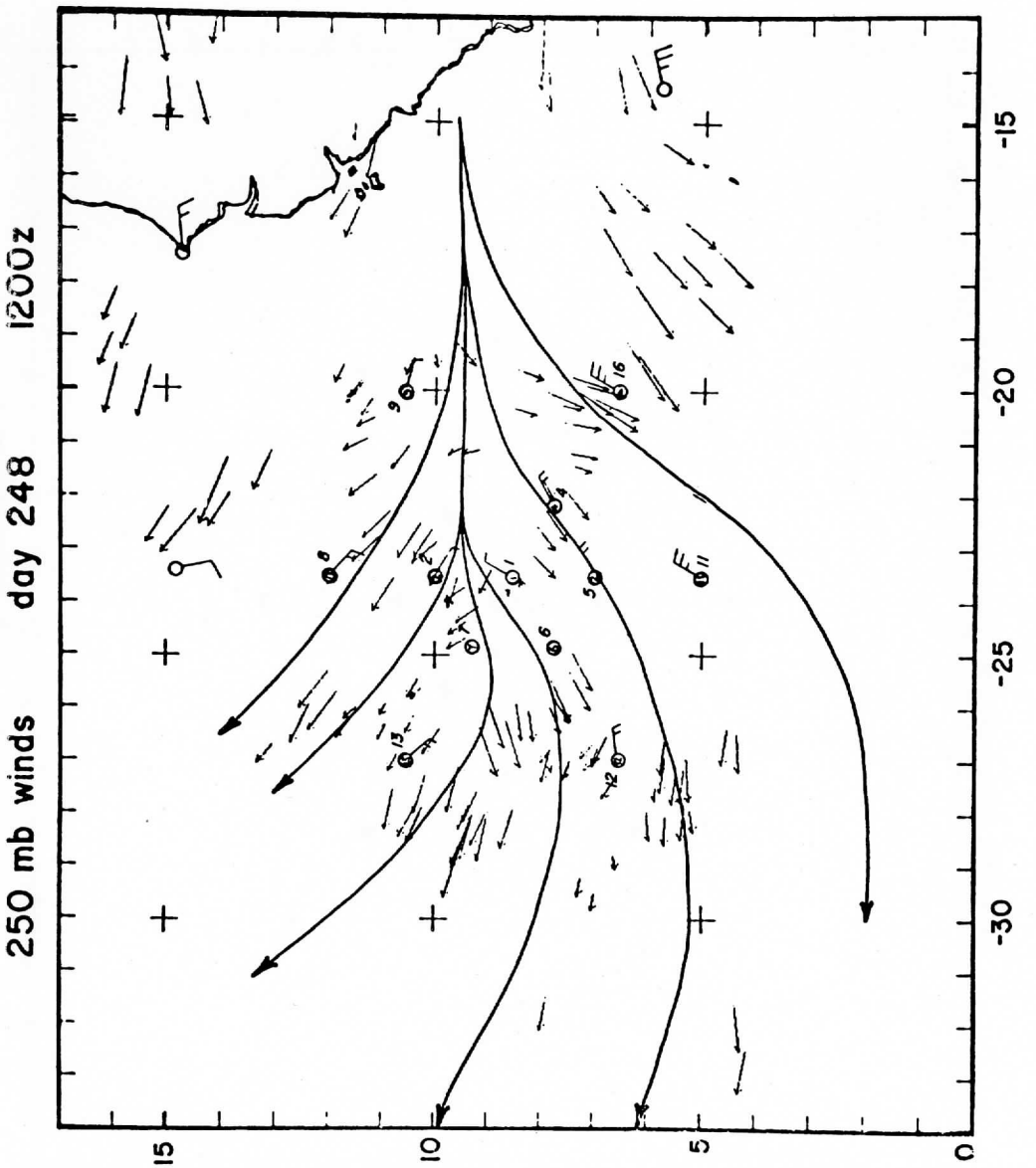


Figure 3b

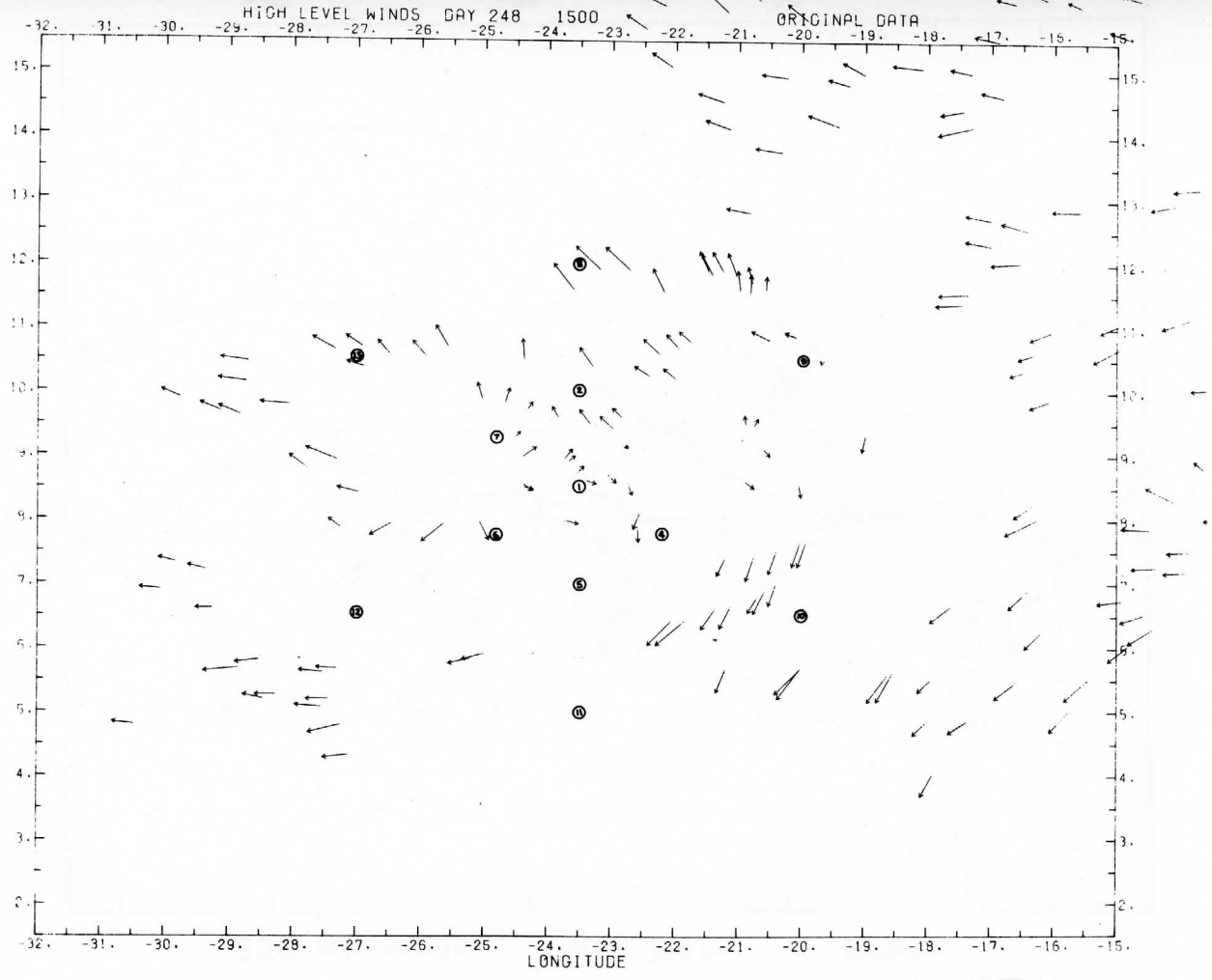
HIGH LEVEL WINDS DAY 248 1500
ORIGINAL DATA
LATITUDE
LONGITUDE
-32. -31. -30. -29. -28. -27. -26. -25. -24. -23. -22. -21. -20. -19. -18. -17. -16. -15.
15. 14. 13. 12. 11. 10. 9. 8. 7. 6. 5. 4. 3. 2.

Figure 3c

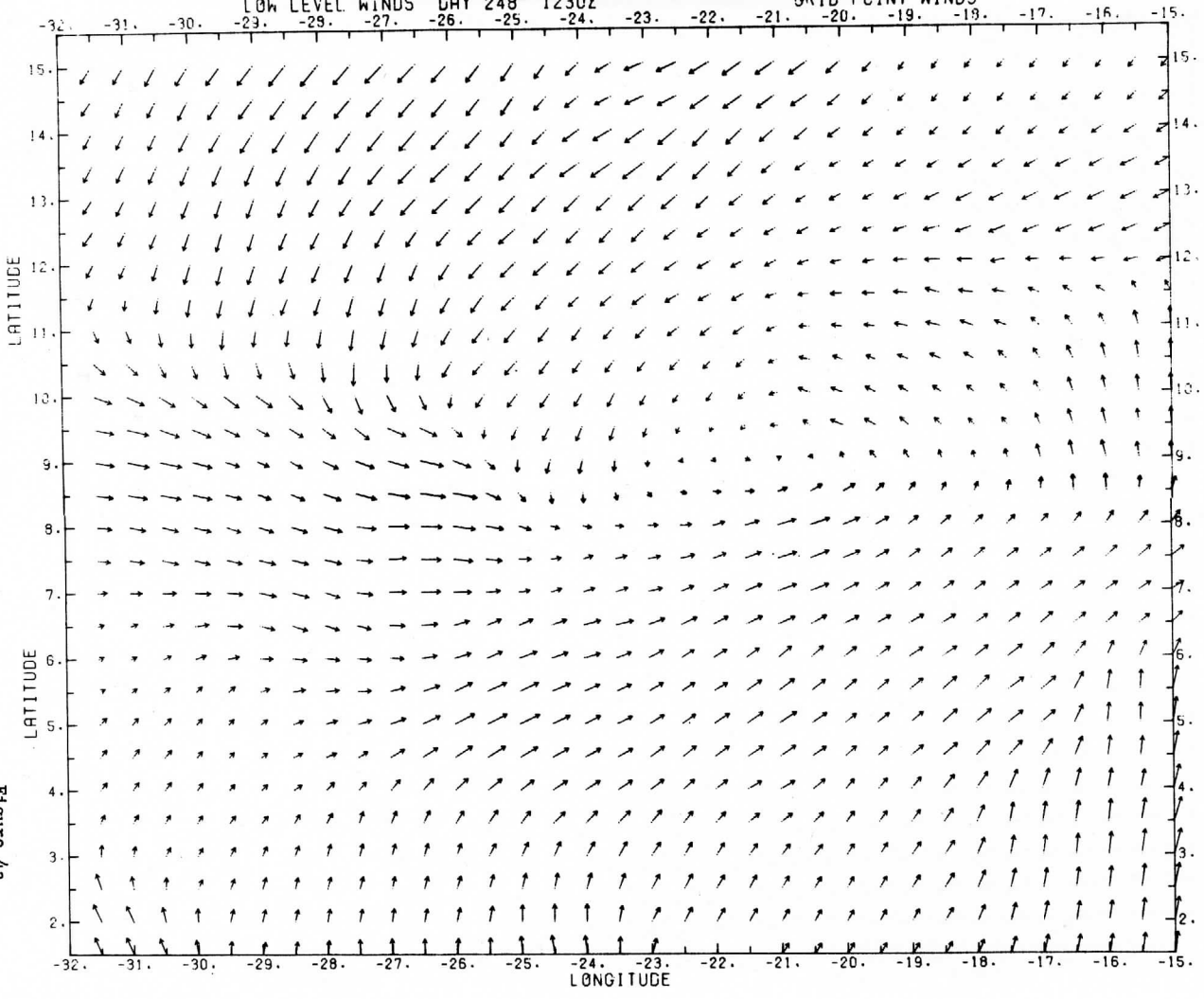
LOW LEVEL WINDS DAY 248 1230Z
GRID POINT WINDS
LATITUDE
LONGITUDE
-32. -31. -30. -29. -28. -27. -26. -25. -24. -23. -22. -21. -20. -19. -18. -17. -16. -15.
15. 14. 13. 12. 11. 10. 9. 8. 7. 6. 5. 4. 3. 2.

Figure 4a

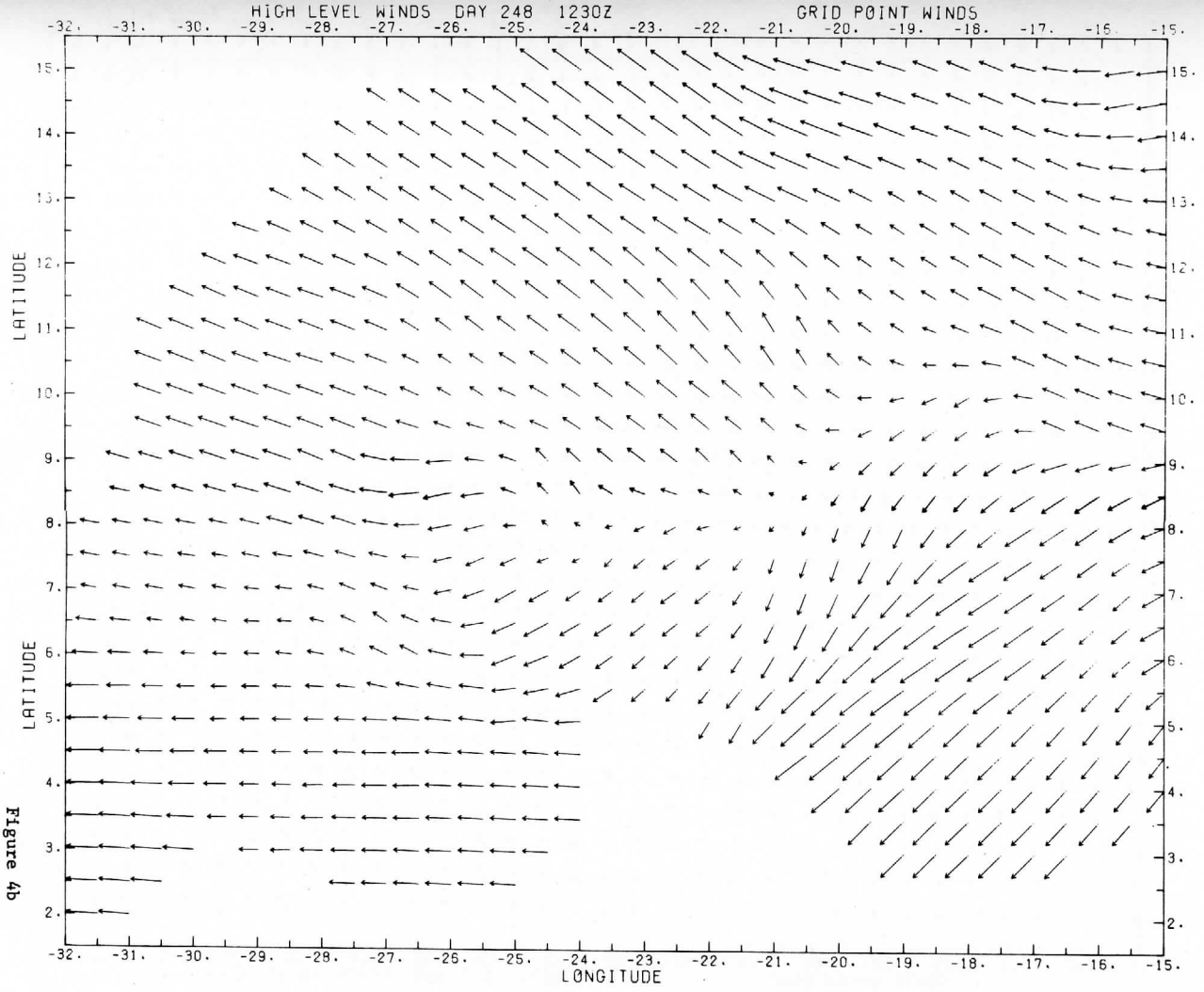
HIGH LEVEL WINDS DAY 248 1230Z
GRID POINT WINDS
LATITUDE
LONGITUDE
-32. -31. -30. -29. -28. -27. -26. -25. -24. -23. -22. -21. -20. -19. -18. -17. -16. -15.
15. 14. 13. 12. 11. 10. 9. 8. 7. 6. 5. 4. 3. 2.

Figure 4b

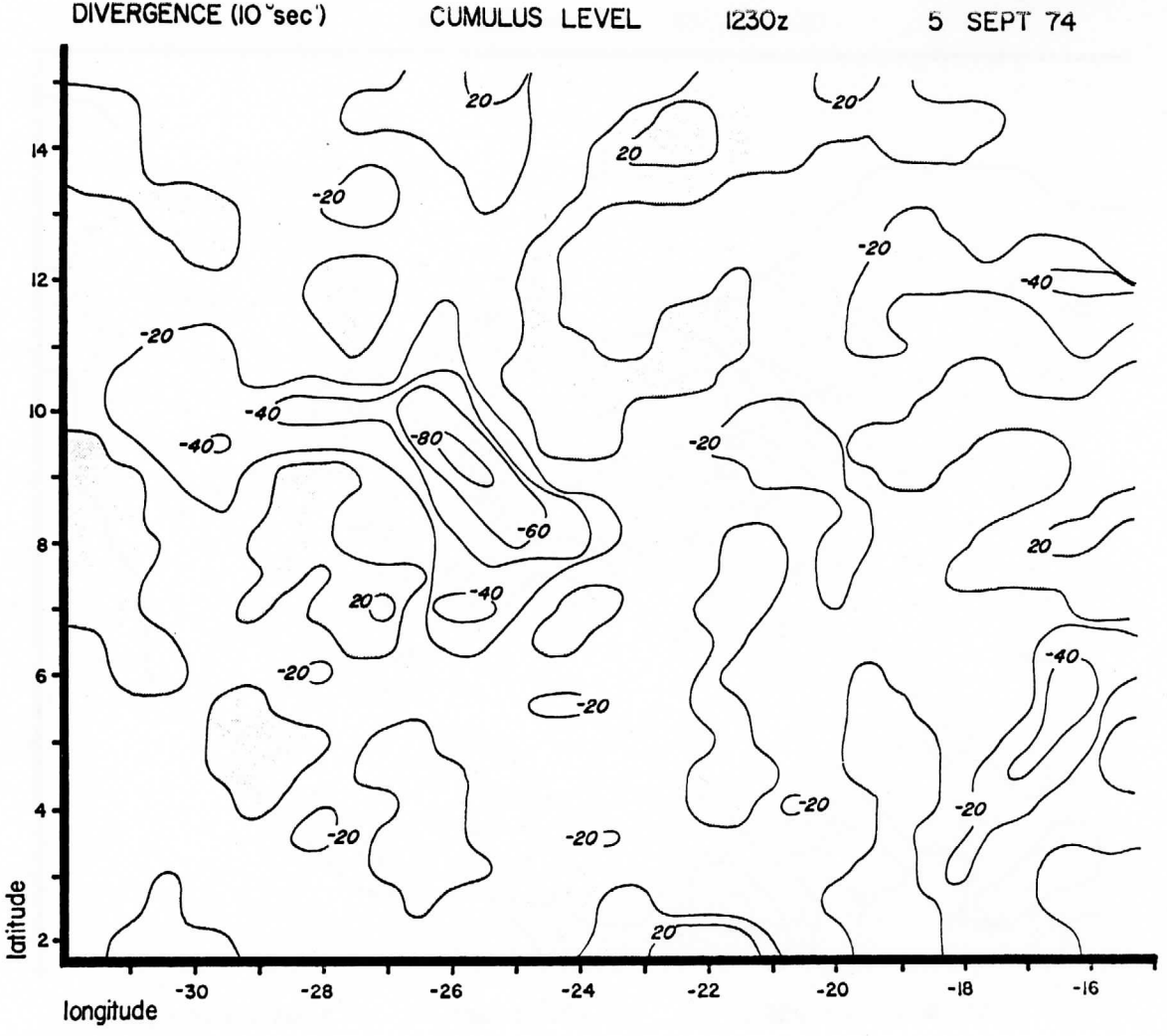
DIVERGENCE (10⁻⁵sec⁻¹)
CUMULUS LEVEL
1230z
5 SEPT 74
latitude
longitude
14
12
10
8
6
4
2
-30
-28
-26
-24
-22
-20
-18
-16
20
-20
-40
-80
-60

Figure 5a

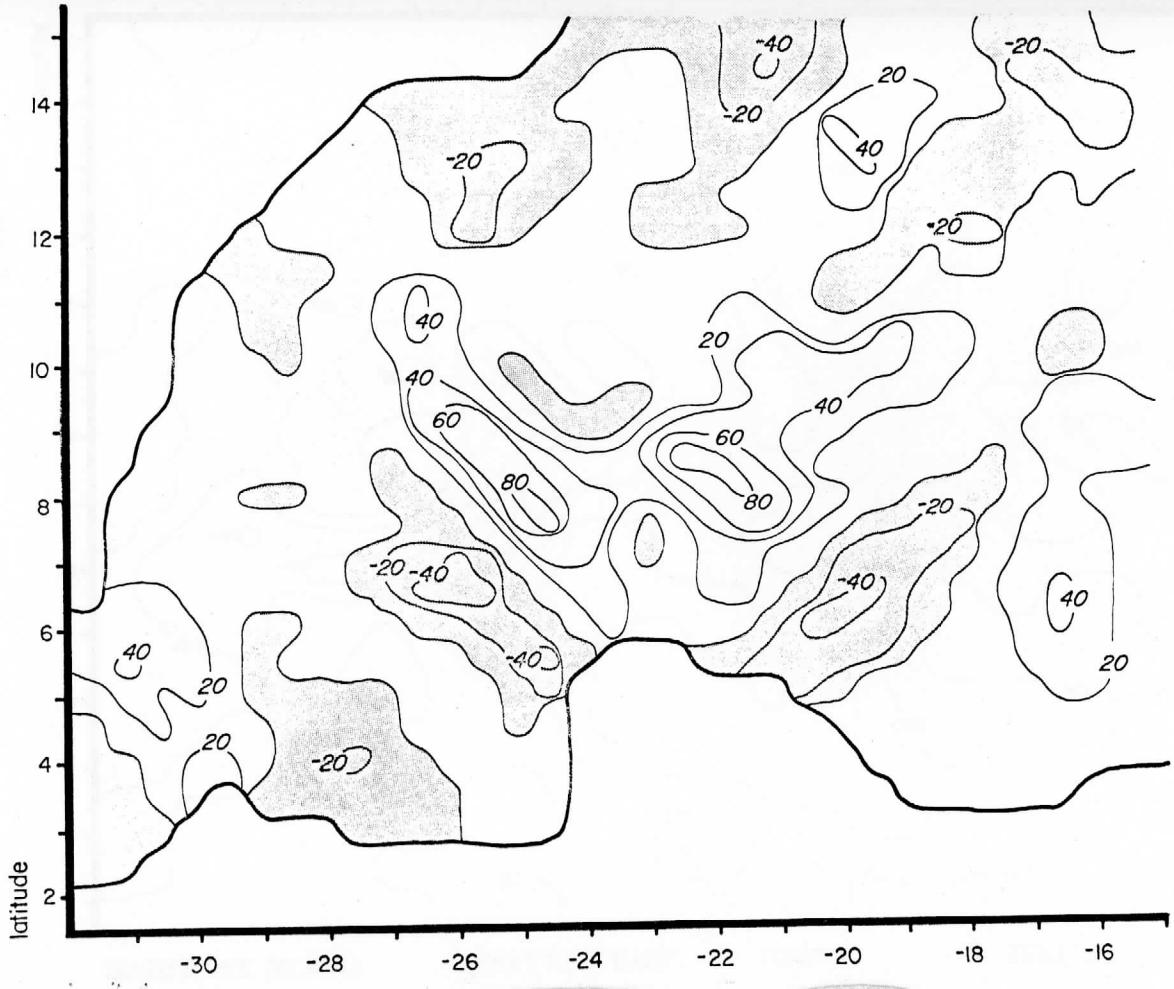
DIVERGENCE (10⁻⁵sec⁻¹)
CIRRUS LEVEL
1230z
5 SEPT 74
latitude
14
12
10
8
6
4
2
-30
-28
-26
-24
-22
-20
-18
-16
-40
-20
20
40
60
80

Figure 5b

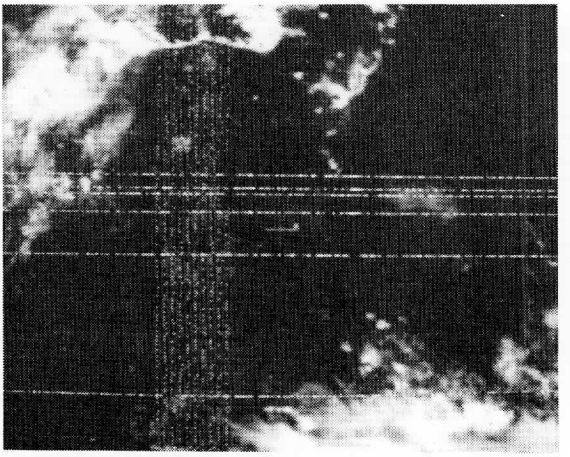


Figure 6a

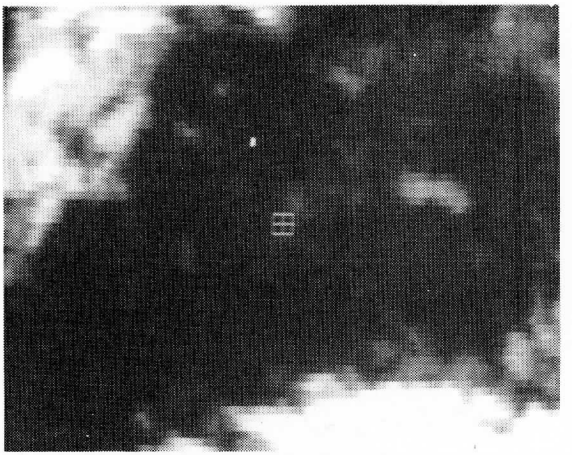

Figure 6b

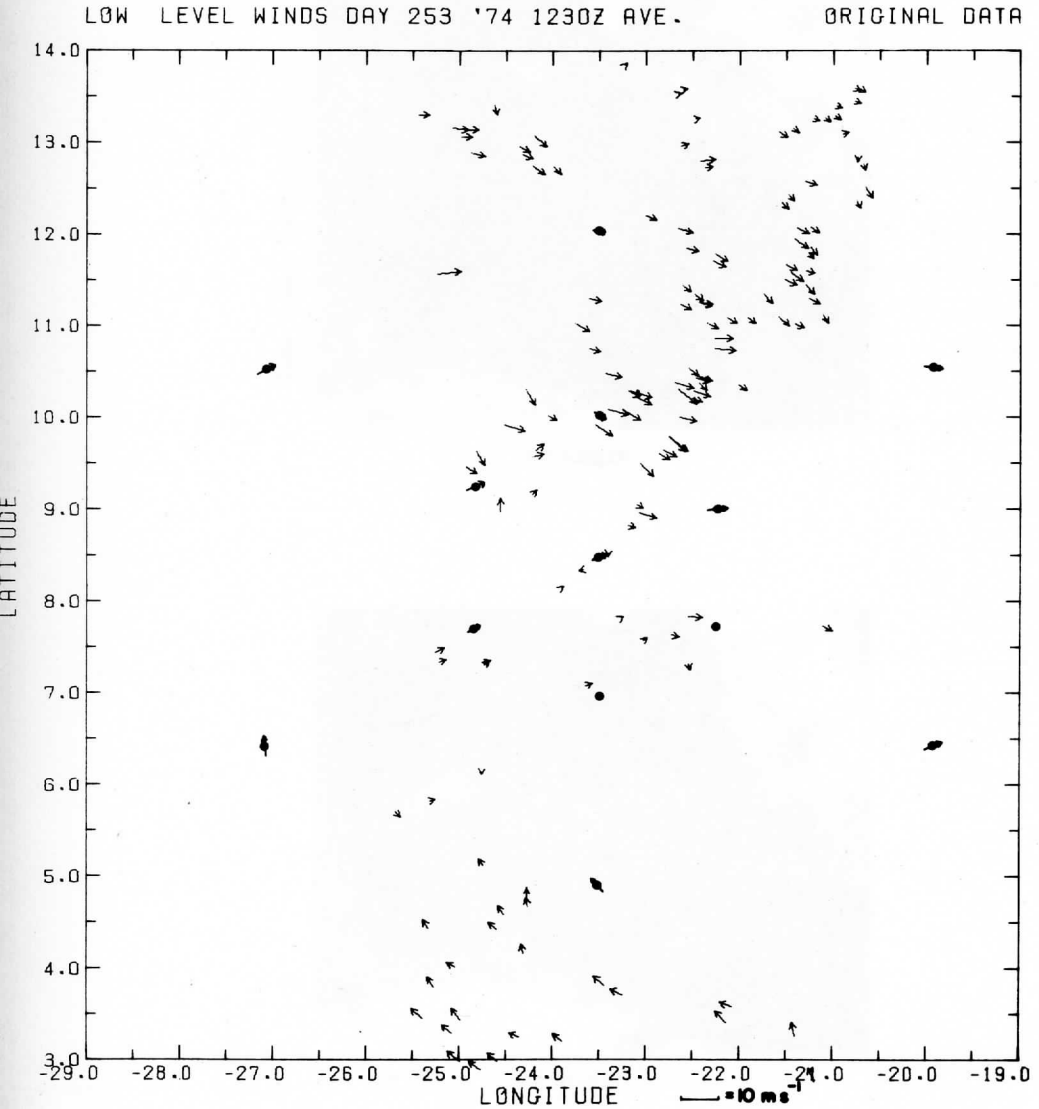
LOW LEVEL WINDS DAY 253 '74 1230Z AVE.
ORIGINAL DATA
14.0
13.0
12.0
11.0
10.0
9.0
8.0
7.0
6.0
5.0
4.0
3.0
LATITUDE
-29.0
-28.0
-27.0
-26.0
-25.0
-24.0
-23.0
-22.0
-21.0
-20.0
-19.0
LONGITUDE
=10 ms-1

Figure 7a

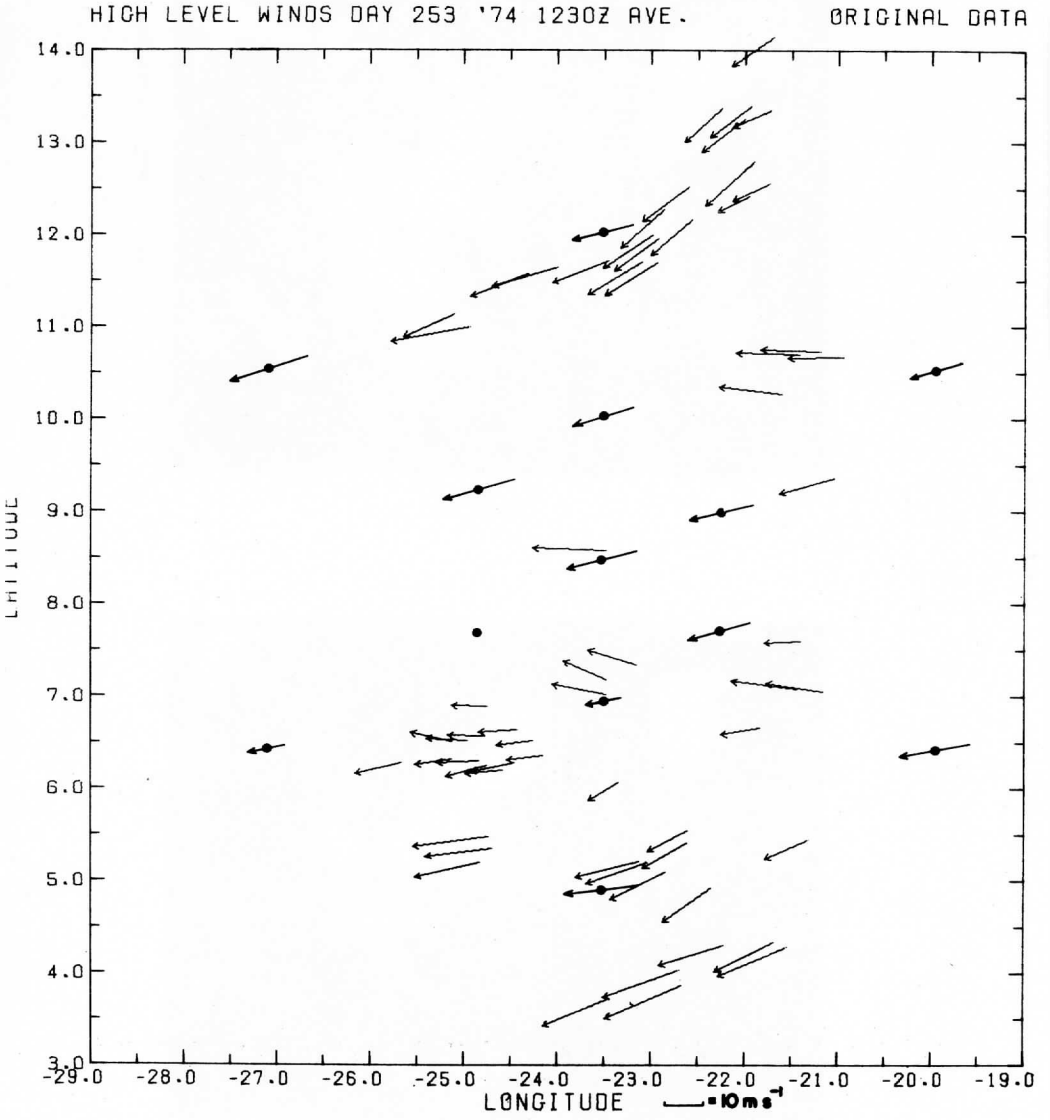
HIGH LEVEL WINDS DAY 253 '74 1230Z AVE.
ORIGINAL DATA
14.0
13.0
12.0
11.0
10.0
9.0
8.0
7.0
6.0
5.0
4.0
3.0
LATITUDE
-29.0
-28.0
-27.0
-26.0
-25.0
-24.0
-23.0
-22.0
-21.0
-20.0
-19.0
LONGITUDE
10ms⁻¹

**Figure 7b**

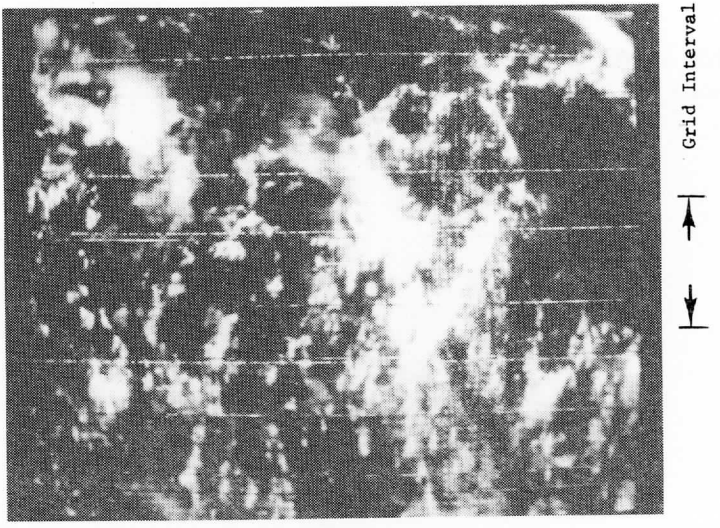


Figure 8a

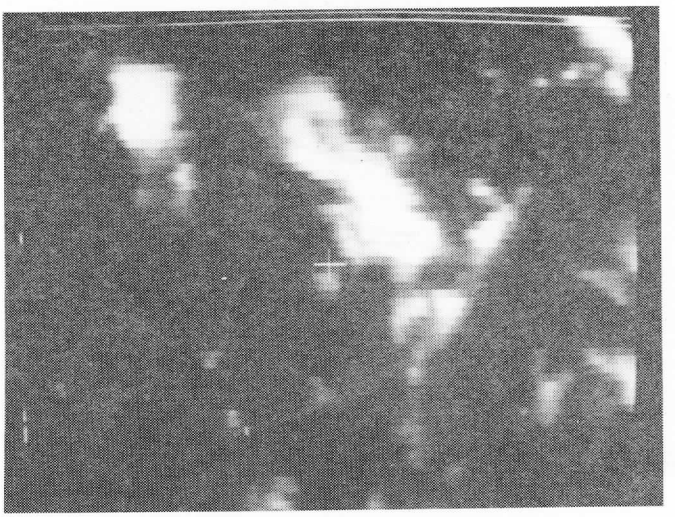

Figure 8b

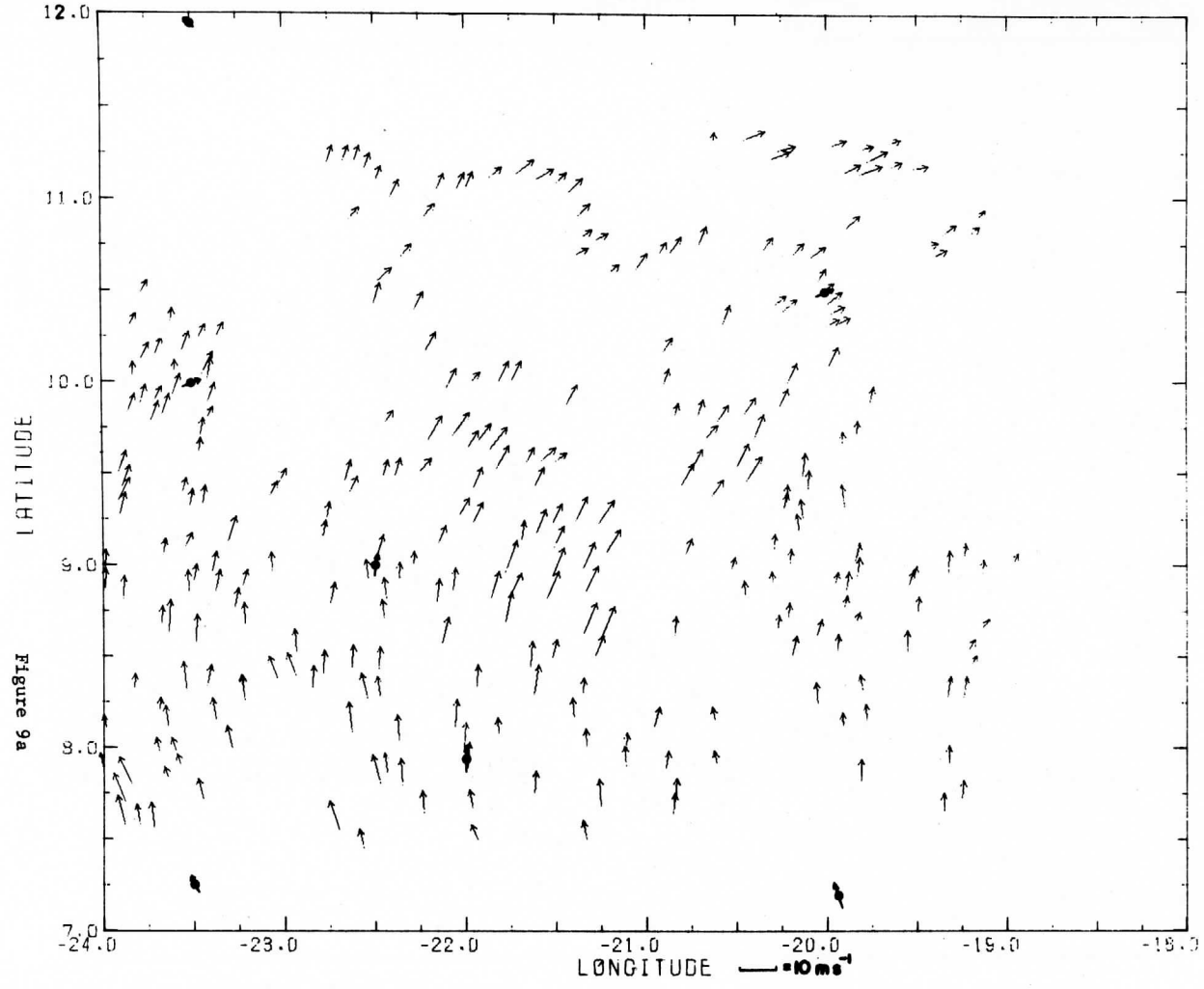
LOW LEVEL WINDS DAY 261 '74 1330Z
ORIGINAL DATA
12.0
11.0
10.0
9.0
8.0
7.0
LATITUDE
-24.0
-23.0
-22.0
-21.0
-20.0
-19.0
-18.0
LONGITUDE
=10 ms⁻¹

Figure 9a

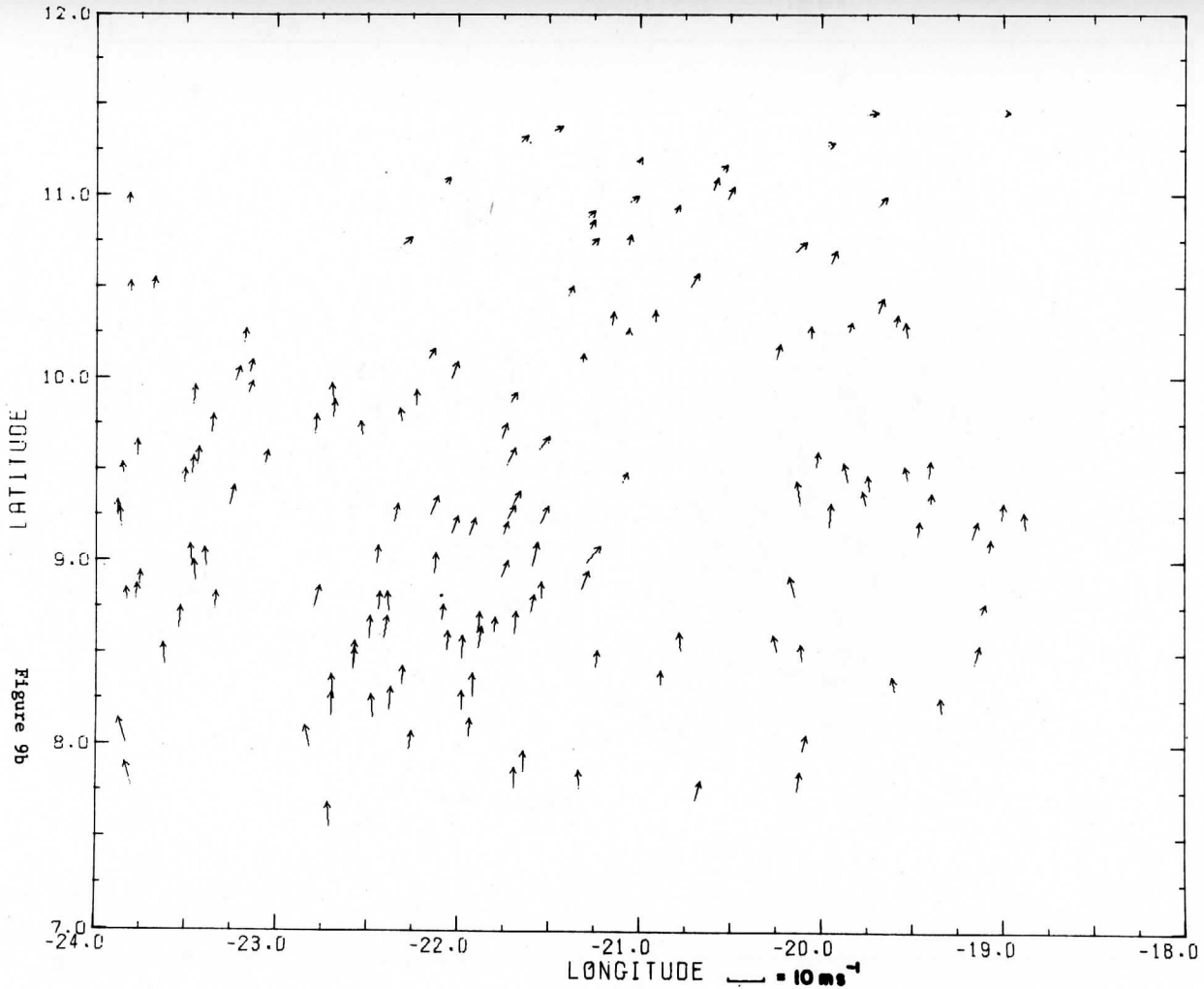
12.0
11.0
10.0
9.0
8.0
7.0
LATITUDE
-24.0
-23.0
-22.0
-21.0
-20.0
-19.0
-18.0
LONGITUDE
= 10 ms⁻¹

Figure 9b

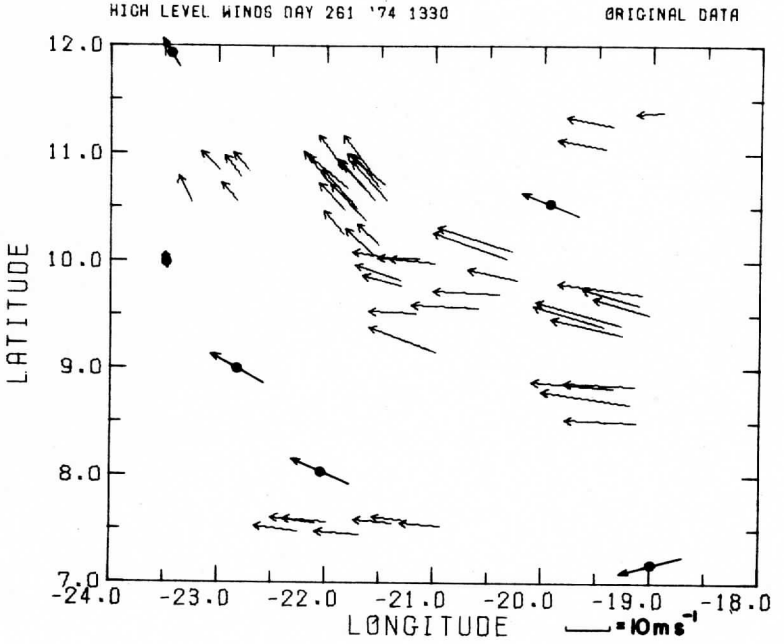


Figure 10a

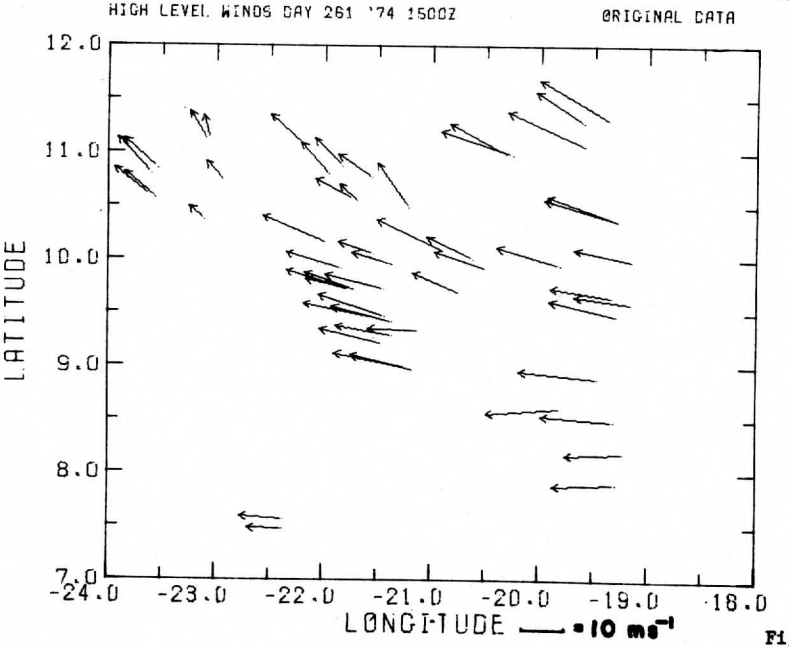


Figure 10b

# CLIMATOLOGY BASED ON WINDS DERIVED FROM CLOUD MOTIONS

Barry B. Hinton

## ABSTRACT

Two data sets were used to derive cloud motion vectors, one for August-September 1975 in the American sector and the other for January-February 1976 in the Pacific sector. The possibility of constructing a climatology of this kind of data was explored. It appears that the meridional motions have different statistical properties than conventional data. It is argued that this is because meridional transport takes place in 'bursts' which are relatively compact in both space and time, and that clouds are correlated with this activity.

## 1. INTRODUCTION

The data bases for most statistical general circulation studies to date have come from the world network of radiosonde stations. Fig. 1, taken from the study by Gray et al. (1976), is typical of the data coverage available. Land areas between 30° and 60°N are well covered, but in general, coverage over ocean areas is unsatisfactory and practically negligible in the Southern Hemisphere. To improve the distribution some researchers have added wind reports from aircraft pilots ('AIREPS' or 'PIREPS'). Fig. 2 illustrates the coverage from this source, also from the work of Gray et al. (1976). Cloud motion vectors previously have been used in the work of Gray et al. (1976), Krishnamurti (1971, 1975) and Gaby and Poteat (1973). All used data from either ATS 1 or ATS 3. These spacecraft had spin scan cameras with sensitivity only in the visible to near infrared band. Techniques were developed for differentiating 'high' clouds from 'low' clouds, and these were generally assigned to 200 mb or 850 mb heights respectively (Hubert and Whitney, 1971).

The present study uses data from SMS/GOES spacecraft which have, in addition to a visible channel, a 'thermal IR' channel near 12 μm, well outside the region of the spectrum seriously contaminated by solar radiation. This permits day and night thermal-IR images in addition to visible images. Using the IR data, cloud temperatures can be measured or estimated--depending upon their thickness--to assist in the assignment of an altitude to the cloud. This may be done using a temperature height profile derived from a model atmosphere, or from an analysis of sounding data. Improved data quality is also obtained as a result of the higher spatial resolution of the images, and improved tracking techniques.

The main purpose of this report is to discover the properties of these satellite derived winds. Consequently, we limit ourselves to comparisons

with conventional data but do not combine data sets. Dyer (1973) showed that statistics derived from constant density superpressure balloons and statistics derived at grid points (i.e. radiosondes) could not be merged in a straightforward fashion. Even though both kinds of measurement are valid, they are of a different nature and this difference must be properly considered. Similarly, cloud motion vectors should be combined with other data only when their nature is understood and considered.

The raw material for the present study are data sets generated in the course of two Data Systems Tests conducted in preparation for the Global Atmospheric Research Program's First GARP Global Experiment. The data were generated on a near real-time basis in an operational environment by teams of operator-analysts using the WINDCO software and the capabilities of the McIDAS system (Chatters and Suomi, 1975). More information on the Data Systems Tests and methods used to generate cloud winds are found in Appendix A.

Numerous papers have been written on general circulation statistics, and many of these have grown out of the work at MIT which recently has been summarized in a two volume monograph (Newell et al., 1972, 1974) emphasizing the latitude band from 50°N to 50°S. It should be noted that the data set covered in this publication has a very high degree of overlap with that discussed by Oort and Rasmussen (1971). Van Loon et al. (1971) have given geostrophic winds for the Southern Hemisphere. At the upper level, observations are available from the EOLE balloons (Morel and Bandeen, 1973), and will soon be available for the TWERLE balloons (TWERLE Team, 1977). Lorenz has provided a comprehensive review of work on the general circulation through about 1970 (Lorenz, 1971). Finally, there are discussions in the reviews of Arakawa (1975) and Yanai (1975) covering work through 1974.

## 2. DATA COVERAGE

To achieve good geographical distribution the spacecraft field of view was divided into 380 'boxes' 5° longitude 'wide' by 5° latitude 'high' by 100 mb thick. The center of this array was the nominal subsatellite point (0°N 75°W for August-September 1975 and 0°N 135°W for January-February 1976). During each data generation period as many winds as possible, up to five, were obtained for each of these boxes. No attempt was made to obtain vectors beyond about 55° satellite-earth zenith angle. The coverage area is illustrated in Appendix B. The maximum number of winds would then be of the order of $16 \cdot 10^3$ per time period or $64 \cdot 10^3$ per day, since winds were obtained four times per day. The actual numbers of wind vectors obtained were much smaller for two reasons. First, at a given time many areas may contain no trackable clouds; second, high clouds will conceal low clouds. A more realistic number of potential observations is $7 \cdot 10^3$ per day. Through the period of each test reasonable geographic coverage was obtained, especially for the 700 mb and 200 mb levels during the August-September test. Somewhat better coverage was obtained at the 700, 800, 900, and 200 mb levels for the January-February test. Tables 1 and 2 summarize the large amount of data available.

In effect the wind measurements are sampled through a 'window' which is a function of cloudiness. This produces a sampling bias,[1] which must be carefully examined.

Cloud free regions are preferentially associated with descending air, implying unobserved convergence at upper levels and divergent motions at lower levels. On the other hand, ascending air will be preferentially associated with high level divergence and lower level convergence. Moreover, it will also be associated with clouds, especially high clouds, which might in turn conceal lower clouds. In the case of either ascending, or descending air, however, there will often be modestly developed cellular tracer clouds at low to middle levels.

## 3. DISCUSSION OF RESULTS

One useful way of looking at general circulation data has been to consider zonal average quantities. For comparison purposes, charts of the u and v velocity components are shown in Figs. 3 through 6. Note that these are not true zonal averages, since they do not represent integrations of u and v over all longitudes. They are weighted by the sampling windows, and are more nearly comparable to a zonal-sector average. In spite of this, we will represent these quantities with notation similar to that usually reserved for zonal averages completely encircling the earth. Thus:

$$[\bar{u}]_s = \sum_{\text{boxes}} n_{box} (\bar{u})_{box} / \sum_{\text{boxes}} n_{box} \qquad (1)$$

$$[\bar{v}]_s = \sum_{\text{boxes}} n_{box} (\bar{v})_{box} / \sum_{\text{boxes}} n_{box} \qquad (2)$$

where the sums extend over all boxes in a latitude band. Symbols are explained in Table 3.

This weighting function is an obvious one and should more clearly show the intrinsic relationship of the clouds to the derived winds. Preliminary investigations with weights proportional to $n_{box}^{1/2}$ or weights of either 0 or 1 (depending on whether $n_{box}$ is greater than a threshold value) did not radically change the zonal averages. There is, however, much need for further investigation on the choice of the best weighting function, and modifications of strategies for obtaining optimum data distributions.

---

[1] Note that this bias is a matter entirely distinct from the accuracy of the winds. When tracers are properly selected Bauer's (1976) results indicate that cloud winds are about as accurate as radiosonde winds.

The basic structure of $[\bar{u}]_s$ in Figs. 3 and 5 is similar to the comparison data reproduced in Appendix C.

The results of $[\bar{v}]_s$ (Figs. 4 and 6) require more discussion since there are qualitative disagreements with some of the comparison data (Appendix C). Another way of investigating $[\bar{v}]_s$ is to consider $\psi$, the mass flux across a latitude circle in the 'slab' of atmosphere between pressure level $p_0$ and p. If $p_0$ is the surface and p is an arbitrary altitude, then

$$\psi = \frac{2\pi a \cos\phi}{g} \int_{p_1}^{p_0} [\bar{v}]\, dp \qquad (3)$$

If p is 0, or small enough that most of the atmosphere lies between $p_0$ and p, we expect that $\psi$ will also be 0 or very small. If p is not small, then air is "piling up" somewhere. Thus, we can investigate the meridional circulation of Figs. 4 and 6 by summing the $[\bar{v}]_s$ values over pressure at each latitude to obtain $\psi^*$. It follows from (3) that

$$\psi^* \approx \psi g/(2\pi a) \qquad (4)$$

In Figs. 8 and 9, we see that $\psi^*$ is not small at 100 mb at most latitudes.

This reflects the fact that the net upper level divergence (or convergence) in the data is not balanced by lower level convergence (or divergence) in the data. The two most likely reasons for this are:

- The 'cloud bias problem' mentioned above
- The fact that the convergence or divergence of the zonal velocity over the sector is ignored.

The first item partially derives from the choice of weighting function in constructing the quasi-zonal averages in this paper. Each longitude is in effect weighted by the number of measurements. It should be recalled, however, that in the derivation of the data, an attempt was made to weight each box equally and not 'pile up' more than five vectors per box per time period. The weight is proportional to cloudiness when there are few clouds, but attains a constant value when many trackable clouds are available. Clouds do not have the same conservative properties as air. It is possible to have a net flow across latitude circles, since clouds can be created preferentially at one latitude, then advected to, and destroyed at another latitude.

The second item is complicated by the mountain ridges of the continents, particularly the Andes, which constitute a barrier which may effect an appreciable low level convergence in the u-component. Fig. 7 shows that over much of South America this barrier exceeds 700 mb.

Many writers avoid discussing divergences, possibly since the v-values are mistrusted a priori. Two works which have considered them (or equivalently, $\omega$, the vertical motion in pressure coordinates) found it necessary to intervene in the analysis. In Oort and Rasmussen (1971) we find:

> "For the $\bar{u}$ and $\bar{v}$-fields, the monthly mean divergence was calculated; and if it was larger in absolute value than $5 \cdot 10^{-6}$ sec$^{-1}$, the divergent part of the u- and v-analyses in the vicinity of these regions was corrected."

For all transport calculations they used modified or 'balanced' values for $[\bar{v}]$. To insure 'nice winds' some workers have preferred to consider only geostrophic components (Van Loon et al., 1971). Newell et al. (1972) calculated a first guess at $\omega$, the vertical motion in pressure coordinates, from the divergence of u and v, which they then modified by constraining it to be zero at 1000 mb (not necessarily the surface) and at 100 mb. The adjustment was related in a linear fashion to pressure, according to the relation:

$$\bar{\omega}_{adj} = \bar{\omega}(p) - \bar{\omega}(100)(1000 - p)/(1000 - 100) \qquad (5)$$

They go on to argue that even if the entire globe were covered as densely with data points as the United States, the uncertainty of $[\bar{v}]$ would still be comparable to the magnitude of $[\bar{v}]$ at mid-latitudes. The situation is most unsatisfactory at 200 mb. The meridional winds from cloud motions seem to balance about as well as those that Newell et al. (1972) present for specific longitude sectors. (These figures are not reproduced here.)

Considering all these difficulties concerning the balancing of the $[\bar{v}]_s$ values, consider the qualitative nature of the circulation illustrated in Figs. 4 and 6. Surprisingly, both show a circulation with a significant direct component extending poleward to $\pm 50°$ latitude below about 400 mb. A possible explanation is that this is an eddy process which appears in zonal mean cloud winds because the clouds are correlated with the eddy motions of 40°.

Figs. 10 through 13 which show the standard deviations of $[\bar{u}]$ and $[\bar{v}]$ generally agree with comparison data, as found in Newell et al. (1972) for example. Typically, the standard deviation of $[\bar{v}]$ is larger than the value of $[\bar{v}]$, but for $[\bar{u}]$ the situation is quite different. For the most part $[\bar{u}]$ is larger than its standard deviation, though this cannot be true in the regions where $[\bar{u}]$ changes sign and has a very small value. In general then, $[\bar{u}]$ at a given latitude is an average over u values of about the same magnitude and the same sign. The value of $[\bar{v}]$, at a given latitude, tends to be the residual of somewhat larger magnitudes of v of both signs in roughly equal numbers. Because the standard deviation of $[\bar{v}]$ tends to be larger than $[\bar{v}]$, a modest correlation of v with cloudiness will influence

the observed values of v and thus $[\overline{v}]_s$. A similar logic applies to functions containing v raised to odd powers, such as $[\overline{uv}]$.

Fig. 14 shows the $[\overline{uv}]$ results for the August-September data. This conforms to the pattern seen in other studies, in that there are maxima of positive values in the northern hemisphere near 40°, one over the equator and another in the southern hemisphere poleward of about 50°S. There is a single peak of negative values at mid-latitudes in the southern hemisphere, and negative values poleward of 50°N in the northern hemisphere. The numerical value of $[\overline{uv}]$ over the equator compares well with other data (e.g. Newell et al., 1972). Elsewhere, however, the present study obtains much larger magnitudes. This disagreement might come in part from the longitudinal variations expected for $[\overline{uv}]$.

The peak in the August-September data near 33° latitude at 400 mb arises mainly from cloud data between 47 and 72°W longitude in the domain of strong westerlies. Thus, many of these data are found in the 1500 km immediately downwind of the ridge of the Andes reaching about 3000 m (or 700 mb) and lining up with Cerro Mercedario at 70°W, 32°S, Cerro Aconcagua at 68°W, 33°S, and Portezuelo d. Tupungato at 70°W, 34°S all of which exceed 6950 m (~420 mb) in altitude. Numerous other features lie above 5000 m (~540 mb) in this region. These orographic features provide torques and probably modify the cloud population available for tracking. This region does not provide a rich supply of clouds, as reflected in the relatively small number of samples available at this latitude (Table 2). Most originate in a contiguous three day time period. Even if the single large value at 35°S, 400 mb is argued away, all regions, except over the equator, still show unexpectedly large magnitudes.

For the January-February data (Fig. 15) we obtain a similar result. The pattern is quite consistent with other work, but the magnitudes seem large. In fact, the same maximum value of about 350 $m^2 \cdot s^{-2}$ now appears at mid-latitudes in the northern hemisphere. In this case the data are distributed more evenly in both longitude and time, and roughly twice as many samples are available. A positive correlation of trackable cloud with poleward v-values provides a simple explanation.

Now let us consider variations with longitude as well as latitude. Plots of the u and v fields may be found in Appendix B. It is impossible to present a detailed written comparison with other data, so we shall limit the discussion to a few general remarks.

The broad patterns of the $\overline{u}$ values seem reasonably consistent with prior work. The patterns of $\overline{v}$-values can be rationalized in terms of the typical patterns of cloudiness, and can be accommodated to the figures in Newell et al. (1972) with some distortions over land. But the $\overline{v}$ patterns are often much different over the oceans. This is not surprising, considering the distribution of conventional data available. The study of Gray et al. (1976) also incorporated cloud motions and pilot reports to some degree. Subjective comparison with their results shows their 200 mb winter fields agree except with respect to the magnitudes of $\overline{v}$, which are larger in the

present study. The 700 mb winter data for $\bar{v}$ seem to have few distinctive features in common; $\bar{u}$ values of the present study appear to be greater. With respect to the summer data at 700 mb, we find similarity in both the $\bar{u}$ and $\bar{v}$ fields, but some disparity in magnitude; the values of Gray et al. again seem a little weaker. The same is true for the summer 200 mb $\bar{u}$ and $\bar{v}$-values.

It should be noted that the fields of Gray et al. are based on the NMC operational objective tropical analysis which may tend to lessen the spatial modulation of the component fields. On the other hand, we preferred to let the data 'speak for themselves' at this stage in order to better understand the physical content, though objective analysis is a valuable and appropriate tool.

## 4. INTERPRETATION

Two reasons (among several) for using an objective analysis scheme are to excise inconsistent data, and to eliminate 'unwanted eddies', or 'turbulence', on some scale. One can hardly argue with the first objective. Once the nature of cloud winds and the purpose for which they are to be used are understood, appropriate constraints should be applied. We shall see below that cloud winds may be intimately related to "turbulence", and that it may be possible to exploit this relationship to more clearly understand the fundamental processes of the atmosphere.

Ramage (1976) has reconsidered the role of atmospheric turbulence. Conventionally, it is supposed that turbulence might be accounted for by including the appropriate eddy coefficients in the Navier-Stokes equations. However, considering the work of Mollo-Christensen, Ramage points out that turbulence is anisotropic and intermittent, or occurs in 'bursts' producing "most of the fluid's Reynolds stresses in less than 10 percent of the time." This intermittency is presumed to arise by nonlinear interactions. Atmospheric motions possess extreme Reynolds numbers, are stratified, contain shear, latent heat, and convective instability zones. They meander and they contain waves that can transmit energy over long distances. Furthermore, these processes may dominate the transport of properties between fluid masses.

Ramage then points out two examples of intermittent turbulent processes. One, (quoted from the work of Gentey et al., 1970) concerning Hurricane Gladys revealed that,

> "....within the radius of surface winds exceeding 15 m $s^{-1}$, all the surface convergence was concentrated in a single massive cloud, occupying only 7% of the area, while within that cloud only a few percent of the area was occupied by active cloud towers."

The second example is the "hot tower" hypothesis in which Riehl and Malkus (1961) postulated intense cumulonimbus clouds to supply energy needed at higher latitudes. They calculated that only 1500 to 5000 of these clouds, occupying 0.7 percent of the zone 10°N to 10°S, would be required.

In regions of surface convergence, buoyant forces generated by condensation would seem to stimulate burst generation. A subsiding region with upper level convergence inhibits condensation, or even encourages evaporation. In brief, turbulent bursts are to be associated with clouds--especially deep convective clouds--and with the fundamental transport processes.

This picture is in general agreement with the results given above showing surprisingly vigorous meridional transports associated with the cloud motion vectors. It also agrees with the qualitative circulation system we derived from the cloud motion vectors. This indicated a direct circulation system linking the equatorial tropics and mid-latitudes. This is probably an eddy process, and it appears in the data because of correlations of cloudiness with the winds--especially the v-component. It is especially important to note that this in no way prohibits a proper use of cloud motion vectors as data for initializing numerical models or other purposes. At the time and place of the observation, a properly selected and tracked cloud represents air parcel motion very well.

We have shown that a coherent cloud motion vector climatology is feasible. A continuing climatology of cloud winds should be useful for understanding basic transport processes. Based on the results of this simple pilot study, there should be further development of methods to insure uniform and consistent sampling, and of methods to interpret the observations in order to realize the potential benefits of such a climatology. For example, the implications of other weighting functions should be explored.

## ACKNOWLEDGEMENTS

**This research was supported by National Aeronautics and Space Administration Contract NAS5-21798. We are grateful to Dick Daly for programming assistance, and to the Goddard Institute for Space Studies for their cooperation in facilitating data analysis. Thanks are due as well to Fred Mosher for supplying the information in Appendix A.**

## REFERENCES

Arakawa, A., 1975: General Circulation of the Atmosphere. Rev. Geophys. and Space Phys., (13), 668-680.

Bauer, K., 1976: A Comparison of Cloud Motion Winds with Coinciding Radiosonde Winds. Mon. Wea. Rev., (104), 922-931.

Chatters, G. C. and V. E. Suomi, 1975: The Applications of McIDAS. IEEE Trans. Geoscience Electronics, (GE 13), 137-146.

Dyer, A. J., 1973: Do GHOST Balloons Measure Eulerian Mean Velocities? J. Atmos. Sci., (30),510-513.

Gaby, D. C., and K. O. Poteat, 1973: ATS-3 Satellite-derived Low-Level Winds: A Preliminary Climatology. J. Appl. Met., (12), 1054-1061.

Gray, T. I. Jr., J. R. Irwin, A. F. Kruger and M. S. Varnadore, 1976: Average Circulation in the Tropopause Over the Tropics, January 1968-August 1972, NOAA, U.S. Dept. of Commerce, Supt. of Documents, U.S. GPO, Washington, D.C.

Hubert, L. F. and L. F. Whitney, Jr., 1971: Wind Estimation from Geostationary Satellite Pictures. Mon. Wea. Rev., (99), 665-672.

Krishnamurti, T. N., 1971: Observational Study of the Tropical Upper Tropospheric Motion Field During the Northern Hemisphere Summer. J. Appl. Met., (96), 197-207.

Krishnamurti, T. N., E. G. Astling, M. Kanamitsu, 1975: 200 mb Wind Field: June, July, August 1972. Rept. Dept. of Meteorology, Florida State University.

Lorenz, E. N., 1971: The Nature of the Global Circulation of the Atmosphere: A Present View, in The Global Circulation of the Atmosphere, World Meteorological Organization, Geneva.

Morel, P. and W. Bandeen, 1973: The EOLE Experiment: Early Results and Current Objectives. Bull. Am. Met. Soc., (54), 298.

Morel, P. and M. Desbois, 1974: Mean 200 mb Circulation in the Southern Hemisphere Deduced from EOLE Balloon Flights. J. Atm. Sci., (31), 394-407.

Newell, R. E., J. W. Kidson, D. G. Vincent and G. J. Boer, 1972, 1974: The General Circulation of the Tropical Atmosphere. The Massachusetts Institute of Technology Press, Cambridge, Mass. Vol. 1, 1972; Vol. 2, 1974.

Oort, A. H. and E. M. Rasmusson, 1971: Atmospheric Circulation Statistics. NOAA Professional Paper 5, U.S. Dept. of Commerce, Supt. of Documents, U.S. GPO, Washington, D.C.

Ramage, C.S., 1976: Prognosis for Weather Forecasting. Bull. Am. Met. Soc., (57), 4-10.

Riehl, H. and J.S. Malkus, 1961: On the Heat Balance in the Equatorial Trough Zone. Geophysica, (6), 503-538.

Sadler, J. C., 1972: The Mean Winds of the Upper Troposphere Over the Central and Eastern Pacific. Tech. Paper No. 8-72, Environmental Prediction Research Facility, Naval Postgraduate School, Monterey, Cal.

TWERLE Team, 1977: The TWERLE Experiment, Submitted to Bull. Am. Met. Soc.

Van Loon, H., J.J. Taljaard, R.L. Jenne and H.L. Crutcher, 1971: Climate of the Upper Air: Vol. II - Zonal Geostrophic Winds. NCAR TN/STR-57, National Center for Atmospheric Research, Boulder, Colorado.

Yanai, M., 1975: Tropical Meteorology. Rev. Geophys. and Space Phys., (13), 685-710.

Table 1. Number of observations in each latitude band at each altitude for the August-September data.

| Lat. | Ht. (mb) 100 | 200 | 300 | 400 | 500 | 600 | 700 | 800 | 900 | Total |
|---|---|---|---|---|---|---|---|---|---|---|
| -60 | 0 | 0 | 66 | 320 | 96 | 76 | 82 | 130 | 66 | 836 |
| -55 | 0 | 0 | 243 | 387 | 136 | 64 | 120 | 166 | 81 | 1197 |
| -50 | 0 | 31 | 288 | 455 | 167 | 144 | 101 | 150 | 107 | 1443 |
| -45 | 0 | 263 | 104 | 312 | 152 | 120 | 160 | 370 | 75 | 1556 |
| -40 | 1 | 309 | 0 | 265 | 115 | 100 | 257 | 661 | 109 | 1817 |
| -35 | 0 | 139 | 22 | 111 | 43 | 99 | 270 | 804 | 132 | 1620 |
| -30 | 0 | 32 | 91 | 11 | 31 | 103 | 58 | 525 | 112 | 963 |
| -25 | 0 | 107 | 242 | 110 | 44 | 148 | 568 | 3284 | 273 | 4776 |
| -20 | 0 | 167 | 182 | 91 | 138 | 184 | 3262 | 755 | 23 | 4802 |
| -15 | 223 | 142 | 344 | 186 | 201 | 194 | 3400 | 393 | 38 | 5121 |
| -10 | 850 | 135 | 356 | 205 | 412 | 223 | 2670 | 321 | 35 | 5207 |
| - 5 | 230 | 70 | 13 | 52 | 97 | 67 | 397 | 64 | 0 | 990 |
| 0 | 12 | 1332 | 338 | 283 | 612 | 315 | 1194 | 502 | 179 | 4767 |
| 5 | 16 | 2282 | 464 | 326 | 484 | 267 | 396 | 257 | 113 | 4605 |
| 10 | 75 | 2684 | 374 | 241 | 254 | 149 | 403 | 460 | 211 | 4851 |
| 15 | 30 | 1844 | 260 | 156 | 228 | 172 | 626 | 677 | 287 | 4280 |
| 20 | 14 | 550 | 174 | 72 | 95 | 42 | 242 | 281 | 164 | 1634 |
| 25 | 20 | 1239 | 382 | 204 | 186 | 86 | 421 | 511 | 322 | 3371 |
| 30 | 2 | 1011 | 303 | 154 | 144 | 85 | 408 | 411 | 208 | 2726 |
| 35 | 2 | 823 | 357 | 240 | 152 | 93 | 348 | 267 | 112 | 2394 |
| 40 | 1 | 666 | 432 | 234 | 196 | 82 | 245 | 167 | 44 | 2067 |
| 45 | 0 | 381 | 405 | 146 | 217 | 107 | 171 | 82 | 13 | 1522 |
| 50 | 0 | 162 | 426 | 165 | 160 | 89 | 139 | 32 | 5 | 1178 |
| 55 | 0 | 54 | 283 | 86 | 70 | 41 | 58 | 14 | 0 | 606 |
| Total | 1476 | 14423 | 6149 | 4812 | 4430 | 3050 | 15996 | 11284 | 2709 | 64329 |

Table 2. Number of observations in each latitude band at each altitude for the January-February data.

| Lat. | Ht. (mb) 100 | 200 | 300 | 400 | 500 | 600 | 700 | 800 | 900 | Total |
|---|---|---|---|---|---|---|---|---|---|---|
| -60 | 0 | 0 | 0 | 4 | 0 | 0 | 0 | 1 | 5 | 10 |
| -55 | 18 | 88 | 367 | 360 | 142 | 66 | 55 | 25 | 519 | 1640 |
| -50 | 34 | 206 | 846 | 556 | 146 | 114 | 198 | 78 | 976 | 3154 |
| -45 | 43 | 393 | 1039 | 538 | 79 | 151 | 350 | 193 | 1263 | 4049 |
| -40 | 89 | 739 | 1078 | 362 | 102 | 251 | 566 | 267 | 1767 | 5221 |
| -35 | 161 | 1574 | 1074 | 276 | 94 | 484 | 679 | 328 | 2426 | 7096 |
| -30 | 235 | 2169 | 595 | 180 | 72 | 473 | 1022 | 385 | 2219 | 7350 |
| -25 | 562 | 3758 | 800 | 262 | 111 | 459 | 1884 | 622 | 3215 | 11673 |
| -20 | 456 | 3531 | 681 | 254 | 76 | 105 | 1448 | 424 | 2737 | 9712 |
| -15 | 245 | 2558 | 488 | 273 | 136 | 60 | 1305 | 563 | 3218 | 8846 |
| -10 | 55 | 1256 | 351 | 433 | 297 | 80 | 935 | 515 | 3456 | 7378 |
| - 5 | 11 | 291 | 93 | 140 | 130 | 64 | 390 | 223 | 1623 | 2965 |
| 0 | 3 | 1010 | 434 | 365 | 402 | 425 | 1413 | 581 | 2444 | 7077 |
| 5 | 2 | 1729 | 589 | 360 | 342 | 271 | 1180 | 431 | 2100 | 7004 |
| 10 | 7 | 1967 | 588 | 366 | 179 | 113 | 947 | 397 | 2210 | 6774 |
| 15 | 25 | 2016 | 836 | 309 | 106 | 94 | 771 | 364 | 2415 | 6936 |
| 20 | 32 | 2465 | 1302 | 352 | 159 | 223 | 959 | 357 | 3348 | 9197 |
| 25 | 33 | 1762 | 1238 | 389 | 156 | 107 | 542 | 292 | 2457 | 6976 |
| 30 | 100 | 1153 | 1549 | 622 | 328 | 171 | 240 | 171 | 1593 | 5927 |
| 35 | 254 | 603 | 1613 | 963 | 407 | 230 | 201 | 113 | 972 | 5356 |
| 40 | 276 | 220 | 1109 | 1252 | 521 | 235 | 179 | 81 | 1021 | 4894 |
| 45 | 123 | 78 | 644 | 1237 | 484 | 217 | 141 | 81 | 891 | 3896 |
| 50 | 31 | 19 | 161 | 396 | 231 | 118 | 77 | 14 | 408 | 1455 |
| 55 | 0 | 0 | 0 | 0 | 0 | 0 | 1 | 0 | 1 | 2 |
| Total | 2795 | 29585 | 17475 | 10249 | 4700 | 4511 | 15483 | 6506 | 43284 | 134588 |

Table 3. Symbols

| | |
|---|---|
| $a$ | radius of earth |
| $g$ | acceleration of gravity |
| $n_{box}$ | number of observations in a 5° by 5° by 100 mb data collection 'box' |
| $u$ | local value of zonal wind component |
| $\bar{u}$ | time average of u |
| $[\ ]$ | zonal average (over all longitudes) |
| $[\ ]_s$ | zonal average weighted by the number observations |
| $v$ | local value of meridional wind component |
| $\bar{v}$ | time average of v |
| $\phi$ | latitude |
| $\psi$ | the pseudo streamfunction for meridional flow, strictly defined only for zonally symmetric flow |
| $\psi^*$ | a function proportional to $\psi$, but with $[\bar{v}]_s$ substituted for $[\bar{v}]$ |

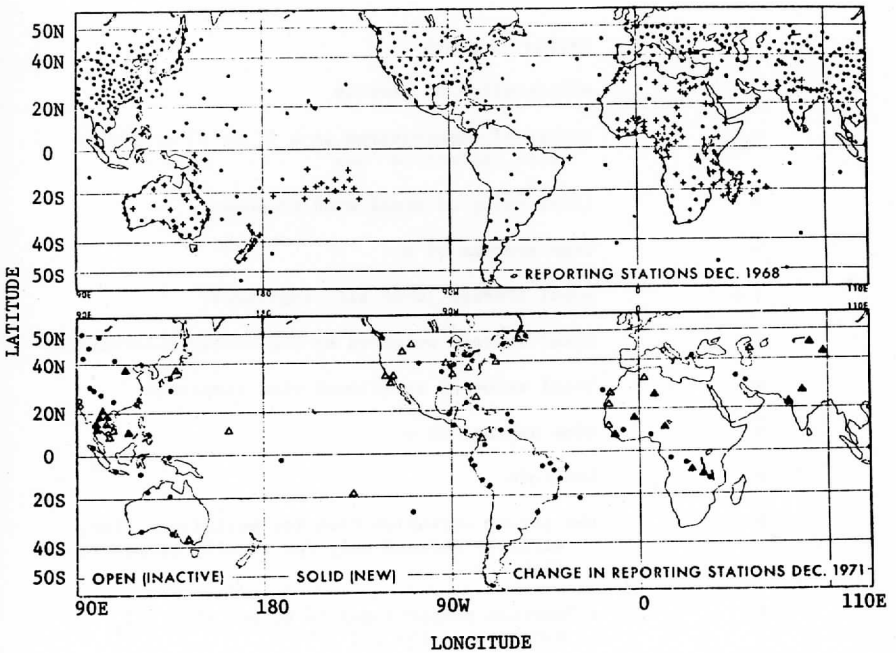


FIGURE 1: Top panel: Observation network for NMC tropical analysis. [Crosses: wind reports. Circles: rawin/radiosonde reports.] Bottom panel: Stations added or removed from network. [Solid triangles: wind stations added. Solid circles: rawin/radiosonde stations added. Open symbols: stations removed.]

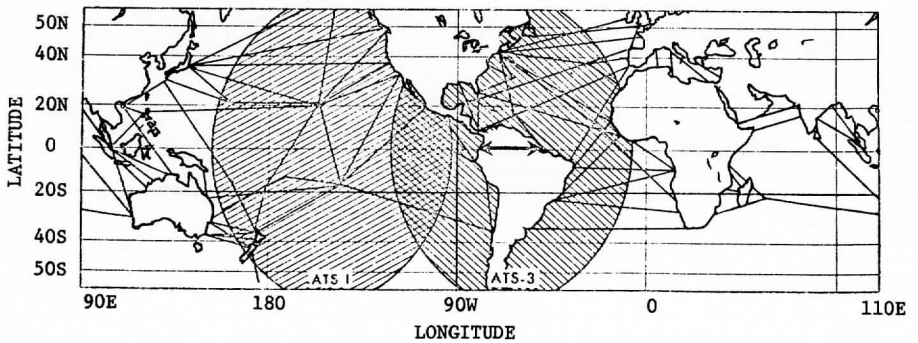


FIGURE 2: Principal intercontinental aircraft routes [solid lines] for which pilot wind reports are available; and the areas of coverage of ATS-1 and ATS-3 data [crosshatch] used by Gray et al.(1976).

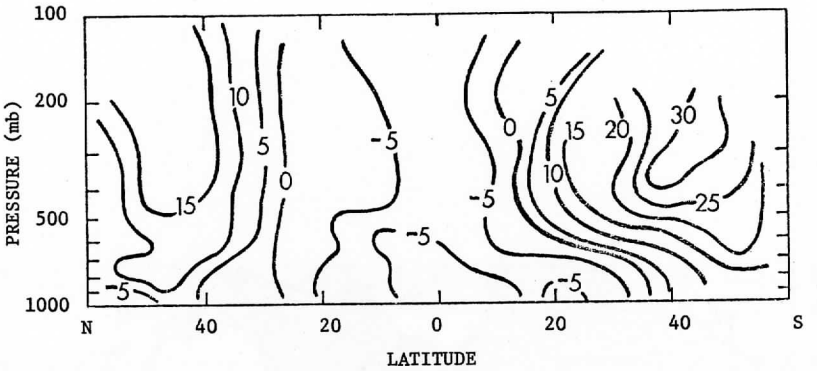


FIGURE 3: Zonally averaged zonal wind component, $[\bar{u}]_s$, for August-September 1975 ($m\text{-}s^{-1}$). Positive values denote winds blowing from west to east.

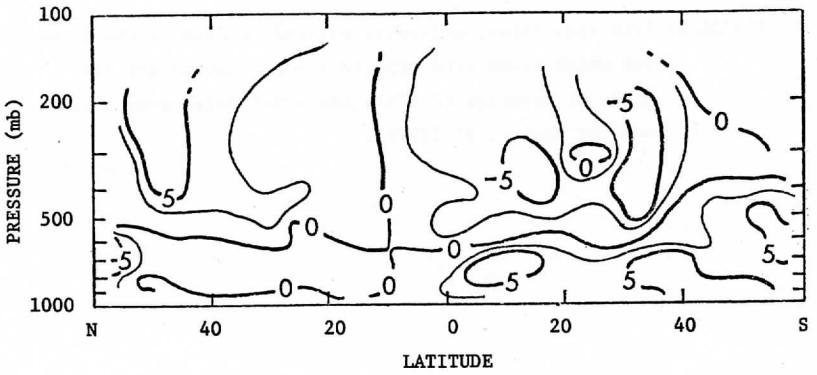


FIGURE 4: Zonally averaged meridional wind component, $[\bar{v}]_s$, for August-September 1975 ($m\text{-}s^{-1}$). Positive values denote winds blowing from south to north. Unlabeled contours are 2.5 and -2.5 $m\text{-}s^{-1}$.

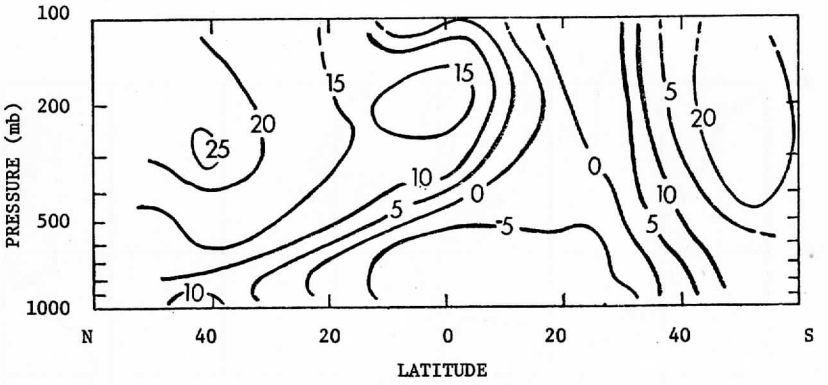


FIGURE 5: Zonally averaged zonal wind component, $[u]_s$ , for January-February 1976 ($m\text{-}s^{-1}$). Positive values denote winds blowing from west to east.

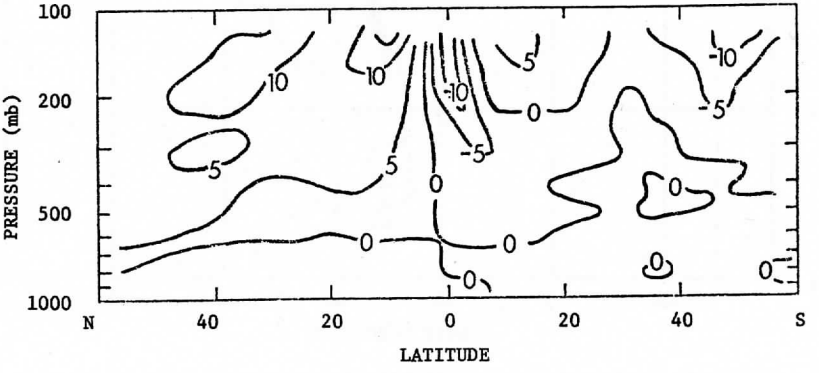


FIGURE 6: Zonally averaged meridional wind component, $[v]_s$ , for January-February 1976 ($m\text{-}s^{-1}$). Positive values denote winds blowing from south to north.

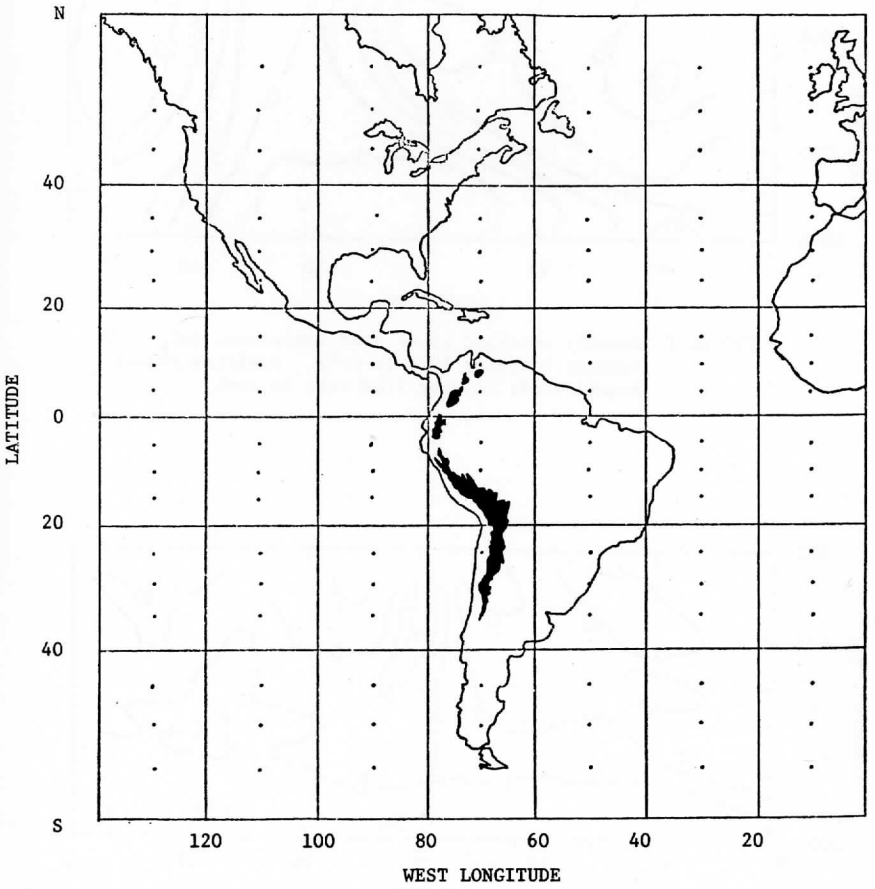


FIGURE 7: Surface features with height exceeding the 700 mb level.

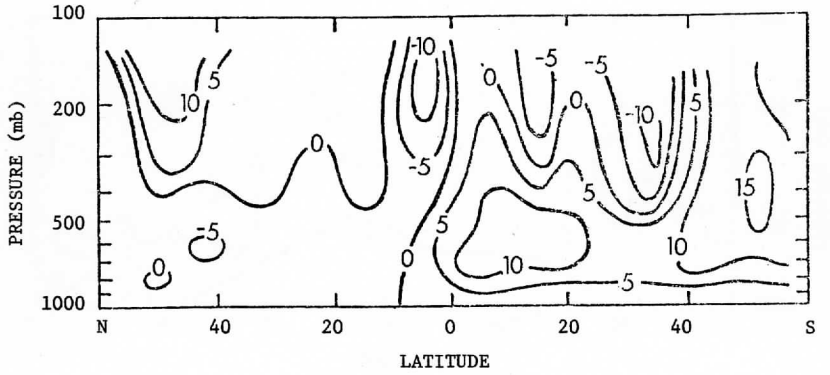


FIGURE 8: The pseudo-stream function, $\psi^*$, for August-September.

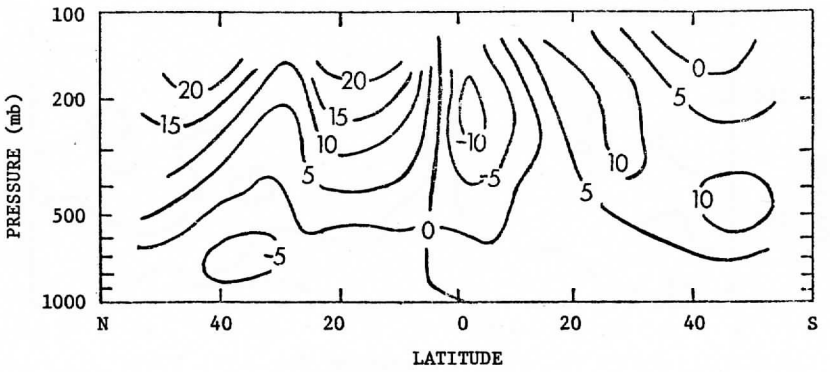


FIGURE 9: The pseudo-stream function, $\psi^*$, for January-February.

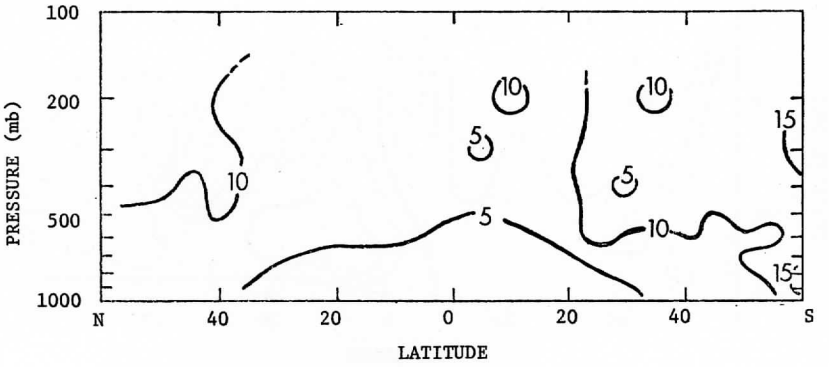


FIGURE 10: Standard deviation of the August-September zonal wind ($m\text{-}s^{-1}$).

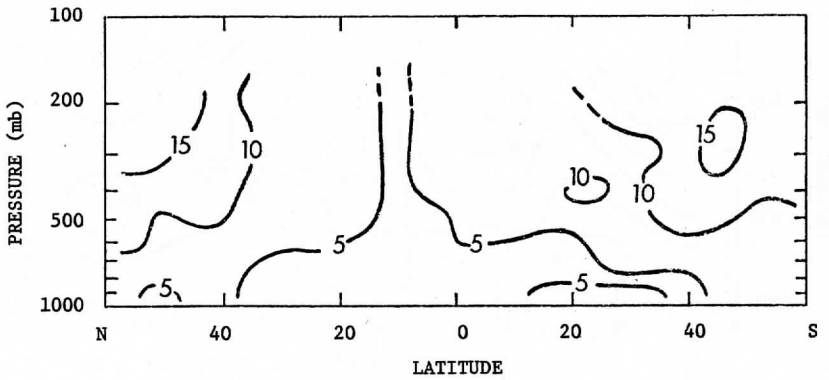


FIGURE 11: Standard deviation of the August-September meridional wind ($m\text{-}s^{-1}$).

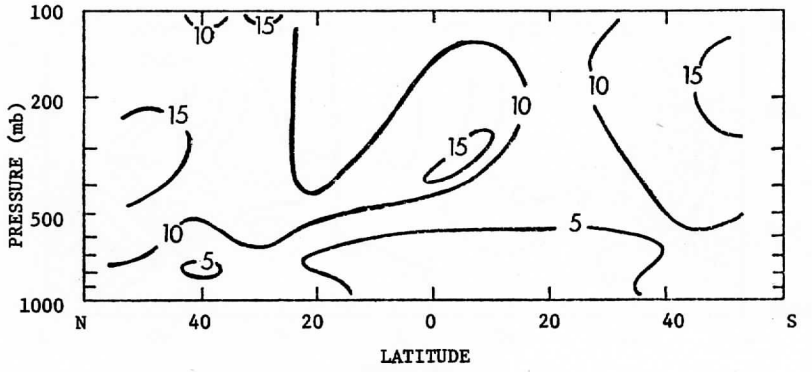


FIGURE 12: Standard deviation of the January-February zonal wind ($m\text{-}s^{-1}$).

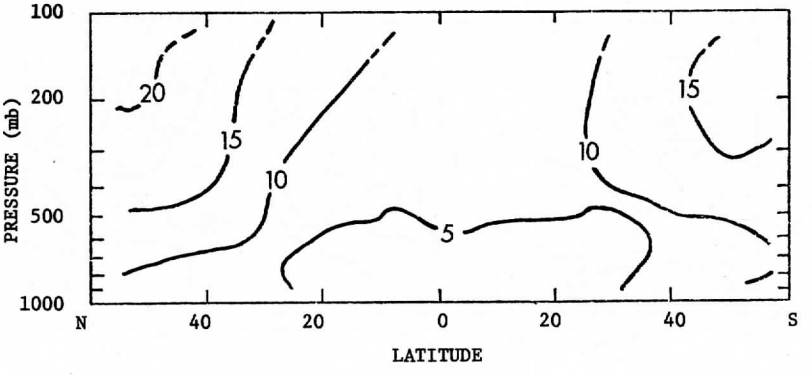


FIGURE 13: Standard deviation of the January-February meridional wind ($m\text{-}s^{-1}$).

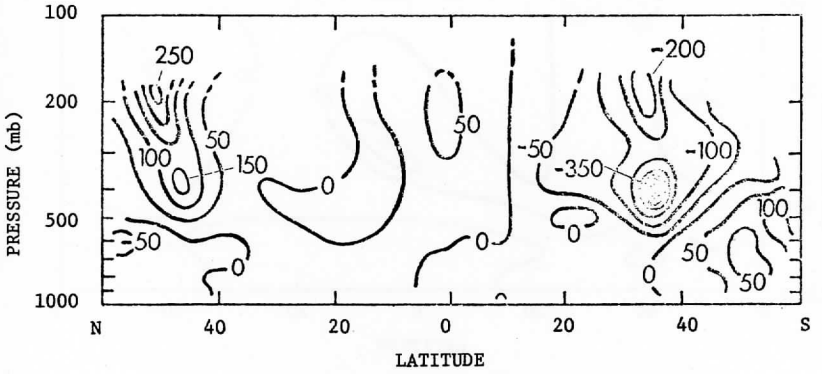


FIGURE 14: Meridional transport of zonal momentum, $[\overline{uv}]_s$ , for August-September ($m^2$-$s^{-2}$).

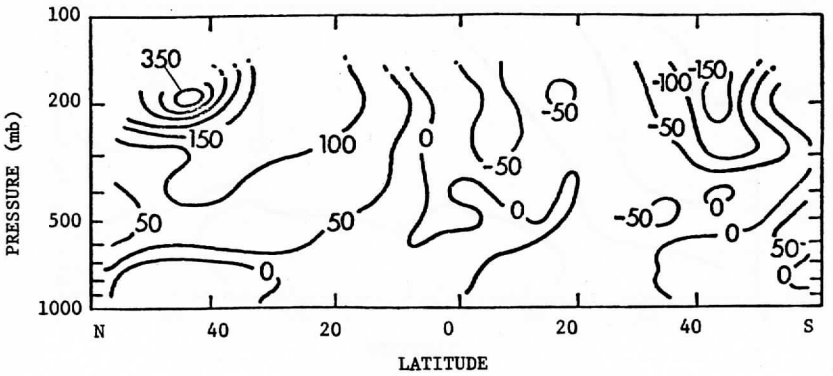


FIGURE 15: Meridional transport of zonal momentum, $[\overline{uv}]_s$ , for January-February ($m^2s^{-2}$).

## APPENDIX A

The Space Science and Engineering Center (SSEC) of the University of Wisconsin participated in the August-September 1975 Data Systems Test (DST) from August 16 through September 21. Winds were derived from cloud motions using SMS-1 image data in the American sector. Four data sets were produced each day. Out of a possible 142 data sets during this period, a total of 135 were produced.

SSEC also participated in the January-February Data Systems Test (DST) from January 5 through March 5. Cloud tracked winds were measured over the Pacific regions using SMS-2 images. Again, four wind sets per day were produced, and transmitted to the collection point at Goddard Institute of Space Sciences (GISS) in real time from January 16 through March 5, with only a few down-time periods due to equipment failure. An archive of the satellite images was kept for the entire DST period. Wind sets for the period January 5-15, and for the gaps due to equipment failure, were generated from images on archive tape after March 5 and transmitted to GISS. A complete 60-day wind set is available for DST analysis programs.

The cloud motions were measured on the McIDAS (Man-computer Interactive Data Access System). This is an image storage, display and processing system consisting of data archive, data access, video display, operator console and computer control sections. Central to the system is a computer which controls the display section, operator console, and computer peripherals. Data enters the system from an antenna on the roof of SSEC which receives the stretched SMS data. This data can either be archived on a special slant-track recorder, or used in real time. The data is re-formatted by the computer into standard analog TV format and is transferred to an analog video refresh disk. The registration of images is done by using a predictive navigation system. This navigation is capable of predicting the position of every pixel 24 hours in advance with an accuracy of approximately one pixel. This predictive navigation and ingestion system is capable of producing aligned sequences of images in real time so that, when the satellite finishes sending the images, they are ready immediately for cloud wind tracking.

Tracking may be done by either of two primary methods: cursor tracking of the cloud to the nearest TV line and element (pixel tracking); or image match tracking to obtain better resolution (correlation tracking). Pixel tracking has been facilitated by the addition of a function called the velocity cursor. The operator positions a cursor over the cloud to be tracked using a "joy stick". The velocity cursor function then automatically displaces the cursor from one picture to the next, according to the position of a second joy stick.

Correlation tracking requires the operator to roughly track the cloud by placing the cloud within a box for each picture in a set. The computer then performs a correlation analysis to align the brightness field and "fine-tune" the operator's tracking. Correlation tracking is more accurate than pixel tracking, but it requires well-defined clouds moving in a single layer flow. Single pixel tracking can be invoked by the operator for tracking in multi-layer flow, or for matching the motion of the cursor to the motion of a pattern of clouds if individual clouds cannot be tracked.

Quality control can be applied to the derived wind measurements in several ways. The measurement can be made twice, using three images. Wind measurements which do not agree within an operator-set residual criteria are flagged to be in error. The height measurement also is made twice. If, during correlation, the best match of the two images occurs on the boundary of the data matrix, the data is also flagged.

The operators-- all meteorologists -- were instructed to make measurements which would describe the meteorology of the situation with as many levels as possible. They were to use their own judgement about what would produce the best results for a given situation.

The August-September 1975 DST was very successful in terms of the operational gathering of large numbers of wind vectors from cloud motions. All was not perfect, however. During the DST two major failures of equipment had to be overcome without disrupting operations.

Another area which needed improvement was the placement of the height of the wind vector. Evaluation of the placement of the winds by NESS showed that the level could be more than 100 mb off if climatic soundings rather than synoptic soundings were used for the temperature-to-height conversion. Since world-wide synoptic sounding data is not available at Wisconsin, the temperature-to-height conversion was carried out by GISS for the January-February DST. Each wind vector sent from Wisconsin was tagged with a cloud-top temperature and a cloud thickness estimate.

The cloud-top temperature was obtained using the visible data to determine the emissivity and correcting the infrared data with this emissivity. If only infrared data was available, the coldest part of the cloud was used as the temperature estimate. Frequently the operators would determine the cloud-top temperature of a denser cloud and then manually assign this temperature to all the clouds moving with the same general speed and direction as this dense cloud. This would overcome many of the problems of determining the temperature of thin clouds from IR-only data.

When visible data was available, the visible optical thickness was used to determine physical thickness of the cloud. An empirical conversion factor was derived using stratus clouds over the U.S. during winter. This factor was applied to all types of clouds, even though the theoretical

validity is only for clouds with horizontal extent much larger than vertical. The curves of optical thickness vs. brightness essentially saturate at large optical thicknesses. Cloud thicknesses greater than 5 km were not obtainable, so that the thicknesses of very deep clouds were underestimated. The thickness of very thin clouds (less than .5 km) was overestimated slightly.

When no visible data was available, the thickness estimation was difficult because there was no inherent thickness information in IR data. All clouds above 550 mb were assigned arbitrarily a thickness of 100 m. Otherwise the thickness estimate was obtained by taking the height difference between the warmest and the coldest parts of the cloud being tracked. For trade wind cumulus, this agreed closely with the thickness determined from the visible data. For stratus clouds, this infrared technique would frequently overestimate the thickness of the cloud, so the operators would sometimes modify the thickness calculation for stratus clouds.

The conversion of the temperature and thickness into height of the wind was performed at GISS using the most recent global analysis. The time of this analysis would generally differ from the time of the wind vectors by 18 to 24 hours. The problem of where to put the wind vector within the cloud also was difficult. The procedure used was to obtain the height of the top and bottom of the cloud from synoptic analysis. If the bottom of the cloud was below 850 mb, the wind was placed at the bottom of the cloud. If the resultant height was below 950 mb, the vector was placed at 950 mb. If the top of the cloud was above 300 mb, the wind vector was placed at the top of the cloud. All other vectors were placed at the middle of the cloud.

The Write Random, Read Rastor Memory (WRRRM) is an overlay device which permits the plotting of wind vectors over the cloud being tracked as soon as the computation of the wind has been completed. This gives instant feedback to the operator, since he can see the wind field develop as he works. One of the problems with the August-September DST was that where the clouds presented easy targets, the operators had a tendency to "overkill." To help the operator gauge the density of wind measurements, a grid of latitude, longitude and continental boundaries was put on the WRRRM. The combination of the real time vector feedback and the spacing of the vectors within the grids avoided redundant measurements that did not add to the meteorological information in an area.

To estimate the coverage of the wind sets, the number of $5^{o}$ square GARP grids which had at least one wind measurement was calculated for each set. If one considers $50^{o}$ from the sub-satellite point as the maximum useable zenith angle, there are a possible 314 GARP grids visible from a single satellite. A $55^{o}$ useable angle results in a possible 380 GARP grids. During this DST, an average of 346 GARP grids per wind set had at least one wind measurement. The number of GARP grids with measurements increased throughout the DST. During the first half, an average of 324 grids had measurements. During the second half, the average was 364. To compare

this with the August-September coverage, a one-week sample of the August-September data from the middle of the DST (days 236 to 241) was examined. An average of 324 GARP grids had wind measurements for this period. Figs. A1, A2 and A3 show the coverage available on a typical day at high, middle and low levels.

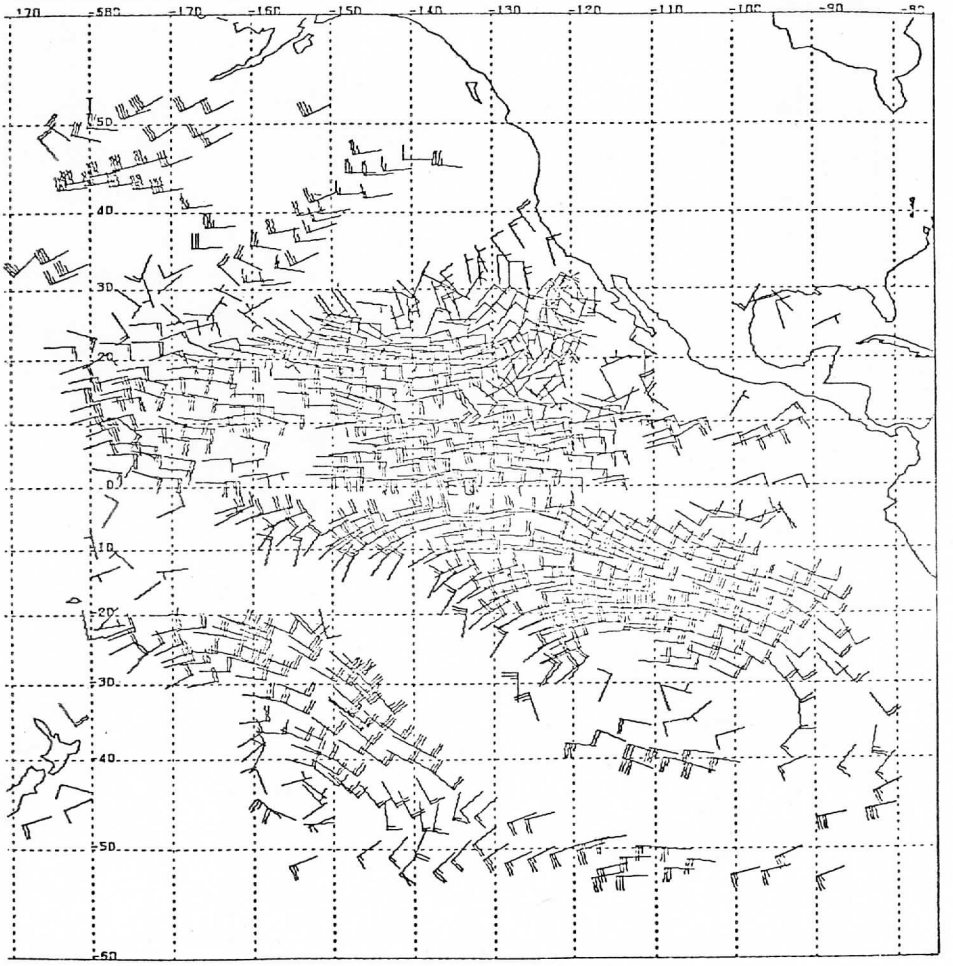


FIGURE A1: Low Level Winds for 11 February 1976.

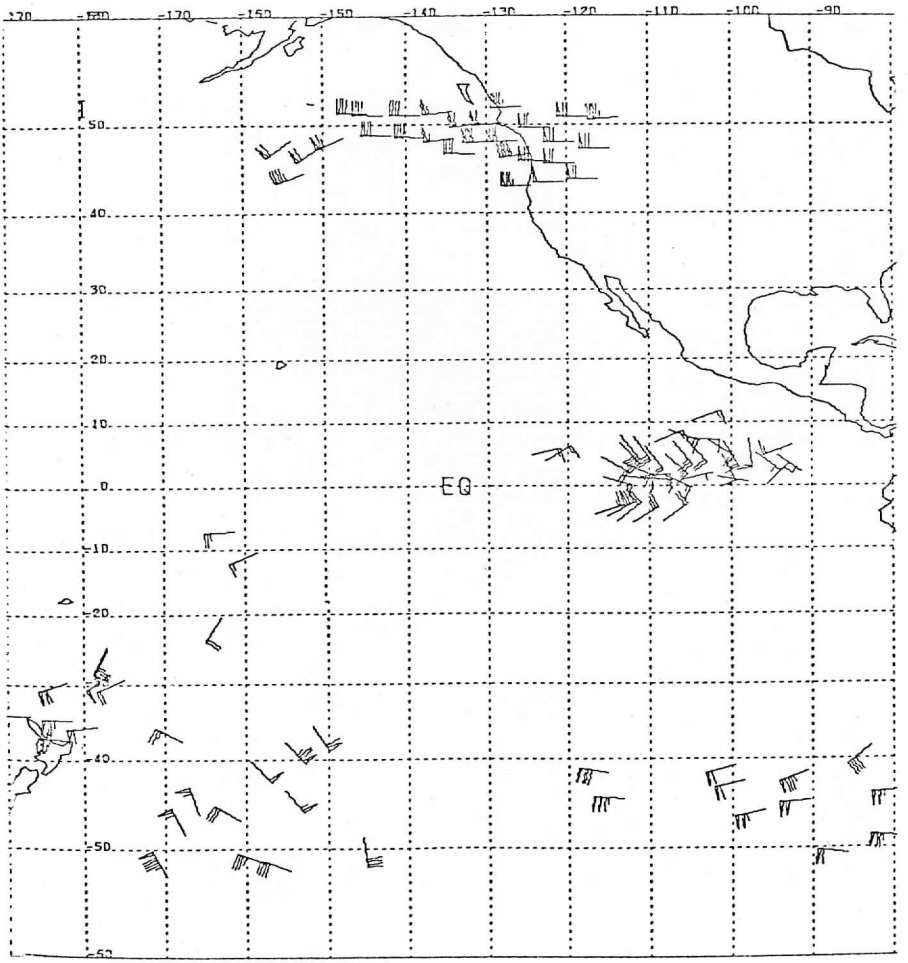


FIGURE A2: Mid-Level Winds for 11 February 1976.

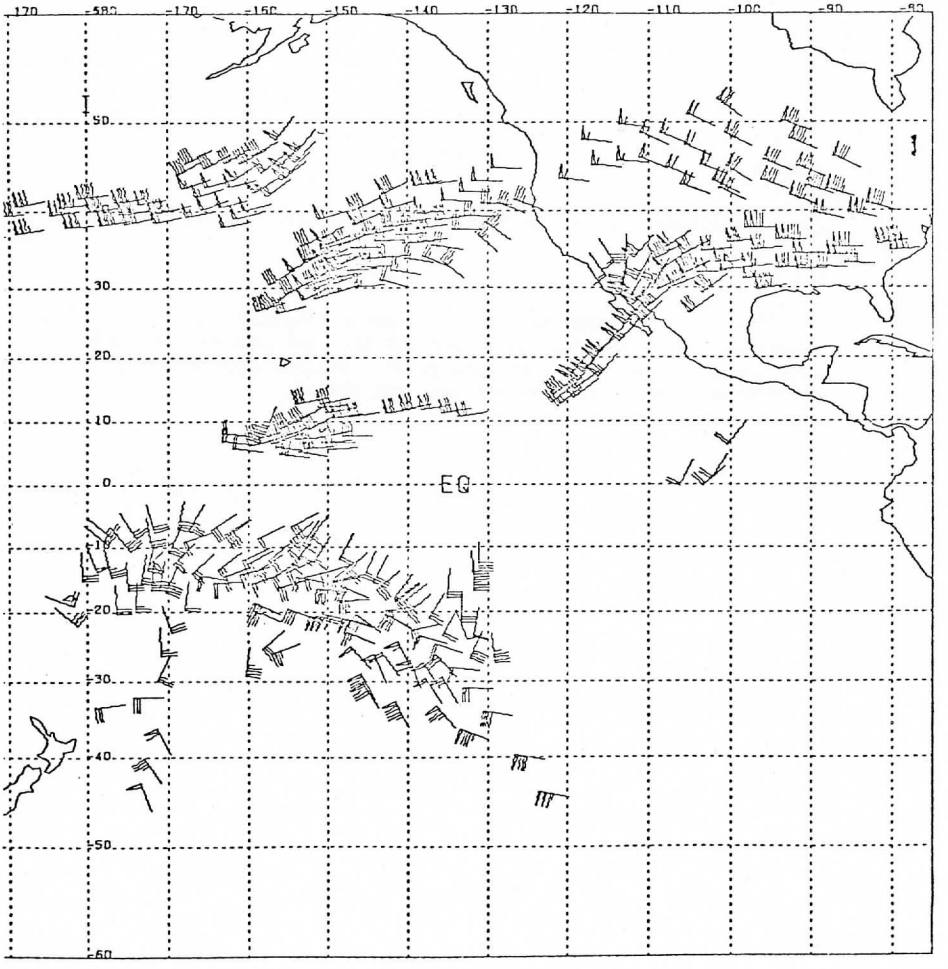


FIGURE A3: High Level Winds for 11 February 1976.

## APPENDIX B

### Latitude - Longitude Variation of the Wind Components

Figures B1 through B4 show the u and v components for the August-September data at 700 mb and 200 mb. The January-February data are shown in Figures B5 through B8. Regions with no data, or with fewer than ten observations, are shaded.

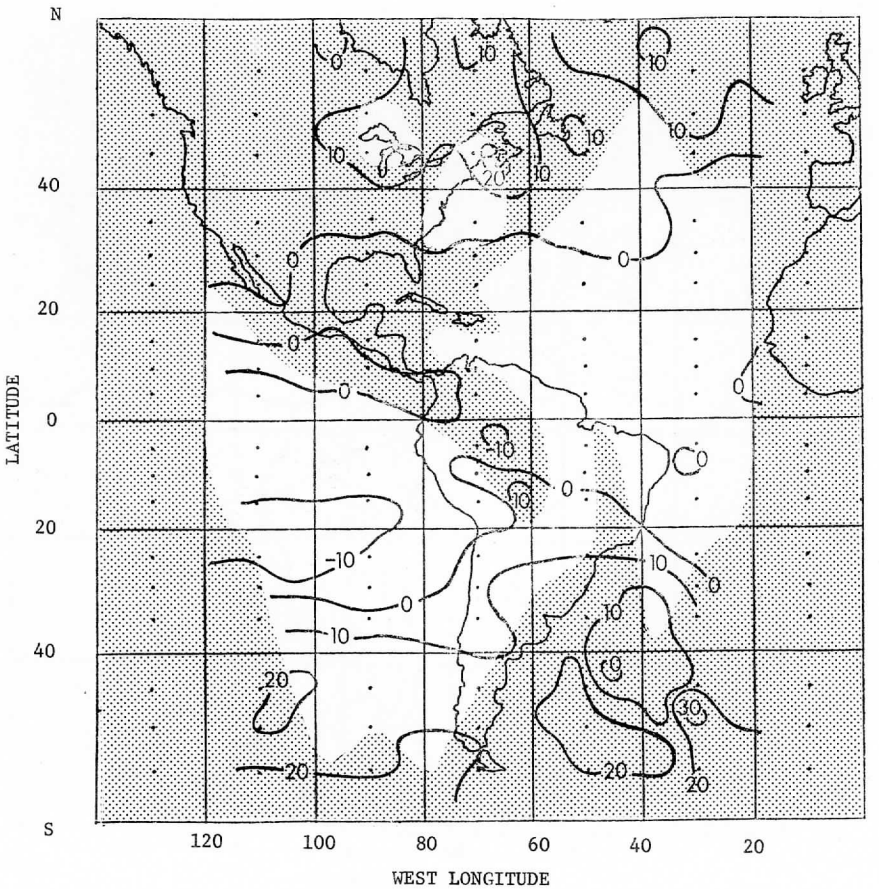


FIGURE B1: The August-September zonal velocity component, $\bar{u}$ , at the 700 mb level ($m\text{-}s^{-1}$).

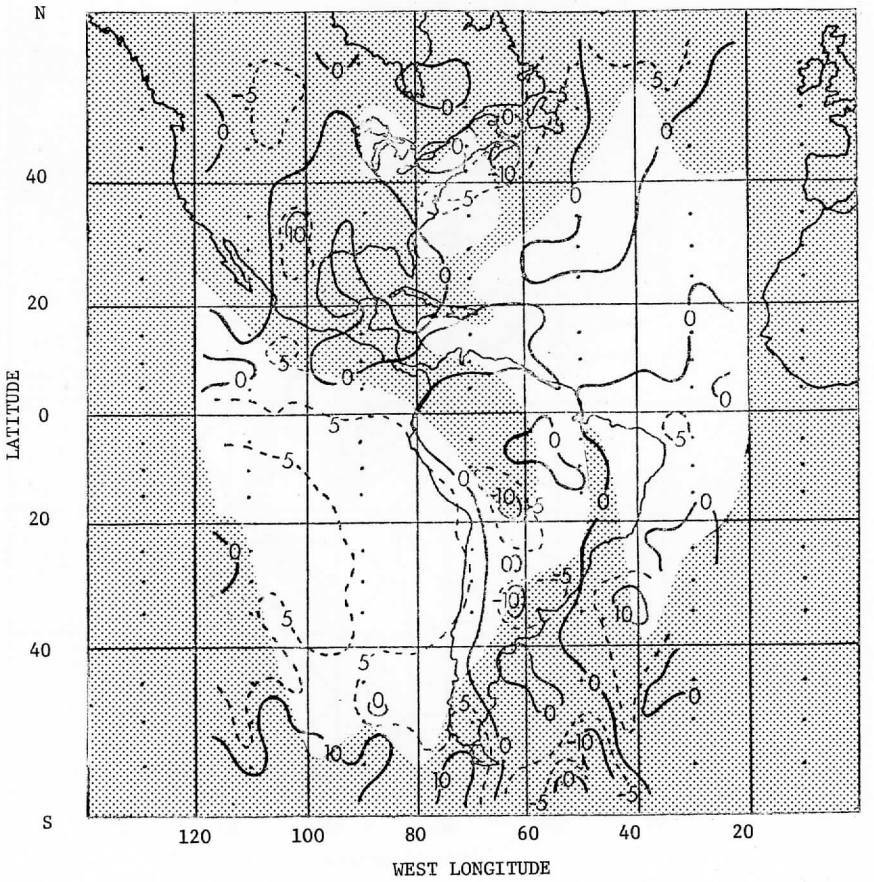


FIGURE B2: The August-September meridional velocity component, $\bar{v}$ , at the 700 mb level ($m\text{-}s^{-1}$).

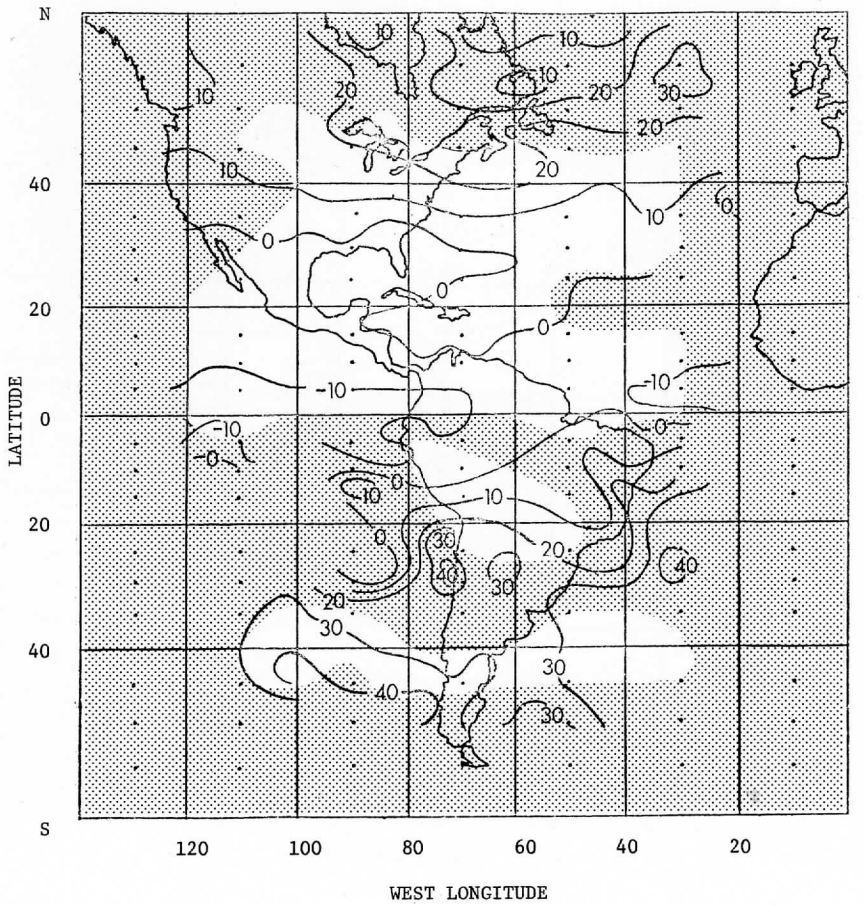


FIGURE B3: The August-September zonal velocity component, $\bar{u}$ , at the 200 mb level ($m\text{-}s^{-1}$).

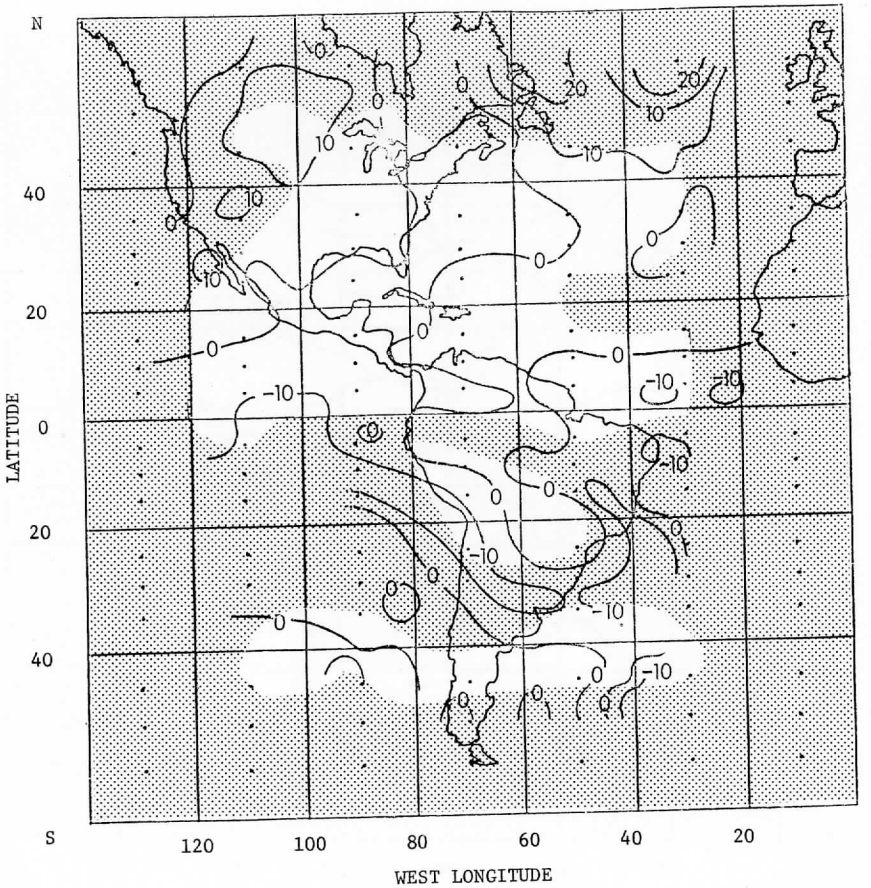


FIGURE B4: The August-September meridional velocity component, $\overline{v}$ , at the 200 mb level ($m\text{-}s^{-1}$).

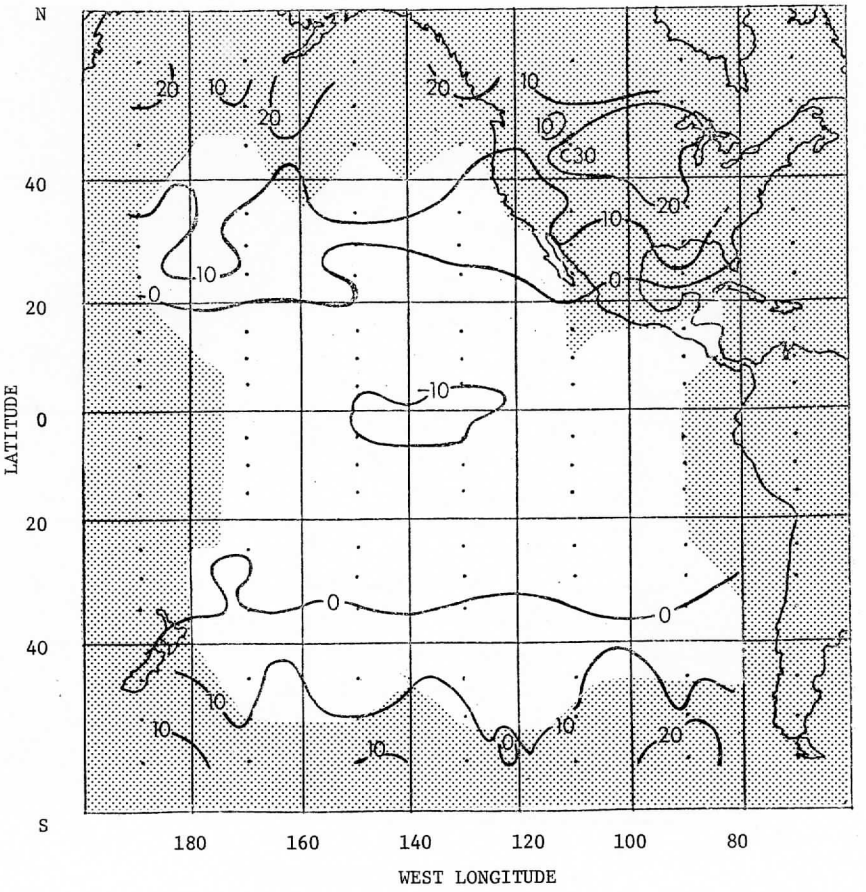


FIGURE B5: The January-February zonal velocity component, $\bar{u}$, at the 700 mb level ($m\text{-}s^{-1}$).

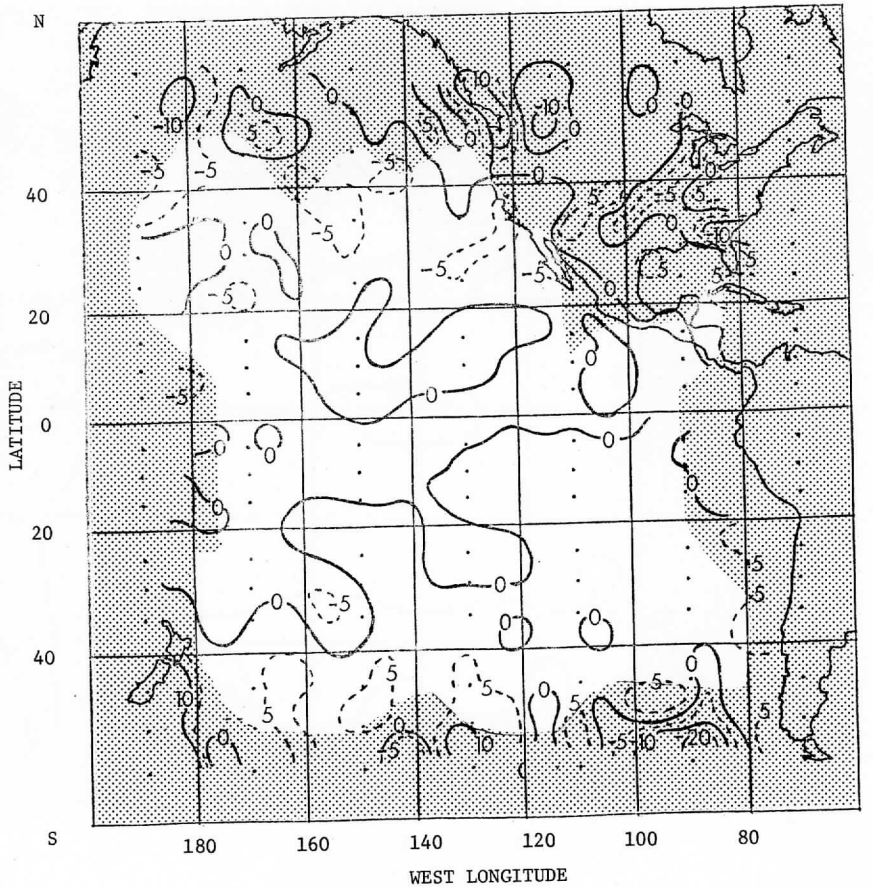


FIGURE B6: The January-February meridional velocity component, $\overline{v}$, at the 700 mb level ($m\text{-}s^{-1}$).

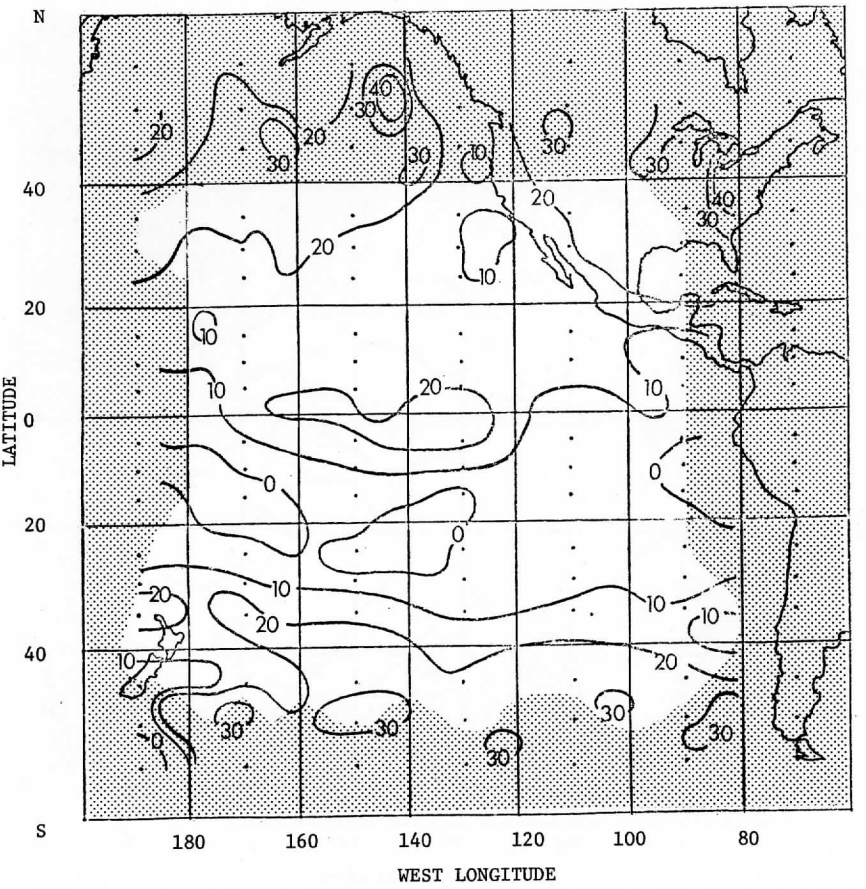


FIGURE B7: The January-February zonal velocity component, $\bar{u}$ , at the 200 mb level ($m\text{-}s^{-1}$).

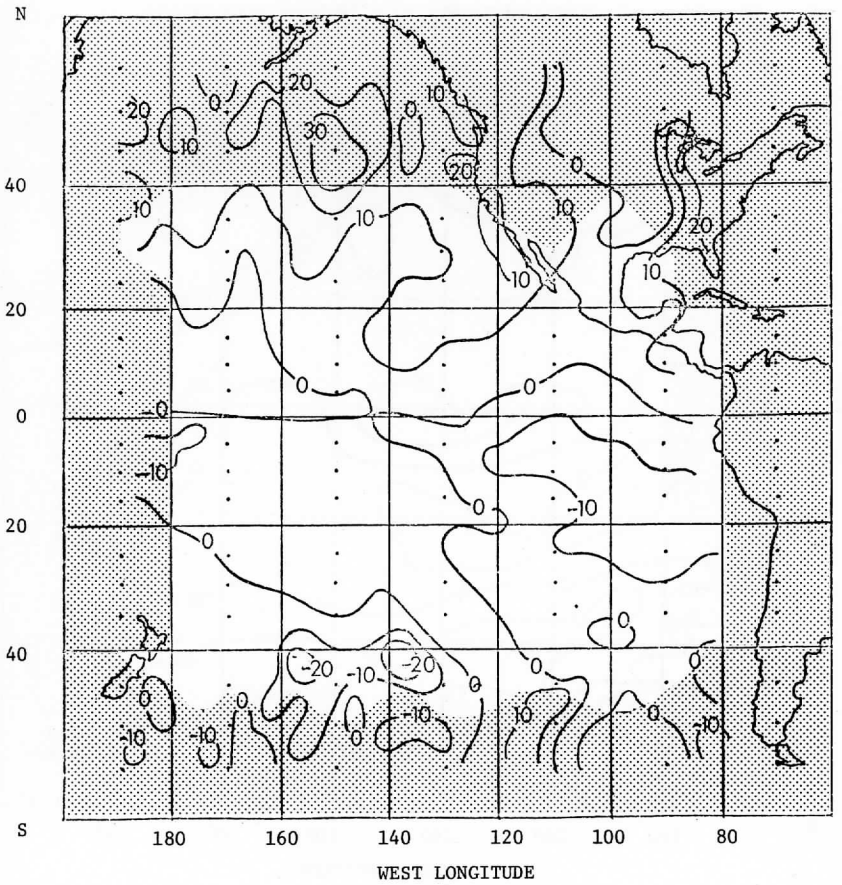


FIGURE B8: The January-February meridional velocity component, $\overline{v}$ , at the 200 mb level ($m\text{-}s^{-1}$).

# APPENDIX C

## Seasonal Comparison Data

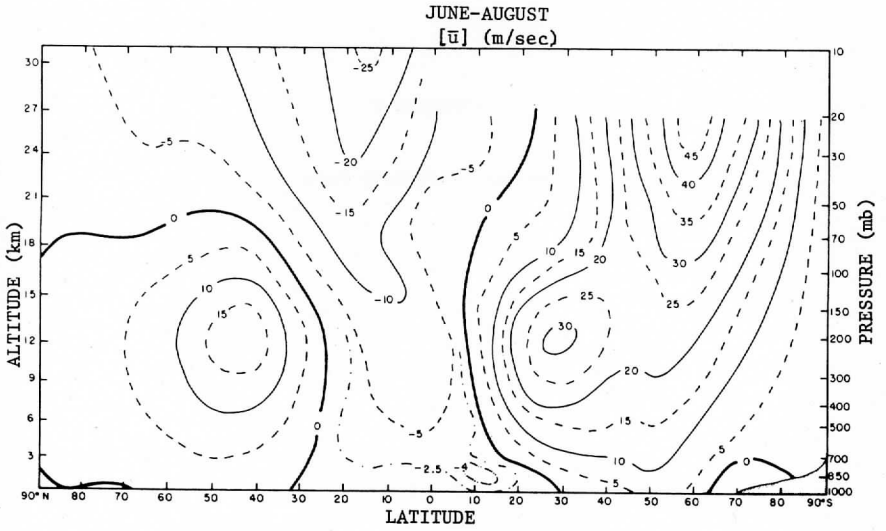


FIGURE C1: The June - August zonally averaged zonal wind.
(from Newell et al., 1972)

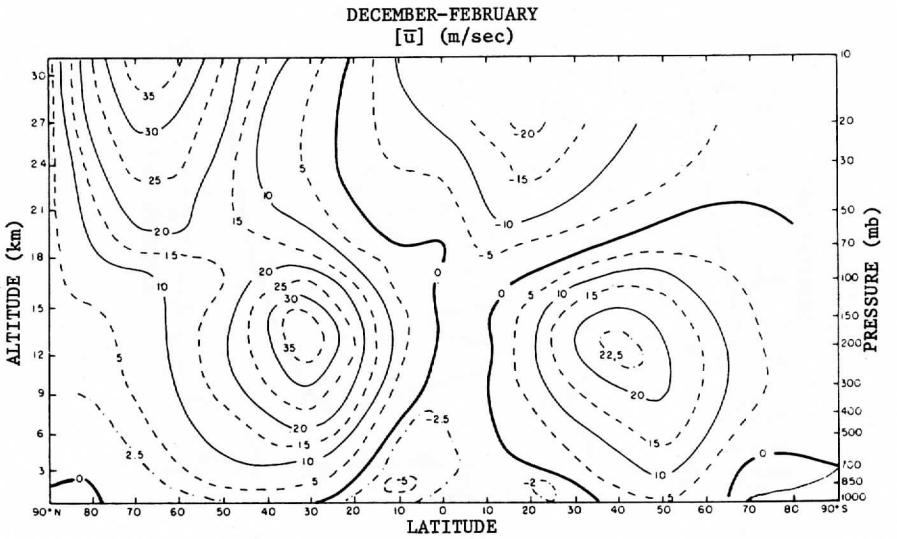


FIGURE C2: The December - August zonally averaged zonal wind.
(from Newell et al., 1972)

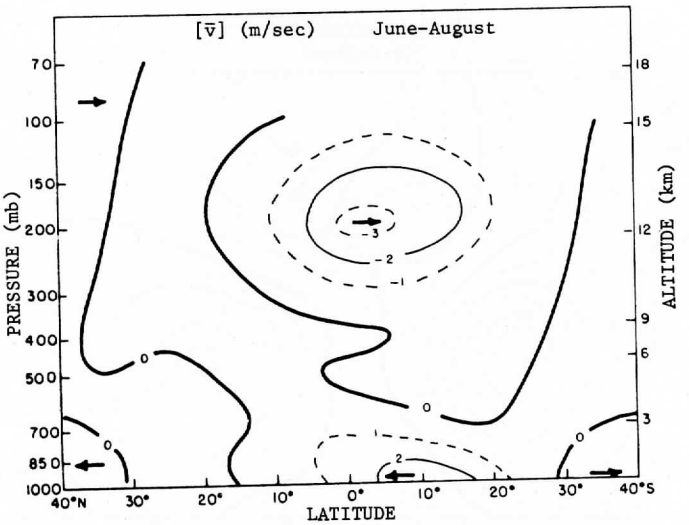


FIGURE C3: The June-August zonally averaged meridional wind. (from Newell et al., 1972)

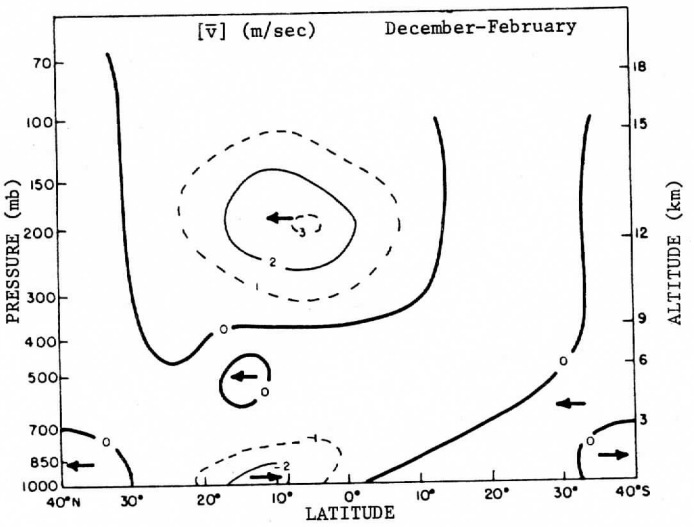


FIGURE C4: The December-February zonally averaged meridional wind. (from Newell et al., 1972)

(continued from back cover)

97042. Experiments in Medical Communications via the ATS-1 Satellite. 136 pages. 1972. $7.50

97043. Specifications for a Vertical Temperature and Moisture Sounder for the Synchronous Meteorological Satellites. 82 pages. 1972. $5.00

97044. Scientific Requirements of Sea Surface Measurements for the GARP Tropical Experiment. 18 pages. 1972. $2.50

97045. Studies of the Atmosphere Using Aerospace Probings: Annual Report, 1971, Vol. II: Application Studies. 104 pages. 1972. $5.00

97046. Multidisciplinary Studies of the Social, Economic and Political Impact Resulting from Recent Advances in Satellite Meteorology: An Interim Report, Vol. 3. 252 pages. 1972. $10.00

97047. Multidisciplinary Studies of the Social, Economic and Political Impact Resulting from Recent Advances in Satellite Meteorology: An Interim Report, Vol. 4. 199 pages. 1972. $10.00

97048. Satellite Teleconferencing: An Annotated Bibliography. 130 pages. 1972. $7.50

97049. Measurements from Satellite Platforms: Annual Scientific Report on NAS5-11542, 1971-72. 228 pages. 1972. $7.50

97050. Synchronous Meteorological Satellite Sounder Specification: Final Report under NASA Contract NAS5-21607. 73 pages. $5.00

97051. Multidisciplinary Studies of the Social, Economic and Political Impact Resulting from Recent Advances in Satellite Meteorology: An Interim Report, Vol. 5. 290 pages. 1973. $10.00

97052. Measurements from Satellite Platforms: Annual Scientific Report on NAS5-21798, 1972-73. 331 pages. 1974. $10.00

97053. Visual Channel Data Analysis for Synchronous Meteorological Satellite: Scientific Report on NOAA/NESS Grant NG-26-72. 252 pages. 1974. $7.50

97054. Studies of the Atmosphere Using Aerospace Probes. Annual Report, 1973. 272 pages. 1974. $7.50

97055. Meteorological Measurements from Satellite Platforms: Annual Scientific Report on NAS5-21798, 1973-74. 97 pages. 1975. $5.00

97056. Studies of the Atmosphere Using Aerospace Probes. Annual Report, 1974. 154 pages. 1975. $5.00

97057. Multidisciplinary Studies of the Social, Economic and Political Impact Resulting from Recent Advances in Satellite Meteorology: Final Report, Vol. 6. 100 pages. $10.00

97058. Studies of the Atmosphere Using Aerospace Probes. Annual Report, 1975. 91 pages. $7.50

REPORTS AVAILABLE FROM

THE UNIVERSITY OF WISCONSIN PRESS, BOX 1379, MADISON, WISCONSIN 53701

---

97024. Studies in Atmospheric Energetics Based on Aerospace Probings: Annual Report, 1966. 129 pages. 1967. $5.00

97026. Studies in Atmospheric Energetics Based on Aerospace Probings: Annual Report, 1968. 162 pages. 1969. $5.00

97027. Radiation Experiment in the Vicinity of Barbados: Final Report, NSF Grant Ga. 12603. 100 pages. 1970. $5.00

97028. The Study of Radiation in a Tropical Atmosphere: Final Report. 100 pages. 1970. $5.00

97029. The Educational and Social Uses of Communications Satellites: A Bibliography. 42 pages. 1970. $3.50

97030. Measurements from Satellite Platforms: Annual Scientific Report on NAS5-11542, 1968-69. 388 pages. 1970. $10.00

97031. A Pilot Study on the Application of Geosynchronous Meteorological Satellite Data to Very Short Range Terminal Forecasting. 113 pages. 1970. $5.00

97032. Studies of the Atmosphere Using Aerospace Probings: Annual Report, 1969. 243 pages. 1970. $7.50

97033. Teleconferencing: A Bibliography. 42 pages. 1971. $3.50

97034. Legal and Political Aspects of Satellite Telecommunication: An Annotated Bibliography. 126 pages. 1971. $7.50

97035. Multidisciplinary Studies of the Social, Economic and Political Impact Resulting from Recent Advances in Satellite Meteorology: An Interim Report, Vol. 1. 459 pages. 1971. $15.00

97036. Multidisciplinary Studies of the Social, Economic and Political Impact Resulting from Recent Advances in Satellite Meteorology: An Interim Report, Vol. 2. 431 pages. 1971. $15.00

97037. Measurements from Satellite Platforms: Annual Scientific Report on NAS5-11542, 1969-70. 180 pages. 1971. $7.50

97038. Studies of the Atmosphere Using Aerospace Probings: Annual Report, 1970. 69 pages. 1971. $5.00

97039. Legal Aspects of Satellite Teleconferencing. 213 pages. 1971. $7.50

97040. Teleconferencing in Wisconsin. 240 pages. 1971. $10.00

97041. Measurements from Satellite Platforms: Annual Scientific Report on NAS5-11542, 1970-71. 270 pages. 1972. $10.00